

**Synthesis and Characterization of Boron Nanotubes and
other Related Boron Nanomaterials by Dual Pulsed Laser
Ablation**

By

Adebisi Mufutau Amobi

Supervisor: Dr. Mathew K. Moodley

A Dissertation in the Discipline of Physics.

School of Chemistry and Physics

College of Agriculture, Engineering and Sciences

In partial fulfillment of the requirements for the Degree of

Doctor of Philosophy

In the University of KwaZulu - Natal

Westville, Durban, South Africa

August 2019

DECLARATION

I declare that this dissertation is original work and is being submitted for the degree of Doctor of Philosophy at the University of KwaZulu – Natal, School of Chemistry and Physics, Westville Campus, Durban, South Africa. This dissertation has not been submitted before for any degree or examination at any other University.



26 / 08 / 2019

Adebisi Mufutau Amobi

ABSTRACT

Developments in nanotechnology in the last 30 years have provided the increasing usage of nanostructured particles in many applications. Boron nanomaterials (BNMs) are a good example of such nanoparticles. The uniqueness of boron nanomaterials set it apart from other similar nanomaterials. It has a wide field of promising applications ranging from quantum computing to materials science and medicine. Quasi-one-dimensional nanomaterials like nanowires, nanotubes, bamboo-like – nanotubes, nanosheets, nanoribbons, and nanorods are of great interest in fundamental research as well as their potential uses in many technological applications, such as field emitters, electronics, pharmaceutical, and novel circuitry elements, sensor devices and after appropriate functionalization in biomedical due to their applications.

In this dissertation, the laser furnace technique was utilized to study the synthesis of boron nanomaterials. In the study, we achieved the synthesis of single-walled boron nanotubes and among other nanostructured materials of boron such as bamboo like – nanotubes, nanowires, and nanorods. These kinds of nanomaterials were synthesized through the use of the dual pulsed laser ablation technique. Experiments were conducted in a tube furnace. The boron composite target was ablated by sequential 1064 and 532 nm laser pulses at a furnace temperature of 1000 °C or 1100 °C in argon/nitrogen gas using different pressure and flow rates.

The investigation involved varying the parameters such as gas pressure, gas flow rate, and furnace temperature. We observed the effect of varying these parameters on the synthesis of boron nanomaterials. To verify these effects, the as – prepared boron nanomaterials were characterized by scanning electron microscopy (SEM), high-resolution transmission electron microscopy (HRTEM), X-ray diffraction (XRD), Raman spectroscopy (RS), ultraviolet-visible (UV- VIS), photoluminescence (PL) and vibration sample magnetometer (VSM). It was found that the variation of the argon/nitrogen pressure and flow rate influence the quantity, quality and type of the as-prepared boron nanomaterials, since these parameters affected the plasma dynamics. The low flow rate and low pressure reduced the cross section for a collision between the plasma constituents, in particular, between the boron atoms and the metal catalysts which affected the probability of nucleation and growth of boron nanomaterials.

The temperature was found to be the critical process parameter in the nucleation and the growth of boron nanomaterials. It was found that as the synthesis temperature increased to 1100 °C, there is also an increase in the nucleation and the growth of boron nanomaterials. It was discovered that an argon/nitrogen pressure of 400 Torr, the flow rate of 200 sccm and temperature of 1100 °C produced more boron nanomaterials at a rate of 100 mg/h with the highest quality of single-walled boron nanotubes (SWBNTs) with diameters ranging from 0.4 to 2.0 nm and 2.0 microns in length.

The density gradient ultracentrifugation was carried out on boron as – prepared nanomaterials which resulted in the separation into different diameters of single-walled boron nanotubes. It was discovered that SWBNTs with smallest diameters of about 1.43 nm were found at the lower density, while the SWBNTs with larger diameters of 2.05 nm were obtained at higher density. These diameters were obtained by HRTEM analyses and the length up to one micrometer was also observed. The lattice fringes of 0.34 nm were found by HRTEM imaging in bamboo like-nanotubes, nanowires and nanorods. The lattices spacing from the fringes is consistent with the recent theoretical calculations of bulk boron of 0.35 nm. SEM analyses revealed the tubular and spherical structures of SWBNTs synthesized. XRD results showed that α – boron and β – boron were the solid phases formed in the products. It was observed that the crystallinity and size of the materials increased with an increase in furnace temperature. Raman analyses showed certain peaks below 500 cm^{-1} , which is attributed to tubular structures similar to the peaks observed in a single-walled carbon nanotube. Raman peaks attributed to α – boron cluster was also observed at 788, 878 and 965 cm^{-1} , confirming that SWBNTs formed from most stable sheets of α – boron. The statistical analyses of width distributions of the synthesized SWBNTs revealed variations in their diameters obtained according to each sample layer. The strong exciton absorption peak SWBNTs around 279 nm was revealed by UV-VIS results, while the luminescence of SWBNTs was found around 332 nm with photoluminescence analyses. Ferromagnetic properties of SWBNTs materials at room temperature were determined through VSM measurements. Finally, a simple model of vapour liquid solid (VLS) mechanism process has been developed to describe the formation of the SWBNTs.

CERTIFICATION

I certify that this work was carried out by Mr. M.A. Adebisi in the Discipline of Physics, University of KwaZulu – Natal, School of Chemistry and Physics, Westville Campus, Durban, South Africa.



26 / 08 / 2019

Dr. Mathew K. Moodley
Ph.D.(Wits)
School of Chemistry and Physics
Discipline of Physics
University of KwaZulu-Natal, Durban.

DEDICATION

This research is dedicated to Almighty Allah, the most merciful.

ACKNOWLEDGMENTS

First and foremost, I am grateful to the Almighty Allah for his protection that cannot be quantified throughout the period of this research.

I wish to express my profound gratitude to my honorable supervisor, Dr. M.K. Moodley, for his financial assistance, guidance, constructive criticisms, generosity and for developing the spirit of success in me during the period of my research. My prayer is that God will continue to bless him and his family always.

My special thanks go to the Council for Scientific and Industrial Research (CSIR) who provided the instruments for my research in boron related nanomaterials and the Thuthuka NRF for their financial support for the success of my research work

A million of thanks go to my great father Prof. J.O. Obemeata who painstakingly supporting me in my research both spiritually and financially.

I appreciate the relentless effort of my loving mother for making me what I am today. May Almighty Allah let her live longer to reap the good fruits she had laboured on me.

I also acknowledge my great brother Dr. Adebisi Dauda Akanji, who has been supporting me as my father since, before and after the death of my father. I pray that Almighty Allah will continue providing for him and his entire family.

My conscience will not be at rest if I fail to thank my dearest one, Mrs Ganiyu Fatima, Mrs Adebisi E.F., Mr. Adebisi.A.A, Dr. Azeez .S.A, Mrs Azeez R.A, Mrs Oladosu K.A, Mr Oladosu D.T, Mr Sulaiman S.A, Iya Aisha, Adebisi Saheed, Ganiyu Adekunle, Oladosu Musirafat, Adebisi Idayat, Adebisi Sofiyat, Adebisi Quoseem Adebisi Abass, Adebisi Abebat and all other members in the family which I cannot mention for their tremendous assistance towards the completion of this research, Almighty Allah will be with you all.

A trillion of thanks goes to my beloved wife and children, Mrs. Adebisi Tohibat and Azeezat and Abdulsalam for their total support for the success of my career. I pray that Almighty Allah makes them great on the surface of the earth and successful.

I wish to express my sincere gratitude to my colleagues most importantly Mr. Patrick Itegbeyogene, Mr. Olabisi, Mr. Hassan, Mr. Taiwo and Mr. Abdul Rasheed for their valuable time and effort on the series of prayers for the success of this work.

I also want my appreciation to some of the MSc students of the Department of Physics, most especially those who participated in setting up the laboratory, special thanks to Mr. Mkoma Kingu and Mr. Victor Anyanwu.

I wish to express my profound appreciation to my friends Alfa Abdullah Ayomakeran, Alfa Rofiu, Daddy Faruq, Abiodun Babalola, Saheed Shittu, Oyelakin Surajudeen, Tijani Binyamin, Segun Faweyinmi and Mr. Adeyemi Tola. Allah blesses you all.

I also remember my late father Dr. Adebisi Sulaiman Amoo, may his gentle soul continue to rest in perfect peace.

On a personal note, I will like to thank my mother for the understanding and support during my long period of absence when she was alone when I was in South Africa.

PUBLICATIONS

Publication in peer review journal.

M.A. Adebisi, C-D Chen, K. Bharuth-Ram, M. Maaza, C. Ronning^{x, y}, E. Manikandan, D. Motaung, P. Christopher and M.K. Moodley, Synthesis and Characterization of Boron Nanomaterials in the form of Nanotubes, Rods, Wires and Bamboo-like nanotubes by Double Pulsed Laser Ablation. (Patent pending)

M. A. Adebisi, and Dr. M. K. Moodley, Density Gradient Ultracentrifugation of Boron Nanomaterials: Separation of Boron Related Nanomaterials into Different Lengths and Diameters. (Patent pending)

KEYWORDS

“Synthesis and Characterization of Boron Nanotubes and other Related Boron Nanomaterials by Dual Pulsed Laser Ablation”

Boron Nanomaterials

Boron Nanostructures

Boron Nanotubes

Carbon Nanotubes

Dual Pulsed Laser Ablation

Raman Spectroscopy

Scanning Electron Microscopy

Transmission Electron Microscopy

X-Ray Diffraction

Vibration Sample Magnetometer

Adebisi Mufutau Amobi

August 2019

LIST OF ABBREVIATIONS

LA	:	Laser ablation
CVD	:	Chemical vapour deposition
BNMs	:	Boron nanomaterials
mg	:	Milligram
cm	:	Centimetre
mbar	:	Millibar
min	:	Minutes
s	:	Second
E	:	Energy
sccm	:	Standard cubic centimetres
SEM	:	Scanning electron microscopy
HRTEM	:	High resolution transmission electron microscopy
EDS	:	Energy dispersive x-ray spectroscopy.
RBM	:	Radial breathing modes
BNTs	:	Boron nanotubes
CNTs	:	Carbon nanotubes
SWBNTs	:	Single walled boron nanotubes
DGU	:	Density gradient ultracentrifugation
DGM	:	Density gradient medium
XRD	:	X -ray diffraction
PL	:	Photoluminescence
RS	:	Raman spectroscopy
DPLA	:	Dual pulse laser ablation
RBM	:	Radial breathing mode
VSM	:	Vibration sample magnetometer.

LIST OF SYMBOLS

α	:	Alpha
μ	:	Microns
μm	:	Micrometre
\AA	:	Angstrom
β	:	Beta
λ	:	Wavelength
θ	:	Theta
nm	:	Nanometre
Co	:	Cobalt
Ni	:	Nickel
Ar	:	Argon
N	:	Nitrogen
C	:	Carbon
$^{\circ}\text{C}$:	Degree Celsius
B	:	Boron
BN	:	Boron Nitride

TABLE OF CONTENTS

Declaration -----	II
Abstract -----	III
Certification -----	V
Dedication -----	VI
Acknowledgments-----	VII
Publication -----	VIII
Keywords -----	IX
List of abbreviations -----	X
List of symbols -----	XI
Table of contents -----	XII
List of figures -----	XVI
List of tables -----	XXII

Chapter One

1. Introduction	1
1.1 Boron and Applications of Boron -----	1
1.2 Boron allotropes-----	2
1.2.1 α -Boron-----	2
1.2.2 β -Boron -----	6
1.2.3 γ -Boron -----	9
1.2.4 δ -Boron-----	11
1.2.5 ε -boron-----	12
1.3 Nanomaterials-----	14
1.3.1 Properties of boron nanomaterials (BNMs)-----	15
1.3.2 Applications of Boron nanomaterials-----	17
1.3.3 Literature survey of boron nanomaterials -----	18
1.4 Boron nanotubes as an alternative to carbon nanotubes -----	20
1.5 Objectives of research -----	21
1.6 Motivation for the Dissertation -----	21

1.7 Research Questions -----	22
1.8 Outline of the Dissertation -----	23

Chapter 2

2. Elemental Boron	25
2.1 Elemental Boron -----	25
2.1.1 Different polymorphous of boron -----	25
2.1.2 Boron nanotubes -----	25
2.2 Introduction to Boron Nanostructures -----	27
2.2.1 Boron Nanowires -----	28
2.2.2 Boron Nanosheets -----	29
2.2.3 Boron Nanoribbons -----	32
2.2.4 Boron Nanoclusters -----	33
2.2.5 Boron Nanotubes -----	34
2.2.5.1 Properties of Boron Nanotubes -----	36
2.2.5.1.1 BNTs Surface Electron affinity and Work function--	36
2.2.5.1.2 Electrical and Field emission properties of BNTs----	38
2.2.5.1.3 Similarities and differences between BNTs	
and CNTs -----	40
2.3 Theoretical/computational studies of boron nanomaterials -----	41
2.3.1 Special Challenges on Boron Nanotubes, (BNTs) -----	41
2.3.2 Stability and Conductivity Properties of the Boron Sheets -----	42
2.4 Purification and Centrifugation of single walled nanotubes -----	43
2.4.1 Purification and processing of SWNTs -----	43
2.4.2 Purification of SWNTs by centrifugation method -----	43
2.4.3 Sorting single-walled nanotubes (SWNTs) by the density gradient	
Ultracentrifugation (DGU) technique -----	44
2.5 Synthesis techniques of nanomaterials -----	46
2.5.1 Laser ablation (LA) technique -----	46
2.5.2 Chemical Vapor Deposition (CVD) Technique -----	47
2.5.3 Ball Milling and Annealing Technique -----	48

2.5.4 Arc Discharge (AD) Technique -----	50
2.6 Characterization techniques -----	51
2.6.1 Raman Spectroscopy -----	51
2.6.2 High-Resolution Transmission Electron Microscope (HRTEM) -----	53
2.6.2.1 Selected Area Electron Diffraction (SAED) -----	55
2.6.3 Scanning Electron Microscopy (SEM) -----	56
2.6.3.1 Energy Dispersive X-ray Spectroscopy (EDS/EDX) -----	58
2.6.4 X-Ray Diffraction (XRD) -----	58
2.6.5 Ultraviolet-Visible (UV–VIS) spectroscopy -----	60
2.6.6 Photoluminescence (PL) -----	61

Chapter 3

3. The Laser synthesis of single-walled boron nanotube	63
3.1 Preparation of laser ablated target -----	63
3.2 Experimental design for a laser synthesis of SWBNTs -----	64
3.2.1 Equipment for the synthesis of BNTs -----	64
3.2.1.1 A pulsed Q-switched Nd: YAG laser -----	64
3.2.1.2 A Carbolite Furnace with three different temperature zones ---	65
3.2.1.3 Pressure control, Mass Flow control, and vacuum systems ----	65
3.2.1.4 Optical and mechanical components with motion assistant software -----	65
3.2.2 Description of the experimental setup and experimental conditions for boron nanotubes -----	66
3.3 Conditions under which hexagonal boron nitride and boron composite targets were ablated by DPLA -----	69
3.3.1 Carbolite furnace, nitrogen and argon gas flow conditions -----	69
3.3.2 Operational system in the experiment -----	69
3.3.3 Main points on synthesized as-prepared samples by DPLA method ----	76
3.3.3.1 The sample key of labeling -----	76

Chapter 4

4. Boron nanomaterials synthesized by using a boron nitride target	77
4.1 Characterization of BNMs by SEM -----	77
4.2 Transmission Electron Microscopy (TEM) Analysis -----	81
4.3 Energy Dispersive X-Ray Spectroscopy (EDS) -----	85
4.4 X-Ray Diffraction (XRD) Analysis -----	88
4.5 Raman Spectroscopy (RS) Analysis -----	91
4.6 Ultraviolet-Visible (UV-VIS) Analyses -----	95
4.7 Photoluminescence (PL) Analyses -----	98
4.8 Vapour Liquid Solid (VLS) mechanism process -----	101

Chapter 5

5. Single-walled boron nanotubes synthesized using a boron target	104
5.1 Characterization of SWBNTs by SEM -----	104
5.2 Characterization of SWBNTs by HRTEM -----	106
5.3 Image analysis on the HRTEM micrograph of SWBNTs -----	111
5.5 Raman spectroscopy -----	114
5.6 X-Ray Diffraction (XRD) -----	118
5.7 Ultra Violet-Visible (UV – VIS) Spectroscopy -----	119
5.8 Vibrating Sample Magnetometer (VSM) -----	121
5.9 Vapour Liquid Solid (VLS) mechanism -----	124

Chapter 6

6. Density gradient ultracentrifugation (DGU) of SWBNTs	128
6.1 Introduction -----	128
6.1.1 Theory of density gradient ultracentrifugation -----	128
6.2 Experimental method -----	131
6.2.1 Surfactant DGU separation and preparation of density gradient medium (DGM) -----	132

6.3 Results and Discussions	135
6.3.1 Characterization of SWBNTs by SEM and EDS	135
6.3.2 Characterization of SWBNTs by HRTEM and EDS	139
6.3.3 Characterization of SWBNTs by Raman	143
6.4 Image analyses on the SEM and HRTEM micrographs of SWBNTs	152

Chapter 7

7. Conclusions and Future Work	161
7.1 Conclusions	161
7.2 Future Work	164

List of Figures

1.1 (a) Structure of B ₁₂ icosahedra -----	3
1.1 (b) The crystal structure of α-B along the y -direction, showing the six intercluster 2e2c bonds for the central B ₁₂ cluster -----	4
1.1 (c) The crystal structure of α-B along the c axis, the crystallographically independent atoms B1 and B2 are indicated with six inter-icosahedral 2e3c bonds of the central B ₁₂ cluster -----	5
1.2 Raman spectrum of a single crystal of α-B -----	6
1.3 (a) Structure of β-B, in hexagonal settings -----	7
1.3 (b) Structure of β-B, in rhombohedral settings -----	8
1.4 Structure of γ-boron: B ₁₂ icosahedra are connected by B ₂ dumbbells -----	9
1.5 Raman spectrum of a single crystal of γ -boron -----	10
1.6 Structure of T-50 (δ-B) -----	11
1.7 Raman spectrum of a single crystal of δ-boron -----	12
1.8 Structure of ε-B in hexagonal settings -----	13
1.9 Raman spectrum of a single crystal of ε-boron -----	14
1.10 (a) and (b): Show the I-V curves response of the BNWs with Ni/Au electrodes. The bottom inset of Figure 1.10 (a) contains the current versus gate-voltage data biased at 10 V, demonstrating that the BNW is a p-type semiconductor -----	15
1.11 Electrical resistance (R) versus temperature (T) of superconducting BNWs at 84 GPa measured at different magnetic fields in the low T range. The inset is the R-T curve in the temperature range of 0.08–300 K under zero magnetic field -----	16
1.12 Field emission J-E curve of the boron nanowires; the inset is the corresponding F–N plot -----	17
2.1 Shows the different chemical compositions of strain energy for armchair nanotubes -----	26
2.2 (a) Shows the boron atom at the ground state with five electrons and its electronics Configuration -----	27
2.2 (b) Revealed boron in its most stable state by promoting an electron from the 2s to the 2p orbital -----	27

2.3 (a) HRTEM image of amorphous BNWs synthesized by laser ablation (LA) technique --	29
2.3 (b) HRTEM image of crystalline BNWs synthesized via CVD method -----	29
2.4 Reveal LEED patterns for (a) The pristine silicon (100) and (b) silicon (100) with a ½ monolayer of boron -----	30
2.5 Show high-resolution images of boron induces reconstructions on a Si (001) surface and where A and B denote the structural subunits of reconstructions. (a) Reconstructions and region of clean Si (001) outlined (b) A high-resolution image of occupied surface electronics states, (c) Unoccupied electronics states -----	30
2.6 Atomic structure of proposed idealized triangular and reconstructed monolayer boron sheet -----	31
2.7 Atomic structure of a proposed α -boron sheet using density functional calculations -----	31
2.8 Shows atomic structure of nanoribbons derived from an α -boron sheet (a) linear and (b) armchair edge. The electron localization function (ELF) plot for nanoribbons derived from (c) a stable α -boron sheet and (d) a reconstructed boron sheet -----	32
2.9 Ground-state structures along with structural symmetry of neutral boron nanoclusters obtained using the 3-21G basis set -----	33
2.10 Shows representative quasi-planar and 3D nanoclusters of boron respectively -----	34
2.11 (a) Raman spectra of a boron nanotube. The inset shows the micrograph of the boron nanotube. (b) The Electron energy loss spectrum of a boron nanotube on a SiO ₂ substrate -----	35
2.12 The UPS spectra of the pure BNWs film and a mixture of BNTs and BNWs film -----	37
2.13 SEM images of the individual BNT ‘A’, BNT ‘B’ and BNT ‘C’ -----	39
2.14 (a) The electric transport curves of single BNTs, A, B and C. (b) The field emission I–E curves of the three individual BNTs (A, B and C) -----	40
2.15 The first column indicates the lattice structure of boron sheets while the second and third columns show armchair and zigzag BNTs respectively. (a) α – sheet, (b) Buckled triangular and (c) Distorted hexagonal -----	42
2.16 Shows a schematic of the resuspension-centrifugation-decantation cycle for removal of heavy particles and purification of SWNTs -----	44
2.17 Revealed the solution of SWNTs that was centrifuged in a linear gradient -----	45

2.18 The schematic of the laser ablation technique apparatus and a high-power laser which was directed on a graphite target and then vaporizing the graphite -----	46
2.19 Schematic apparatus of a chemical vapor deposition (CVD) technique -----	47
2.20 Schematic diagram of the ball milling technique -----	49
2.21 Schematic diagram of the annealing process -----	49
2.22 Schematic apparatus of an arc discharge technique used for the production of Nanotubes -----	50
2.23 Shows the schematic apparatus of Raman Spectroscopy -----	51
2.24 Shows the schematic illustration of the energy transitions involved in Raman Spectroscopy -----	52
2.25 Schematic apparatus revealing the basic principle and components of the HRTEM. [Source: Hebrew University of Jerusalem, cited April 10, 2018: Available from https://www.researchgate.net/publication/263849645] -----	54
2.27 Schematic diagram of the basic components of a scanning electron microscope -----	55
2.26 Shows the schematic of an HRTEM operating in the diffraction mode -----	57
2.28 Diffraction of the X-ray beam from a crystalline material -----	59
2.29 The schematic diagram of ultraviolet-visible spectroscopy -----	60
2.30 Shows the schematic diagram of the PL measurement system -----	61
3.1 Experimental set up for the synthesis of boron nanotubes by the double pulsed laser furnace method -----	68
3.2 A photograph of experimental set up for the synthesis of boron nanomaterials (BNMs) by the double pulsed laser ablation technique inside the carbolite furnace -----	70
3.3 Photograph showing the front-end of quartz, the Brewster window from the side and the inlet gas connection -----	70
3.4 Photograph showing the back-end of the quartz tube, the clamping of the target, support rod and connection with the vacuum system-----	71
3.5 Shows the photograph of the laser ablation experimental laboratory -----	72
3.6 BNTs synthesized in the hot zone. The material was carried to the back and condensed on cooler sections of the quartz tube and appeared like a dark deposit. The as-prepared sample was collected over a period of 40 minutes after the experiment-----	74
3.7 A removed vacuum flange revealing the as-prepared sample of BNTs-----	74

3.8 A typical sample of the as-prepared sample synthesized scrapped from the insides of the quartz tube and collected in a petri dish for analyses-----	75
4.1 Shown SEM images obtained using h - BN target at a different pressure, flow rate and temperature with a high yield of a different kind of boron nanomaterials	
(a) BN 400P 200F 1100T, showed ‘worms like’ nanostructures	
(b) BN 1000P 500F 1100T, showed fibrous boron nanomaterials	
(c) BN 400P 400F 1000T, showed ‘spaghetti-like’ nanostructures and	
(d) BN 400P 200F 1000T, showed ‘pebbles like sticks’ nanostructures -----	79
4.2 HRTEM images of boron nanomaterials synthesized using h-BN target at different pressures, nitrogen flow rates and temperatures (a) BN 400P 200F 1100T, showed BNTs, (b) BN 1000P 500F 1100T, showed bamboo nanotubes, (c) BN 400P 400F 1000T, revealed BNWs and (d) BN 400P 200F 1000T, showed BNRs -----	83
4.3 (a) SEM energy dispersive x-ray spectroscopy spectrum of BNTs obtained from BN 400P 200F 1100T of the as-prepared BNTs with a high peak from boron -----	86
4.3 (b) The Energy Dispersive X-ray spectroscopy spectrum of SWBNTs of BN 400P 200F 1100T obtained from HRTEM by supernatant sample liquid indicated a high peak of boron. The inset EDS table in the spectrum shown the percentage weight of each element presents in the SWBNTs synthesized.	87
4.4 X ray diffraction spectra of boron nanomaterials synthesized from h-BN target at different pressures, nitrogen flow rates and temperatures (a) BN 400P 200F 1100T, showed BNTs, (b) BN 1000P 500F 1100T, showed bamboo nanotubes, (c) BN 400P 400F 1000T, revealed BNWs and (d) BN 400P 200F 1000T, showed BNRs-----	90
4.5 Raman spectra of boron nanomaterials synthesized from h-BN target at different pressures, nitrogen flow rates and temperatures (a) BN 400P 200F 1100T, showed BNTs, (b) BN 1000P 500F 1100T, showed bamboo nanotubes, (c) BN 400P 400F 1000T, revealed BNWs and (d) BN 400P 200F 1000T, showed BNRs-----	93
4.5 (e) Raman spectra of the bulk hexagonal boron nitride powder (h-BN, Sigma Aldrich) -----	94

4.6 UV-VIS spectra of boron nanomaterials synthesized from h-BN target at different pressures, nitrogen flow rates and temperatures (a) BN 400P 200F 1100T, showed BNTs, (b) BN 1000P 500F 1100T, showed bamboo nanotubes, (c) BN 400P 400F 1000T, revealed BNWs and (d) BN 400P 200F 1000T, showed BNRs-----	97
4.7 Photoluminescence spectra of boron nanomaterials synthesized from h-BN target at different pressures, nitrogen flow rates and temperatures (a) BN 400P 200F 1100T, showed BNTs, (b) BN 1000P 500F 1100T, showed bamboo nanotubes, (c) BN 400P 400F 1000T, revealed BNWs and (d) BN 400P 200F 1000T, showed BNRs-----	100
4.8 Indicate the schematic diagram of the (a) Boron nanomaterials growth apparatus. The output from a pulsed laser is focused onto a BN/NiCo target located at centre within a quartz tube, the reaction temperature is controlled by a tube furnace, (b) VLS mechanism process for the growth of boron nanomaterials grown on the surface of the catalyst-----	102
5.1 (a) SEM image shows the densely – packed of SWBNTs with lengths in micrometers and diameters in the range of nanometers. (b) EDX spectrum analyses results that revealed the highest peak of boron-----	105
5.2 (a) The HRTEM image shown the SWBNTs of 1.5 nm in diameter and length in micrometers. Also, nickel and cobalt as catalysts found in the SWBNTs synthesized with DPLA technique were indicated by yellow arrows -----	107
5.2 (b) The HRTEM image of the single-walled boron nanotubes of different diameters and lengths, which mixed with catalysts. (c) The HRTEM image of an SWBNT that revealed the open ends of the tube-----	108
5.2 (d) Shows the lattice fringes observed with the interlayers spacing of 0.38 nm (e) Shows SAED measurement, that reveals a sharp spot pattern, which suggests that the boron nanotubes have good single crystalline structures-----	109
5.2 (f) The EDX spectrum of HRTEM analyses results that revealed the highest peak of boron-----	110
5.3 (a) HRTEM of SWBNTs diameters measured-----	112
5.3 (b) Distribution of SWBNTs diameters measured in the HRTEM image and fitted to the log-normal distribution-----	113

5.5 Revealed Raman spectrum of SWBNTs excited at the 514 nm laser on as – prepared sample synthesized at the temperature of 1100 °C-----	115
5.6 XRD spectra of BNTs synthesized by DPLA technique, revealed the peak around 22.0° At 100 (h k l) which indicate that the growth of BNTs is along 100 directions-----	118
5.7 UV – VIS spectrum of SWBNTs synthesized by the DPLA method at a temperature of 1100 °C with a strong absorption peak at 272 nm-----	120
5.8 Magnetic measurements (a)Single walled boron nanotubes synthesized by the DPLA method at a temperature of 1100°C, (b)Bulk boron material, (c)Sediment from Density gradient ultracentrifugation material. Recorded at room temperature with the VSM instrument-----	122
5.9 (a) Schematic diagram of the boron nanotubes growth apparatus. The output from a pulsed laser is focused onto a B/NiCo target located at centre within a quartz tube; the reaction temperature is controlled by a tube furnace. (b) Boron nanotubes growth process. Laser ablation of the B/NiCo target creates a dense plasma plume, hot vapor that condenses into nanoclusters as the B and NiCo species cool through collisions with the buffer gas. The furnace temperature is controlled to maintain the NiCo nanocluster in a liquid state. Boron nanotube growth begins after the liquid becomes supersaturated in B and continues as long as the NiCo nanoclusters remain in a liquid state and B reactant is available. Growth terminates when the boron nanotube passes out of the hot zone of the reactor-----	126
6.1 Centrifugation of SWBNTs in a centrifuge-----	128
6.2 Centrifugation schematic of the separation of SWBNTs in a centrifuge with a horizontal Rotor-----	130
6.2 (a) Before DGU, SWBNTs mixed with a sodium cholate in Optiprep density gradient solution (b) After DGU, sorted isolated small SWBNTs bundles on top and sediments of large SWBNTs bundles at the bottom-----	134
6.3 (a) The final position of SWBNTs separated into four layers, at 32,000 rpm for 3hrs, (b) Corresponding to each layer obtained in Figure 6.3(a) from different layers, at 50, 000 rpm for 2 hrs and (c) The final position of SWBNTs when distilled water is used-----	134

6.4 The SEM images of SWBNTs obtained from different layers after the DGU operated at 50,000 rpm for 2hours (a) Layer four, (b) Layer three, (c) Layer two and (d) Layer one. Each of this layer depicted the bundles of SWBNTs-----	137
6.4 (e) The EDS spectrum obtained from SEM image after the DGU at 50,000 rpm for 2hours confirming the purity of the SWBNTs-----	138
6.5 The HRTEM images of SWBNTs obtained from the DGU at 50.000 rpm in 2 hours at different levels (a) Layer 4, SWBNTs of 1.43 nm in diameter, (b) Layer 3, SWBNTs diameter of 1.71 nm (c) Layer 2, SWBNTs of 1.93 nm in diameter and (d) Layer 1, SWBNTs of 2.05 nm in diameter with a catalyst at the top----	141
6.5 (e) The EDS spectrum obtained from HRTEM images after the DGU at 50,000 rpm for 2hours confirming the purity of the SWBNTs-----	142
6.6 Raman spectra excited at 514 nm laser on (a) Layer 4 (b) Layer 3, (c) Layer 2 and (d) Layer 1, which correspond to the results obtained from the four layers, in the centrifuge tube after the DGU-----	147
6.7 SEM images of tubular structures of boron taken randomly in each layer after ultracentrifugation (a) Layer 4 (Top), (b) Layer 3 (c) Layer 2, (d) Layer 1(Bottom)-----	154
6.8 HRTEM images of SWBNTs taken at random positions after ultracentrifugation (a) Layer 4(Top), (b) Layer 3 (c) Layer 2, (d) Layer 1(Bottom)-----	157
6.9 Distribution of the diameters of SWBNTs measured in HRTEM images from layer 4 to 1 and fitted to log-normal distribution-----	159

List of Tables

2.1 Shown the chiral indices, diameters and radial breathing modes of each boron nanotubes-----	36
3.1 Revealed the chemical composition hexagonal boron nitride/boron powder metal catalyst targets used in the research-----	64
3.2 Shows the specification of laser and properties of the beam at which the laser exists the aperture-----	64
3.3 Experimental conditions under which both the hexagonal boron nitride (h-BN) and boron composite targets were ablated during the synthesis by laser ablation technique---	67
3.4 A summary of as-prepared BNMs samples synthesized by utilizing Target BN / B-----	76
4.1 Revealed the percentage weight of each element present in the BNTs synthesized-----	86
4.2 X-ray diffraction peaks observed in boron nanomaterials synthesized-----	90
5.1 Indicated EDX from the SEM spectrum with the percentage of each elemental composition that presents in the as-prepared sample-----	106
5.2 EDS of the HRTEM spectrum indicating the percentage of each elemental composition that presents in the SWBNTs-----	110
5.3 (a)SWBNTs diameters measured in HRTEM image and statistical parameters for Lognormal distribution fitting-----	113
5.3 (b) The Density of SWBNTs synthesized at P400 F200 T1100 in the HRTEM image----	114
5.5 Shown Raman active modes in BNTs synthesized by the DPLA method at the temperature of 1100 °C compared with α – boron (in cm^{-1}) predicted and synthesized through theoretical calculations and experimental values respectively-----	116
5.6 X-ray diffraction peaks of BNTs synthesized by the dual pulsed laser ablation technique at the temperature of 1100 °C-----	119
5.7 Magnetization data of SWBNTs, pure bulk boron and along with DGU sediment at room temperature-----	123
6.1 The elemental composition of each element presents in the SWBNTs-----	138
6.2 EDS table from HRTEM analysis shown the elemental composition of each element present in the SWBNTs-----	142
6.3 Raman active modes in α – boron (in cm^{-1}) and the experimental results obtained from layer 4 of BNTs is compared with theoretical calculations and experimental results of Vast et al and theoretical calculations by Shirai et al-----	148

6.4 Raman active modes in α – boron (in cm^{-1}) and experimental results obtained from layer 3 of the BNTs is compared with theoretical calculations and experimental results of Vast et al and theoretical calculations by Shirai et al-----	148
6.5 The Raman active modes in α – boron (in cm^{-1}) and experimental results obtained from layer 2 of the as-prepared BNTs is compared with theoretical calculations and experimental results of Vast et al and theoretical calculations by Shirai et al-----	149
6.6 Raman active modes in α – boron (in cm^{-1}) and experimental results obtained from layer 1 of the BNTs is compared with theoretical calculations and experimental results of Vast et al and theoretical calculations by Shirai et al-----	149
6.7 Density of tubular structures of boron observed in the SEM images of each layer-----	154
6.8 SWBNTs diameters measured in HRTEM images from layer 4 to 1 and statistical parameters for lognormal distribution fitting-----	157

Chapter 1

1.Introduction

1.1 Boron and Applications of Boron

Boron, the 5th element of the Periodic table, is a non-metallic hard material with a high melting point of 2075 °C and boiling temperature of 4000 °C. In its powder form it is black-greyish or dark-brown in colour. At ambient conditions, boron is known as a weak semiconductor and its electric conductivity rapidly increases with temperature, so that at 600 °C it is 100 times higher than at room temperature [1]. Boron has two naturally occurring and stable isotopes, ¹¹B and ¹⁰B [2]. ¹⁰B has high neutron capture cross-section, high heat-resistance, and nontoxicity so it is used as a material for the control rods of nuclear reactors, for radiation shielding, and for a neutron counting detector as well as in medicine as in boron neutron capture therapy [3-7]. For producing a distinctive green colour, amorphous boron is used in pyrotechnic flares as well as in rocket fuel igniters [8]. Use of amorphous boron as a gasket material in high-pressure experiments improves hydrostatic conditions and quality of X-ray diffraction patterns [9]. High hardness, exceptional chemical stability in crystalline form, the formation of electron-deficient bonds, pressure-induced metallization, and superconductivity and partially unknown phase diagram still make elemental boron very attractive to scientists [10-16]. Boron is not found in nature as an elemental material, but it forms compounds, which due to a variety of their physical and chemical properties play an important role in human activities since antiquity [17]. They are widely used as superhard materials, superconductors, dielectrics, and B-doped semiconductors as well as reinforcing chemical additives. Composites on the base of boron are characterized by extreme strength and lightweight used as filaments for advanced aerospace structures and in personal security as bullet-proof vests [18]. Boron forms several commercially important compounds. One of them is boron oxide. It is used as a fluxing agent in ceramics and glassmaking. It makes glass tough and heat-resistant. In the production of borosilicate glasses and glass fibres boron oxide plays an important role alongside with borax ($\text{Na}_2\text{B}_4\text{O}_7 \cdot 10 \text{H}_2\text{O}$). The borosilicate glass is non-conducting and used as insulator layers in the semiconductor industry. The chemical stability of borosilicate glasses allows their use as materials for chemical tools. Borax is also used as a cleansing fluid, a water softener, insecticide, herbicide, and disinfectant.

Metal borides are also hard and durable materials and are employed as mechanical parts exposed to high strain like turbine and rotor blades, sports equipment [19, 20]. Due to their high electrical conductivity metal borides serve as electrode materials, for example, as high energy batteries [20, 21]. MgB_2 is a superconductor at 39 K and used in form of wires for tomographs [13, 22]. LaB_6 along with being a superconductor with a relatively low transition temperature of 0.45 K has a low work function which allows it to be used in transmission electron microscopy and electron beam lithography [22]. Hafnium boride has a high melting point at 3543 K and low thermal expansion coefficient that leads to its successful use in thermal shock experiments [23, 24]. The most interesting of boron compounds are boron nitride and boron carbide. Boron nitride is the second hardest material superseded only by diamond, Vickers with hardness is 49-54 GPa [25, 26]. Its remarkable chemical and thermal stability allows its use in high-temperature equipment. Boron nitride nanotubes are like carbon nanotubes, but more thermally and chemically stable. Unlike carbon nanotubes, boron nitride nanotubes are electrical insulators. Boron carbide is one of the most widely used hard materials, surpassed only by diamond and boron nitride. Due to its high melting point and thermal stability, high abrasion resistance, extreme hardness, and low density, boron carbide is used for manufacturing shielding powders and coatings, applied as energy absorbers for dynamic protection. Mechanical properties of boron carbide and limits of its stability under loading are thus of both scientific and practical interest for ballistic applications. Theoreticians predicted a phase transition in boron carbide at 25 GPa, [27].

1.2 Boron allotropes

Currently boron has five allotropes namely α -B, β -B, γ -B, δ -B, and ϵ -B [14], and all of the allotropes have a similar structural feature. B_{12} icosahedron as a major building block. Each allotrope possesses a unique Raman spectrum [15, 28].

1.2.1. α - Boron

Since first crystallization of pure boron in 1909 and some successful synthesis in the 1950s and 1960s, there was a long time of the absence of any references of synthesis of the α -boron single crystal [14, 29-33].

Recently a methodology of reproducible synthesis was developed using high pressure and high temperature as the main force of transformation [34, 35]. Rhombohedral α -B with space group $\overline{R3m}$ has the simplest structure among all of the boron phases: it consists of B_{12} icosahedra located at the corners of its rhombohedral unit cell [34-39]. Figure 1.1a represents structure of B_{12} icosahedra with 12 atoms.

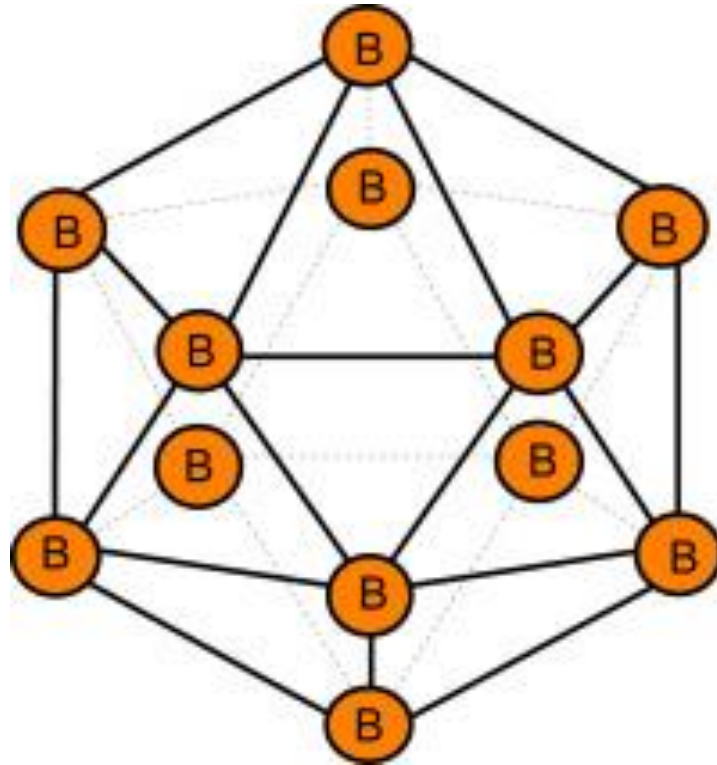
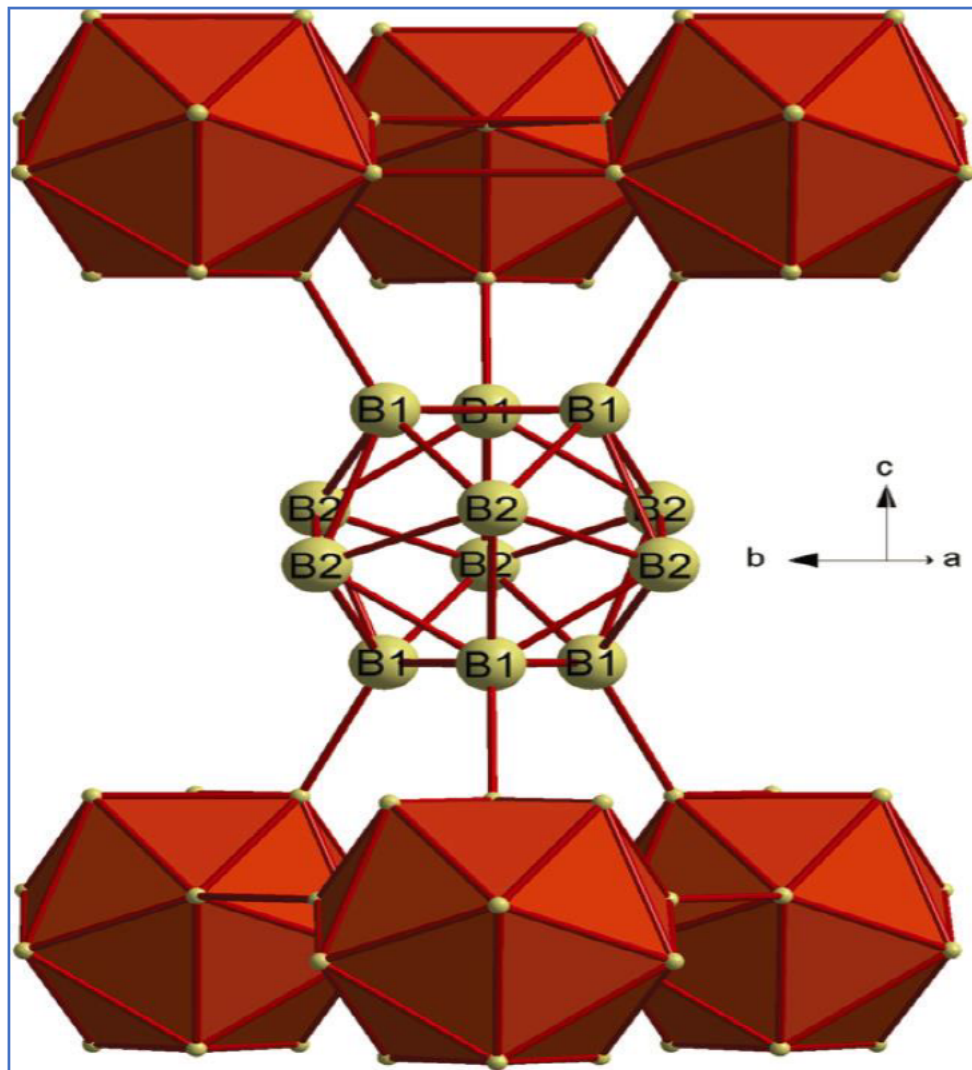


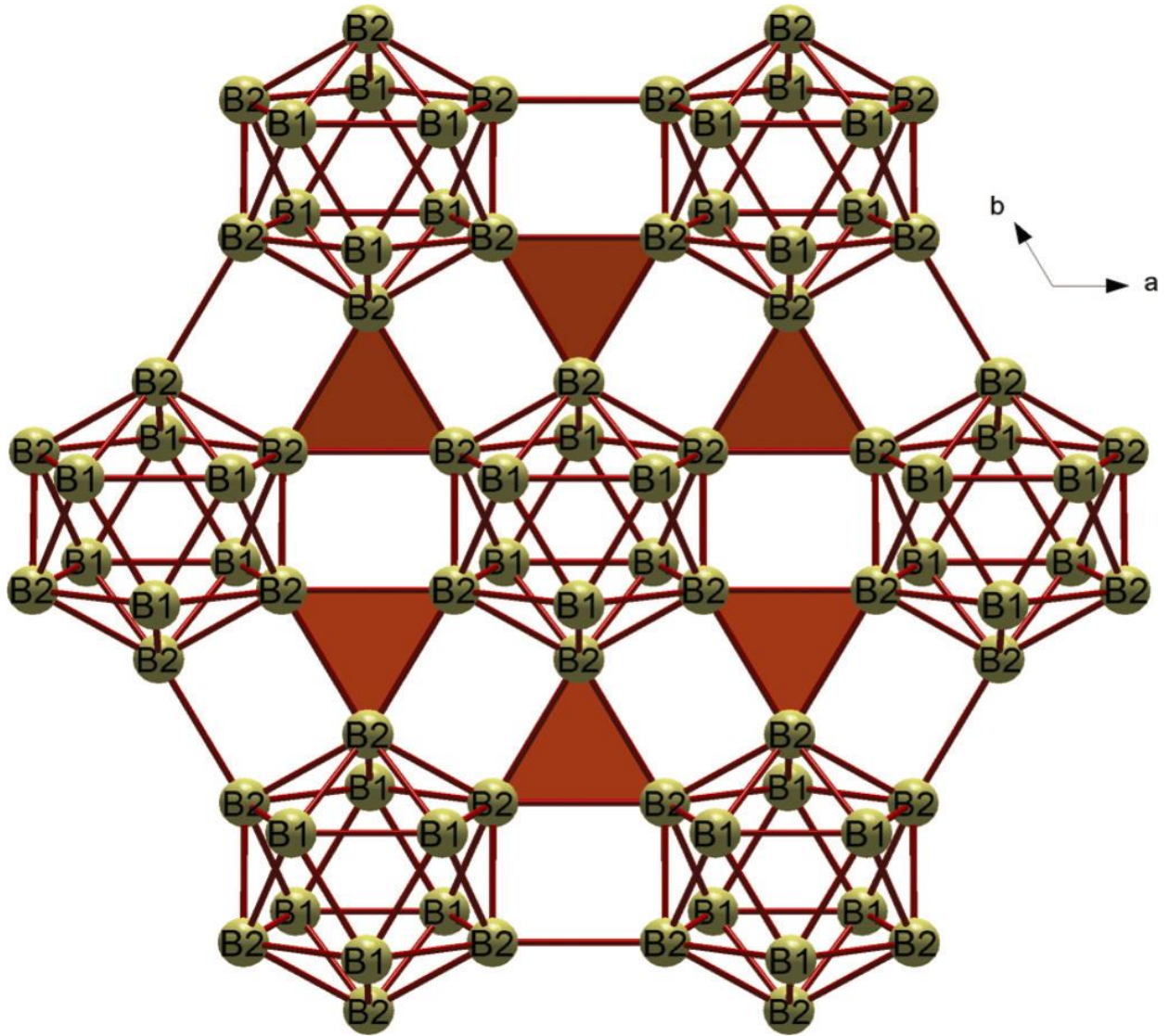
Figure 1.1a: Structure of B_{12} icosahedra [11]

Unit cell parameters are refined from single crystal X-ray diffraction: $a = 4.9179(5) \text{ \AA}$, $c = 12.5805(16) \text{ \AA}$ in hexagonal settings [34, 39]. Its structure was established long ago in Figure. 1.1 (b) and (c), the bonding situation in α -B at ambient pressure was clarified by Mondal *et al* in 2013, only recently due to the analysis of the electron-density in α -B based on experimental single-crystal X-ray diffraction data [11]. It was found that icosahedra form “close-packed” layers and between them, there are $2e2c$ (two-electron two-centre) B1-B1 inter cluster bonds of similar nature as the $2e2c$ bonds in γ -B in Figure. 1.1(b) [12]. While within the same layer in Figure. 1.1 (c), icosahedra are held together by electron deficient $2e3c$ (two-electron three-centre) B2-B2-B2 bonds

which are different from the $2e3c$ bond in γ -B [11]. α -B is extremely hard Vickers hardness on polycrystalline aggregates is 382 GPa, with density of 2.46 g/cm^3 , thermally and chemically inert [40]. It has a direct band gap semiconductor of 2.0 to 2.4 eV [31, 40, 41].



(b)



(c)

Figure 1.1: The crystal structure of α -B (b) along the y -direction, showing the six intercluster $2e2c$ bonds for the central B_{12} cluster. (c) along the c axis, the crystallographically independent atoms B1 and B2 are indicated with six inter-icosahedral $2e3c$ bonds of the central B_{12} cluster [41].

Raman spectroscopy investigations of α -B were first started by Richter and Ploog in 1964 [42]. Since that time, along with theoretical calculations and assignment of the Raman modes at ambient conditions as shown in Figure 1.2, a number of high-pressure experiments have been performed [36, 43-48]. Raman spectroscopy measurements at room temperature to 80 GPa on polycrystalline samples and on single crystals up to 30 GPa and 71 GPa did not show any phase transitions in α -B in according with powder X-ray diffraction experiments up to 106 GPa and 200 GPa [36, 47-49].

IR spectroscopy studies were performed experimentally on powder samples at ambient conditions and theoretically in numerous works [45, 46, 50-53]. The bands were identified in the Raman spectrum in the range from 400 to 1300 cm^{-1} .

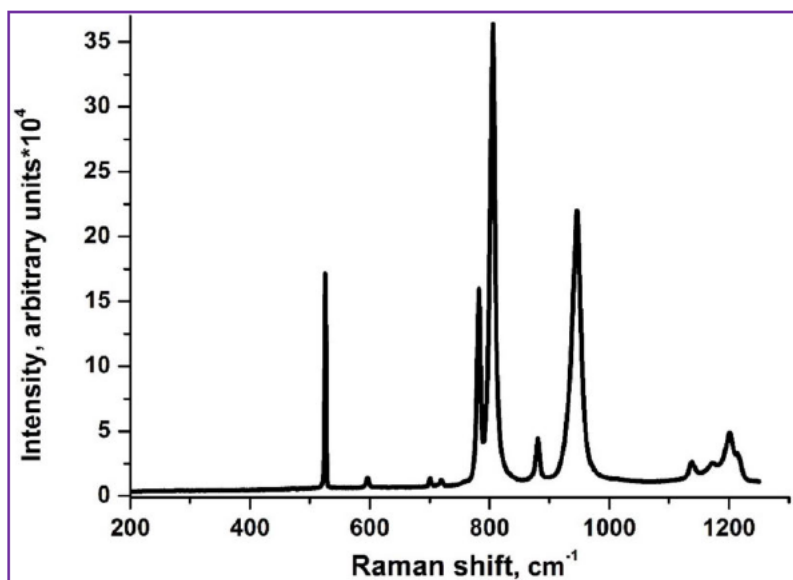


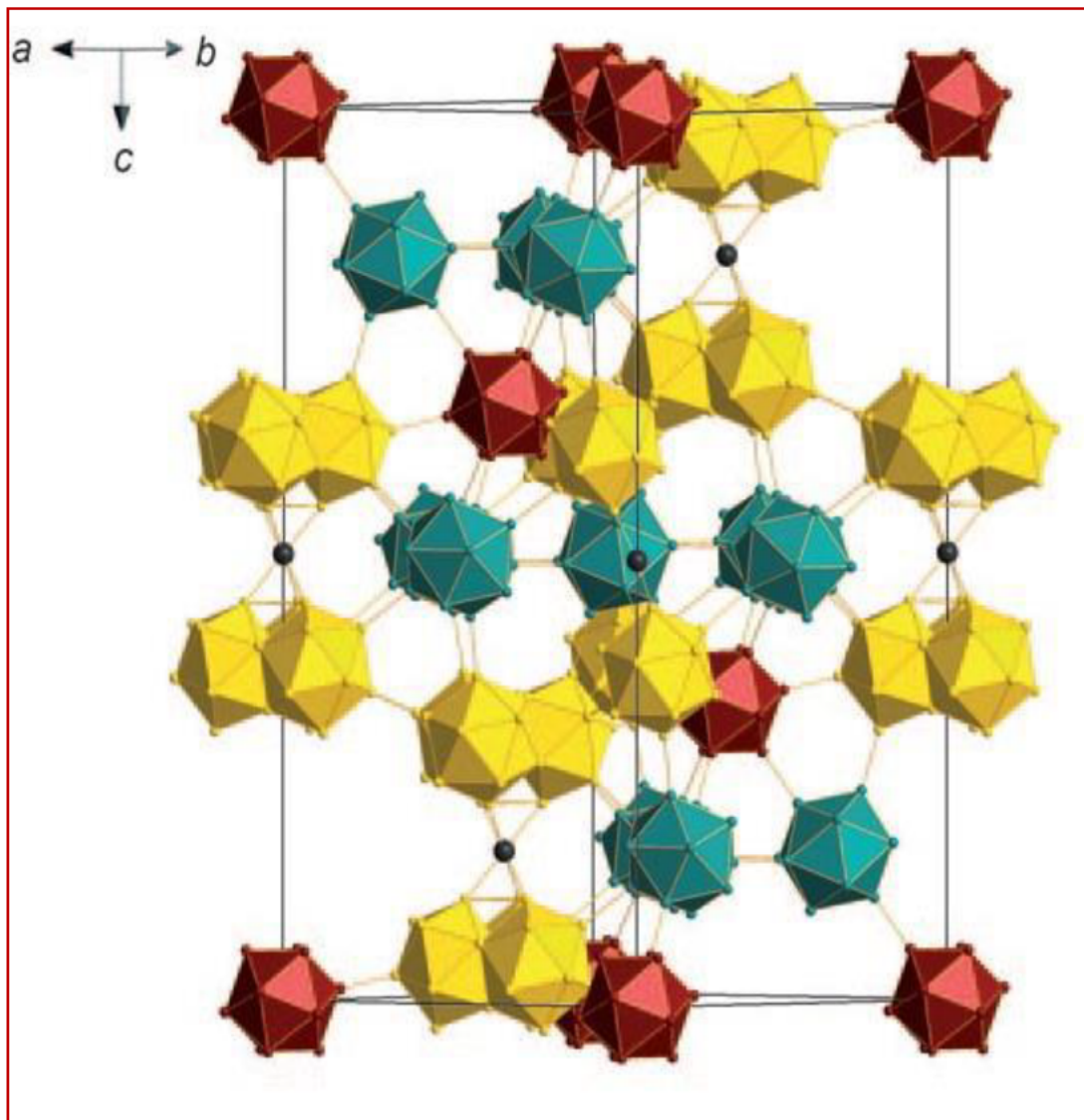
Figure I.2: Raman spectrum of a single crystal of α -B [46].

It is more than 100 years since α -boron was obtained in a crystalline form for the first time, but many problems remain. Accurate determination of atomic coordinates and thermal parameters of α -B is required. High-pressure IR spectroscopy can recognize metallization of α -B theoretically predicted at about 50 GPa, however, no reference was found so far. Structural stability at pressures higher than 100 GPa needs to be verified.

1.2.2 β -Boron

When heated up to 1473 K at ambient pressure, α -B transforms into β -B. β -B is the most common phase and the one commercially available [36]. It can be crystallized from the melt at ambient pressure as well as synthesized by the chemical vapor deposition technique. β -B was the first pure boron phase discovered [54, 55]. The structure was solved several years later. β -boron crystallizes in form of crystals with a rhombohedral structure of space group $\bar{R}3m$ with the unit cell parameters $a = 10.9321 \text{ \AA}$, $c = 23.8183 \text{ \AA}$ in a hexagonal setting [56-59]. The

modern view on the structure is based on single-crystal X-ray diffraction experiment suggesting 320 atoms per a hexagonal unit cell distributed over 20 crystallographically independent positions [59]. The crystal structure contains B_{12} icosahedra, B_{28} -B- B_{28} fragments and interstitial B atoms as shown in Figure 1.3(a) and (b). B_{28} fragments consist of 3 B_{12} icosahedra sharing their faces. B_{12} icosahedra form 3-dimensional framework with B_{28} -B- B_{28} fragments inside the voids. The main feature of β -B that makes its structure the most complex among all known boron allotropes is the presence of voids and partially occupied positions [45]. Availability of β -boron leads to a lot of studies on optical, electrical and mechanical properties [60-62]. In a conductivity measurement, a transformation of β -B from a wide band gap semiconductor to a superconductor at 160 GPa was found which agrees with previous theoretical predictions [13, 63].



(a)

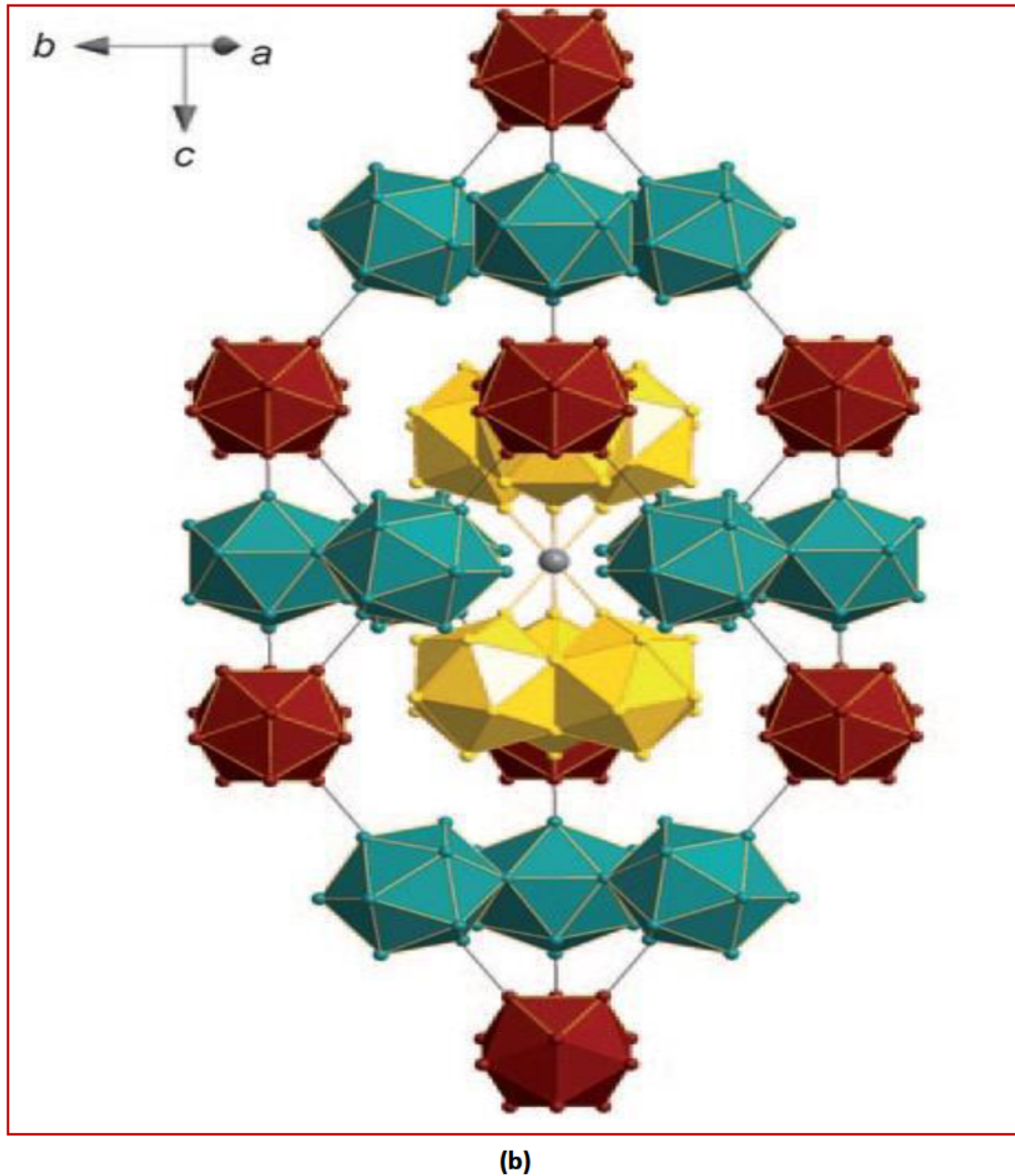


Figure 1.3: Structure of β -B, (a) in hexagonal settings, (b) in rhombohedral settings [64]

Due to its complexity, the structure of β -B is poorly understood. The determination of the equation of state is an important tool to progress in the understanding of boron. The equation of state of β -B was measured in the ranges of 0–10 GPa by means of neutron powder diffraction, in the ranges of 0–30 GPa at different temperatures by powder X-ray diffraction and in the ranges of 2–97 GPa using powder and single-crystal X-ray diffraction [65–67]. The β -B is found to be more compressible with bulk modulus $K = 185\text{--}210$ GPa, in comparison

with α -B of bulk modulus $K = 213\text{--}224$ GPa [47, 65, 66]. There was a transition to T-192 which is known as tetragonal-II phase, it wasn't reproduced, this was detected upon double-sided laser heating of the sample at pressures above 10 GPa [66]. This transition wasn't observed where the pressure-induced amorphization at about 100 GPa was observed [67]. Further investigations of β -B at high pressures are required for this reason.

1.2.3 γ -Boron

The existence of a high-pressure boron phase was reported for the first time in 1965 as a powder, γ -B is a reddish-coloured [68]. Its orthorhombic structure has a $Pnmm$ space group [68]. Unit cell parameters, $a = 5.05634$ Å, $b = 5.61265$ Å and $c = 6.97107$ Å were refined from single crystal X-ray diffraction data [68, 69]. The structure of γ -B consists of B_{12} icosahedra and B_2 dumbbells covalently bonded with each other [12, 69-71], as shown in Figure 1.4.

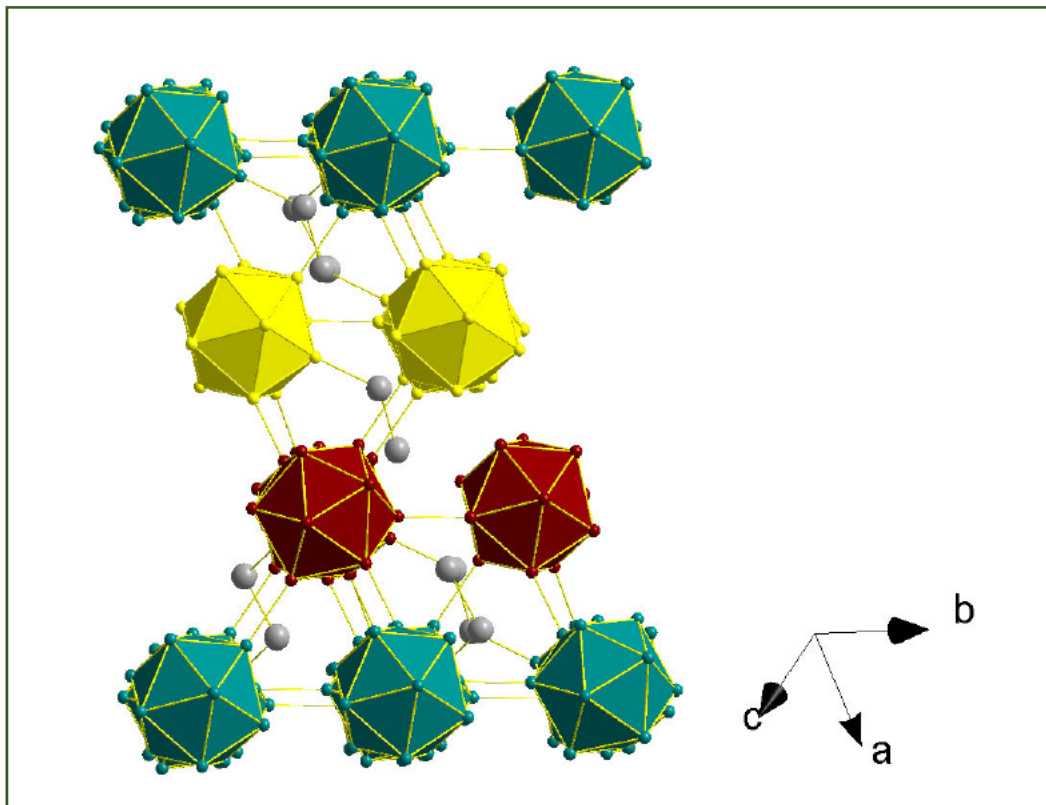


Figure 1.4: Structure of γ -boron: B_{12} icosahedra are connected by B_2 dumbbells [69]

The Raman spectrum is unique for the high-pressure high-temperature modification of boron as shown in Figure 1.5.

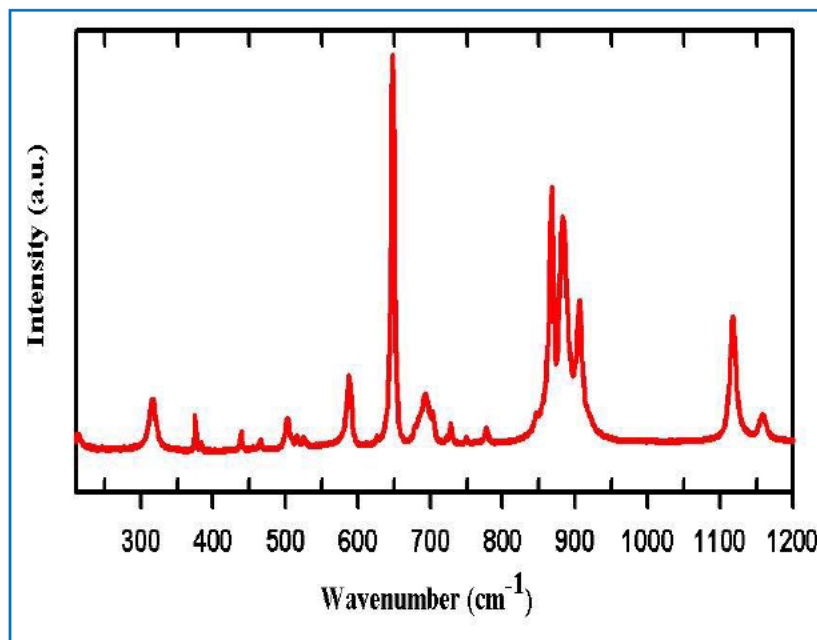


Figure 1.5. Raman spectrum of a single crystal of γ -boron [72].

γ -B was experimentally demonstrated to be stable up to 30 GPa and 2000 K [69]. It is theoretically predicted to be stable in the pressure range from 19 GPa to 78 GPa, to 89 GPa or to 93 GPa [69, 73, 74]. Experimental charge density studies revealed covalent polycenter bonds in B₁₂ icosahedron, the electron-deficient 1e2c bond between two neighbouring polyhedral and a unique polar-covalent 2e3c bond between a pair of atoms of one B₁₂ group and one atom of the dumbbell [12]. This unique bond explains the observed charge separation in γ -B [12]. γ -B is extremely hard the Vickers microhardness being 58 GPa and very dense with X-ray density 2.541 g/cm³ [69, 75]. It is optically transparent with an optical absorption edge of 2.1 eV, a poor electrical conductor with resistivity on the order of 10⁶ Ω ·cm at ambient conditions. Resistivity decreases with increasing temperature, indicating semiconductor behaviour of γ -boron [72]. At about 40 GPa γ -B undergoes an isostructural phase transformation, probably due to reducing of the polarity of covalent bonds visualized by discontinuous behaviour in the mode Grueneisen parameter and splitting of several Raman peaks [75-77].

1.2.4, δ -Boron

The tetragonal phase of boron, T-50 or δ -B, was a matter of serious discussion since its discovery in 1943 by Labengayer [78]. Theoretical calculations predicted instability of B_{50} due to its electronic configuration and that it can be stabilized by small amounts of foreign atoms such as carbon, nitrogen or transition elements [79, 80]. Only recently this phase was synthesized in the presence of other boron allotropes [28]. δ -B crystallizes as needle-shaped grey-reddish semi-transparent crystals. The structure refined by means of single crystal X-ray diffraction is tetragonal of $P4_2/mmm$ space group with the unit cell parameters $a = 8.7089 \text{ \AA}$, $c = 5.0751 \text{ \AA}$ [28]. The unit cell of δ -B consists of 50 boron atoms. They form four icosahedra, and two atoms localize in the intericosahedral space [81], as shown in Figure 1.6.

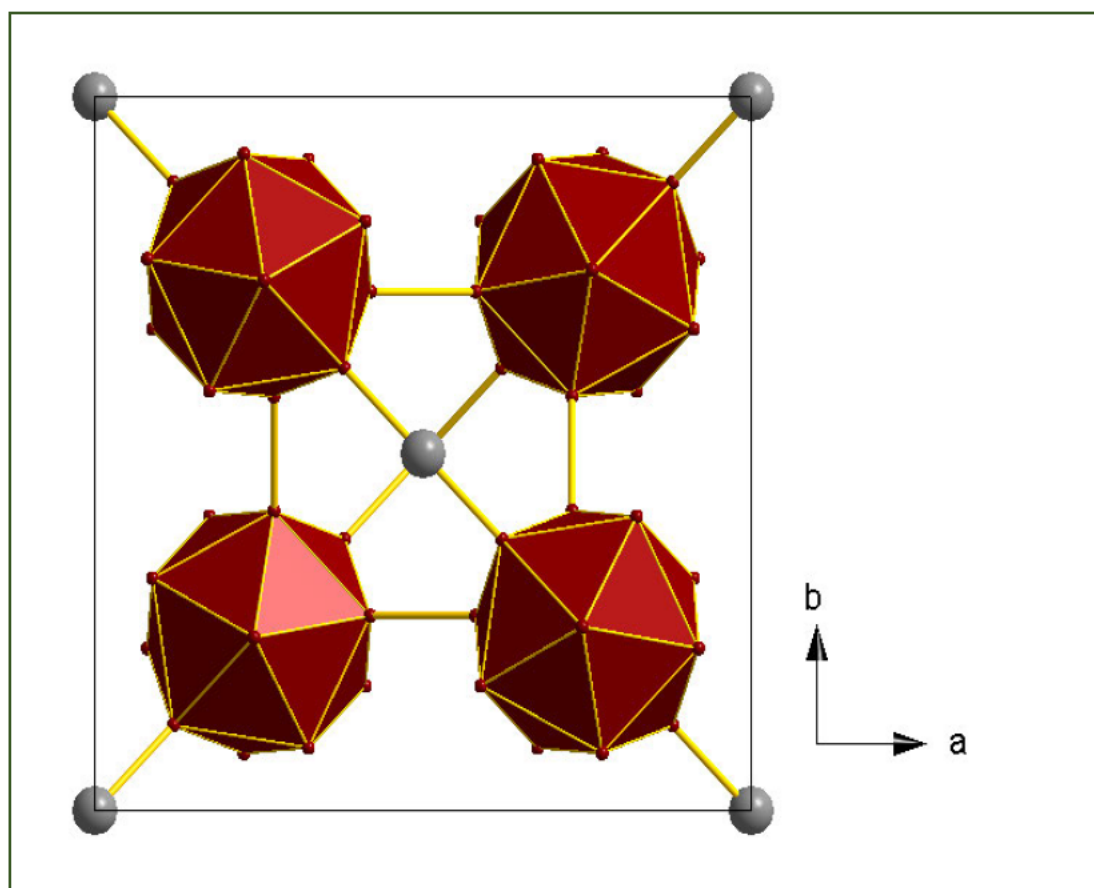


Figure 1.6: Structure of T-50 (δ -B) [28].

Raman spectrum of δ -B is drastically distinct from those of other boron polymorphs. It has one dominating intense Raman peak at 491 cm^{-1} , as shown in Figure 1.7

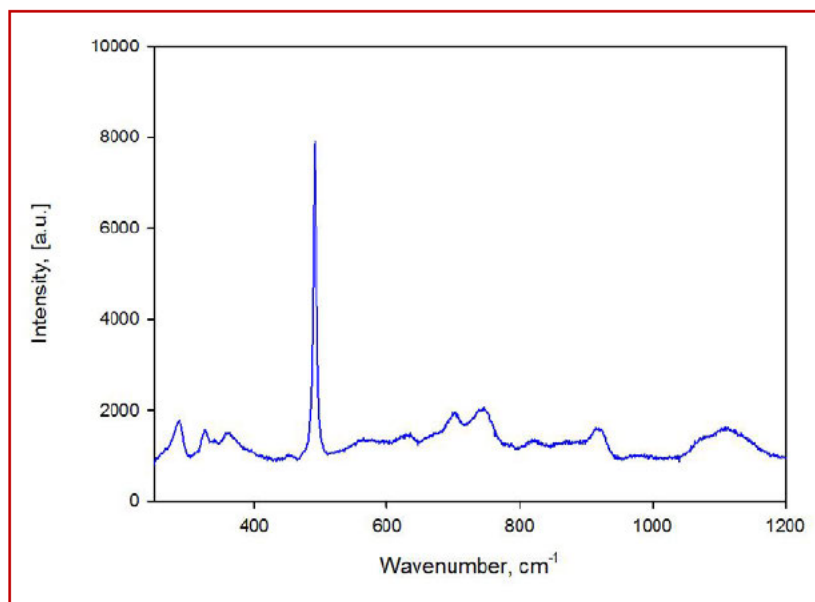


Figure 1.7: Raman spectrum of a single crystal of δ -boron [28].

According to the experimental studies, δ -B crystals appeared at pressures above 9 GPa in the field of stability of γ -B and always in the presence of other boron polymorphs, which points towards metastability of this boron phase [28].

1.2.5, ϵ -boron

In a relatively narrow pressure-temperature field, at pressures of 8–9 GPa and temperatures of 1873 – 2073 K, yellow-reddish-orange, transparent, plate-shaped crystals of ϵ -B were found [28]. This boron phase has the rhombohedral structure of space group $R\bar{3}m$ with unit cell parameters $a = 5.59407\text{ \AA}$, $c = 12.075616\text{ \AA}$ with the hexagonal setting. The arrangement of B_{12} icosahedra is like that in the α -B structure. In the intericosahedral space, there are tree-atomic linear groups consisting of boron atoms oriented along the main body-diagonal of the unit cell as revealed in Figure 1.8. The structure resembles the stoichiometric B_{13}C_2 with C-B-C linear groups instead of B-B-B groups of ϵ -B [10, 28, 68].

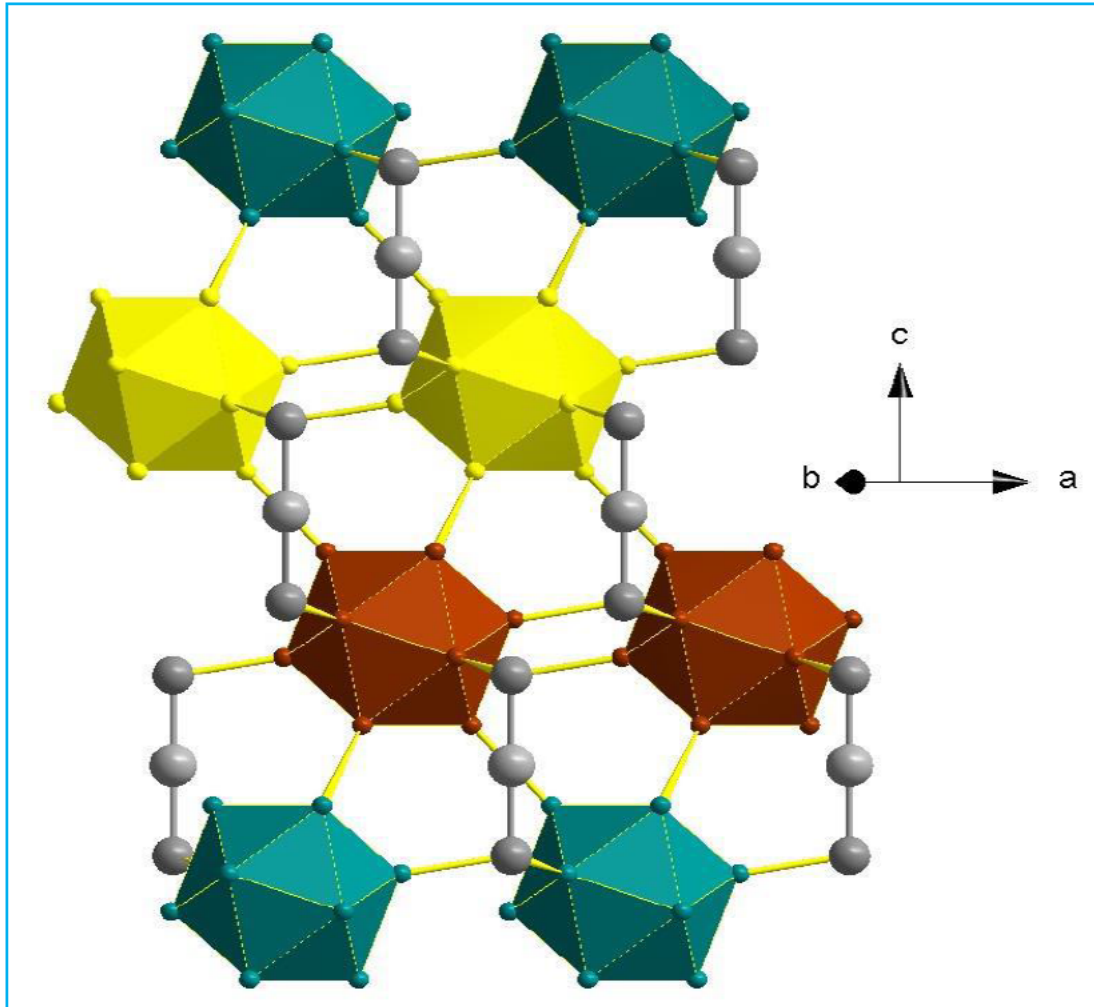


Figure 1.8: Structure of ϵ -B in hexagonal settings [28].

The Raman spectrum of ϵ -B is different from the spectra of any other boron polymorphs, but alike to that of boron carbide $B_{13}C_2$ with a small shift of about 5 cm^{-1} [28], as shown in Figure 1.9. Considering that the crystals appeared only in the presence of the other boron phases and upon heating at high pressure they transformed to β -B or γ -B depending on the stability fields, this phase is metastable.

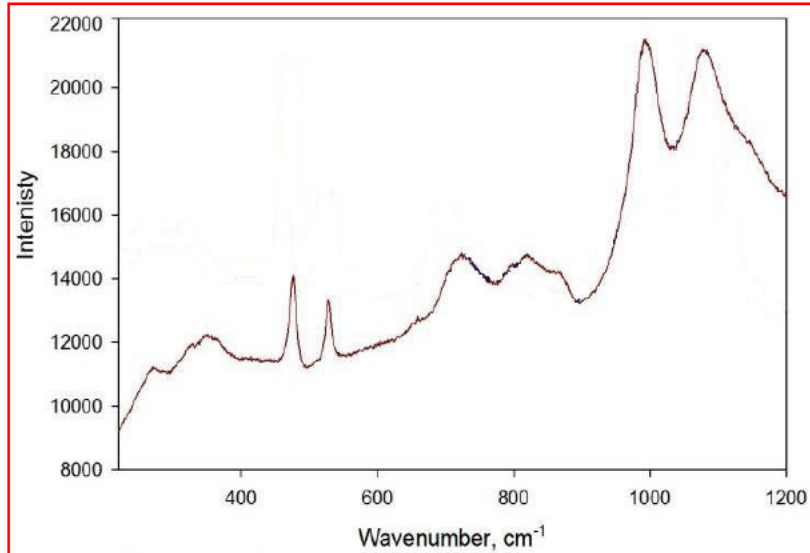


Figure 1.9: Raman spectrum of a single crystal of ϵ -boron [28].

Microhardness of ϵ -boron from 55-60 GPa which is higher compared to boron carbide 38 GPa despite the similarities in the structure [28]. ϵ -B is as hard as γ -B at 60 GPa but harder than other boron allotropes [28, 68, 81].

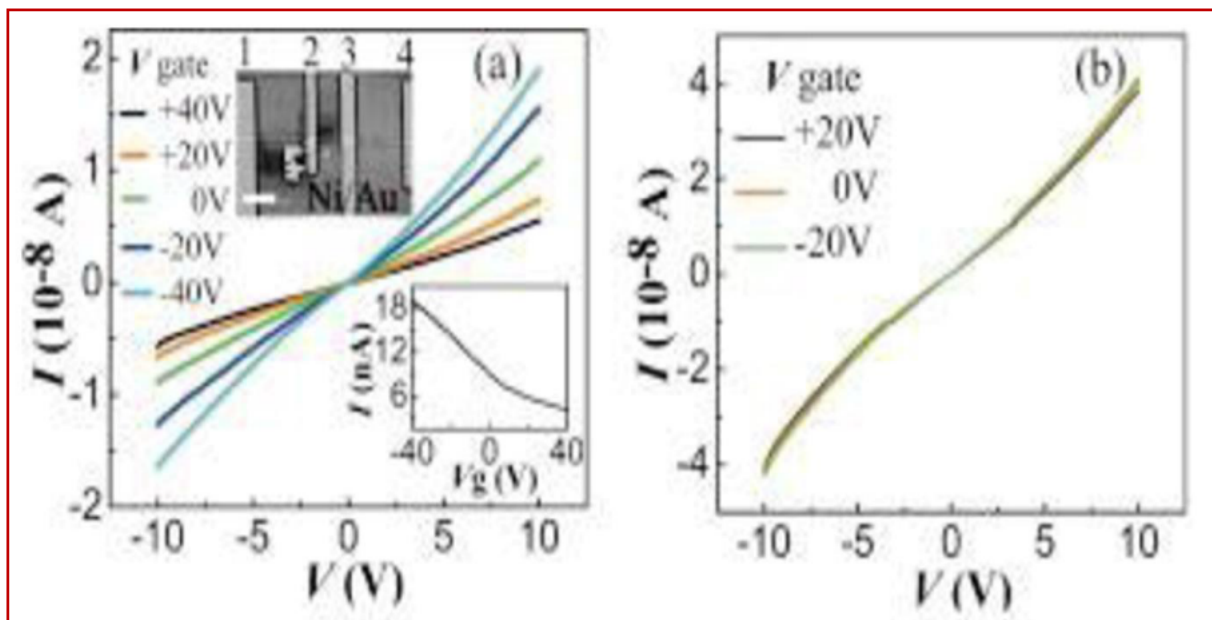
1.3 Nanomaterials

In materials science, a nanomaterial is a material that measures between 1 and 100 nm in at least one dimension [82]. Different types of nanomaterials have been identified from simple nanoparticles to complex structures that self-assemble to form structures that look similar [83]. Due to the small size of nanomaterials, physics that govern the behaviour of materials changes [84]. Because of this, nanomaterials became very important materials to study. Nanomaterials provide a means to study how material properties such as electric transport, field emission, and Young's modulus, vary when their nanoscale properties are compared to their properties in bulk materials [85-87]. Applications of nanomaterials have been successfully fulfilled in many technological fields [84]. For example, semiconductor nanowires junctions have been used to fabricate logic gates and also have been shown to be capable of basic computation [88]. A few descriptions of nanomaterials are explained below. A nanowire is one of the nanomaterials with a structure that is restricted to the nanoscale in two dimensions and has a diameter of nanometres [82]. Nanowires are of particular interest to those interested in building small scale nanodevices because they may potentially be used as building blocks [89]. Nanotubes and

nanowires are similar, but nanotubes are attributed to hollow core structures. They were usually synthesized with smaller diameters compared to nanowires [90]. Other nanomaterials were listed as follows, nanoplatelets, nanosheet, nanoribbon, and nanobelt [91-97]. These were synthesized to be nanoscale in a single direction. Due to the way they were synthesized, it makes them long, wide and thin like a belt [84].

1.3.1 Properties of boron nanomaterials (BNMs)

We considered the properties of boron nanowires (BNWs) as one of the boron nanomaterials (BNMs). The crystalline BNWs were studied with mechanical resonance technique and tensile testing was done under mechanical response [98]. According to simple beam theory, the mechanical resonance of BNWs was excited and their frequencies were used to obtain Young's modulus of the nanowires [99]. In Figure 1.10 (a) and (b), the individual BNWs synthesized were distinguished as p-type semiconductors with low carrier mobility through electrical transport studies [100, 101]. There are six stable configurations of BNWs obtained by growing along different base vectors from the unit cell of the bulk α - rhombohedral boron (α - B) and β - rhombohedral (β - B) [102].



Figures 1.10 (a) and (b): Show the I - V curves response of the BNWs with Ni/Au electrodes. The bottom inset of Figure 1.10 (a) contains the current versus gate-voltage data biased at 10 V, demonstrating that the BNW is a p-type semiconductor [101].

Theoretical studies about the electronics and magnetic properties revealed that for α – boron and the β – boron-based nanowires, the magnetic property was dependent on the growth direction [83]. When the boron nanowires grew along the base vector [001], they exhibited ferromagnetism with magnetic moments of 1.98 and 2.62 μ_B for α – c [001] and β – c [001] directions respectively. Electronically, BNWs exhibits semiconducting properties with a band gap of 0.19 eV when grown along the α – c [001] directions [83]. BNWs possessed the unique direction dependence of the magnetic and semiconducting behaviours, that was quietly different from that of bulk boron materials. From theoretical investigations, these would bring BNWs to many promising applications [103, 104]. Sun *et al*, studied the high pressure-induced superconductivity in BNWs through rhombohedral boron crystal structure [105]. In Figure 1.11, BNWs superconductivity properties were found with temperature and pressure at 1.5 K and 84 GPa, respectively [106, 107], while bulk β - rhombohedral boron was still a semiconductor at the same pressure and temperature [83].

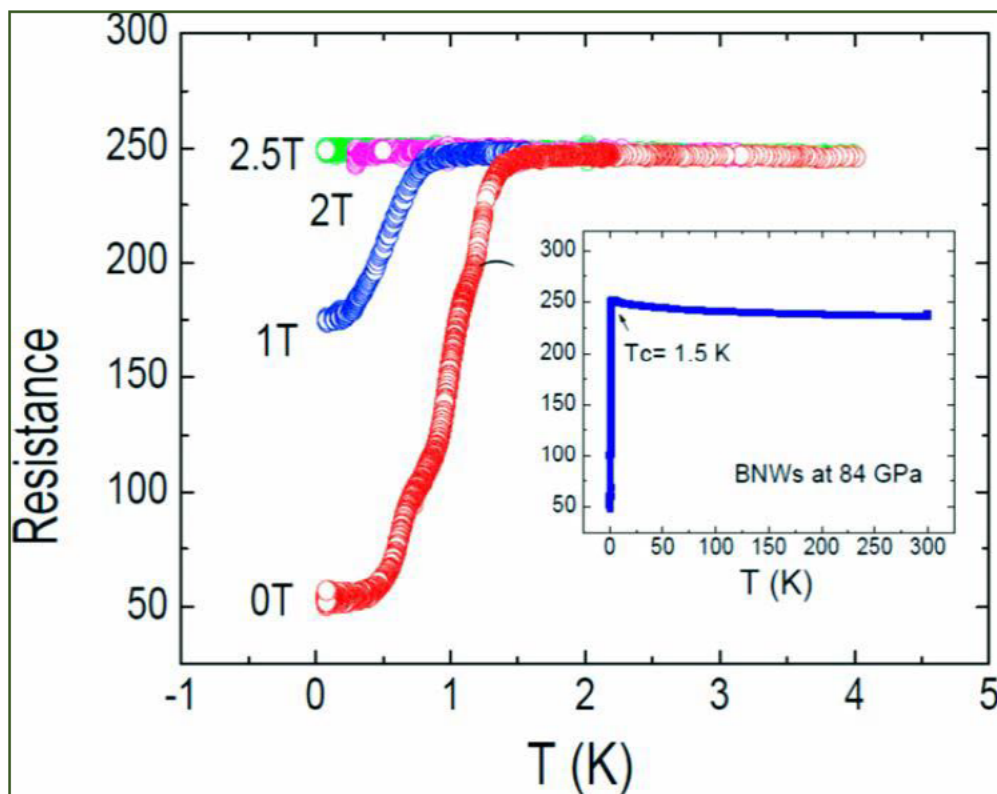


Figure 1.11: Electrical resistance (R) versus temperature (T) of superconducting BNWs at 84 GPa measured at different magnetic fields in the low T range. The inset is the R - T curve in the temperature range of 0.08–300 K under zero magnetic field [107].

In Figure 1.12, good field emission characteristics were found with BNWs films according to some theoretical reports. The turn-on field of BNWs was $9.0 \text{ V}/\mu\text{m}$ and threshold field was $14 \text{ V}/\mu\text{m}$ [108].

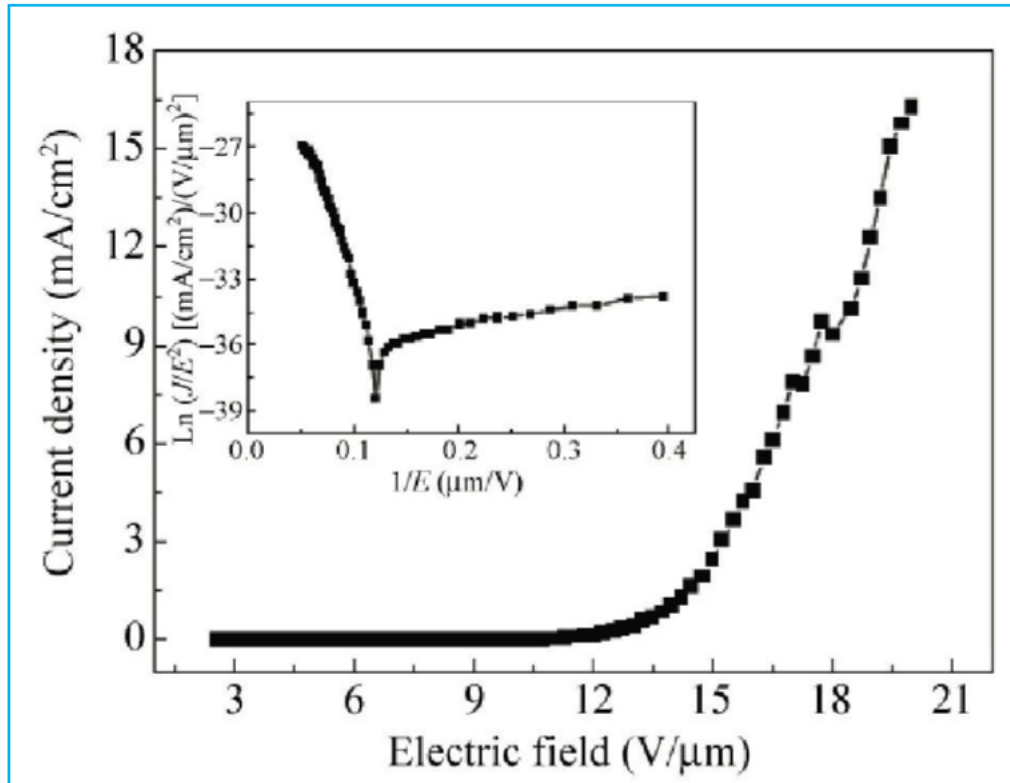


Figure 1.12: Field emission J - E curve of the boron nanowires; the inset is the corresponding F - N plot [108].

The value of the turn-on field of BNWs is suitable than that of GaN nanowires and In_2O_3 nanowires, but greater than that of CNTs with the turn-on electric field of $2\text{-}3\text{V}/\text{m}$ and graphene has a turn-on electric field of $0.7 \text{ V}/\text{m}$, which is less than that of BNWs [109, 110]. In addition to the properties mentioned, BNMs with special properties such as mechanical, magnetic, conductive and optical properties, have been reported.

1.3.2 Applications of Boron nanomaterials.

Boron nanomaterials (BNMs) are applicable in different areas, such as abrasive compounds, semiconductors, flat plane display, electron emission nanodevices and high-hardness [86, 111]. The electrical-transport studies on individual boron nanowires (BNWs) established them as p -type semiconductors with low carrier mobility [112]. It was also known that BNWs with both

α - and β - rhombohedral crystal structures could serve as superconductors [105]. BNWs are also applicable in the field emission, such as flat plane display and electron emission nanodevices [106]. The bulk boron materials have been used in various fields like bleaching agents, insecticides, magnets, high hardness, and abrasive compounds, shielding in nuclear reactors and fields of glass, ceramics, detergent formulations [113]. Some applications of the BNMs have been mentioned and more applications need to be investigated by learning from well-developed applications of bulk boron materials such as for those researchers in the fields of glass, ceramics, magnets, high hardness, abrasive, and shielding in nuclear reactors for future purposes.

1.3.3 Boron nanomaterials

In 2006 Gao *et al* synthesized a crystalline BNWs with a diameter close to 10 nm and length of several microns observed by using Si (100) as a substrate and a simple radio-frequency magnetron sputtering process under argon (Ar) gas with gold (Au) catalyst [103]. The product was influenced by sputtering parameters, such as substrate temperature, pressure and time. This technique required the vacuum at 5.0×10^{-5} Torr and highly pure argon (Ar) gas of purity 99.99% for sputtering deposition growth. Guo *et al*, investigated amorphous boron-rich nanowires obtained on [Zirconium diboride](#) (ZrB_2) particles using diborane as the gas precursor in a chemical vapor deposition (CVD) process under 20 Torr pressure and at 900 °C temperature [114]. The diborane gas used as a precursor is toxic and harmful to the environment. Vapor-liquid-solid (VLS) of boron nanowires were carried out either using a bottom-up or top-down growth mode [104]. Tian *et al* studied the pattern BNWs on the substrate of silicon (100) wafer by the thermo-reduction technique [86]. Three factors are associated with this thermo-reduction technique, such as the concentration of the nanoparticles solution, the dosage of the solution and the temperature of the wafer. Considering these factors, Tian *et al* [111], also synthesized flexible boron nanowires through thermo-reduction technique in boron-oxygen compound. The feather-like BNWs with large-scale arrays were synthesized by utilizing a magnetron sputtering technique with a target of pure boron and a mixture of boron oxide as a binder [115]. The branched boron nanofibers always nucleated and grew on the same sidewall of the backbone nanowire. Yang *et al* [116], synthesized aligned single crystal BNWs by utilising nanochannel Al_2O_3 as a substrate and a CVD technique. Using pulsed laser ablation (PLA) technique at different temperatures, a crystalline BNWs had been reported to have formed Pt-coated sapphire substrate under pressure of 50 Pa [117].

For the PLA technique, the growth depends on the synthesis temperature, the intensity of laser beams and the type of metal catalysts used [118]. Zhang *et al*, used boron powder as boron source and silicon and nickel as catalysts to synthesize BNWs [119]. For BNWs to nucleate and grow in this technique, silicon and nickel were critical in the synthesis. There was a significant improvement on the BNWs synthesized when silicon as a catalyst was added. All the techniques mentioned above have been utilized to synthesize BNMs. Ciuparu *et al*, synthesized single-walled boron nanotubes (SWBNTs) with a small diameter of about 3 nm for the first time by CVD technique [120]. Liu *et al* synthesized huge amounts of BNTs six years later, BNTs are multi-layered nanotubes with the spacing between two adjacent layers about 3.2 Å [121]. Their conductivity and field emission properties were confirmed and compared to that of those CNTs. A modified CVD method similar to the CVD technique used by Ciuparu *et al* for the first time was used successfully by Liu and Iqbal to synthesize double-walled BNTs and boron nanofibers (BNFs) with a narrow diameter of about 10 nm [122]. In addition, various techniques, for example, CVD which has been extensively discussed above and other methods mentioned, had been successfully used to synthesize BNTs, BNWs and BNFs. The recent dual pulsed laser ablation (DPLA) technique introduced in this research is to make effort aimed to experimentally verify the presence of such tubes and if possible the prediction about their electrical properties. Also, to optimize and control the diameter distribution in the single-walled boron nanotubes (SWBNTs), by considering the synthesis procedures which call for more serious attention. Of all the techniques discussed above so far, there was a lack of product purity because of the carbon contamination contained in the product. In this research, a dual pulse laser ablation (DPLA) technique will be adopted for the synthesis of BNMs precisely boron nanotubes. The parameters such as synthesis temperature, the composition of the targets and gas flow rate are systematically controlled and considered. Argon (Ar) and nitrogen (Ni) gases utilized as the precursor gases are not toxic or harmful to the environment and society at large. Therefore, this tends to make the DPLA technique more useful, as a technique to synthesize BNMs. This technique remains a great challenge when compared to other methods because is very easy, highly cost-effective, highly productive, but also an environment-friendly technique for BNMs.

1.4 Boron nanotubes as an alternative to carbon nanotubes

To understand why we should study boron nanotubes (BNTs), we may first make some reference to the already existent and well-known carbon nanotubes (CNTs) and then justify why it could be advantageous to use crystalline boron-based tubes. Since their discovery in 1991 by S. Iijima, carbon nanotubes have been regarded as potential elements to revolutionize a variety of technologies ranging from electronics (further miniaturization of circuits and novel transistors) to microscopy techniques (filled with iron to be used in Magnetic Force Microscopy) and even medical applications (functionalized to deliver drugs with high targeting specificity) [123]. Their wide range of potential applications is fuelled by several remarkable properties, such as their enormous chemical stability, high aspect ratio (greater than 1000^1) [83], their great mechanical strength (as high as 1000 GPa around 5 times that of steel) and their stunning electrical and field emission properties (capable of ballistic transport emitting current densities up to 10 mA/cm^2) [124]. Their integration on a wide range of devices has been thoroughly pursued with different degrees of success depending on the specific feature needed for each application.

Despite their proven capacity to carry huge density currents, there is an outstanding issue: the electrical properties of a single-walled carbon nanotube depend strongly on its crystalline structure, its chirality, and the problem of producing tubes of a determined chirality is not yet resolved. Neither are there efficient methods that can be applied at the industrial scale to separate tubes of certain chirality from a mixture of tubes. We can think about at least three ways to circumvent this obstacle:

- (a) A new synthesis method has to be developed in order to produce tubes with a certain desired chirality.
- (b) A new efficient and cheap separation method has to be developed in order to be considered for industrial production pathways.
- (c) An alternative to carbon nanotubes whose electrical properties do not depend on chirality issues must be sought, that is a (ideally) tubular structure made of a different material that presents comparable or higher current density capacities than that of carbon nanotubes.

When carbon nanotubes are produced by any known method we have a mixture of metallic and semiconducting tubes that are not easily separable. The latter issue has been one of the major obstacles to fully integrate carbon nanotubes as electrical components of a commercial device. In the context of point (c) boron appears as an increasingly interesting alternative in the search of alternatives to noncarbon-based nanotubular structure to work as electrical components.

1.5 Objectives of research

The goal of the present work is to achieve the growth of one-dimensional boron nanostructures. The experimental guidelines for the synthesis of boron nanotubes (BNTs) will be followed. We set as a secondary objective to attempt optimization of their procedure by trying to comprehend the underlying dynamical growth process associated with the catalyst-assisted DPLA. Within the frame of optimization, we explored the use of catalysts (Ni and Co) for the synthesis of BNTs.

The third aspect of this research is to perform density gradient ultracentrifugation (DGU) for samples, by separating it into different diameters, lengths and characterize each layer observed after the centrifugation.

Fourthly, all the synthesized nanomaterials will be characterized, with the help of instruments, such as scanning electron microscopy (SEM), high resolution transmission electron microscopy (HRTEM), energy dispersive x-ray spectroscopy (EDS), x-ray diffraction (XRD), ultra-violet visible (UV- VIS), photoluminescence (PL), vibration sample magnetometer (VSM) and Raman spectroscopy (RS). All these characterizations enable us to determine their chemical composition, elemental composition, and morphology as well as their preferred crystalline phases and growth direction.

Lastly, we will set the guidelines for future work on research concerning with further optimization, especially regarding the selectivity of the grown structures by carefully defining the relevant experimental conditions.

1.6 Motivation for the Dissertation

Techniques for synthesizing one-dimensional nanostructures are highly valued since these nanostructures have a great potential to be integrated into novel devices. The applicability of such structures is dictated by their chemical composition since their electrical, optical and field emission properties depend upon it. Boron appears as an increasingly interesting material to synthesize such structures since it possesses a unique set of properties. Highly pure boron is not found in nature, pure boron is a rather complicated business because of its unusually high reactivity, therefore, to turn boron-based one-dimensional nanostructures into an attractive viable component of manufactured devices it is essential to develop a highly efficient and selective technique for their synthesis.

Boron nanotubes (BNTs) are nanostructures of great interest within the scientific community for several reasons. BNTs possess a large phase coherence length, it is relatively easy to reach the one-dimensional regime in boron-based nanostructures. This feature makes BNTs ideal candidates to study phenomena such as superconductivity or the so-called “quantum phase slip” in one dimension. Boron nanotubes are also considered as potential candidates to form part in novel circuitry elements. The experimental reports on the synthesis of BNTs are rather scarce. For these reasons, it is interesting to explore new synthesis procedures. Dual Pulsed Laser Ablation (DPLA) is a synthesis technique [125], that has been successfully tested for the synthesis of carbon nanotubes (CNTs) and carbon structures of other morphologies, this success and its relative simplicity made the DPLA techniques a natural candidate to be applied in order to synthesize boron nanostructures. The results obtained by the DPLA method varied based on different precursors and parameters [120, 126, 127]. There is still a lot of work to do concerning the selectivity of such experiments as well as to obtain a deeper understanding of the growth process of such structures and how this could affect the selectivity. On the other hand, we have not found reports on the synthesis of BNTs via DPLA. Therefore, it would be of major interest in the development of a DPLA protocol which could synthesize such BNTs in large amounts.

1.7 Research Questions

The questions in current BNMs research is to explain how they grow, when they grow or nucleate and how we can control their growth. In this dissertation, an investigation of these questions is pursued to achieve a better understanding of the problem and to contribute to the body of knowledge that would eventually unravel the mysteries surrounding the controlled growth of BNMs. To do this, the dual pulsed laser ablation (DPLA) technique to synthesize BNMs has been employed [125]. Hexagonal boron nitride and boron targets containing a small percentage of transition metal catalysts have been used. These two targets were ablated. The ablated as-prepared BNMs formed during the time of the plasma plume later condensed at the back of the cooler region of the quartz tube. In this region, as-prepared nanomaterials collected is purely rich in BNMs. A parametric investigation was established to formulate a picture of how BNMs is grown, and which type of BNMs is grown. All these involved changing of furnace temperature, the pressure, the flow rate of nitrogen/argon gas used in the synthesis experiments. With all these conditions, it is observed that different BNMs were synthesized. These were characterized by applying Raman spectroscopy (RS), X-ray diffraction (XRD),

Ultraviolet-visible (UV-VIS) spectroscopy, Scanning electron microscopy (SEM), Transmission electron microscopy (TEM), Energy dispersive x-ray spectroscopy (EDS), Photoluminescence (PL) spectroscopy, and the Vibration sample magnetometer (VSM).

1.8 Outline of the Dissertation

Chapter 1 includes the basic background of boron material, BNMs, literature survey on BNMs, objectives of research, the motivation for the dissertation, a motivation for research questions speculated as a result of the lack of better understanding relating to the synthesis of BNMs.

In chapter 2, boron and boron nanostructures are discussed, including boron as an element, different polymorphs of boron, synthesis of BNMs, theoretical studies of BNMs and purification and centrifugation of BNMs. It also includes methods of characterizing BNMs, while there are many analytical techniques employed to investigate BNMs. In this dissertation, the focus was on applying, Raman spectroscopy (RS), X-ray diffraction (XRD), Ultraviolet-visible (UV-VIS) spectroscopy, Field emission scanning electron microscopy (FESEM), High resolution transmission electron microscopy (HRTEM), Energy Dispersive X-Ray (EDS) spectroscopy and Photoluminescence (PL) spectroscopy. These techniques have been widely utilized to distinguish between BNMs. The details on these analytical techniques to distinguish between BNMs are extensively discussed.

In chapter 3, the laser synthesis of BNMs is discussed, including the background information on laser and interaction between the laser – materials, the description of the experimental technique and experimental design utilized to synthesize BNMs. This chapter also includes the target preparations and experimental conditions used during the period of synthesis.

In chapter 4, results and discussions of the experiment of synthesized BNMs from hexagonal boron nitride are presented. The main focus of this chapter is the results obtained and discussions of the characterization of the materials synthesized by utilizing Raman spectroscopy (RS), X-ray diffraction (XRD) spectroscopy, Ultraviolet-visible (UV-VIS) spectroscopy, Scanning electron microscopy (SEM), Transmission electron microscopy (TEM), Energy Dispersive X-Ray (EDS) and Photoluminescence (PL) spectroscopy on the as-prepared products.

In chapter 5, results and discussion on SWBNTs synthesized using the boron target are presented. This chapter focuses on the results acquired and discussions of the characterization of the materials synthesized using, Raman spectroscopy (RS), X-ray diffraction (XRD) spectroscopy, Ultraviolet-visible (UV-VIS) spectroscopy, Scanning electron microscopy (SEM), Transmission electron microscopy (TEM), Energy Dispersive X-Ray (EDS), Photoluminescence (PL) spectroscopy and vibration sample magnetometer (VSM) on the as-prepared SWBNTs.

In chapter 6, results and discussion on density gradient ultracentrifugation of single-walled boron nanotubes are presented. The chapter focussed on the results obtained from each layer and discussions of the characterization of the layers produced. Using Raman spectroscopy (RS), field emission scanning electron microscopy (FESEM), high-resolution transmission electron microscopy (HRTEM) and energy dispersive x-ray spectroscopy (EDS) on the SWBNTs results were obtained from each layer. Image analyses on the HRTEM and SEM images of boron nanotubes were also analyzed.

In chapter 7, a brief conclusion is presented on the results and proposed future research that could extend the scope of the present study.

Chapter 2

2.1 Elemental Boron

Boron is the fifth element in the periodic table and just one place before carbon. Boron is the only non-metallic element of group III [90]. Boron is a so-called electron deficient element, which means that it has fewer valence electrons (three) than available orbitals (four), therefore, conventional 2 electron - 2 center bonds are insufficient to solve the problem of electron deficiency. Instead, a complex mixture of two – center bond and multicentre electronic bonds is formed in elemental boron [83]. These bonds are of the covalent kind [83]. Pure elemental boron is not found in nature, but it can be extracted from minerals like ulexite ($\text{NaCaB}_5\text{O}_6(\text{OH})_6 \cdot 5\text{H}_2\text{O}$) and borax ($\text{Na}_2\text{B}_4\text{O}_7 \cdot 10\text{H}_2\text{O}$) to get boron that is highly purified in nature [83].

2.1.1 Different polymorphous of boron

Boron has three recognized crystalline allotropes α – rhombohedral, β – rhombohedral and β – tetragonal [83], of which the β – rhombohedral lattice with 106.7 atoms per unit cell is the most stable [102]. These crystalline phases are composed by arrangements of icosahedral clusters B_{12} strongly bonded together by covalent bonds. This crystalline packing provides boron with an extremely high hardness, great chemical stability as well as a high melting point of approximately 2300 °C [83]. All crystalline boron phases are known to be semiconductors in their bulk state, in particular, the β – rhombohedral boron in ambient conditions presents a semiconductor behaviour with a band gap of approximate 1.5 eV [128]. At high pressures of 250 GPa and a critical temperature of 11K boron turns out to be superconductors [13]. In the crystalline phases mentioned, an elemental α – tetragonal boron allotrope containing 50 atoms per unit cell has been reported [128]. There is strong evidence suggesting that such a lattice should incorporate small amounts of foreign elements in order to be stable since T-50 does not have enough electrons to provide chemical stability [129].

2.1.2 Boron nanotubes

The chemistry of boron is rather versatile and complex and so B_{12} cannot be safely regarded as the only building block of boron crystalline structures. This issue was first questioned by

Boustani and Quandt [130], who proposed a so-called Aufbau principle that allows the construction of structures such as nanotubes by assembling and bending of novel quasi-planar boron clusters [131]. This conception has fuelled a series of theoretical and experimental works on the search for new boron crystalline phases in two and one – dimensional arrangements. The theoretical work on the viability of boron nanotube (BNTs) by Boustani and Quandt has served as a cornerstone which set in motion the pursuit for an experimental method to synthesize BNTs, and this search diversified into synthesis of all kinds of boron nanostructures such as nanowires, nanoribbons, nanobelts, nanosheets, nanofibers, nanowebs, nanotubes, nanorods, nanocones, and bamboo-like nanotubes [131]. The considerable efforts to experimentally synthesize boron nanotubes arose because of their predicted structural stability. Boustani *et al* calculated that the strain energy of such nanotubes, which is defined as the energetical difference between an atom in the tube and that of the same atom forming part of an infinite flat sheet [130].

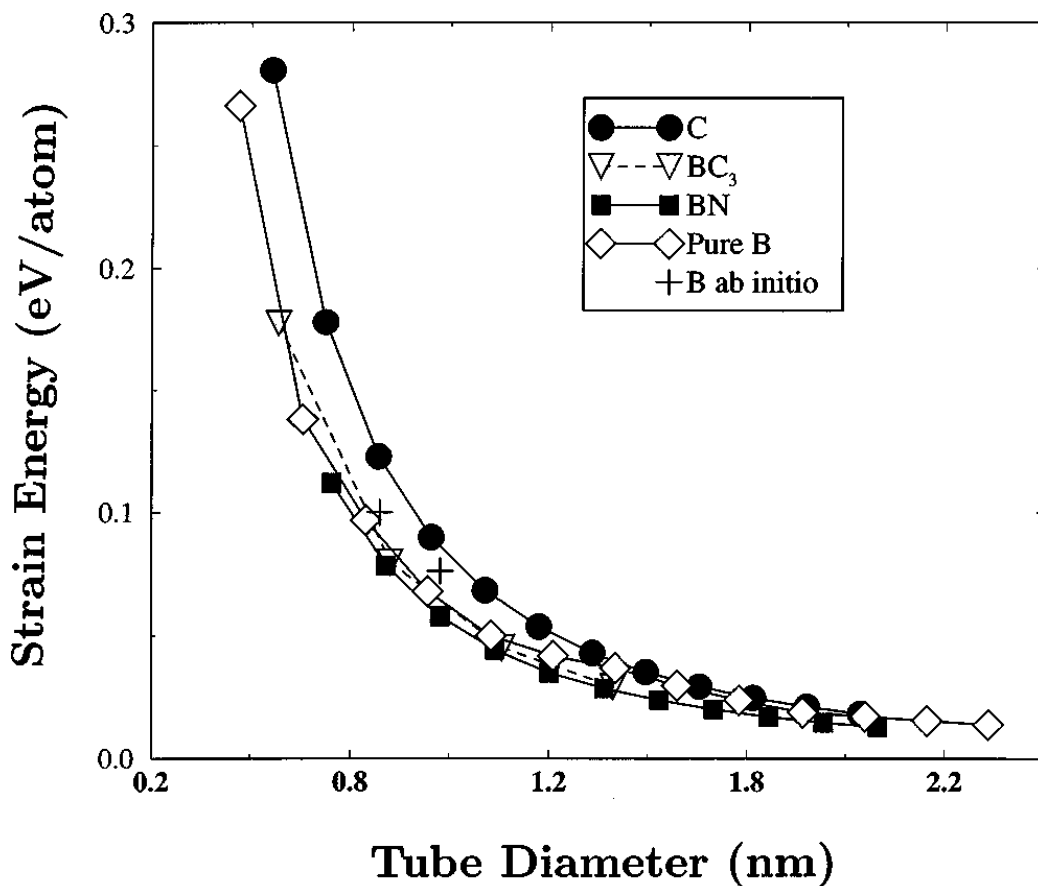


Figure 2.1: Shows the different chemical compositions of strain energy for armchair nanotubes [30].

For boron nanotubes with a certain stable lattice structure and a certain diameter, the strain energy can be lower than that of carbon nanotubes (CNTs) and comparable to that of compounds such as BN and BC_3 , as was shown in Figure 2.1. Chemical stability is not the only reason why the pursuit for the successful synthesis of BNTs that has been consistently become a serious topic within the scientific researchers. Apart from structural viability, BNTs of all proposed lattice structures are predicted to have a strong conductive behaviour independent of diameter, if one assumes smooth nanotubes, that is without superficial buckling and chirality matters, in order words, they are all predicted to be metallic in contrast to the case of CNTs whose conductive properties depend on their chirality [131-134]. BNTs has been successfully synthesized and documented through the CVD method by some group of researchers [120].

2.2 Introduction to Boron Nanostructures

Boron is a unique element both in the solar system as well as in the earth's crust. Boron is produced by cosmic ray spallation and since the geochemical processes have greatly concentrated boron, it is not considered as a rare element from the perspectives of commercial availability. One of the earliest accounts of the use of boron has been found in the Chinese civilization in the form of borax glazes since AD300. Boron was first partially isolated in 1808 by French chemist Joseph L. Gay-Lussac and L. J. Thenard by reducing boric acid at high temperature [135] and independently by Sir Humphry Davy utilising electrolysis [136]. Boron occurs in two naturally occurring isotopes, B_{10} and B_{11} . The B_{11} isotope forms the major chunk of the naturally existing isotopes, the existence of the B_{10} isotope is of considerable significance due to its large cross-section for thermal neutron capture. The boron atom has five electrons and its electronic configuration in the ground state can be represented in Figure 2.2(a) and (b) below.

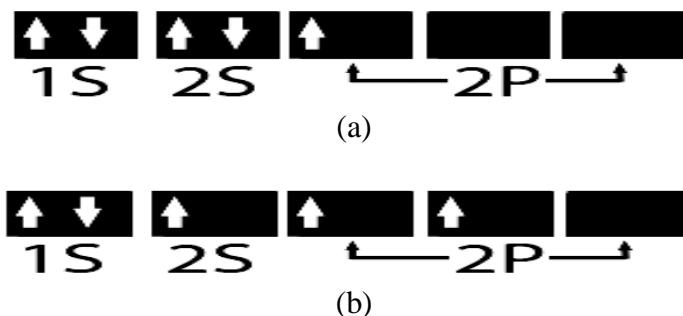


Figure 2.2: (a) Shows the boron atom at the ground state with five electrons and its electronic configuration, (b) Revealed boron in its most stable state by promoting an electron from the 2s to the 2p orbital.

The singlet state can be observed in borylene (B-H). In terms of electron orbitals, this six-electron molecule has a core-shell (1σ), a bonding pair (2σ), and a lone pair of electrons (3σ) on the boron atoms [137]. Boron in the most stable compounds exhibits an oxidation state of +3, which is achieved by promoting an electron from the $2s$ to the $2p$ orbital as shown in Figure 2.2(b) above [138]. This causes strong electron acceptor properties of boron compounds and due to the very high ionization potentials, boron (III) does not show the chemistry of B^{3+} ions but that of covalent boron (III) compounds. The tetra-coordinated boron compounds, depending on the ligands, are found to be observed in negative, neutral, and positive charge states. The conventional localized bond between two atoms uses an atomic orbital from each atom and is filled by two electrons [139]. This does not hold true for electron deficient compounds such as that of boron. The bonding in these compounds has been described by Eberhardt, Crawford, and Lipscomb by utilising a three-center localized molecular orbital employing three orbitals but a single electron pair. The two-electron, three-centered bonding in boron has been able to provide insights into the structural and electronic properties of boron nanostructures [140]. The chapter explains different boron nanostructures such as nanoclusters, nanosheets, nanotubes, and nanowires that have been experimentally realized or theoretically investigated.

2.2.1 Boron Nanowires

Nanowires are simple to visualize, they are thin and very elongated solid rods, not hollow as in the case of nanotubes, with a cross section not surpassing a few hundreds of nanometres. The nanowire can be amorphous or crystalline. Nanowires are of great interest to the scientific researchers since a good number of applications can be predicted for such nanostructures, especially if they are metallic or semiconductor type. Nanowires are the most investigated boron nanostructures experimentally [141]. They have been synthesized both in crystalline and amorphous forms [120, 142, 143], using different growth techniques such as chemical vapor deposition, magnetic sputtering techniques, and laser ablation of targets using pulsed lasers [141, 144, 145] as shown in Figure 2.3(a) and (b) below.

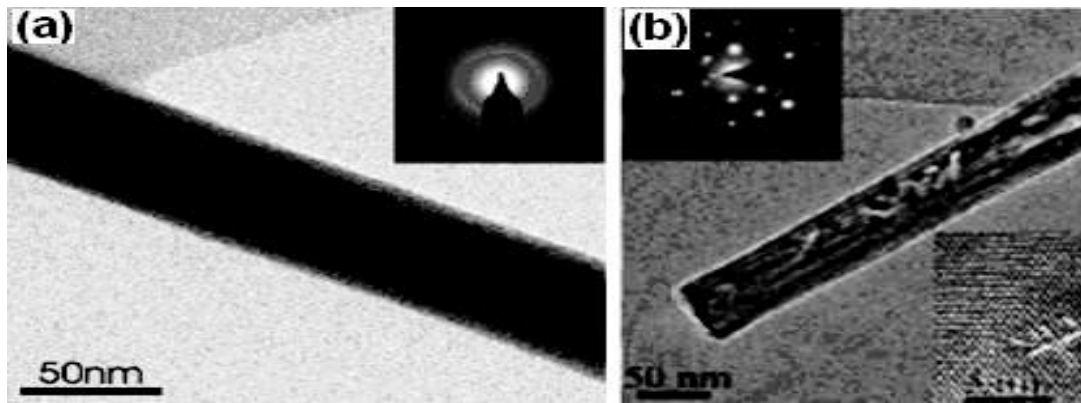


Figure 2.3: Show HRTEM images (a) Amorphous BNWs synthesized by laser ablation (LA) technique.[146], (b) Crystalline BNWs synthesized via CVD method[147].

Experimental results indicate that the presence of catalytic elements is one of the most crucial conditions for the growth of crystalline boron nanowires [101, 148]. Crystalline boron nanowires are understood to be semiconducting near room temperatures [101]. The conductivities of these nanowires is robust and does not change even on application of large strain, indicating that these nanostructures are highly resilient [149], even under highly strained conditions [145, 150]. These nanostructures also exhibit excellent field emission properties [150].

2.2.2 Boron Nanosheets

The experimental discovery of boron nanotubes has motivated the investigation of the structural properties of monolayer boron sheets [120]. Weir et al reported the monoatomic layer of boron nanosheets growth on a silicon (100) substrate [151]. It is observed that $\frac{1}{2}$ monolayer coverage forms an ordered 2×1 structure and can be distinguished using a low-energy electron diffraction (LEED) pattern. The LEED pattern for pristine silicon shows $(\frac{1}{2}, 0)$ as the most intense half order, whereas $(1, \frac{1}{2})$ forms the most intense $\frac{1}{2}$ -order spot in the diffraction pattern from a boron-covered surface [152], as revealed in Figure 2.4 (a) and (b).

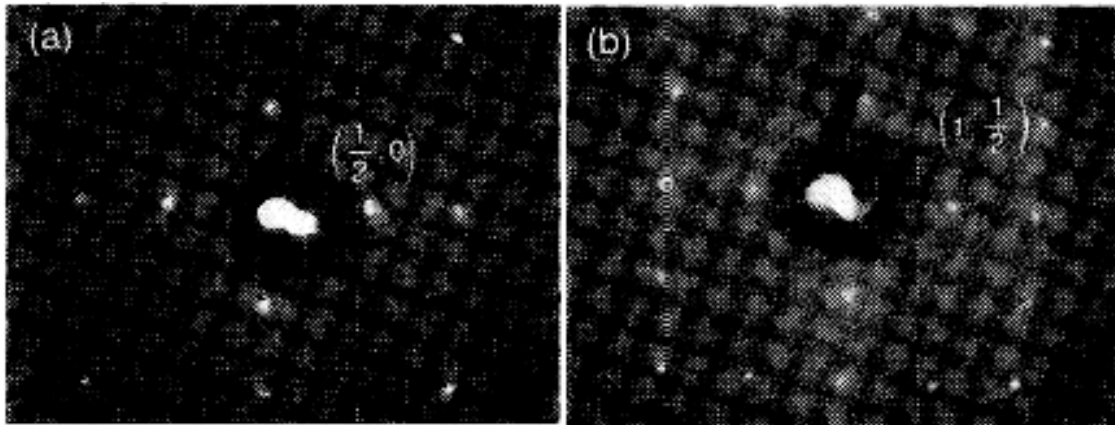


Figure 2.4: *Reveal LEED patterns for (a) The pristine silicon (100) and (b) silicon (100) with a $\frac{1}{2}$ monolayer of boron [152].*

Investigation of the local structure using scanning tunnelling microscopy along with tunnelling spectroscopy suggests that the principal structural subunit is an ordered arrangement of four boron atoms at substitutional sites in the first bulk silicon-like layer [153], which is then capped with an ordered arrangement of silicon dimmers and dimer vacancies as shown in Figure 2.5 below.

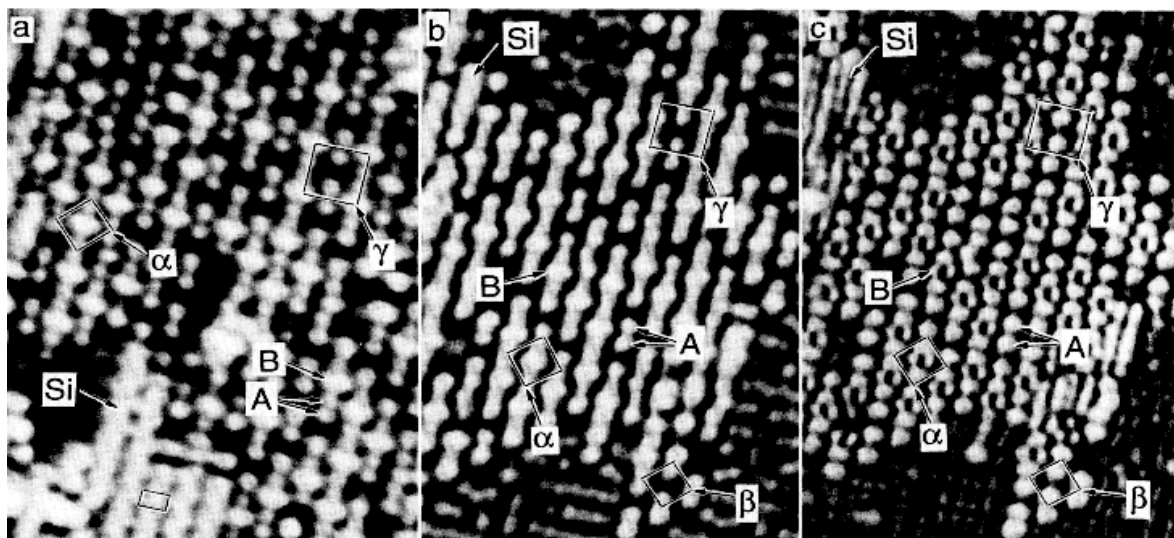


Figure 2.5: *Show high-resolution images of boron induces reconstructions on a Si (001) surface and where A and B denote the structural subunits of reconstructions. (a) Reconstructions and region of clean Si (001) outlined (b) A high-resolution image of occupied surface electronics states, (c) Unoccupied electronics states [154].*

These ordered surface reconstructions are stable under vacuum and can be preserved as metastable states at the solid-solid interfaces [154]. A lot of effort has been made to synthesize

and study the structural properties of monolayer boron sheets; however, no experimental verification of stabilized monolayer boron sheets under normal conditions has been reported. Different atomic models of monolayer boron sheets such as the idealized and buckled triangular (1212) reconstructed (1221), and hexagonal sheets have been proposed using computational methods [155-157], as shown in Figure 2.6.

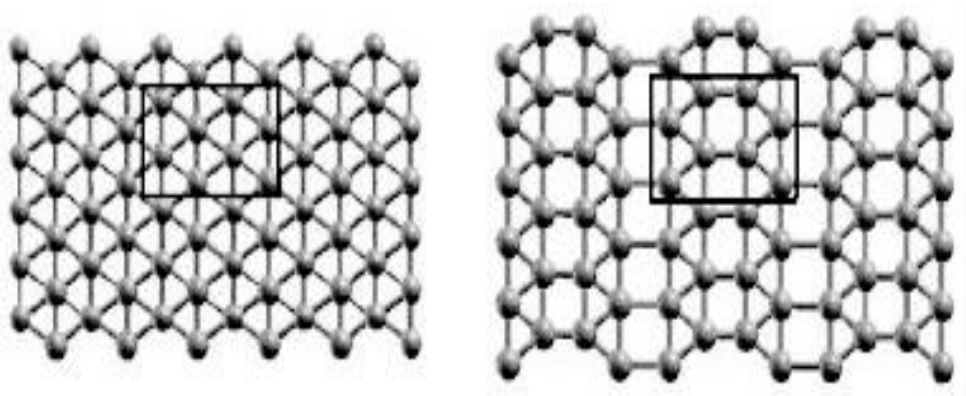


Figure 2.6: Atomic structure of proposed idealized triangular and reconstructed monolayer boron sheet [155].

One of these models, particularly the hexagonal monolayer boron sheet, has been inspired by the atomic model of graphene sheets. First-principles calculations have recently indicated the α -boron sheets to be the most stable ground structure of monolayer boron sheets [158], as shown in Figure 2.7.

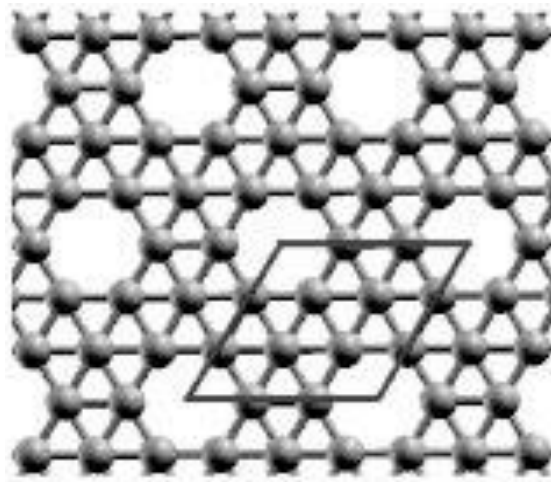


Figure 2.7: Atomic structure of a proposed α -boron sheet using density functional calculations [159].

These sheets form precursors to B_{80} clusters and conduct only by means of out-of-plane P_z orbitals [158, 159]. The holes in the α -boron sheets are understood to serve as scavengers of extra electrons from the adjacent filled hexagons [158, 160].

2.2.3 Boron Nanoribbons

Nanoribbons can be synthesized using either top-down or bottom approaches [95]. Carbon nanoribbons are the most explored quasi-2D nanostructures and have been synthesized by controlled unzipping single-walled carbon nanotubes, lithography, and wet chemical methods [161, 162]. Xu *et al* utilized catalyst-free pyrolysis of diborane at 630 °C-750 °C at low pressure to synthesise single crystalline α -boron nanoribbons [95]. Nanoribbons synthesized using this technique have been investigated for thermal transport properties. The thermal conductivity of bundled boron nanoribbons is higher than that of a single nanoribbon [142], and their thermal transport properties can be reversibly modified by wetting the van der Waals interface between nanoribbons and various solutions. The properties of boron nanowires have been reported using first-principles density functional theory. These nanoribbons were derived by cutting α -boron sheets along different directions, producing linear and armchair-edged nanoribbons as shown in Figure 2.8.

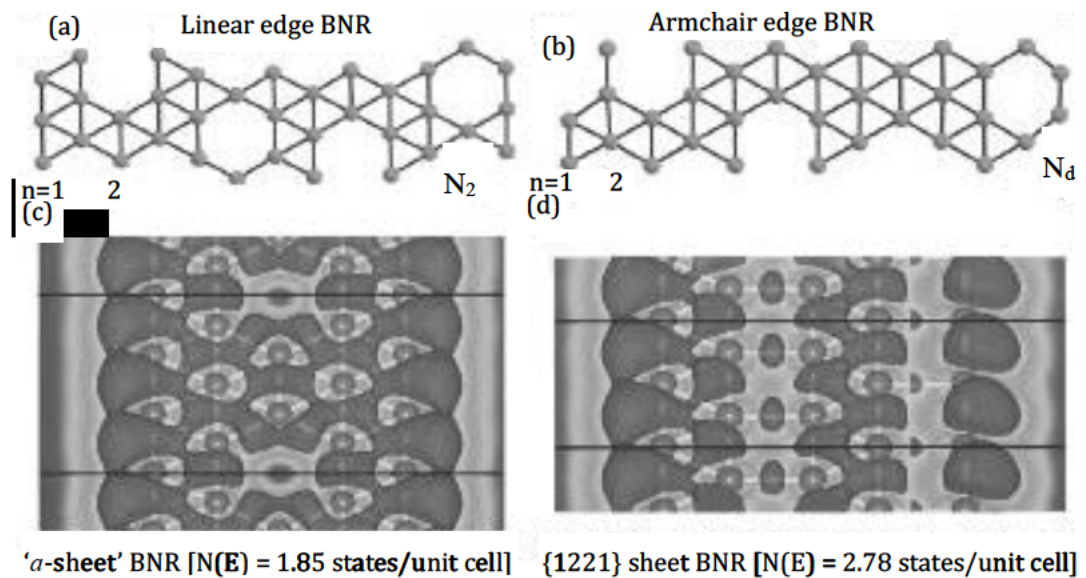


Figure 2.8: Shows atomic structure of nanoribbons derived from an α -boron sheet (a) linear and (b) armchair edge. The electron localization function (ELF) plot for nanoribbons derived from (c) a stable α -boron sheet and (d) a reconstructed boron sheet [143].

A comparative study of the electron localization function shows that the delocalization of π - electrons orbitals occurs more in nanoribbons derived from α -boron sheets than in those derived from other precursors [143]. These preliminary reports on boron nanoribbons using ab initio methods and experimental investigations suggest that nanodevices capable of thermal management can be invented using these nanostructures

2.2.4 Boron Nanoclusters

Anderson and Hanley rediscovered of the B_{13+} nanocluster [163]. Both theoretical and experimental reports have been surfaced for investigating their interactions, structures, and stability [164-166]. Theoretical investigations based on ab initio quantum chemical techniques by Boustani [130] that have been predicted the ground-state structural configurations of small boron nanoclusters are found to be planar [166], as shown in Figure 2.9.

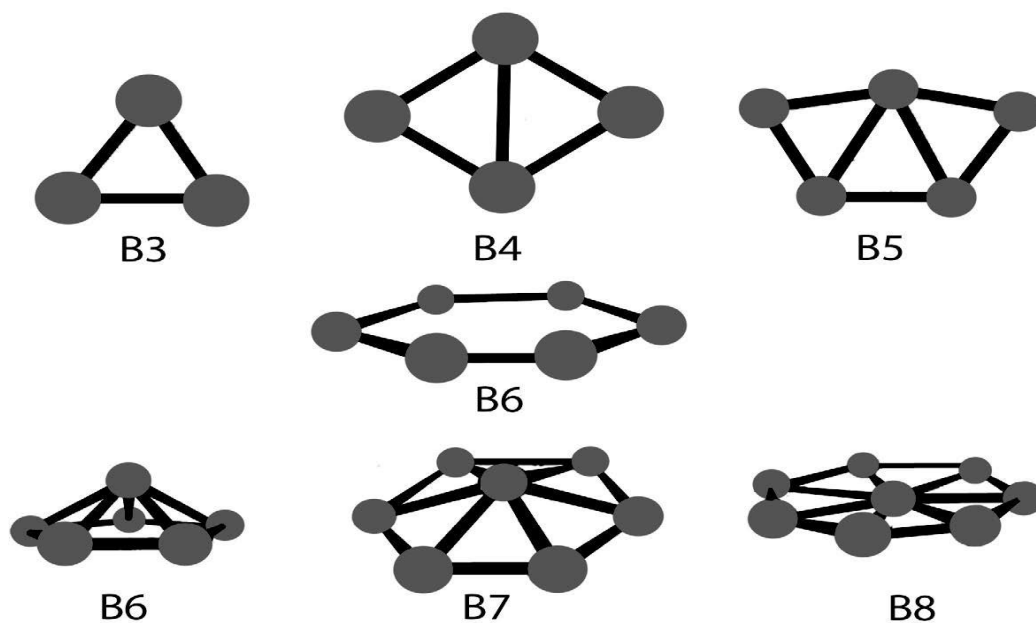


Figure 2.9: Ground-state structures along with structural symmetry of neutral boron nanoclusters obtained using the 3-21G basis set [166].

This elemental set comprises of boron clusters B_n , where $n = 2-8$ [167]. The symmetries of different elemental clusters are C_{2v} , for B_3 , B_5 , and B_7 , C_{5v} for B_6 , D_{7h} for B_8 , D_{2h} , for B_4 and planar B_6 nanoribbons clusters. This set of clusters forms the structural basis for larger nanoclusters [168]. The set of quasi-planar and convex clusters is mainly composed of units

of hexagonal pyramids which belong to this elemental set of clusters. The B_6 clusters are found to exist in planar hexagonal and pentagonal pyramid conformations [130], and form the most stable elements of this set [169]. Larger nanoclusters of boron acquire quasi-planar and very compact 3D structures, as shown in Figure 2.9 above [168]. Quasi-planar boron nanoclusters can be constructed from hexagonal pyramidal subunits by dovetailing each other and forming axial bonds [168], also, when the out-of-plane apices of these subunits either lie above the plane of peripheral atoms, such nanoclusters are known as convex clusters. Quasi-planar boron nanostructures are obtained when the apices of subunits lie alternately above and below the plane containing peripheral atoms [170].

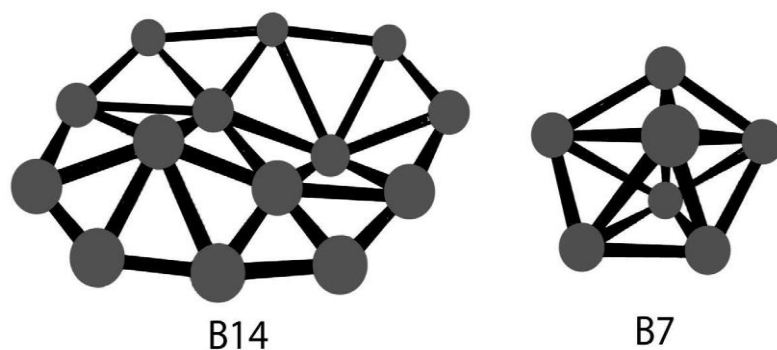


Figure 2.10: Shows representative quasi-planar and 3D nanoclusters of boron respectively [166].

The structures of 3D nanoclusters are similar to well-known α - and β -rhombohedral boron crystals [168], as shown in Figure 2.10 above. The 3D nanoclusters can be classified into compact 3D and open 3D nanoclusters. The very compact 3D clusters consist of trigonal, square, pentagonal, hexagonal, and heptagonal bipyramids [171]. The open 3D structures have low point group symmetries [172]. Ab initio calculations at the Hartree – Fock self-consistent field (HF-SCF) level [173], have suggested that the energies of 3D nanoclusters are higher than those of convex or quasi-planar clusters. The insight into the structure of boron nanoclusters is expected to pin down the atomic structure of higher-dimensional boron nanostructures [174].

2.2.5 Boron Nanotubes

Boron nanotubes are a new class of nanomaterials that have been theoretically predicted to exist in stable form, the exact atomic structure and hence their electronic properties are a subject of discussion. Theoretically, a nanotube is formed by rolling up the boron nanosheet joining

the two ends of the chiral vector [175]. Variation of the tube diameter and chiral angles control the properties of the various nanotubes formed [176]. Single-walled boron nanotubes (SWBNTs) are semiconducting or metallic depending on the variation of chiral angle and tube diameter that has been confirmed experimentally [177]. It is predictable that if boron nanotubes can be synthesized, their electrical properties are, also controlled by variation of chiral angle and tube diameter [178, 179]. BNTs is going to create great interest more than boron nitride nanotubes (BNNTs) and carbon nanotubes (CNTs) in the future. Ciuparu et al first reported the synthesis of SWBNTs with a diameter of 3 nm [120], using a technique called catalyst template assisted growth [120]. BNTs samples were investigated using Raman spectroscopy and showed phonon modes to suggest their tubular structures [120]. The presence of vibration modes below 500 cm^{-1} in the Raman spectra has been understood due to the presence of radial breathing modes in BNT samples. The electron energy loss spectra suggest the presence of B K-edge, indicating its origin from the boron tubular nanostructures, as shown in Figure 2.11 (a) and (b).

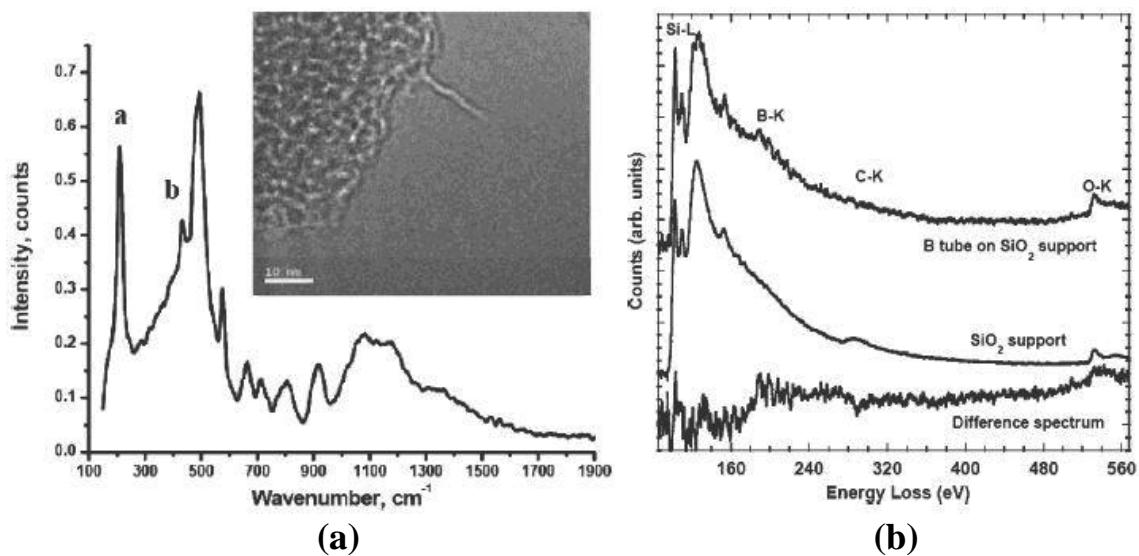


Figure 2.11: (a) Raman spectra of a boron nanotube. The inset shows the micrograph of the boron nanotube. (b) The Electron energy loss spectrum of a boron nanotube on a SiO_2 substrate [120].

Double - walled boron nanotubes (DWBNTs) and multi-walled boron nanotubes (MWBNTs) mixed with boron nanofibers (BNFs) were also prepared with a diameter range of 10 to 30 nm [180]. Szwacki *et al* predicted that the boron buckyball B_{80} would have a stable hollow cage,

which is symmetrically similar to the icosahedral structure of C_{60} [181]. A flat stable boron sheet has been predicted which is composed of a hybrid of triangular and hexagonal configurations [182]. By first principle calculations, the vibrational frequencies, free energy, and heat capacity of the flat hybridized sheet and buckled triangular sheet are compared to verify the thermodynamic stability of the boron sheet [183, 184]. Amongst the earliest investigations, idealized triangular, hexagonal, and reconstructed (1221) boron sheets were considered as precursors to boron nanotubes [155, 159, 162]. With the recent predictions of α -boron sheets as being the most stable monolayer sheets, the properties of boron nanotubes formed by rolling these sheets have been investigated [159]. Ab initio investigations suggest that the radial breathing modes of nanotubes formed by rolling an α -boron sheet depend strongly upon the chirality [159]. In Table 2.1, the chiral indices, diameters and radial breathing modes of each boron nanotubes were shown below.

Table 2.1: Shown the chiral indices, diameters and radial breathing modes of each boron nanotubes

Nanotubes chiral indices	Diameters (\AA)	f_{RBM} (cm^{-1})
5,5	8.13	238.9
9,0	8.63	224.8
6,6	9.93	195.5
12,0	11.31	170.6
7,7	11.37	173.7
8,8	13.13	150.2
18,0	16.50	119.2

The frequency of 210 cm^{-1} observed from the experiment reported by Ciuparu et al is in close range with calculated frequencies [120].

2.2.5.1 Properties of Boron Nanotubes

2.2.5.1.1 BNTs Surface Electron affinity and Work function

In field emission, BNTs as one of the boron nanostructures was found as potential materials, that has been considered as best. The most important factors about the BNTs are the affinity of their surface electrons that strongly affect field emission properties [126]. To measure the work function or electron affinity of any nanostructures effectively. The ultraviolet photoemission

spectroscopy (UPS) is the best instrument to be utilized, for semiconductor nanostructures which is actually based on the energy band gap of the semiconductor materials [185]. The work function or electron affinity of the nanostructures is defined as the energy difference between the vacuum level and the bottom of the conduction band [186]. To confirm the surface electron affinity of boron nanostructures, Liu *et al* compared two samples [126]. The first sample is a mixture of film of BNTs and BNWs, while the second one is the pure BNWs film using silicon as the substrate. These two samples have similar densities and characteristics, as shown in the UPS spectra in Figure 2.12.

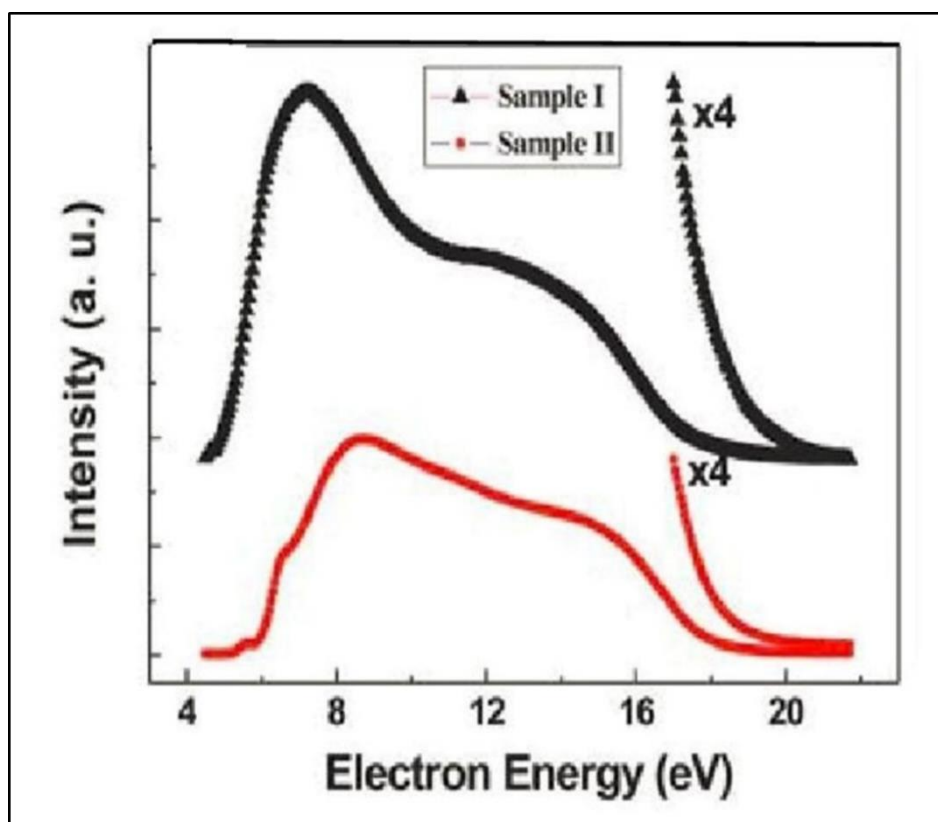


Figure 2.12: The UPS spectra of the pure BNWs film and a mixture of BNTs and BNWs film, [126].

The spectral width of each sample was established by using a linear extrapolating method, the width (W_{spectra}) obtained with this method was found to be 15.9 eV and 16.4 eV for pure BNWs film and a mixture of BNTs and BNWs film respectively. A relation was deduced to determine the surface electron affinity X of the two samples [126].

$$X = h\nu - E_g - W_{spectra} \quad (2.1)$$

Given that, E_g is the energy band gap. This energy band gap of boron nanostructures was assumed to be the same as that of bulk boron which is 1.56 eV [150, 187]. The radiation energy of the Helium I line, $h\nu$ is 21.2 eV. The surface electron affinity of the two samples was estimated to be 2.74 eV and 3.24 eV for pure BNWs film and a mixture of BNTs and BNWs film respectively. The results obtained showed that BNTs were found with a lower surface electron affinity than BNWs. The BNTs surface work function value was deduced according to the equation connecting the work function Φ and electron affinity X , which is given as

$$\phi = \chi + \frac{E_g}{2} \quad (2.2)$$

This relation gives the surface work function of pure BNWs film and a mixture of BNTs and BNWs film as 4.52 eV and 4.02 eV respectively. It was noticed that the surface work function of BNTs is lower than that of bulk boron which is 4.6 eV [187].

2.2.5.1.2 Electrical and Field emission properties of BNTs

Electrical properties are one of the properties of BNTs. BNTs possessed metallic properties they have been proved through theoretical studies [131, 166]. Which are independent of its structural tubes whether they are the armchair, zigzag, or chiral, but with experiments, all these are yet to be verified [175, 188]. Electrical properties of BNTs were carried out by Liu et al, using a modified high vacuum system [126]. Experiments were performed on many BNTs. But the typical results of three individual BNTs were picked for comparison to reveal their intrinsic physical properties in both electrical and field emission [150]. The tubes are selected as BNT ‘A’, BNT ‘B’ and BNT ‘C’, as shown in Figure 2.13.

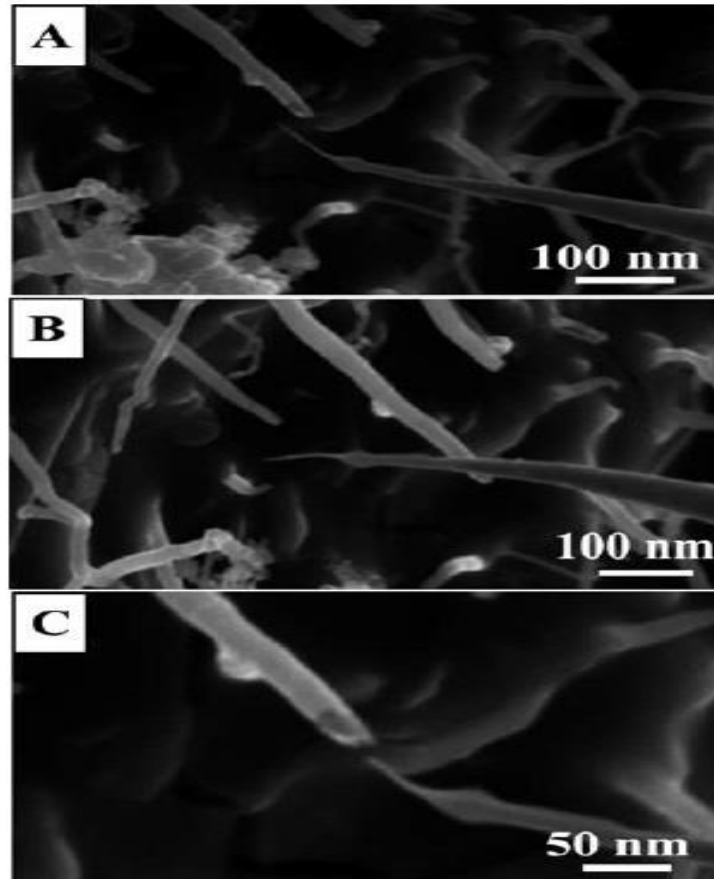


Figure 2.13: SEM images of the individual BNT ‘A’, BNT ‘B’ and BNT ‘C’ [126].

In Figure 2.14A, the electric transport properties of the three-selected individual BNTs can be compared by studying the electric transport I - V curves. It was noticed that the electric transport I - V curves are nearly linear for all the three individual BNTs selected. This indicated the best electric contact that formed between the BNTs and substrate utilised [189]. When average values of the outer diameter of 30 nm, the inner diameter of 20 nm and length of 3 μm were taken it was deduced that BNT ‘C’ with $36.85 \Omega^{-1} \text{cm}^{-1}$ has the best conductivity properties. The conductivity is lower in BNT ‘A’ with $16.76 \Omega^{-1} \text{cm}^{-1}$ when the three BNTs selected were compared. These individual BNTs possessed the conductivity of a metal ($> 10^2 \Omega^{-1} \text{cm}^{-1}$), which means that the electrical transport properties of BNTs can be compared to that of metals.

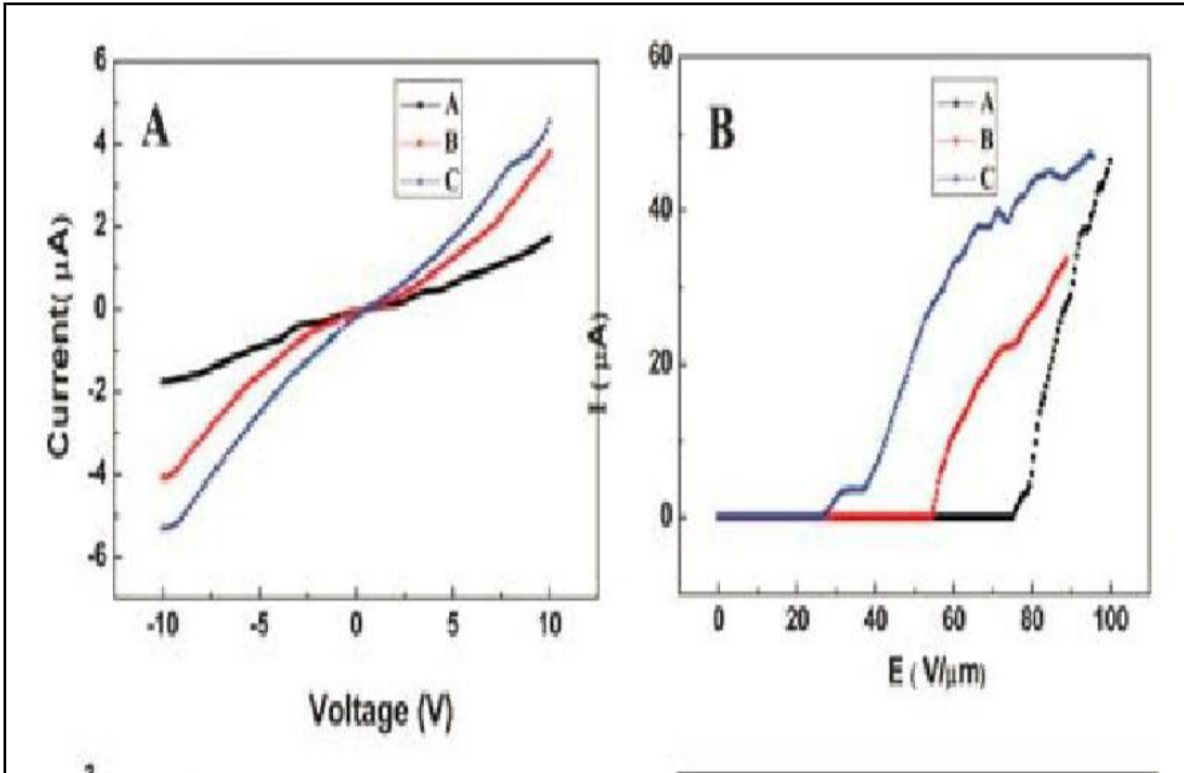


Figure 2.14: (A) The electric transport curves of single BNTs, A, B and C. (B) The field emission I – E curves of the three individual BNTs (A, B and C) [126].

In studying field emission properties of BNTs, Figure 2.13 was utilized. A graph of field emission current against an electrical field (I – E) of BNTs is shown in Figure 2.14B above. It was discovered that the field emission of BNT ‘C’ has the best performance. The poorest amongst the three is BNT ‘A’ with the worst field emission performance. The conclusion was made that any BNT with the highest conductivity is likely to have the best field emission performance [126].

2.2.5.1.3 Similarities and differences between BNTs and CNTs

It was observed that individual BNTs emission current endurance is twice high than that of CNTs, as reported (8-20 μA) [190]. This indicates that BNTs can be more useful than CNTs in most of the applications of high-current point sources and high – power microwave tubes [191]. When the cross-section area ‘A’ of a BNT is considered, which can be deduced from the relation given below,

$$A = \pi (r_{out}^2 - r_{in}^2) \quad (2.3)$$

given that, r_{out} and r_{in} are the outer and inner diameters (30 nm and 20 nm), of a BNT. The cross-section area of a BNT was found to be $3.925 \times 10^{-16} \text{ m}^2$. The emission current density upper limit of BNT can attain $2.04 \times 10^{11} \text{ Am}^{-2}$ [192] and this can be compared to that of the CNTs, which have been reported earlier (10^{11} - 10^{12} Am^{-2}) [193]. This indicates that BNT with the best endurance will have high working current density [126]. BNTs turn – on and threshold field are greater than that of CNTs [194]. The BNTs has improved field emission behaviour, even when compared with BNWs [190]. This BNTs will find a suitable position more than CNTs in field emission applications in the future due to its emission uniformity [195]. BNTs conductivity has been improved to be chirality – independent more than CNTs [126, 196]. The conductivity of BNTs are in the range of 12 - $76 \Omega^{-1} \text{ cm}^{-1}$, these were higher than most of the values reported on other nanostructures. These values are very close to the values reported on CNTs ($10^2 \Omega^{-1} \text{ cm}^{-1}$) and with this BNTs possessed electrical transport properties as CNTs [196]. According to Liu et al, power and luminescent efficiency of BNTs in the luminescent tubes are more than 85% and 0.11 m W^{-1} , which can meet the requirement for lighting devices [126]. BNTs total power consumption P_{total} (78.85 / 80.92 n W) and gate power consumption, P_{gate} (12 nW) is greater than that of CNTs devices P_{gate} (10.72 nW) and P_{total} (77.7 nW) [197]. Because of that, this can be used as the general commercial displays since it is lower than many lighting elements. For example, light emitting diodes and cathode ray tubes using hot filaments when compared the performance of BNTs in luminescent tube application, it was observed that the presence of BNTs will be more beneficial to the tube performance applications than CNTs in the future. BNTs cold cathode luminescent tubes have the threshold field performances that are like CNTs luminescent tubes [64-66]. In outdoor display applications in the future, BNTs will be found more suitable, by increasing its operation luminance effectively very close to that of CNTs.

2.3 Theoretical/computational studies of boron nanomaterials

2.3.1 Special Challenges on Boron Nanotubes, (BNTs)

The first challenge is that the actual exact crystalline structure of BNTs is yet unclear by experimental observations. Secondly, the lattice structure of BNTs has not been clearly characterized by the experiments, there is extensive theoretical literature on the topic [159]. Lastly, there has been a huge progress in the developing of feasible predictions for the actual atomic order in BNTs [198].

2.3.2 Stability and Conductivity Properties of the Boron Sheets

Bezugly and Kunstmam *et al* show a theoretical comparison between the stability and conductivity properties of the three boron sheets, that has been regarded as the most likely sheets to build up to form the real BNTs [134]. They are as follows: α -boron sheet (α -BS), the buckled triangular-boron sheet (BT-BS) and distorted hexagonal-boron sheet (DH-BS) lattices [134], as shown in Figure 2.15. They reached a set of final conclusions, that all BNTs made from all the three sheets are metallic irrespective of their diameter. They found out that the work function of BNTs made from the α -boron sheet is the one that agrees better with the experimental values, which shows that BNTs have an atomic structure related to α -boron sheet [134].

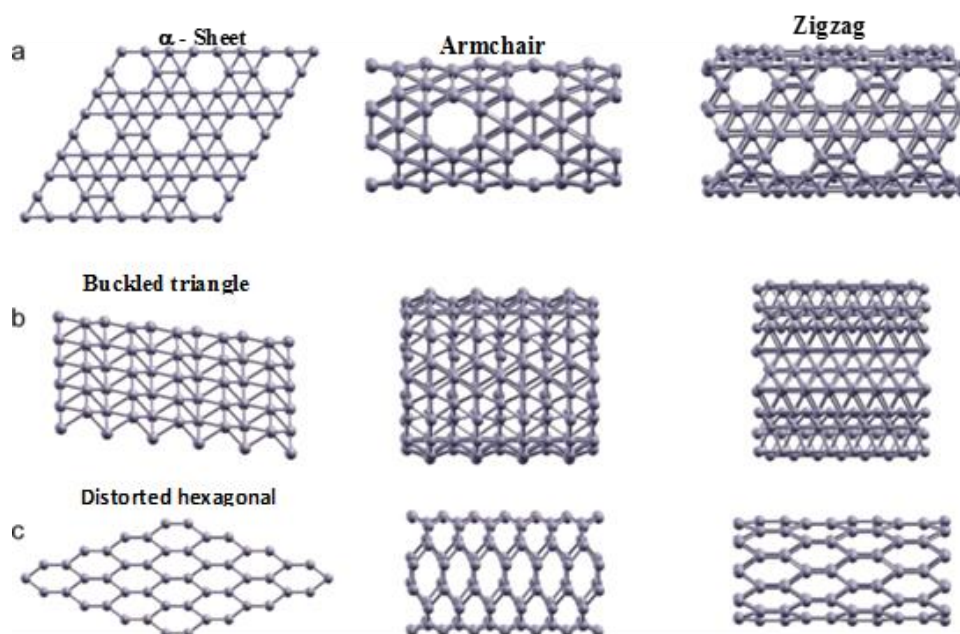


Figure 2.15: The first column indicates the lattice structure of boron sheets while the second and third columns show armchair and zigzag BNTs respectively. (a) α – sheet, (b) Buckled triangular and (c) Distorted hexagonal [134].

BNTs occupy a central role in the realm of boron-based nanostructures. This makes BNTs the only and best quasi – one-dimensional boron nanostructures for technological applications. There is a lot of experimental synthesis of boron nanostructures, such as BNWs, which is the type of boron of one dimensional (1D) – nanostructures. Other examples are boron nanocones (BNCs), boron nanofibers (BNFs), boron nanorods (BNRs) and boron nanoribbons (BNRBs).

2.4 Purification and Centrifugation of single walled nanotubes

2.4.1 Purification and processing of SWNTs

In all applications involving the use of single-walled nanotubes (SWNTs), it is assumed that impurities such as metallic catalysts, e.g. nickel and cobalt, which are necessary for the synthesis process, are removed. The purification and processing of SWNTs form a large component in nanotube research. The research presented in the dissertation also involved the purification and processing of SWNTs. It is inevitable to sidestep the stage of purification and processing in SWNTs. This should be applied to SWBNTs to be useful in some of the applications, such as in a sensing nanoelectronics device, electron emission nanodevices and for nanoscale interconnect applications. Lastly, a summary of the purification technique of sorting inhomogeneous nanomaterials containing SWNTs is reported below.

2.4.2 Purification of SWNTs by centrifugation method

There are many reports and reviews on the purification of SWNTs. Many of them are complicated and therefore, techniques that ease the purification process are favored. The use of a centrifuge is one such technique. Haddon et al. showed that low-speed centrifugation was effective in removing amorphous material [199]. In the experiments, the amorphous material content is preferentially suspended in aqueous dispersions during low-speed centrifugation of 2000 rpm, leaving the single-walled nanotubes (SWNTs) in the sediment. This technique is an effective base on the ζ - potential which is the magnitude of the electrostatic interaction between colloidal particles given as an index. The effectiveness of this technique is built on the ζ - potential which is an index of the magnitude of the electrostatic interaction between colloidal particles. The ζ - potential becomes effective after the as-prepared material is treated with acids to oxidize the metallic catalysts which leave a charge on the different components. The suspension in each of these components attain a different ζ - potential and acquire different mobilities due to electrostatic forces. The use of the centrifuge discriminates between the different components in the suspension. A schematic of the purification process by utilizing a centrifugation technique is shown in Figure 2.16.

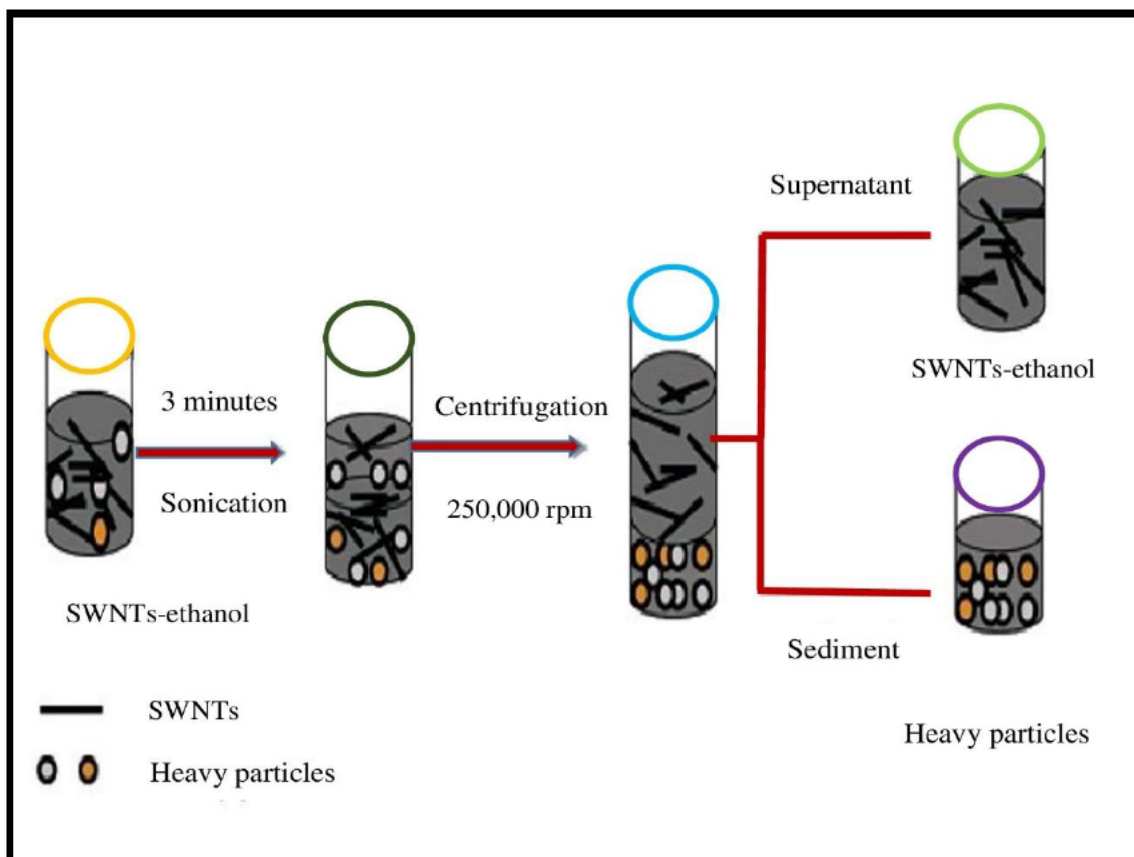


Figure 2.16: Shows a schematic of the resuspension-centrifugation-decantation cycle for removal of heavy particles and purification of SWNTs [199].

A high centrifuge was found to be enriched with supernatant of SWNTs and all the remnant leftover formed the sediment. The reports about the effectiveness of the purification of SWNTs by ultracentrifugation has been as high as 90% by some authors [199].

2.4.3 Sorting single-walled nanotubes (SWNTs) by the density gradient Ultracentrifugation (DGU) technique

SWNTs vary in their diameter and chiral angle, and these physical variations result in striking changes in their electronic and optical behavior. This has prevented their widespread application in high-performance field-effect transistors, optoelectronic near-infrared emitters detectors and chemical sensors. Efficient methods to sort SWNT material according to electronic properties will be needed so that large quantities of these nanomaterials can be produced which are monodisperse in their structure and properties [200]. Hersam *et al.* developed a general approach for sorting SWNTs by diameter, bandgap and electronic type for both metallic and semiconducting, using the technique of density-gradient ultracentrifugation

(DGU) [201]. This method which is scalable exploits the differences in the buoyant densities of mass per volume, between SWNTs of different structures. In the technique, purification is induced by ultracentrifugation in a density gradient. In response to the resulting centripetal force, particles sediment towards their respective buoyant densities and spatially separate in the gradient.[202]. 5mg of as-prepared SWNTs material is dispersed by sonication in a solution of a surfactant such as sodium cholate (SC). The solution is placed on top of an already prepared linear gradient such as OptiPrep and ultracentrifuged at 250 000g for 12 hours. Figure 2.17 shows a solution of SWNTs that was ultracentrifuged in a linear gradient. The separation is made evident by the formation of colored bands of isolated SWNTs sorted by diameter and bandgap. Bundles, aggregates, and insoluble material sediment formed at lower positions in the gradient.

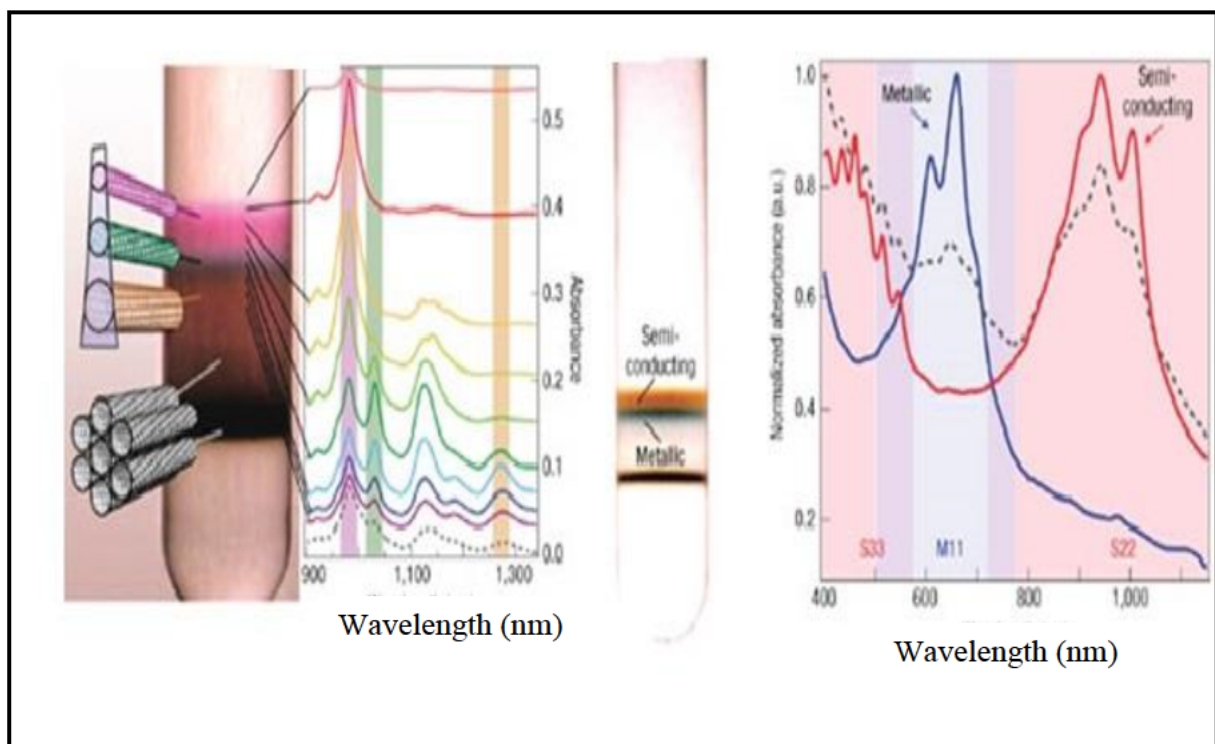


Figure 2.17 Revealed the solution of SWNTs that was centrifuged in a linear gradient [199].

Small-diameter of about 0.7 to 1.1 nm of SWNTs encapsulated with a surfactant is sorted by diameter, followed by DGU [203]. It was observed that smaller-diameter SWNTs are more buoyant and settled at higher points in the centrifuge tube. Larger diameter and bundled SWNTs are less buoyant and settled at the lower parts in the centrifuge tube. Through the

different observation of visible colors in the topmost band's parts which verified the sorting of SWNT diameter. The different fractions of optical absorbance spectra were further confirmed by sorting of SWNTs diameter. Large-diameter ranges between 1.1 to 1.6 nm of SWNTs encapsulated with a co-surfactant mixture are sorted according to electronic type followed by DGU. Sorting by electronic type as metallic fractions are peaked in some region of the absorbance spectrum which was confirmed by optical absorbance spectra, whereas semiconducting fractions are peaked in the various regions of the absorbance spectrum. Therefore, we must take note that M11 from Figure 2.17 stands for first-order optical transitions for metallic of SWNTs and while the S22 and S33 represent the second-order and third-order optical transitions for semiconducting of SWNTs respectively [201].

2.5 Synthesis techniques of nanomaterials

2.5.1 Laser ablation (LA) technique

In a laser ablation technique, a high power YAG laser vaporizes carbon atoms from a catalyst filled graphite target in a reactor held at 1200 °C to produce single-walled carbon nanotubes (SWCNTs) in a flow of inert gas passed through the reactor to carry the grown nanotubes downstream to be collected on a water-cooled copper collector [204], as shown in Figure 2.18 below.

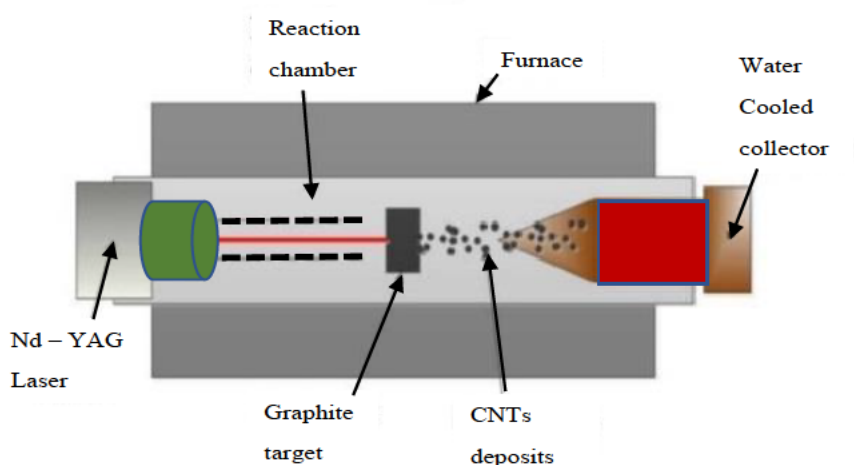


Figure 2.18: The schematic of the laser ablation technique apparatus and a high-power laser which was directed on a graphite target and then vaporizing the graphite [204].

The growth of high-quality SWNTs at the 1-10 g scale coupled with an acid purification process was achieved by Smalley and coworkers by this technique [205]. The laser ablation technique is also the best method to synthesize single wall boron nitride nanotubes (SW-BNNTs) in gram scale quantities [206]. The synthesis of SW- BNNTs is achieved by heating a hexagonal boron nitride (h-BN) target using a continuous wave CO₂ laser under a partial pressure of inert nitrogen (N₂) gas [207]. The temperature at the surface of the target is 3,200 - 3,500K. The products obtained consist of an inhomogeneous mixture of nanotubes and nanoparticles. The ratio of single wall to multiwall BNNTs obtained is 4:1 and are either isolated or organized in small bundles of 2-10 tubes with a diameter of 2 nm and lengths exceeding 1µm [207].

2.5.2 Chemical Vapor Deposition (CVD) Technique

The first thermal CVD to synthesize multi-walled nanotubes (MWNTs) reported by Endo and his research group in 1993 [208], was found to be a more energy-efficient lower temperature and scalable method for the synthesis of SWNTs. The experimental set-up for synthesizing carbon nanotubes using CVD is shown in Figure 2.19. The CVD process for carbon nanotubes uses gaseous hydrocarbons as carbon sources [209]. Gases like; methane (CH₄), carbon monoxide (CO) and acetylene (C₂H₂) were used.

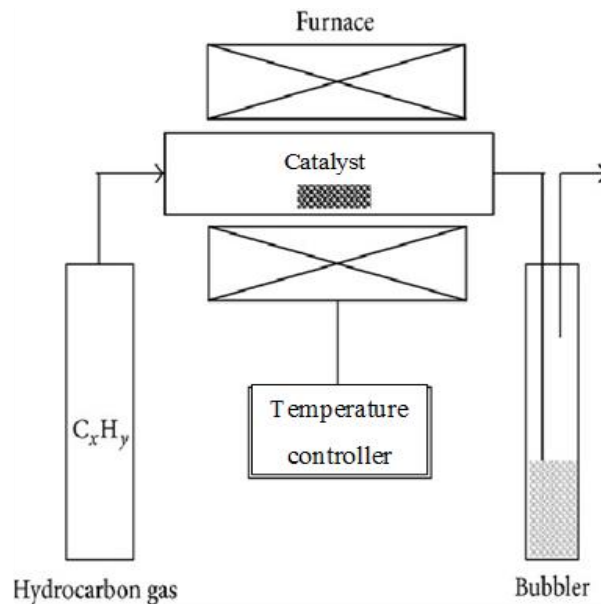


Figure 2.19: Schematic apparatus of a chemical vapor deposition (CVD) technique[209].

The hydrocarbons flow through a quartz tube placed in a furnace at temperatures ranging from 700 °C to 1200 °C to decompose the source molecules to pure carbon over metallic nanoparticle catalysts, such as Co, Ni or Fe alone or in combination with Mo [209]. The reaction times are typically from minutes to hours, compared with extremely short reaction times at more than 3000 °C in the arc and laser ablation methods. The more controllable parameters such as hydrocarbon molecules, transition metal catalyst, temperature, and pressure, in the CVD process [210], makes it possible to control the type of the length and orientation of the growing nanotubes together with in some cases their diameter [211]. The length of the growing nanotubes can be controlled [212]. The controllability and scalability of CVD make it the most promising approach for scale-up to commercial production [213]. This CVD technique was extended to the other family of different approaches to make CNTs, such as methane chemical vapor deposition (MCVD) [208, 210], high-pressure catalytic decomposition of carbon monoxide (HiPCO) [214], carbon monoxide chemical vapor deposition (COCVD) [215], alcohol CVD [216] and plasma enhanced chemical vapor deposition (PECVD) [217]. In addition, CVD was used to synthesize boron nanotubes (BNTs) as shown by Ciuparu *et al* who reported the first synthesis of pure single-walled boron nanotubes (SWBNTs) in 2004 by this method. BNTs were grown using gaseous BCl₃ mixed with hydrogen as the boron source and Mg as catalyst supported on nano-porous MCM-41 zeolite templates at 870 °C [120].

2.5.3 Ball Milling and Annealing Technique

A schematic structure of the ball milling is shown in Figure 2.20. The ball milling is another alternative method of synthesizing nanomaterials, which involves the elemental boron under an ammonia atmosphere, then followed by thermal annealing temperature at 1000-1200 °C under the inert nitrogen gas. Through the technique, high productions of nanomaterials can be synthesized at a low cost. High energy ball milling is required in the technique for the implementation, to observe chemical reactions and structural changes in the precursor used such as boron powder [218]. A schematic structure of the annealing process is shown in Figure 2.21.

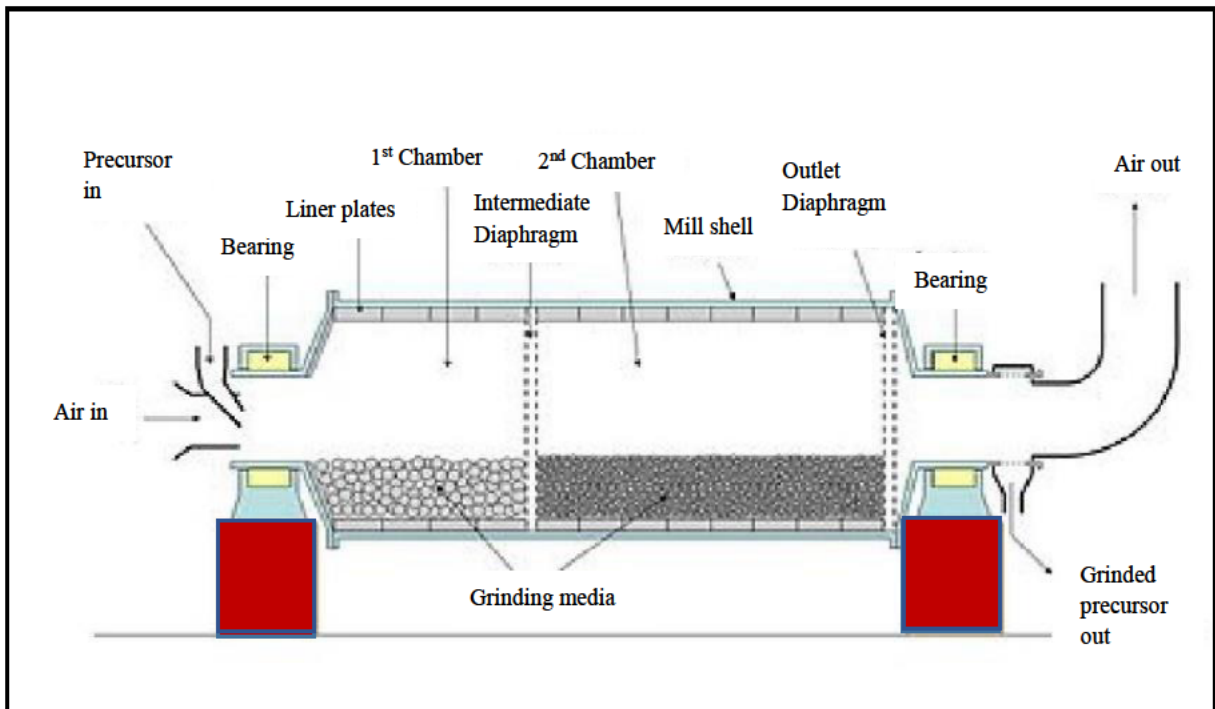


Figure 2.20: Schematic diagram of the ball milling technique [219]

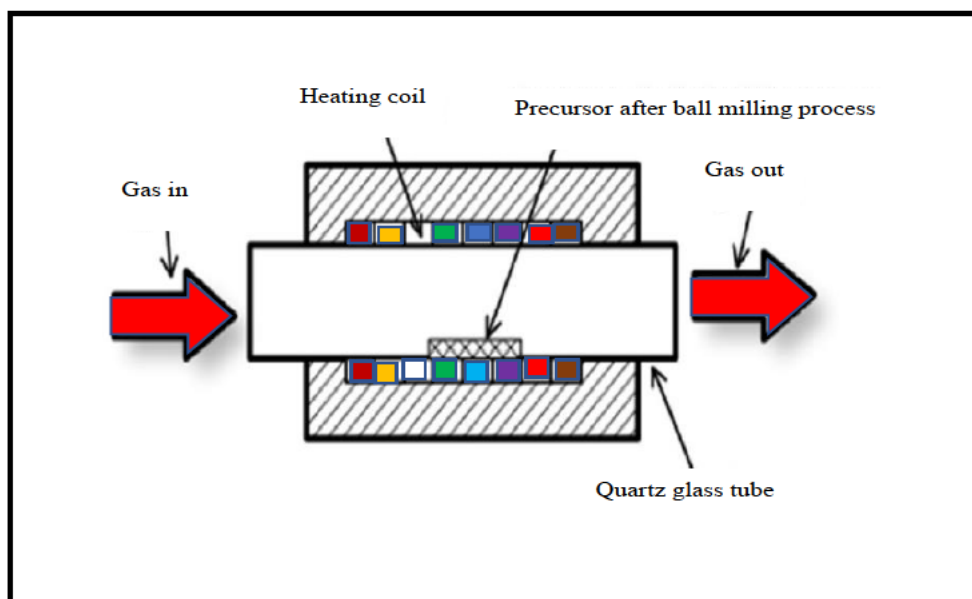


Figure 2.21: Schematic diagram of the annealing process [219].

The ball milling technique is performed for several days. When the ball milling is done, the heat treatment followed it immediately, that is annealing procedure and the nanomaterials are

synthesized from the initial precursor powder. The formation of iron contamination from the ball milling also acts as a catalyst to the synthesis of nanomaterial [220].

2.5.4 Arc Discharge (AD) Technique

The arc discharge technique was first utilized to synthesize the C_{60} fullerene in 1990 [221]. In 1991, a report was made by first observation of a multi-walled carbon nanotube (MWCNT) by Iijima of the NEC Laboratory in Japan through the arc discharge technique [123]. In 1992, bulk quantities of MWCNTs and purification were achieved by utilizing this technique [222]. A metal catalyst is needed for the synthesis of single-walled carbon nanotubes (SWCNTs) at one of the electrodes of the arc discharge system. In 1993, Bethune and co-workers [223] and Iijima [224], were the first group that succeeded in synthesizing SWCNTs, which was achieved through the arc discharge technique. Boron-based nanotubes which are among the non - CNTs were first synthesized by the arc discharge technique in 1995 [225]. Between the two graphite electrodes in the arc discharge system, a hot plasma was established in a plasma of helium gas ignited by high current, carbon atoms are evaporated and then pass through opposing carbon anode and cathode [226], where CNTs are deposited on the cathode and ready for collection. Figure 2.22 below, shown the schematic apparatus of an arc discharge technique used for the synthesis of nanotubes.

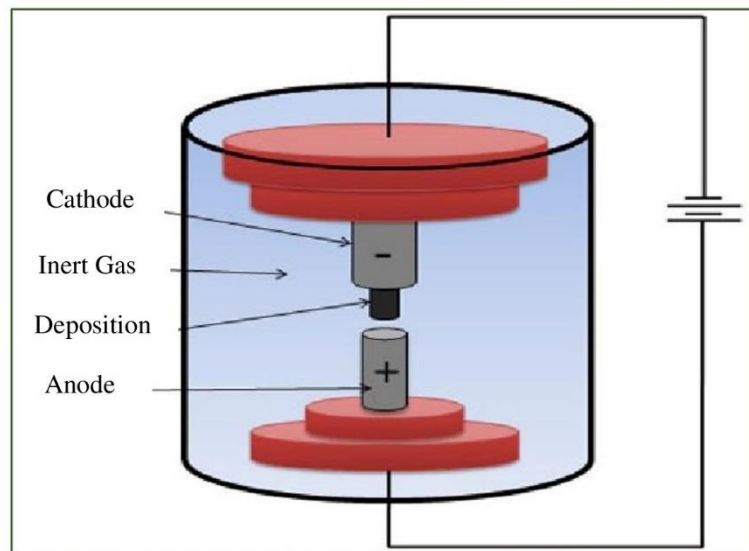


Figure 2.22: Schematic apparatus of an arc discharge technique used for the production of nanotubes[226].

High temperatures are required for fullerene growth but are not necessary for nanotube synthesis, which can be achieved at much lower temperatures by highly scalable chemical vapor deposition techniques discussed before.

2.6 Characterization techniques

2.6.1 Raman Spectroscopy

In 1928, the Indian physicist Chandrasekhara Venkata Raman discovered the effect named after him for which he won the Nobel Prize in Physics in 1930. His discovery was that when light traverses a transparent material, some of the light that is deflected changes in wavelength, as shown in Figure 2.23. This phenomenon now called Raman scattering, is the result of the Raman effect which can be explained as follows: In Raman effect, when light is scattered from a molecule or a solid, liquid or gas, most photons are elastically scattered called Rayleigh scattering, such that the scattered photons have the same energy (that is frequency) and wavelength as the incident photons.

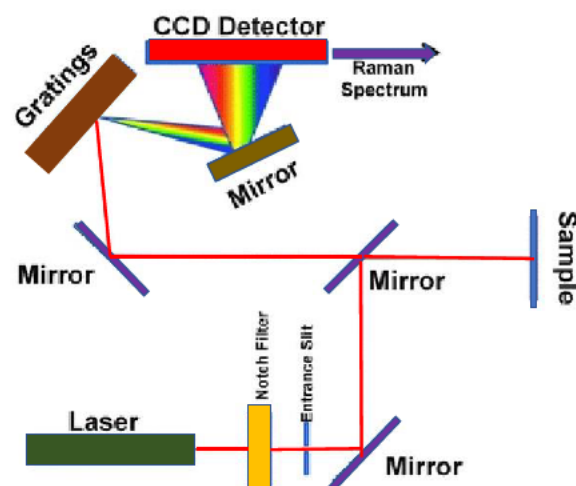


Figure 2.23: Shows the schematic apparatus of Raman Spectroscopy [227].

A small fraction of the scattered light, approximately 1 in 10 million photons are scattered by an excitation in the molecule or solid, liquid or gas due to change in electron polarizability of

the right symmetry, with the scattered photons having a frequency different from, and both lower, with higher intensity and higher than, the frequency of the incident photons [228]. In a gas, Raman scattering can occur with a change in vibrational, rotational or electronic energy of a molecule, (see energy level in Figure 2.24 below). The vibrational Raman effect in solids is primarily used for materials analysis.

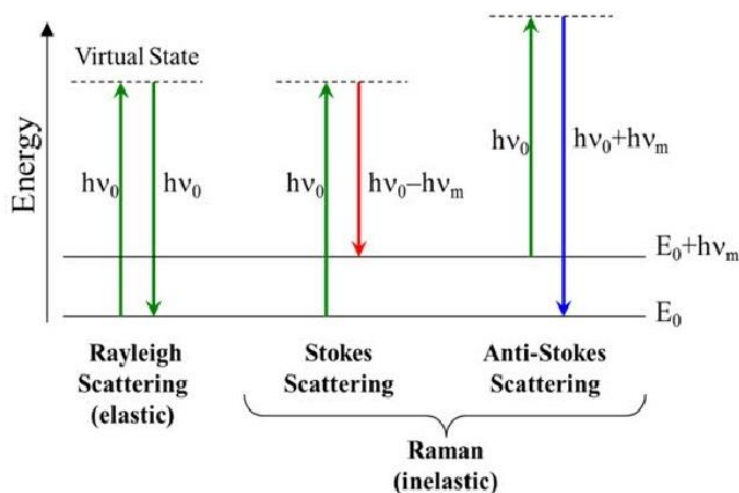


Figure 2.24 Shows the schematic illustration of the energy transitions involved in Raman Spectroscopy [227].

There are two components in Raman scattering, Stokes scattering (downshifted in frequency) and anti-Stokes scattering (upshifted in frequency) as shown in Figure 2.24. Because of its higher frequency, only Stokes spectra are typically recorded. The interaction of light with matter in a linear regime allows the absorption and emission of a photon precisely matching the difference in energy levels of the interacting electron or electrons. The Raman effect corresponds, in perturbation theory, to the absorption and subsequent emission of a photon via an intermediate electronic state, having a virtual energy level. There are several possibilities, such as, no energy exchange between the incident photons and the molecules (and hence no Raman effect), energy exchanges occurring between the incident photons and the molecules (the energy differences are equal to the differences of the vibrational and rotational energy levels of the molecule), molecule absorbs energy: Stokes scattering (the resulting photon of lower energy generates Stokes lines on the red side of the incident spectrum), and molecule loses energy: anti-Stokes scattering (incident photons are shifted to the blue side of the

spectrum, thus generating anti-Stokes lines). Raman spectra are typically expressed in wavenumbers, which have units of inverse length. To convert between spectral wavelength and wavenumbers of a shift in the Raman spectrum, the following relation can be utilized:

$$\Delta\omega = \left(\frac{1}{\lambda_0} - \frac{1}{\lambda_1} \right) \quad (2.4)$$

The Raman shift expressed in wavenumbers is given as $\Delta\omega$ the excitation wavelength is λ_0 and the wavelength of a Raman line is λ_1 . Raman spectroscopy is widely used in chemistry since vibrational information is specific to the chemical bonds and symmetry of molecules. It provides a fingerprint by which the molecule can be identified. A typical Raman spectrum of SWNTs has three important features: low-frequency lines assigned to radial breathing modes (RBM) of the nanotubes, intermediate frequency disorder-induced mode due to defects and/or amorphous carbon on the nanotube sidewalls (D-peak), and a higher energy tangential mode (G-peak). One should note that in the G-peak region there is shoulder also labeled as the G* - peak due to the breakdown of the degeneracy of the G mode in graphite due to rolling up of the graphene sheet. A more sensitive approach Surface Enhanced Raman Spectroscopy (SERS) is used as a surface-sensitive technique that enhances Raman scattering by molecules adsorbed on a nanostructured metal (typically gold or silver) surfaces. Under special conditions, the enhancement factor can be as much as 10^{10} to 10^{11} [229], which means that the technique may be able to detect single molecules [230]. Measurement analysis was carried out on a Jobin Yvon labramHR800.

2.6.2 High-Resolution Transmission Electron Microscope (HRTEM)

Image formation in transmission electron microscopy is essential via a diffraction phenomenon. A modern transmission electron microscope can be schematized as a three lens system: an objective lens, an intermediate lens and a projector lens as shown in Figure 2.25.

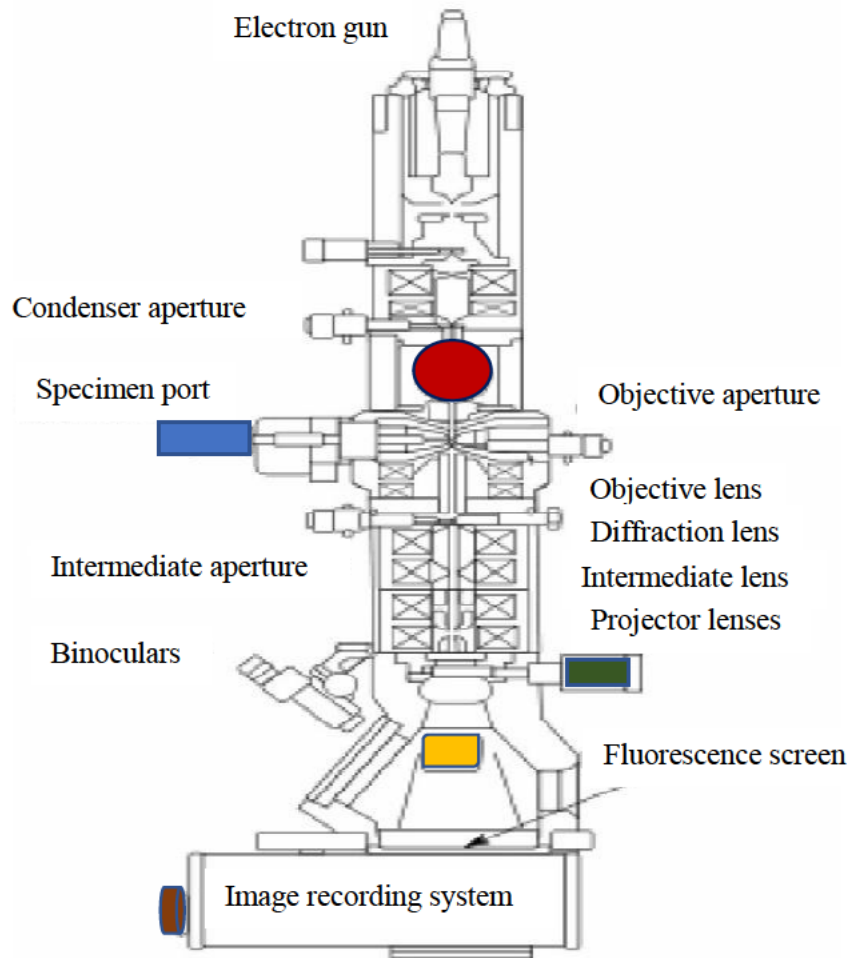


Figure 2.25: Schematic apparatus revealing the basic principle and components of the HRTEM. [Source: Hebrew University of Jerusalem, cited April 10, 2018: Available from <https://www.researchgate.net/publication/263849645>]

The electron beam produced by an electron source is collimated by the condenser lens system and scattered by the specimen. An image is formed in the image plane of the objective lens. The selector aperture allows the selection of one area of the image which is then magnified by the intermediate lens [231]. The intermediate lens is focused on the image plane of the objective lens and an intermediate image is formed in the image plane of the intermediate lens. This image is the object for the projector lens which forms a final image on a fluorescent screen or on the entrance plane of a recording device [232]. Measurement analysis was carried out on a JOEL 2100 HRTEM.

2.6.2.1 Selected Area Electron Diffraction (SAED)

An important principle in the operation of a TEM is the dual wave-particle nature of the electron from the equation 2.5 below.

$$d = \frac{\lambda}{2n \sin\alpha} \approx \frac{\lambda}{2NA} \quad (2.5)$$

Where ‘ λ ’ is the wavelength, ‘NA’ is the numerical aperture of the instrument, and, ‘ d ’ is the maximum resolution. The wavelength of the electrons is much smaller than the crystal spacings in a solid. Figure 2.26, shows a schematic drawing of the selected area electron diffraction.

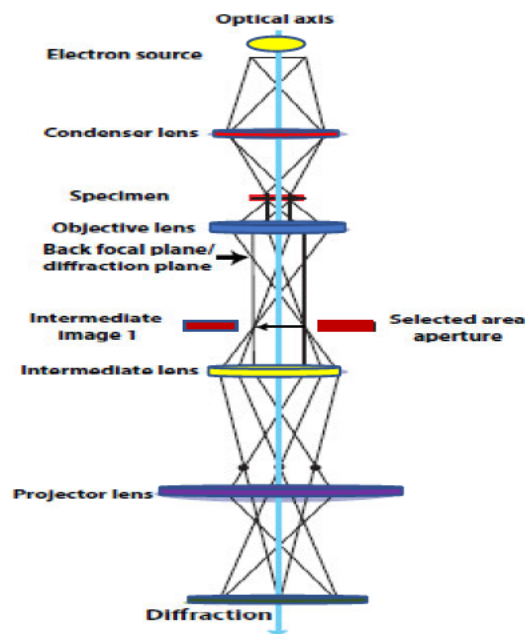


Figure 2.26: Shows the schematic of an HRTEM operating in the diffraction mode[233]

This means that the incident beam will produce electron diffraction patterns strongly dependent on crystal structure and orientation in a sample. A region of a specimen can be selected for examination using an aperture as shown in Figure 2.26 to obtain selected area electron diffraction (SAED). This is important for polycrystalline specimens where more than one crystallite can contribute to the diffraction pattern. SAED of nanoparticles or nanocrystals gives ring patterns analogous to those from X-rays and can be used to discriminate nanocrystalline

from amorphous phases present in the sample. Largely amorphous samples will give rise to broad or diffuse ring patterns. SAED has numerous advantages in comparison to comparable diffraction techniques. Unlike X-ray diffraction, which typically lacks the ability to focus on precise areas of a sample, an electron diffraction pattern can be taken from an area as small as 4 nm^2 . This allows for spatially located crystallographic information. An example of the utilization of this ability would be if one had a composite material that was a mixture of several different morphologies and structures, such as nanowires mixed with nanoparticles of a different structure. In a TEM, one can determine the structure for each morphology separately and image the area under examination [233]. This would not be possible in an X-ray diffraction experiment. The interaction with matter is also much stronger with focused electron beams, which means electron diffraction can be used to generate useful information much more quickly if the sample remains stable in a high energy electron beam. The imaging and the diffraction modes in a TEM are shown in Figure 2.25 and 2.26 respectively. In SAED, a parallel beam of electrons is used to create a diffraction pattern, but in convergent beam electron diffraction (CBED), a convergent cone of electrons is used. The advantage of the CBED is that multiple angles of incidence are used simultaneously, providing 3-D analysis of the crystal. CBED can be far more difficult to interpret than SAED and is only used for appropriate situations.

2.6.3 Scanning Electron Microscopy (SEM)

A Scanning Electron Microscope (SEM) works by using electromagnetic lenses to focus an electron beam into a probe [234]. This probe is then scanned in a raster pattern across the sample. As the electrons travel through the sample they collide inelastically and generate secondary electrons. The secondary electrons can then escape the surface of the material and be collected by the detector using a bias voltage to attract them. The intensity of emission is measured at every point by collecting the emitted secondary electrons. The intensity recorded at each point is used to form an image by representing each collection point as a pixel. Figure 2.27, shows a schematic drawing of the electron and X-ray optics on a combined SEM-EPMA.

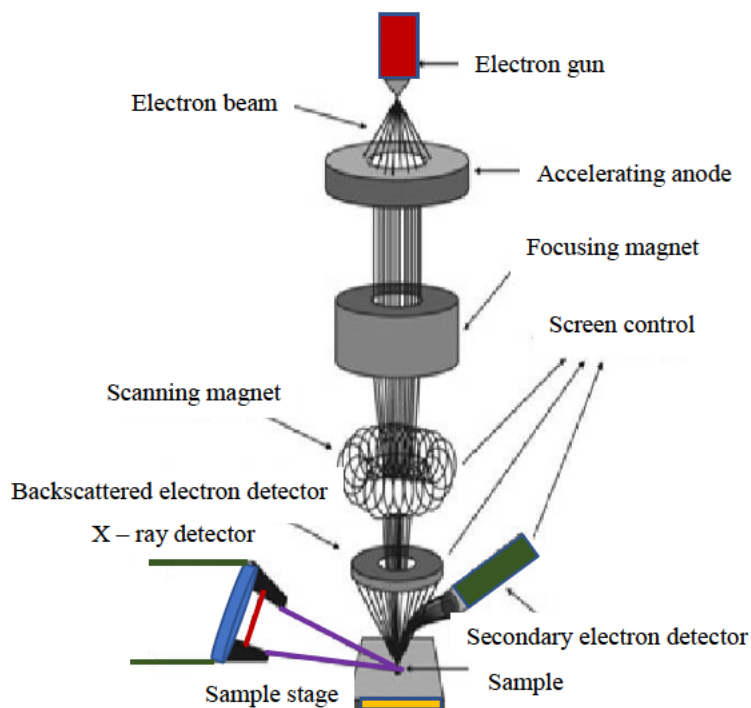


Figure 2.27: Schematic diagram of the basic components of a scanning electron microscope[235]

Because more electrons can escape from the edges of samples, i.e. there is a shorter distance to travel before they escape into the vacuum, there is a difference in contrast and this can be used to form an image of surface topography. Due to the vast number of incoming electrons, it is possible for a charge to build up if the sample is not sufficiently conducting. The build-up of charge on a sample is undesirable as it makes it hard to image the sample at high resolution and the contrast continuously changes. The SEM is useful for looking at bulk material, it is quite surface sensitive but does permeate into the sample to some extent [234]. The depth of penetration can be changed by varying the acceleration voltage. Different accelerating voltages can be used for different purposes. The morphology and composition of boron nanomaterials synthesized placed on carbon paper coated with gold, were characterized by ZEISS Ultra Plus field-emission scanning electron microscopy (FESEM) operated at 10 keV and EDX was taken at a voltage of 20 keV.

2.6.3.1 Energy Dispersive X-ray Spectroscopy (EDS/EDX)

Energy Dispersive X-ray (EDX) analysis is a technique that uses the characteristic emission of X-rays from atoms as the electrons drop into lower orbitals. As high energy electrons pass through the sample, they collide with the electrons orbiting atoms in the sample [236]. If an electron manages to displace an inner shell electron from an atom an electron from a higher electron orbit will drop into the vacant position emitting an X-ray. These X-rays are constantly emitted and can be detected for use in chemical analysis. Each energy gap is different and therefore will produce an X-ray with a unique energy. The energy is measured by the detector and compared to known values of element-specific X-rays. In this way elements present in a specimen can be identified. The abundance of the element can be found by tallying the counts at these specific energies. If EDX is used in conjunction with a scanning probe then the elements at a specific location can be identified or regions of the same element mapped [220]. The accuracy of EDX is limited by the skin depth of the electrons as X-rays can be produced anywhere within the sample that the electrons can penetrate to. The detector can only capture a small number of X-rays due to the uniform angular distribution of emission and the fact that X-rays cannot be focused by lenses. As a rule of operation, the accelerating voltage of the electron gun should be at least twice the value of the characteristic X-ray you wish to observe. This is to make sure that the excitation of the electron can take place

2.6.4 X-Ray Diffraction (XRD)

The diffraction parameters of an X-ray beam diffracted from a crystalline phase is shown in Figure 2.28. The X-ray diffraction is one of the most popular non-destructive analytical techniques, which allows determining the phase composition and crystal structure of the material. X-rays are electromagnetic waves with wavelengths from 0.01 nm to 10 nm. There are two most common ways to produce X-rays: X-ray tubes and synchrotrons. In an X-ray tube, X-rays are generated by bombarding a target of a suitable material with a focused electron beam. In synchrotrons, high-energy electrons are deflected by electromagnetic fields, yielding X-ray emission. X-ray diffraction technique is based on the scattering of X-rays by electrons, which is also known as Thomson scattering. It occurs since the electron oscillates in the electric field of the incoming X-ray beam and an oscillating electric charge radiates electromagnetic waves. X-rays are radiated from the electron at the same frequency as the primary beam.

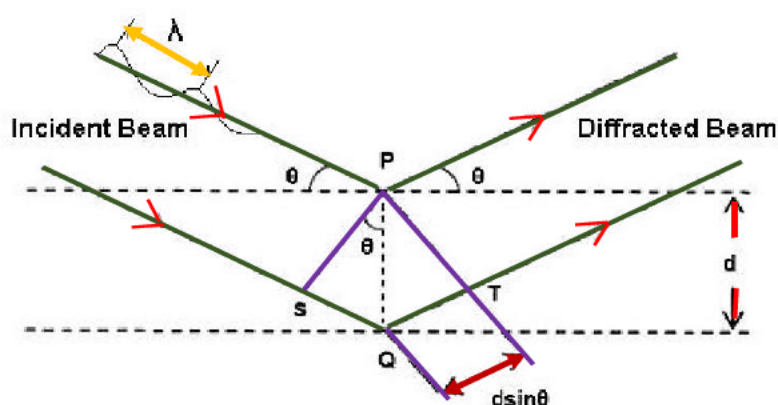


Figure 2.28: Diffraction of the X-ray beam from a crystalline material[237].

As a consequence of the regular arrangement of the atoms in solid matter, a coherent scattering of the X-rays at the atoms results in a constructive interference from the reflections of the atomic planes at certain well-defined angles [238]. The positions of the reflections are calculated using optical path difference $2s$ with $s = d\sin\theta$. Maxima is produced for integral multiples of λ . It results in Bragg's law, which gives the geometrical conditions under which a diffracted beam can be observed:

$$2d\sin\theta = n\lambda \quad (2.6)$$

where,

θ : an angle between the incident and reflected x - rays.

d : interplanar distance between the crystal planes

λ : the wavelength of the X-rays; commonly $\text{CuK}\alpha$

and 'n' accounts for the order of diffraction.

Every d has corresponding indices in the reciprocal space h, k, l . A measuring array of intensities with the corresponding hkl makes possible to determine the structure parameters, the unit cell and solve the structure [237]. In the present work, X-ray diffraction techniques were used for the phase identification and the structure solution. Boron is a light element, which makes it be a weak X-rays scattered. Therefore, acquiring data of acceptable quality requires a long exposure time of the order of 12 hours. Another solution could be to increase beam

intensity, which is possible using synchrotron radiation. The synchrotron radiation is produced by the acceleration of electrons in a very large circle by an external electromagnetic field. The energy of accelerated electrons could reach 8 GeV. Electrons emit very intense electromagnetic radiation with a continuous spectrum from the far infrared to the γ -ray region, called synchrotron radiation. Synchrotron radiation has extremely low beam divergence, strong polarization, and it is emitted in very short pulses, typically less than a nano-second. Using such radiation, it is possible to study very small samples in a very short time [237]. Selection of single crystals and preliminary structural analysis was carried out on a high-brilliance diffractometer Bruker D8 advance equipped with Cu x-ray tube ($\lambda = 1.54056\text{\AA}$) and VANTEC detector.

2.6.5 Ultraviolet-Visible (UV – VIS) spectroscopy

The schematic diagram of a simple dual beam UV-VIS spectroscopy is shown in Figure 2.29. The UV-VIS is one of the basic techniques to characterize the properties of nanomaterials through the interaction with light. This is to measure how much light is reflected, transmitted or absorbed by these nanomaterials. The incident photons create atomic or charge movements in the nanomaterials when the nanomaterials absorbed light. When the absorption as a function of energy is measured, an insight into its electronic and atomic structures of nanomaterials is observed.

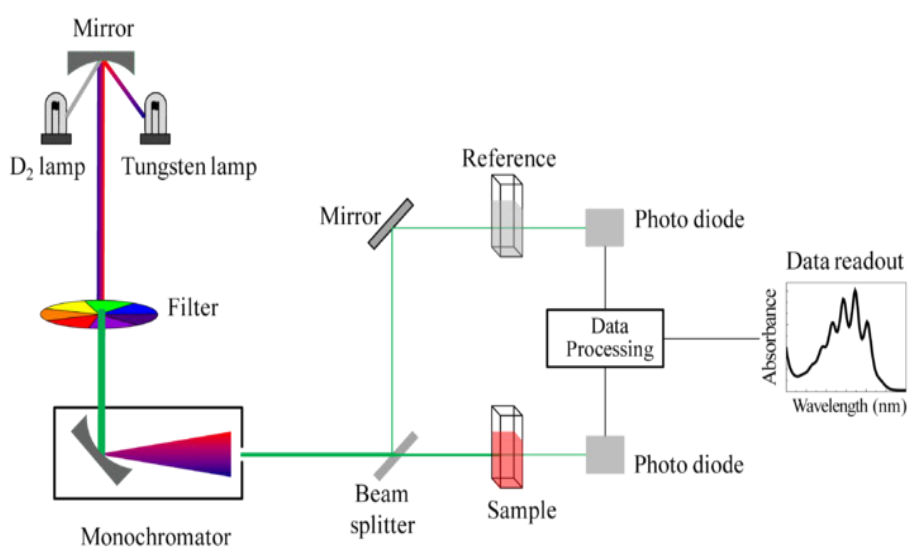


Figure 2.29: The schematic diagram of ultraviolet-visible spectroscopy[239].

The phonons and electron transitions of the materials were affected through the morphology, stress, temperature, and contact with other materials. All these modified the materials light absorption in many ways. This is important because it enables us to know more about the nanomaterials properties through the measurement of its absorption spectrum. All the variables concerned need to be monitored during the experiments. The instrument is used to measure the intensity of transmitted and reflected light. The spectral range covered from the near ultraviolet (λ -200 nm) to the near infra-red (λ -3 μ m). Measurement analysis was carried out on a Perkin Elmer precisely, Lambda 35, UV-VIS spectrometer.

2.6.6 Photoluminescence (PL)

The schematic diagram of a photoluminescence measurement system is shown in Figure 2.30. The report of the application of the photoluminescence (PL) technique to the study of single-walled carbon nanotubes (SWCNTs) dates to 2002. In the intervening half-decade, there has been tremendous progress in this area. This has included many fundamental studies of SWCNT photoluminescence as a basic characterization tool [240]. The term, photoluminescence describes any process in which light is absorbed by a medium to generate an excited state, and then re-emission of light of lower frequency upon recombination to a ground state.

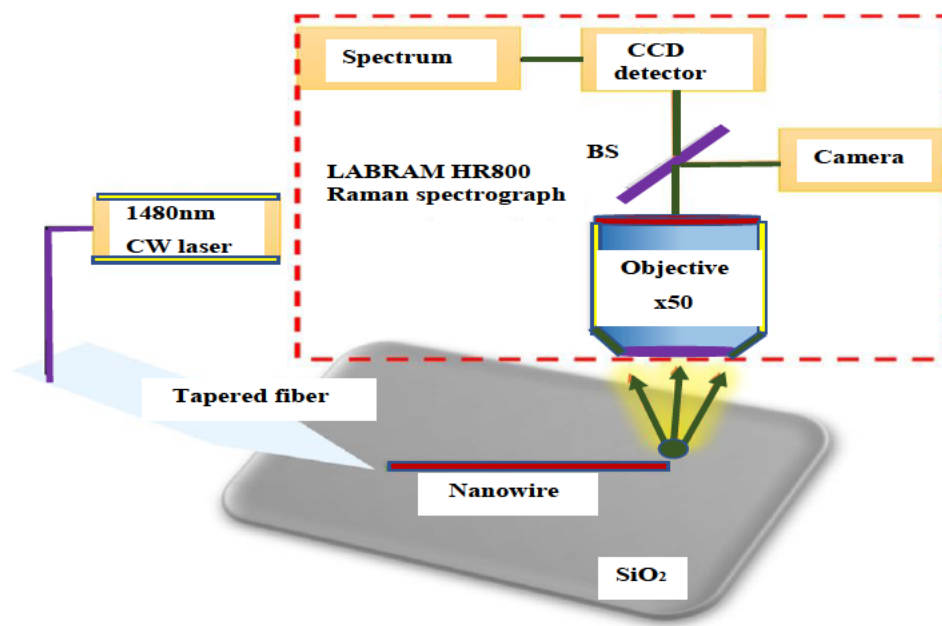


Figure 2.30: Shows the schematic diagram of the PL measurement system [241].

The currently accepted of PL in SWCNT, electron-hole pairs are created in the form of excitons, which are subsequently annihilated with the emission of photons. SWCNTs have a huge potential of being applied in technologically advanced applications. A major obstacle to such efforts has been the diversity of tube diameters, chiral angles, lengths and aggregation in nanotube samples obtained. PL has become an important tool in measuring a fraction of the total population where this fraction represents all semiconducting tubes. The seminal paper by Bachilo *et al* [242], laid the groundwork for use of PL to determine chiral indices (n, m) of semiconducting nanotubes and became the basis for the software program called Nanosizer [243]. Measurement analysis was carried out on a Perkin Elmer precisely, LS 55, Fluorescence spectrometer.

Chapter 3

3. The Laser synthesis of single-walled boron nanotube

3.1 Preparation of laser ablated target

In preparation for single-walled boron nanotubes (SWBNTs) synthesis, two different targets were made each from hexagonal boron nitride (h-BN) and boron powder (Sigma Aldrich 99.99% purity), and a small percentage of metallic catalysts such as nickel (II) nitrate hexahydrate crystal $[\text{Ni}(\text{NO}_3)_2 \cdot 6\text{H}_2\text{O}]$ and cobalt (II) nitrate hexahydrate crystal $[\text{Co}(\text{NO}_3)_2 \cdot 6\text{H}_2\text{O}]$. The productivity of the synthesis is dependent on the type of metal catalysts selected [244, 245], the amounts of catalysts, the catalyst size, and the correctly chosen catalysts [246, 247]. The percentage of total catalyst contribution should not be more than 10% from literature and is generally kept below 5% [248]. The use of an excessive catalyst create difficulties in the purification process and the catalysts used must be removed for better applications in advanced nanoelectronics [248]. The use of bimetallic catalysts produced good qualities and higher yields of BNTs. Two different metal nitrate catalysts were used, which were transition metals. For a successful durable target to hold together during ablation in the furnace at high temperature, a binder product called boron oxide (B_2O_3) must be utilized. This boron oxide material was utilized as the bonding agent. Table 3.1 shows a proportion to make a target to give a final ratio of 97.5% BN:1% Ni:1% Co: 0.5% B_2O_3 and 97.5% B: 1% Ni: 1% Co: 0.5% B_2O_3 in the study. The preparations of the targets were made in this way. Once the correct mixture was prepared, the target was hot pressed in a piston and sleeve apparatus made by stainless steel, to avoid contamination with the target prepared when putting in the vacuum oven. To prevent air entering, a piston and sleeve were bolted tightly and cured at 150 °C (423K) in a vacuum oven for 24 hours. The oven was switched off and allowed to cool down at room temperature. The sleeve was removed, and the hard target hexagonal boron nitride/boron metal catalysts were carefully forced out of the piston with the help of a jack. The target was fixed to a 6.4 mm diameter a stainless-steel tube and positioned at the center of a larger quartz tube (*see Figure 3.2*) with the help of a small stainless-steel holder. The target was baked at 1000 °C for 4 hours to allow out-gassing of all unwanted chemicals, so that a final target composition can be achieved such as, 97.5%BN:1% Ni:1% Co: 0.5% B_2O_3 and 97.5% B: 1% Ni: 1% Co: 0.5% B_2O_3 . In Table 3.1, the details of the target compositions used in the research were provided.

Table 3.1: Revealed the chemical composition hexagonal boron nitride/boron powder metal catalyst targets used in the research

S/N	Target symbol	Boron nitride content at %	Catalysts content at %	Binder (B ₂ O ₃) content at %
1	BN	97.5%	1% Ni, 1% Co	0.5%
	Target symbol	Boron powder Content at %	Catalysts content at %	Binder (B ₂ O ₃) Content at %
2	B	97.5%	1%Ni, 1% Co	0.5%

3.2 Experimental design for a laser synthesis of SWBNTs.

3.2.1 Equipment for the synthesis of BNTs

In the first place, the arrangement of the apparatus to synthesize BNTs was guided by the early reports of some authors, like Ciuparu *et al.* [120], Patel *et al.*[249, 250], Yang *et al.*[198] and Liu *et al.* [126, 251]. During the period 2004 to 2018, various experimental setups and types of equipment were utilized to synthesize BNTs. The significant parts of the equipment used in the research are enumerated below:

3.2.1.1 A pulsed Q-switched Nd: YAG laser

A pulsed Q-switched Nd: YAG laser operated at a pulse repetition frequency of 10 Hz was utilized. The wavelength was 1064 nm and the laser frequency was also doubled to produce 532 nm pulses separated temporarily by about 20 ns from the fundamental operating wavelength. The full specification details about the laser utilized are shown in Table 3.2 below.

Table 3.2: Shows the specification of laser and properties of the beam at which the laser exists the aperture

AQ – switched Nd: YAG Laser	1064 nm	532 nm
Pulse energy (mJ)	250	450
Average power at 10 Hz (W)	7.5	12.5
Pulse width (ns)	10	8
Energy density (J/cm ²)	7.24	6.58

3.2.1.2 A Carbolite Furnace with three different temperature zones

The laser ablation took place inside a sealed quartz tube located in a tube furnace (*see Figure 3.2*). The furnace was 1.2 m long, of the hinged type and produced by Carbolite. This can accommodate a quartz tube of 50 mm outer diameter (OD) and 45 mm inner diameter (ID). It contained three proportion integral derivatives (PID) which controlled the temperature zones divided equally over the length of the furnace. Each zone could be operated independently. It was designed in such a way that, it ensured a uniform temperature for a total length of 1.1 m with a small drop in temperature at both the ends of the tube. The furnace temperature was stable between 600 °C and 1100 °C during the operating system. For all the experiments, the furnace was operated between 1000 °C and 1100 °C, in increments of 100 °C.

3.2.1.3 Pressure control, Mass Flow control, and vacuum systems

Agilent DS 202, which is a standard rotary pump was utilized to evacuate the system to a base pressure of 10^{-2} mbar. Each experiment performed was filled with high purity nitrogen or argon of 5.0 gas. While the vacuum pump was in operation, nitrogen or argon gas flow and pressure were set and kept constant to specified values. It was done by utilizing the MKS 247 D controller with an MKS 640 pressure transducer and a Mass Flow controller device.

3.2.1.4 Optical and mechanical components with motion assistant software

A set of specially coated optical mirrors were utilized to steer the laser beams from the laser towards the position of the target in the furnace. The set of laser mirrors were 50.6 mm in diameter and manufactured by Newport by making use of BK7 glass. These mirrors had optical coatings that were only reflective at an angle of 45° for 532 nm or 1064 nm, also they could reflect both wavelengths equally. A set of specially made mirrors with dielectric coatings were utilized to combine 532 and 1064 nm beams from different optical paths. In other to avoid optical destruction, all the mirrors were coated to withstand a high laser damage threshold ($> 10J:cm^{-2}$).

3.2.2 Description of the experimental setup and experimental conditions for boron nanotubes

A schematic diagram of the experimental set up used to synthesize BNTs is shown in Figure 3.1. The laser and furnace were installed on purpose-built tables to accommodate an optical breadboard. The optical tables are sandwiched by 5 mm stainless steel plates with honeycomb internal structure which keeps the vibrations to a minimum which is an important feature in the laser-optical experiment. The breadboards were designed with holes threaded for M6 bolts and which were separated 25 mm apart from each other. This made it easier to bolt down optomechanical components to ensure that the laser optical beam path was always kept aligned. The furnace and laser were situated parallel and adjacent to each other to keep the optical beam path of the laser beams entering the furnace as soon as possible without any deflection of the laser beams. The set of laser mirrors with anti-reflective (AR) coatings for 532 nm and 1064 nm laser pulses was used to steer the laser beams towards the center of the furnace. All these mirrors were made for 45° reflections and were carefully located with respect to the incident laser pulses in all occasions. In case of laser safety precautions which are customary when a Class 4 pulsed infrared Nd: YAG laser is utilized, an alignment laser was used to correctly position the laser mirrors. In the first step, the alignment laser itself was positioned parallel to the main laser. In the second step, the alignment laser was "coupled" to the main laser in a such a way that it was made collinear with the pulsed lasers beams of the main Nd: YAG laser. This is to ensure that the path taken by the alignment laser was the same as that of the pulsed lasers. This alignment procedure could only be done with pulsed Nd: YAG laser operating in a very low energy mode. For safety, this was significant since the Infra-Red laser beam is imperceptible to the naked eye and its positional status needs to be known at every point in time. All optics and positioning of the target in the furnace were accomplished using the alignment laser. An internal second harmonic generator converted the fundamental wavelength from 1064 nm to 532 nm via a non-linear optical process and not all the 1064 nm pulse energy was converted. The depleted fundamental beam was important in energy and useful, it was transmitted out of the laser through the 1064 nm exit aperture shown by the purple line in Figure 3.1. The new 532 nm laser pulses, indicated by the green line, took a slightly longer optical path but eventually became collinear with the 1064 nm beam with the use of dielectric mirrors, which are labeled DM in Figure 3.1. Combined beams of 1064 and 532 nm were steered towards a motorized mirror that was highly reflective for both beams. The mirrors focused the beam into the vacuum sealed quartz tube and the quartz tube was maintained

horizontally in the furnace 1.2 m in length. The longitudinal axis of the 50 mm outer diameter (OD) quartz tube was collinear with the incoming laser pulses. The laser pulses passed through the quartz tube through a window specially made with an optomechanical mount machined aluminum at Brewster's angle of 54° to the vertical axis. The quartz window fitted was 50 mm in diameter, and 3 mm thick. This window required dual anti-reflecting (AR) coatings for both 532 nm and 1064 nm. The main purpose of having the entrance at Brewster's angle was to minimize reflections at the window interface [252]. At both ends of the quartz tube, automated vacuum fittings were utilized. These provided a very good vacuum seal at both the ends of the quartz tube. Inside the larger quartz tube, the second smaller quartz tube was mounted coaxially. This smaller quartz tube served the purpose of being a gas flow tube and which allowed more laminar gas flow. If no smaller quartz tube had been used, this may not have been possible.

Table 3.3: *Experimental conditions under which both the hexagonal boron nitride (h-BN) and boron composite targets were ablated during the synthesis by laser ablation technique*

Target label	Pressure (Torr)	Flow rate (sccm)	Temperature (°C)	Type of products
BN	400	200	1100	Nanotubes
BN	1000	500	1100	Bamboo nanotubes
BN	400	400	1000	Nanowires
BN	400	200	1000	Nanorods
B	400	200	1100	Nanotubes

The smaller quartz tube had an inner diameter (ID) of 24 mm and it was supported by graphite rings. The target was placed towards the center of the furnace by a stainless steel 6.5 mm tube and made to face the incoming laser pulses. This stainless-steel tube extended from the back of the larger quartz tube. It was supported by a graphite rod through which a hole was drilled for the target holder tube to pass through. The distance between the end of the smaller quartz tube and the target surface was 25 mm. The diameter of each target made was 25 mm and length 40 mm. It was slightly greater than the inner diameter of the smaller quartz tube. The nitrogen or argon gas acted as a buffer that slows down the plasma plume which gives room for conditions under which BNTs is synthesized. The second purpose of this gas was to transfer the BNTs to the rear of the larger quartz tube where they would have deposited in the cooler region for collection.

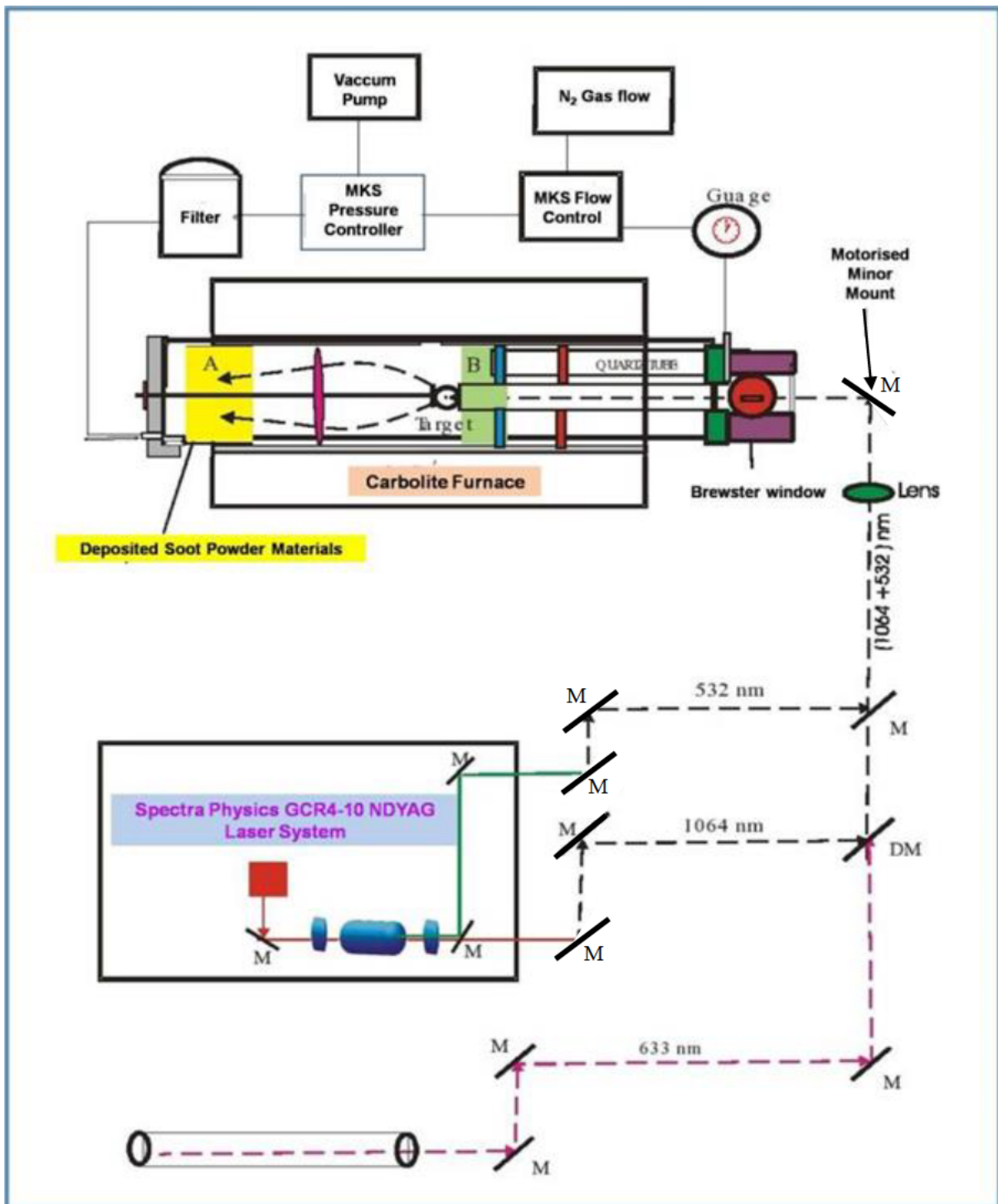


Figure 3.1: Experimental set up for the synthesis of boron nanotubes by the double pulsed laser furnace method [253]

For the easiest in-flow and outflow of nitrogen or argon gas, a gas connection was fitted to the front-end and back-end of the larger quartz tube respectively. Nitrogen or argon gas flow rate and pressure was controlled by an MKS Type 247D system consisting of a Mass-Flow GE50A type and pressure controller MKS Type 640B transducer, respectively. The laser was used to raster the target surface for about 60 minutes to synthesize as-prepared material consisting of significantly huge amounts of BNTs, by means of motion controlled steering mirrors. Before the entrance of the quartz tube, these mirrors were placed. The system needs to be cooled down, after each experiment. The as-synthesized BNTs product was scrapped off the inside back-end of the larger and front-end of the smaller quartz tube into the petri dish, with the help of a spatula and prepared for the characterizations as shown in Figure 3.8.

3.3 Conditions under which hexagonal boron nitride and boron composite targets were ablated by DPLA.

3.3.1 Carbolite furnace, nitrogen and argon gas flow conditions

The furnace temperature plays a significant role in the synthesis of the single-walled boron nanotubes, since the nucleation procedure is driven by the energetics of precursors [254]. The flow rate and pressure of nitrogen or argon gas used have some roles to play in the plasma plume dynamic. It also has an influence on the formation of different types of nanotubes families that formed [244]. Table 3.3 revealed the conditions under which the targets were ablated during the period of the experiment.

3.3.2 Operational system in the experiment.

The mounted target was positioned at the center of the furnace inside the bigger quartz tube with the help rod a stainless-steel of 1/4 inch in diameter and one meter long as shown in the photograph in Figure 3.2. The support stainless-steel rod could slide back and forth, to enable the target to be positioned 25 mm from the end of the inner quartz flow tube. The He-Ne laser was utilized to make sure that the target was centered. At the front-end of the outer quartz tube, the inner quartz tube was carefully put through, and it is supported by graphite rings, follow by the Brewster window (BW), which was carefully fitted and clamped with automated vacuum fittings (AVFs). The inlet nitrogen or argon gas was connected to the Brewster window with the aid of a black rubber flexible tube, as shown in Figure 3.3.

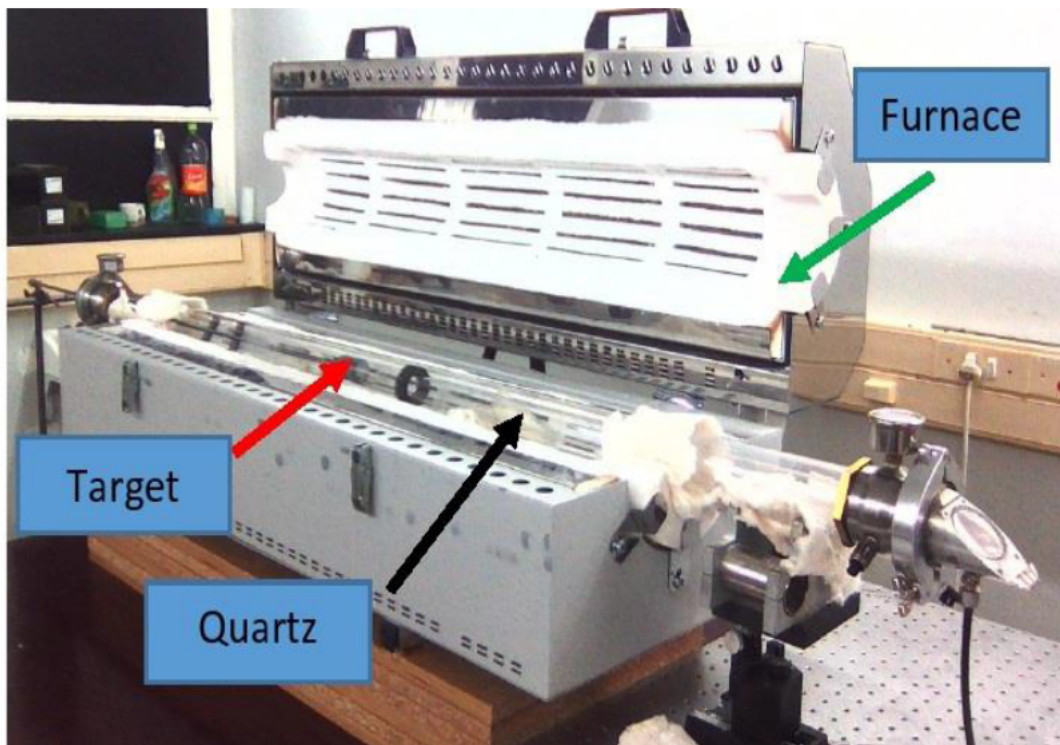


Figure 3.2: A photograph of experimental set up for the synthesis of boron nanomaterials (BNMs) by the double pulsed laser ablation technique inside the carbolite furnace.

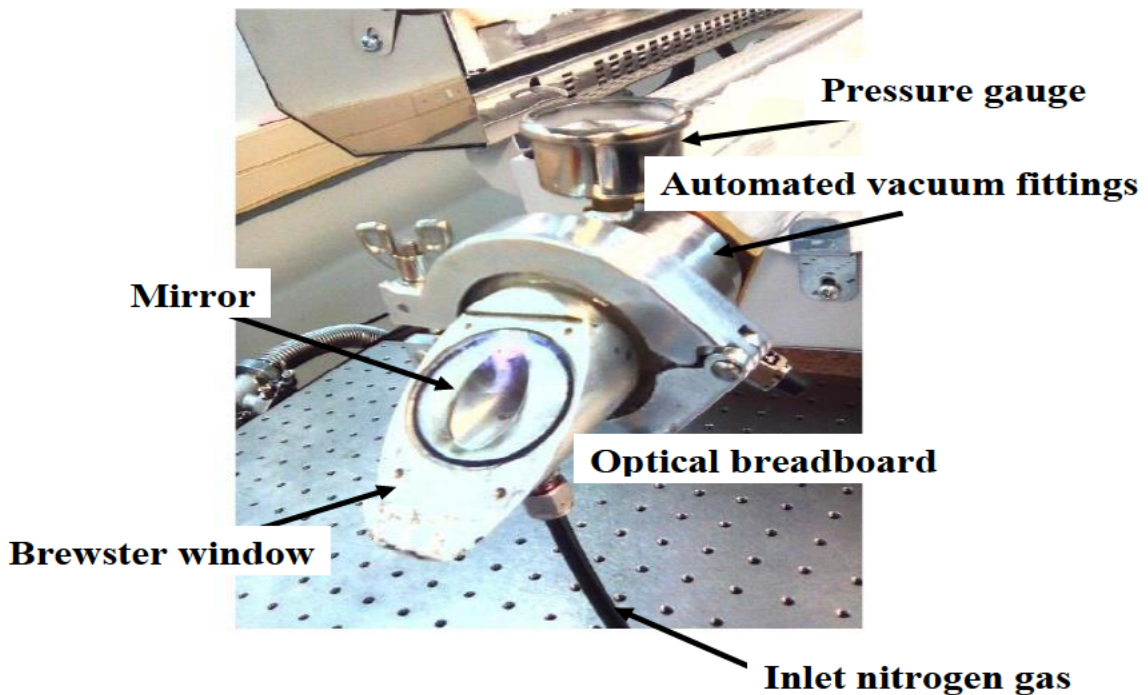


Figure 3.3: Photograph showing the front-end of quartz, the Brewster window from the side and the inlet gas connection.

The target was correctly positioned inside the inner quartz tube. The nut used for securing the support rod at the back of the vacuum flanges, shown in Figure 3.4. was tightened and connected to the vacuum system to pump down the entire quartz tube to a base pressure of 10^{-2} mbar using the Agilent DS202 rotary vein pump. After the system had been pumped down, using the Agilent DS202 rotary vein pump, furnace was closed and switched on to the high temperature. Whenever a new target was synthesized, it must be completely outgassed of all impurities, such as O_2 , NO_2 , CH_4 , H_2 , and other gaseous compounds.

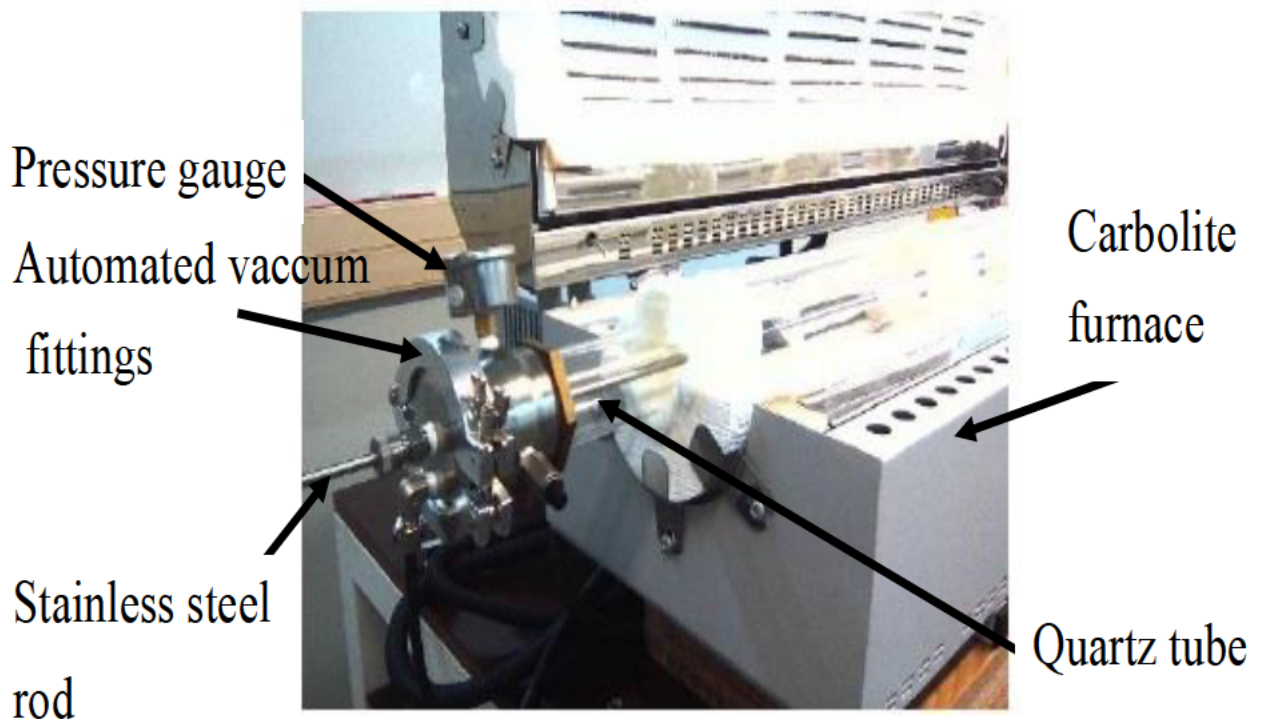


Figure 3.4: Photograph showing the back-end of the quartz tube, the clamping of the target, support rod and connection with the vacuum system.

The product boron oxide (B_2O_3) was used as a binder and alcohol was used to dissolve catalysts. To do this, the outgassing proceeded with the vacuum pump on but performed in a flow of nitrogen or argon gas, to evacuate outgassed products quickly. The temperature was slowly increased in steps of $100\text{ }^\circ\text{C}$ up to operating temperature. This was held for about 60 minutes for each setting. This enabled the outgassing to proceed in a perfect controlled situation in the experiment. This must be strictly followed, if not, the target would have been shattered, due to the excessive and sudden outgassing. In all cases, a new target would require an approximately of 5hours of outgassing before it could be synthesized. After this stage, the flow

rate of gas and pressure (with MFC and MKS 247D respectively) was set through the help of software in the desktop computer for operating conditions mentioned in Table 3.3. This was done to get the lamps and Nd: YAG laser rods warmed up to operating temperature level. After sixty minutes of warming up the system achieves better results. A further thirty minutes, the laser was operated in free running mode. The system was ready to start ablating the target which was already being placed inside the quartz tube. The pressure and flow rate settings were double-checked frequently to be sure of the initial settings prior to the experiment being started. The alignment of the laser entering the furnace through the Brewster window was double-checked by operating the laser at a lower energy level as shown from the laboratory in Figure 3.5. Motion assistant written in Labview as a small software was used to control the motion of the beam passing through the steering windows which allowed the target to be scanned and raster evenly distributed throughout the period of experiments. When the motion of the mirrors was happening, this laser was immediately switched on to full power level. For safety precautions, it was necessary to make sure that the entire system operation was constantly checked at every point in time. Most especially, the laser runs should be of thirty minutes' duration.

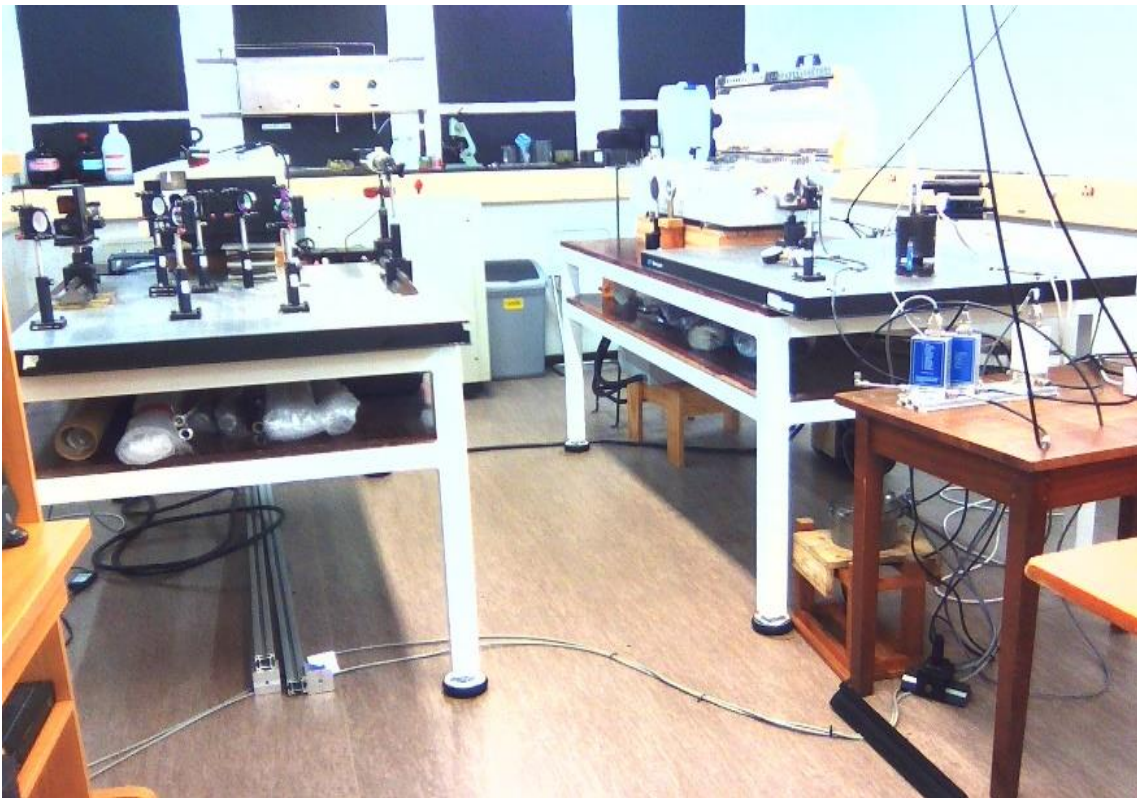


Figure 3.5: Shows the photograph of the laser ablation experimental laboratory

The following important factors were constantly monitored during the time of experiment:

1) PRESSURE: An increased pressure in the system may lead to a leak, a damaged laser entrance window or a clogged vacuum system. When the pressure drops this may be caused by a depleted gas supply. All these need to be put into consideration for the system to run smoothly.

2) TEMPERATURE: The effect of furnace temperature has so many roles to play in the system operation. If the temperature is insufficient or more than required, it may prevent the nucleation of nanotubes.

3) NOISE: The unusual noise that increased in pitch was normally associated with increasing damage on the laser entrance window. This must be normalized before and during the time of the experiments.

It was good to have the entire gas line from the quartz tube to the vacuum pump, including the MKS mass flow and pressure transducers. We need to provide continuous monitoring and frequent cleaning to obtain accurate readings from the instruments used. From the observation, good quality nanotubes could escape from the quartz tube and block the system. A cold trap with a cellulose filter was fixed into the cold trap connected to the vacuum pump line, at the back-end of the quartz tube to rectify this problem. This will surely solve the problem completely without having any clog in the tube line. Some materials will be trapped on this filter, which is going to be useful. For sixty minutes of continuous ablation in the system, the laser will be stopped. The furnace will be switched off as well and allow it to cool down to room temperature. The deposited as-prepared BNTs inside the quartz tube will be collected. Material synthesized in the hot zone will be collected and specially analyzed.



Figure 3.6: BNTs synthesized in the hot zone. The material was carried to the back and condensed on cooler sections of the quartz tube and appeared like a dark deposit. The as-prepared sample was collected over a period of 40 minutes after the experiment.

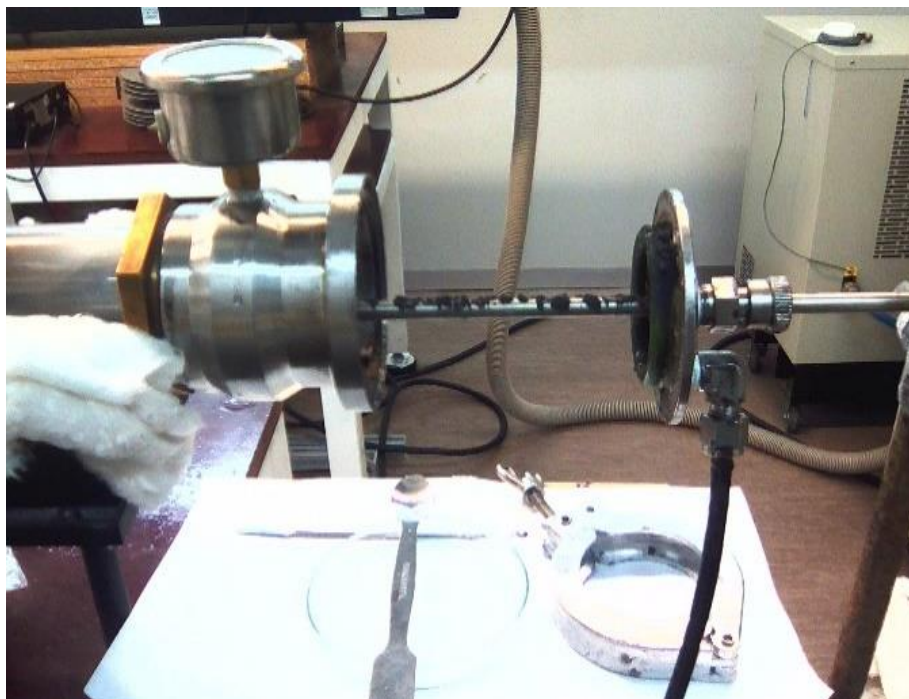


Figure 3.7: A removed vacuum flange revealing the as-prepared sample of BNTs.

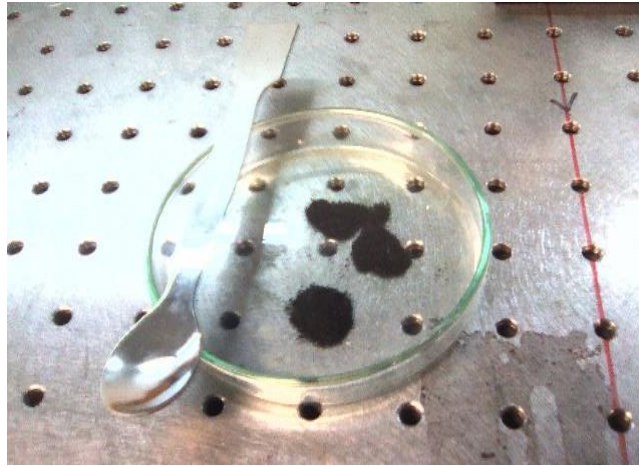


Figure 3.8: A typical sample of the as-prepared sample synthesized scrapped from the insides of the quartz tube and collected in a petri dish for analyses.

Although some will be carried to the back-end and condensed on the cooler sections of the quartz tube, as shown in Figure 3.6, some will be found at the front-end of the smaller quartz tube as it can be observed from the experiment set up in Figure 3.1. After the furnace had cooled to room temperature the vacuum flange holding the target support rod at the back-end of the quartz tube will be carefully removed to get the as-prepared BNTs sample, as shown in Figure 3.7. At this point for proper safety, the use of surgical powder, free gloves are required as well as with a face mask which was also mandatory during the period of collection. The whitish or dark brown as-prepared deposited material will be removed scraping it off by using a rod Teflon disc of diameter 40 mm, as shown in Figure 3.8. With this method, it is going to be easy to remove the sample from the inside wall of the quartz tube. A typical sample of material that will be collected from the synthesis process will be analyzed and characterized, by the following techniques. The FESEM was used to investigate the morphologies of the as-prepared products. Characterization of the structures of boron nanotubes was observed before and after centrifugation with the help of HRTEM. The EDX spectroscopy analyses were performed to analyze the chemical and phase composition of the as-prepared materials. The XRD was utilized to confirm the phase formation of the as-prepared samples. Through the PL, the emission and excitation wavelength, and intrinsic and artificial defects in the materials were observed. Absorption wavelength by UV-VIS was observed. We employed RAMAN spectroscopy to probe the structural nature of the as-prepared samples. Information on the chemical nature of the bonds, vibration behavior of atoms in the nanostructures as well as bonding symmetry can be obtained from the spectra. Particularly in the case of nanotubes, low frequency, radial breathing mode (RBM) and longitudinal and tangential modes were observed.

3.3.3 Main points on synthesized as-prepared samples by DPLA method

3.3.3.1 The sample key of labeling

The different experiments were conducted under different conditions through which the samples were synthesized. Important to identify and label the conditions that will enable us to identify the conditions under which each sample was synthesized. The identification labeling was introduced with some important parameters, such as target description, furnace temperature, nitrogen or argon gas pressure, nitrogen or argon gas flow, the position at which the sample was collected and the number of the experiment. For instance: BN/B P400 F200 T1100 B E1. Therefore, is identified as follows,

- The first label with two or one alphabet letter(s) BN / B and corresponding to the label of the targets as shown in Table 3.3.
- P, the alphabet represents the pressure, then followed by the number which was the digits of the gas pressure utilized in the synthesis.
- The F, the alphabet indicated the gas flow, then followed by the number which was the digits of the gas flow rate selected in the synthesis.
- The alphabet, T, stands for the temperature and the digits' numbers represent the furnace temperature used in the synthesis.
- The B, alphabet referred to the as-produced material collected at the back – end of the quartz tube.
- The last alphabet E stands for the experiment and then followed by a number which indicated the number of the experiment. See Table 3.4 below for tabulation:

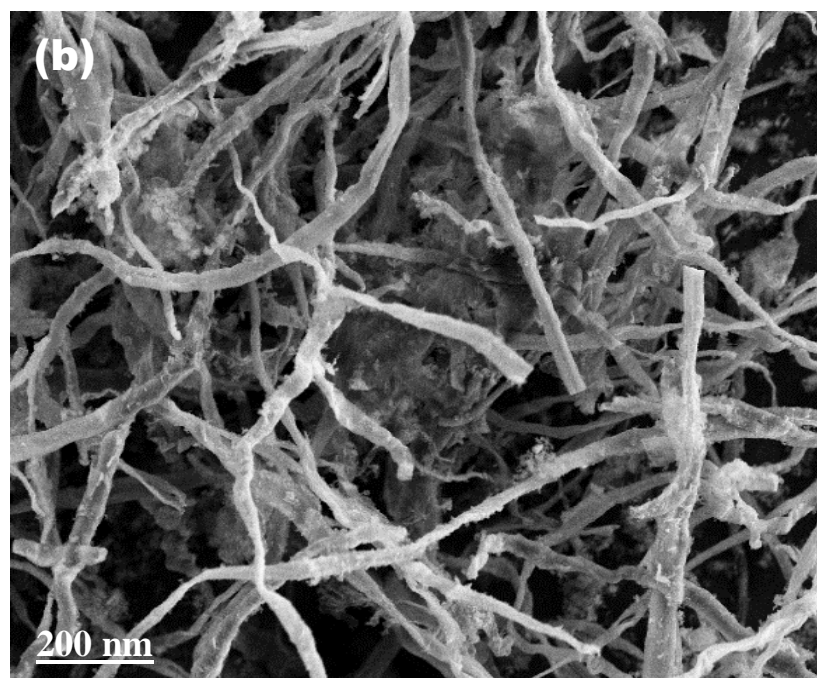
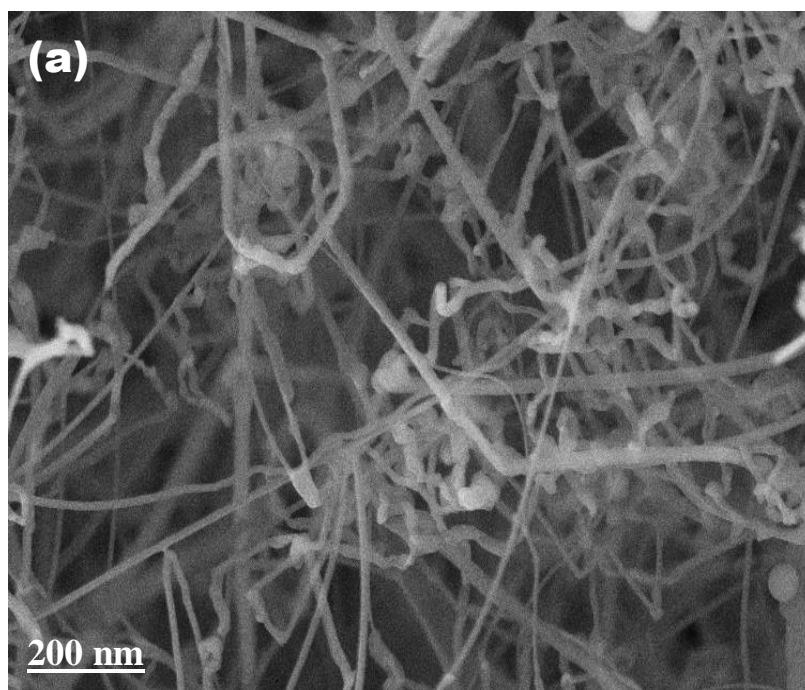
Table 3.4 A summary of as-prepared BNMs samples synthesized by utilizing Target BN / B

Target BN		Temperature 1100 °C	
Pressure (Torr)	Flow (sccm)	Experiment (E)	Mass (mg)
400	200	BN 400P 200F 1100T B E1	175
1000	500	BN 1000P 500F 1100T BE2	100
400	400	BN 400P 400F 1000T B E3	98
400	200	BN 400P 200F 1000T B E4	75
Target B		Temperature 1100 °C	
Pressure (Torr)	Flow (sccm)	Experiment (E)	Mass (mg)
400	200	B 400P 200F 1100T B E1	120

4. Boron nanomaterials synthesized by using a boron nitride (BN) target

4.1 Characterization of BNMs by SEM

The SEM images of samples prepared from laser ablation of a hexagonal boron nitride target mixed with a 1% Co and 1% Ni are shown in Figure 4.1 (a)-(d). The flow of nitrogen gas was monitored at different flow rates and pressures while the furnace temperature was set at 1000 °C and 1100 °C. For each experiment, the synthesized materials were scraped off as thin films coated on the inside walls at the end of the outer quartz tube. The SEM studies on these samples revealed a very high yield of different kind of nanostructures, such as (a) ‘worm-like’, (b) ‘fibrous like’, (c) ‘spaghetti-like’ and ‘pebble stick like’ nanostructures under nitrogen gas at a pressure of 400 to 1000 Torr and at flowrates of 200 to 500 sccm. The high yield is probably because the nitrogen pressure at 400 to 1000 Torr and the flow rate of 200 to 500 sccm restricted the expansion of the vapour plume thereby reduces the rapid decrease in a temperature of the plasma plume due to adiabatic expansion. These results are good compared with the results reported by Wang *et al.*[255] and Zhang *et al.*[148]. At 400 Torr and constant flow rates of 200 sccm the SEM image of Figure 4.1(a) shown presence of single-walled boron nanotubes (SWBNTs) in sample BN 400P 200F 1100T. At 400 Torr irrespective of the flow rates, the SEM images of Figure 4.1(c) and (d) showed excess boron nanowires (BNWs) and boron nanorods (BNRs) respectively. This is probably since an increase in pressure results in high collision probabilities of the evaporated species with the ambient gas molecules and therefore leads to an increase in the probability of catalytic sites. This is clearly shown in the SEM images where more boron nanostructures were observed. It was also observed that, at a pressure of 400 and 1000 Torr, the ablated material traveled backward up along the larger quartz tube. This means that a pressure and flow of the nitrogen gas was sufficient enough to confine the constituents of the plasma plume, that is, the momentum of the plume was lower than that of nitrogen gas. In this instance, the catalysis action and the condensing of the boron plasma plume into tubes are increased.



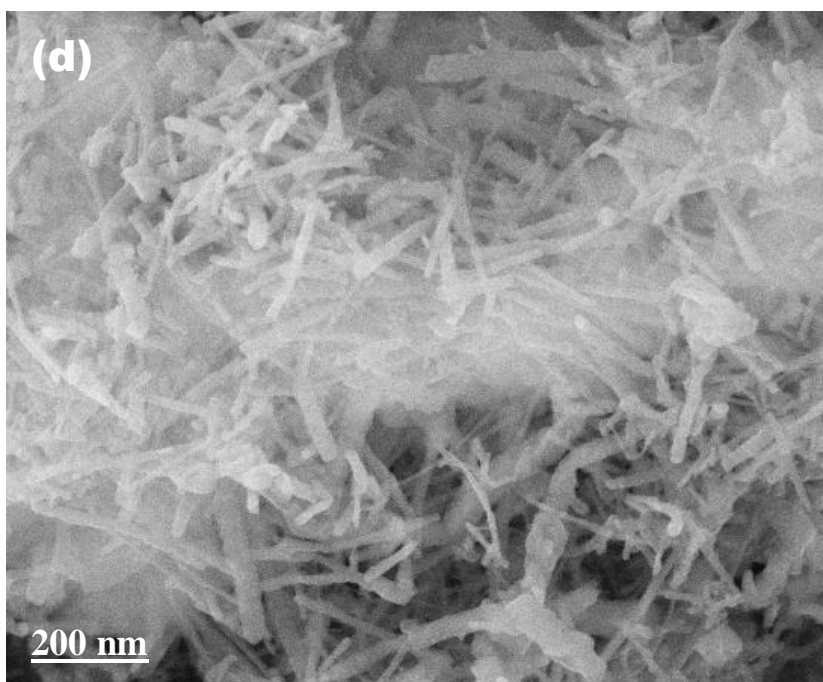
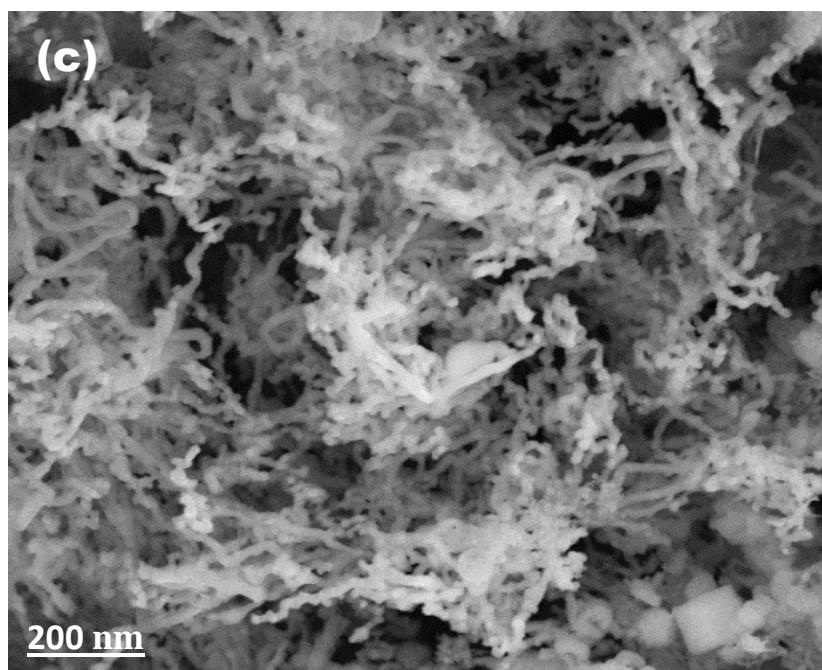
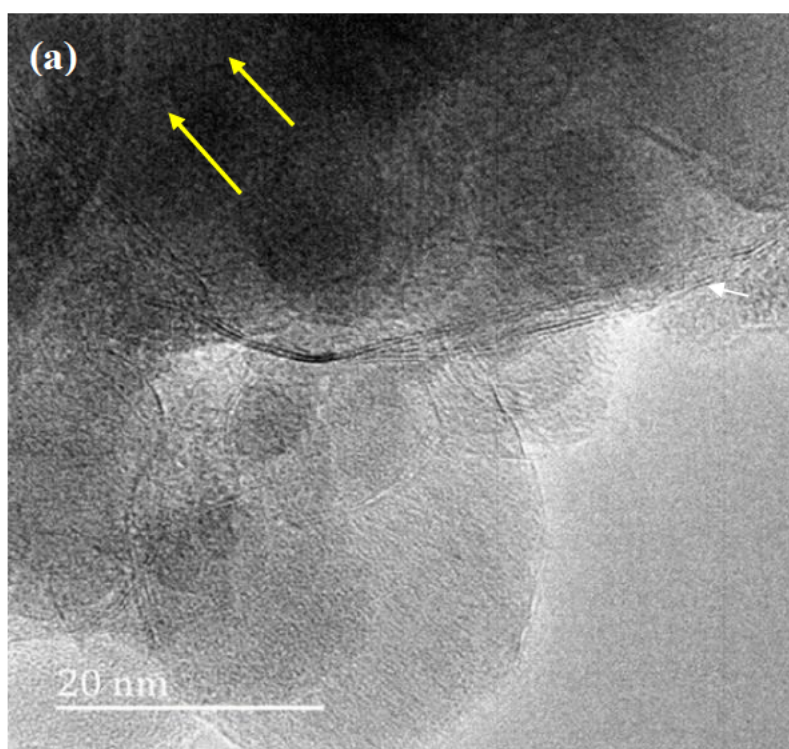


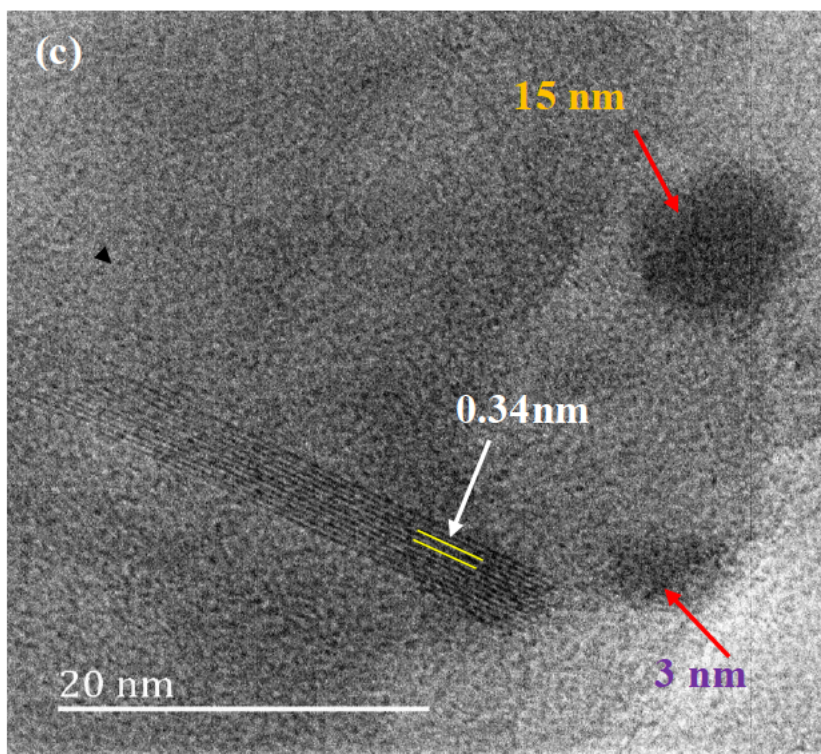
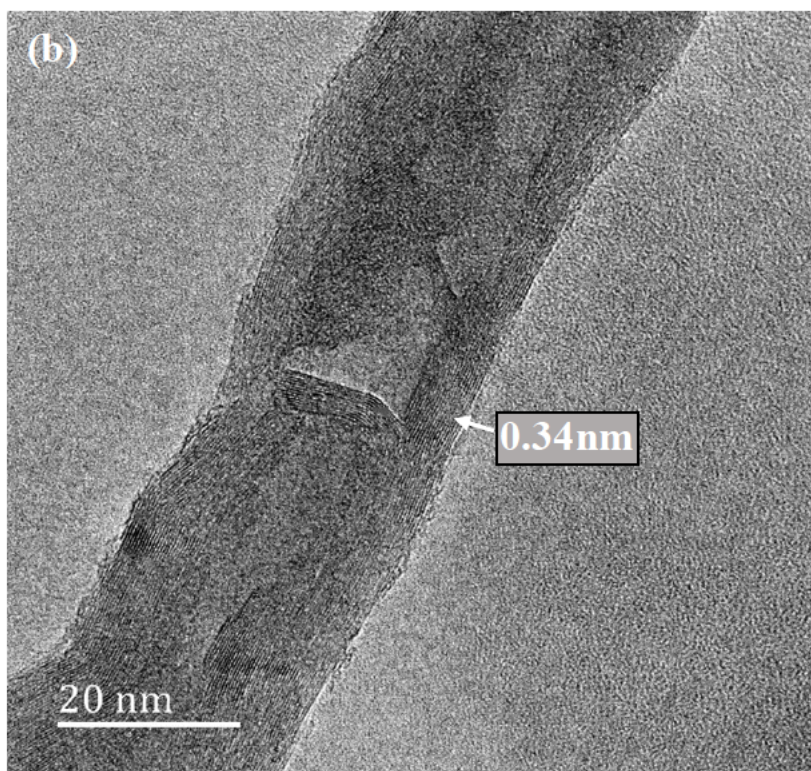
Figure 4.1: Shown SEM images obtained using *h* - BN target at a different pressure, flow rate and temperature with a high yield of a different kind of boron nanomaterials (a) BN 400P 200F 1100T, showed 'worms like' nanostructures (b) BN 1000P 500F 1100T, showed fibrous boron nanomaterials (c) BN 400P 400F 1000T, showed 'spaghetti-like' nanostructures and (d) BN 400P 200F 1000T, showed 'pebbles like sticks' nanostructures.

Briefly, SEM was utilized to measure the quality of the different nanomaterials (i.e. nanotubes, nanowires, nanorods, and bamboo-like nanotubes) that was synthesized under extreme synthesis conditions. These measurements were qualitative in nature since it was not possible to determine with certainty, for example, the ability of SEM to differentiate between samples where the synthesis conditions were almost the same. SEM and transmission electron microscopy (TEM) are two analytical techniques commonly utilized to visually reveal the nanotube contents. SEM analysis of as-prepared nanomaterials collected from ablating the BN target in a 400 sccm, flow of nitrogen gas, at a pressure of 400 Torr in a furnace operating at 1000 °C, showed "spaghetti-like" nanostructures (Figure 4.1 (c)). Under nearly ideal conditions, SEM analysis of sample BN 400P 200F 1000T (Figure 4.1(d)) showed "pebble stick like" nanostructures had formed. When sample BN 400P 200F 1000T was sonicated in ethanol, then dried, SEM images showed nanorods. SEM in Figure 4.1 (a) showed the formation of 'worms like' nanostructures. In Figure 4.1 (b), SEM analysis of the as-prepared sample collected from ablating the h-BN target in a 500 sccm flow of nitrogen gas at a pressure of 1000 Torr in a furnace operating at 1100 °C, showed 'fibrous like' nanostructured. SEM analysis of sample BN 400P 400F 1000T and BN 400P 200F 1100T in Figure 4.1(c) and 4.1(a) respectively showed 'spaghetti-like' and 'worm-like' nanostructures but the structures in Figure 4.1 (a) is much bigger than structures in Figure 4.1 (c). This might be due to different temperature and flow rate used. With SEM analyses, the individualize boron nanostructures is not possible, unlike HRTEM, due to the resolution limit of the instruments. This correlates very well with SEM and HRTEM spectra of the samples as shown in Figure 4.1 (a-d) and 4.2 (a-d). For instance, at a pressure of 400 and 1000 Torr, more of single-walled boron nanotubes and boron nanostructures was found increasing more rapidly other than any pressure used below 400 Torr. At 400 Torr pressures, 200 sccm flow rate and 1100 °C furnace temperature, the SEM and HRTEM spectra revealed a very high yield of single-walled boron nanotubes.

4.2 Transmission Electron Microscopy (TEM) Analysis

A high-resolution transmission electron microscopy (HRTEM) is a very powerful instrument in boron nanomaterials research. The HRTEM instrument is far superior to that of a SEM. HRTEM can distinguish between single-walled boron nanotubes, double - walled boron nanotubes, multi-walled boron nanotubes, fibers, and other boron-based nanomaterials. The sample preparation method used in the HRTEM investigations was described in Chapter Three. Figure 4.2(a-d) shows HRTEM images of samples which were recorded at an accelerating voltage of 200 kV at a specific magnification. The amount of supernatant boron typically deposited on an HRTEM grid is about 0.003 mg/ml and this must be utilized with caution when suggesting it as a fingerprint representative of a whole sample. The SEM image in Figure 4.1(a), " worm " like nanomaterial was also seen in Figure 4.2 (a), as single-walled boron nanotubes (SWBNTs) spread together with material that appeared as darker spots. These spots are metallic catalysts (nickel and cobalt) and appear dark in contrast due to a higher intensity of diffracted electrons, which was also revealed by the EDS measurements.





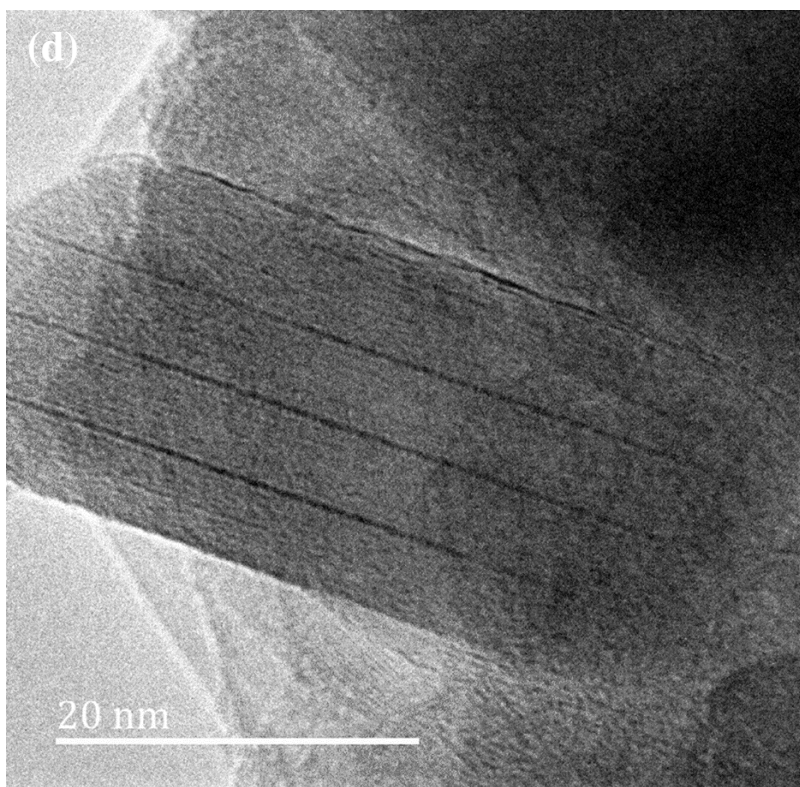


Figure 4.2: HRTEM images of boron nanomaterials synthesized using *h* - BN target at different pressures, nitrogen flow rates and temperatures (a) BN 400P 200F 1100T, showed BNTs, (b) BN 1000P 500F 1100T, showed bamboo nanotubes, (c) BN 400P 400F 1000T, revealed BNWs and (d) BN 400P 200F 1000T, showed BNRs.

Under higher magnification as was observed in Figures 4.2 (a-d), individual strands single-walled boron nanotubes, bamboo-like nanotubes, bundles of nanowires, and nanorods were clearly observed. The nanotubes were observed to be decorated with what appears to be amorphous boron, indicated with yellow arrows. A closer inspection of the area surrounding the catalyst particles indicated with red arrows, which are typically between 3-15 nm in diameter, showed that in most cases, they were attached to BNWs bundles with the interlayer spacing of 0.34 nm, in Figure 4.2 (c). In Figure 4.2 (d), a boron nanorod bundle was seen extending out of the plane of the HRTEM grid. The cylindrical ends of the bundle rods are clearly visible, and the image is not sufficiently resolved to deduce whether the rods ends are either closed or open. The interlayers spacing of boron nanorods is 0.34 nm.

In Figures 4.2 (a), HRTEM image of sample BN P400 F200 T1100 is shown. A closer inspection reveals a significant content of α – boron nanotubes strands which accounted for the A_{1g} and E_g peaks observed in the Raman active mode spectra of the α – boron cluster. In Figure 4.2 (b), the results of an analysis of an HRTEM image obtained from sample BN P1000 F500 T1100 was made to form bamboo-like nanotubes. A measurement of transmitted electrons across the region of interest could be analyzed to reveal lattice spacings of the bamboo-like nanotubes structures. The region indicated with a white arrow was a cross-section of an individual bamboo-like nanotubes with interlayer lattice spacings of 0.34 nm. The cylindrical shape of the bamboo-like nanotubes was clearly visible. The resolution of the image is not sufficient enough to deduce whether the bamboo-like nanotubes end, are either closed or opened. In Figure 4.2 (a) the HRTEM image of the nanotubes indicate some tubular and spherical single-walled boron nanotubes (SWBNTs). These SWBNTs extend over an estimated 100 nm in length with diameters as small as 0.4 nm. It is clear from these HRTEM images that due to the many possible bonding configurations that boron exhibits, the as-prepared materials exhibit a large variation in its morphology [131, 188]. The HRTEM image of boron bamboo-like boron nanostructures in Figure 4.2(b)), exhibit similar characteristics with SWBNTs and boron nanowires (BNWs) in terms of their outer diameters ranging from 0.4 to 2.0 nm and with an interlayer spacing of 0.34 nm between their lattice fringes. In Figure 4.2 (d) HRTEM image of boron nanorods (BNRs) shows a unique multi-ordered stacking in the crystal lattice. This HRTEM image revealed, that the diameters of the nanorods range between 10 and 20 nm. Most of the nanostructures appeared to be crystalline in nature.

The interlayer spacing of 0.34 nm is very close to the theoretical values of 0.2997 nm and 0.3021 nm [131]. This interlayer spacing of 0.34 nm observed in the materials synthesized is very close to the bulk boron interlayer spacing of 0.35 nm. On this basis, we can suggest that SWBNTs found in Figure 4.2 (a) have a structure with the α -rhombohedral boron configuration, which is consistent with the results obtained from XRD and Raman analyses

4.3 Energy Dispersive X-Ray Spectroscopy (EDS)

The EDS spectrum analyses of SEM and HRTEM images obtained in Figure 4.1(a) and 4.2(a) respectively, were shown in Figure 4.3 (a) and (b). The boron nanotubes observed in the HRTEM image in Figure 4.2(a) were formed from SEM image in Figure 4.1(a) that showed ‘worms like ‘nanostructure. The EDS tables analyses obtained from each image revealed the elemental components materials present in the single-walled boron nanotubes. Figure 4.3(a) shows the respective energy dispersive x-ray spectroscopy data demonstrating that the material is mainly composed of boron with traces of catalysts utilized. In Figure 4.3(a) the strong peak of boron appeared at about 0.2 keV and nitrogen peak at 0.3 keV. It was observed that only the smallest amount of catalysts (Ni and Co) at 0.47% and 0.45% respectively as indicated in Table 4.1 was found. The peak at 2.2 keV is associated with gold peak resulting from the gold used to coat the as – prepared BNTs sample on the carbon tape, prior to SEM characterization. The EDS spectrum of HRTEM in Figure 4.3 (b) taken with the JEOL 2100 indicates at least 90% boron as showed in the inset of the EDS table in Figure 4.3 (b). This indicates that the material is purely boron in the form of tubes, rods, bamboo shoots and not boron nitride material as determined through SEM analysis. This difference in observation is purely due to the method in sample preparation prior to the period of the HRTEM characterization. It was noticed that some catalysts are mixed in the sample which was revealed through the energy dispersive X-ray spectroscopy spectra results in Figure 4.3 (b). The inset table of EDS shows the percentage of each component of elements present in the as-prepared BNTs in Figure 4.3 (b). The strong peak of boron appeared at about 0.20 keV. The smallest 0.89% of iron at 6 keV, found in the highly magnified EDS spectrum, was attributed to the stainless-steel holder. The peak found at 1.7 keV associated with the silicon peak, came from the attachment of the quartz tube while scraping as – prepared materials from the quartz tube. Very small amounts of Ni and Co were observed, which is 0.05% at 0.8 keV, as catalysts used in the target.

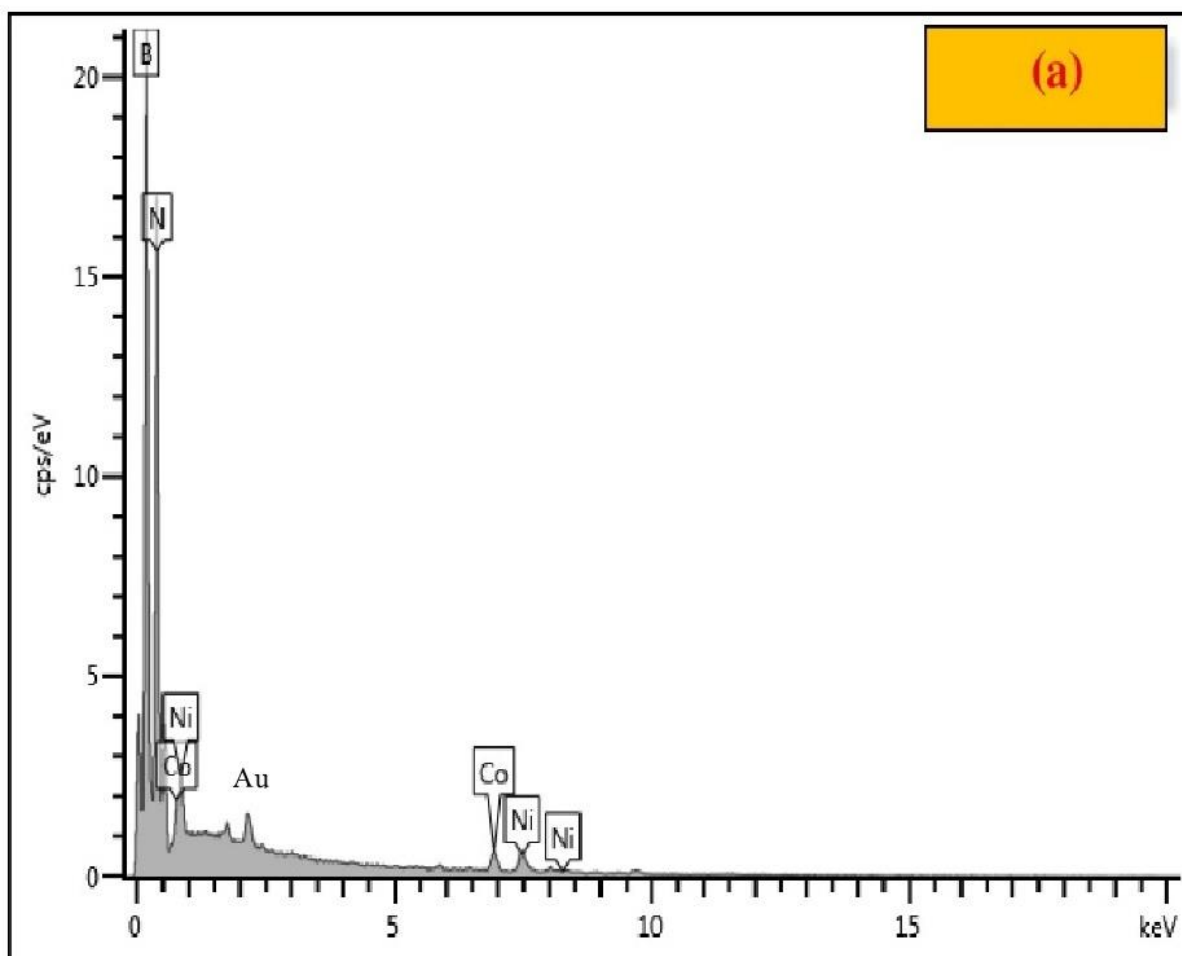


Figure 4.3(a): SEM energy dispersive x-ray spectroscopy spectrum of BNTs obtained from BN 400P 200F 1100T of the as-prepared BNTs with a high peak from boron.

Table 4.1: Revealed the percentage weight of each element present in the BNTs synthesized.

BNTs	Wt. %	Wt. % Sigma
B	53.73	0.48
N	45.34	0.48
Co	0.45	0.03
Ni	0.47	0.03
Total	100	

The small peak at 5.5 keV has attributed to the peak of manganese resulted from the holder. Very small contents of carbon and copper were found in the high - resolution spectrum caused by the copper of high-resolution transmission electron microscopy grid covered with carbon film. In addition, the EDS analysis revealed over 90% pure boron content found in the boron nanotubes, which confirmed the purities of as – prepared SWBNTs.

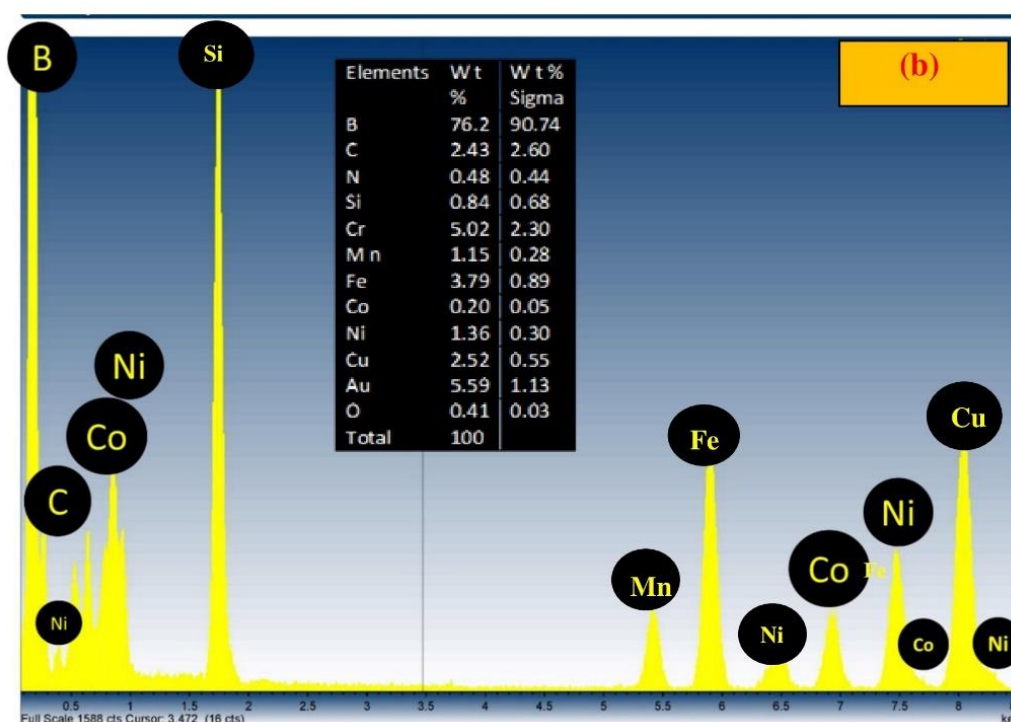
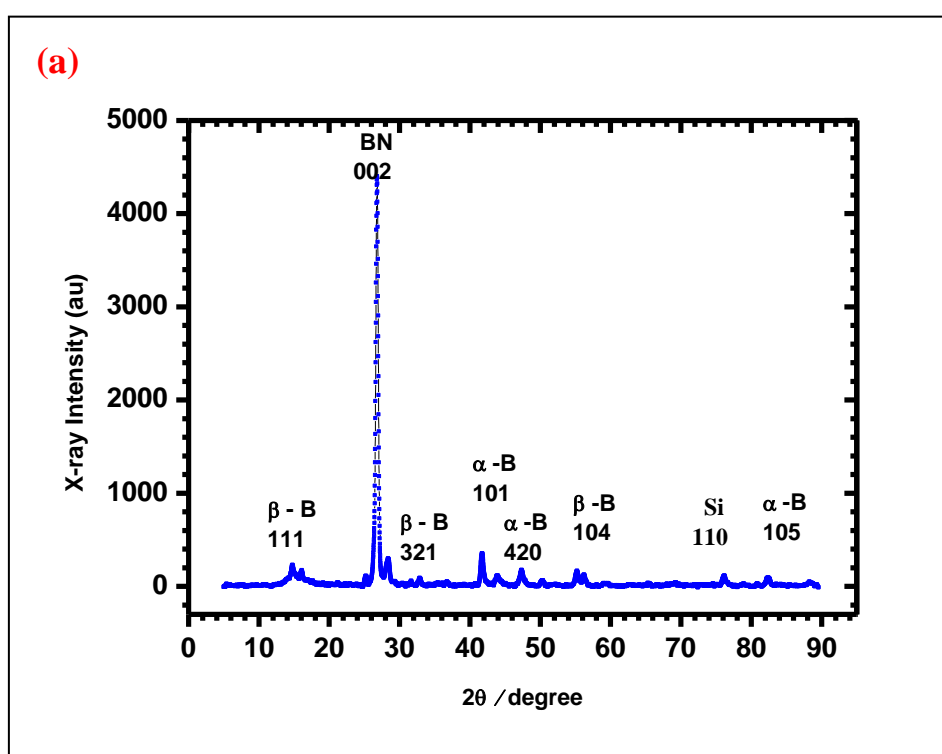


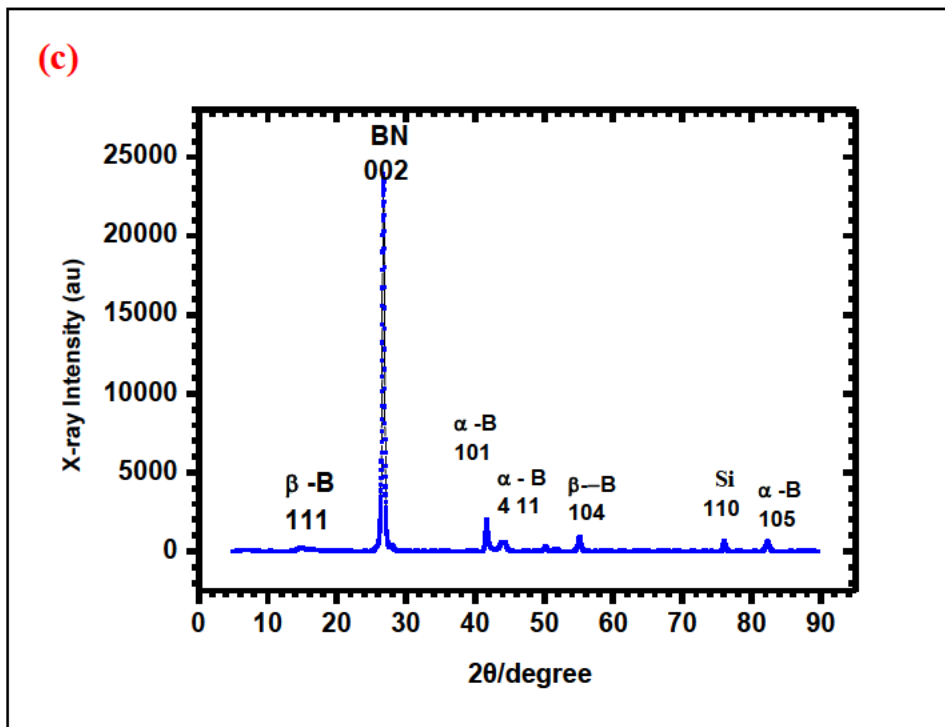
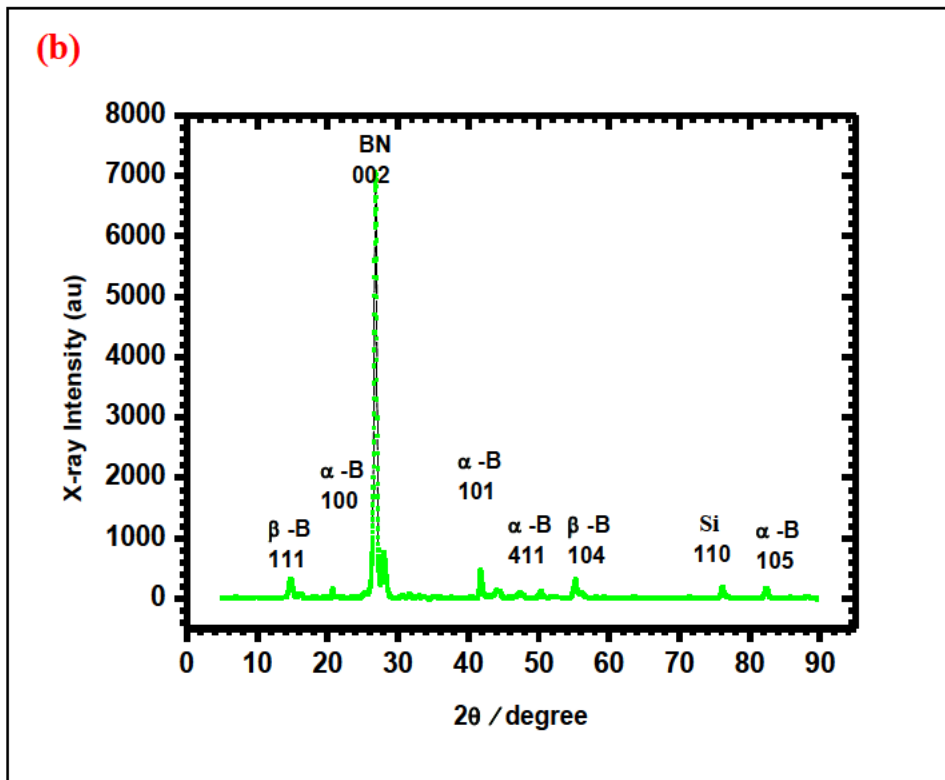
Figure 4.3(b): The Energy Dispersive X-ray spectroscopy spectrum of SWBNTs of BN 400P 200F 1100T obtained from HRTEM by supernatant sample liquid indicated a high peak of boron. The inset EDS table in the spectrum shown the percentage weight of each element present in the SWBNTs synthesized.

Finally, from the HRTEM image that was acquired, it was determined that the diameter of the boron nanotubes range from 0.4 to 2.0 nm. Other boron nanomaterials surrounding the metal catalyst particles had a lattice spacing of 0.34 nm which corresponds very well to the interlayer spacing of bulk boron which is 0.35 nm.

4.4 X-Ray Diffraction (XRD) Analysis

The crystal structure of the as-synthesized boron nanomaterials was analyzed by XRD. Figure 4.4 (a-d) shows the XRD spectra taken from all the synthesized boron nanomaterials (nanotubes, bamboo-like nanotube, nanowires, and nanorods). It was discovered that there is an impurity phase such as silicon. Peaks originating from secondary phases such as α -tetragonal boron (105) at 82.5° and silicon (110) at 75.6° were clearly observed [255].





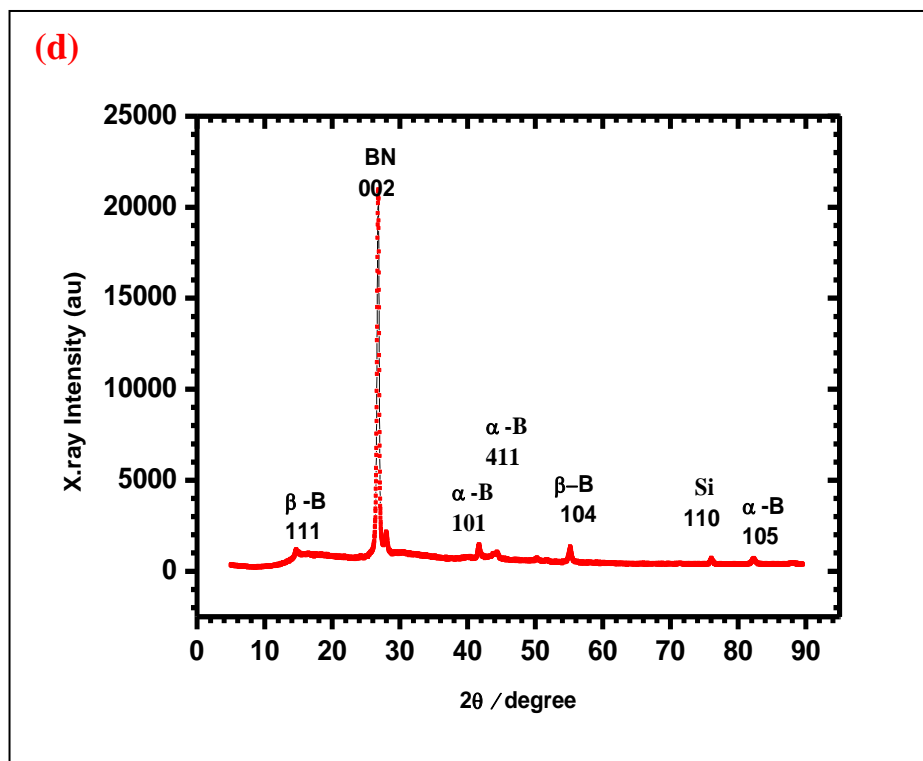


Figure 4.4: X ray diffraction spectra of boron nanomaterials synthesized from h-BN target at different pressures, nitrogen flow rates and temperatures (a) BN 400P 200F 1100T, showed BNTs, (b) BN 1000P 500F 1100T, showed bamboo nanotubes, (c) BN 400P 400F 1000T, revealed BNWs and (d) BN 400P 200F 1000T, showed BNRs.

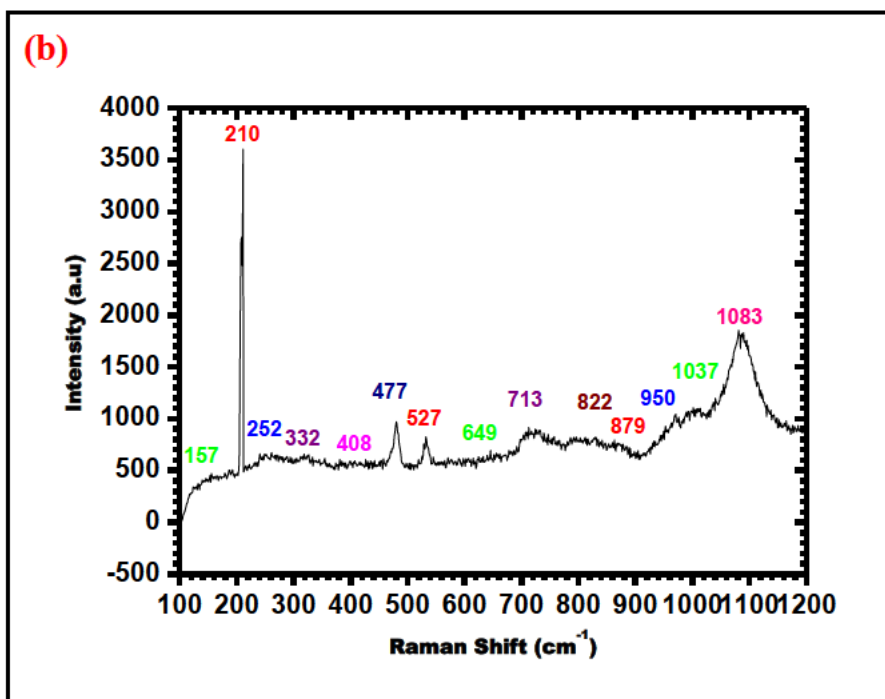
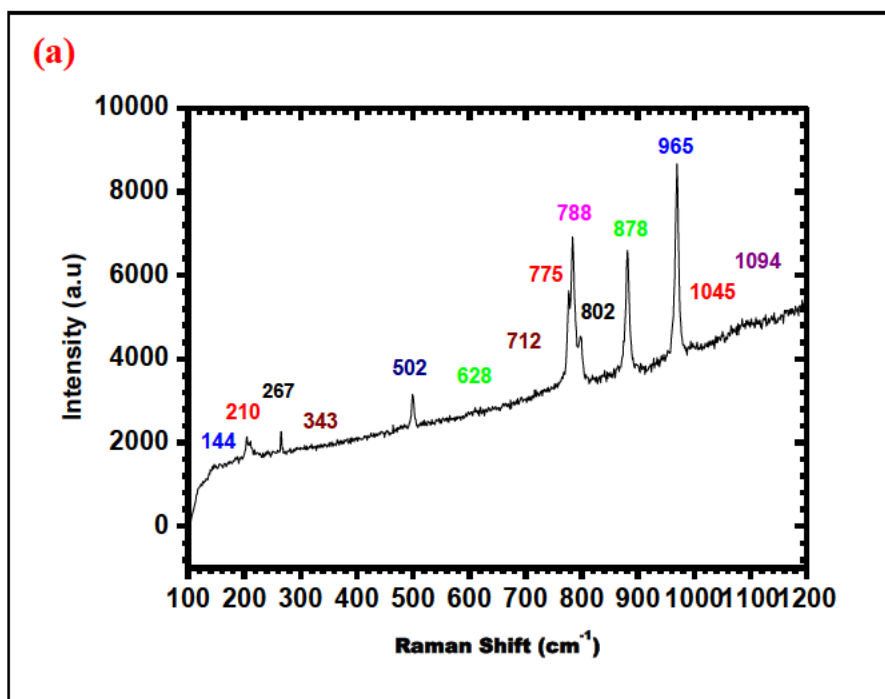
Table 4.2: X-ray diffraction peaks observed in boron nanomaterials synthesized

Element	h	k	l	d (Å)	2 θ (degree)
α -B	1	0	0	4.040	21.982
α -B	1	0	1	4.375	42.966
α -B	1	0	5	1.265	82.542
α -B	4	1	1	1.957	46.358
α -B	4	2	0	1.955	46.356
β -B	1	0	4	2.445	55.312
β -B	1	1	1	6.398	13.831
β -B	3	2	1	2.759	32.430
BN	0	0	2	2.530	26.812
Si	1	1	0	4.041	75.632

The possible explanation is that the silicon originated from a quartz tube utilized during the experiment. The smallest peak at 13.8° is related to β – boron (111) [59]. The peak marked (101) at 42.9° coincided with JCPDS data of α - tetragonal boron [255]. The XRD peak (104) at 55.3° suggested β - rhombohedral boron [255]. All the peaks of β – boron that appeared in the spectra were due to some β – boron that was not totally transformed to α – boron nanotube during the time of the experiment. There are several reports on the theoretical calculation for the crystal structure and optical properties of α - boron crystal which has been experimentally validated [256, 257]. The sharp and strongest peak (002) at 26.8° correspond to the boron nitride peak [255] with a lattice constant of $a = 2.504\text{\AA}$, $b = 2.504\text{\AA}$ and $c = 6.661\text{\AA}$ and the space group of $P6_3/mmc$. [258].

4.5 Raman Spectroscopy (RS) Analysis

Raman spectroscopy is one of the standard instruments to characterize nanotubes of carbon, boron, boron nitride and other tubular structures. The Raman spectra of the experiments are shown in Figure 4.5 (a-d). We are interested in the experiment synthesized single-walled boron nanotubes, that is a sample BN 400P 200F 1100T. In Figure 4.5(a) Raman spectrum of single-walled boron nanotubes (SWBNTs) were found in the radial breathing mode (RBM) in the region between 250 and 600 cm^{-1} with peaks at 267 , 343 and 502 cm^{-1} [120]. The region at peak wavenumbers below 500 cm^{-1} (i.e. 144 , 210 , 267 and 343 cm^{-1}) is considered as a characteristic for tubular structures [120], which corresponds to the RBM of similar peaks that were also reported for the single-walled carbon nanotubes (SWCNTs) [3]. The peaks between 300 and 600 cm^{-1} (i.e. 343 and 502 cm^{-1}) can be attributed to the different tubes with smaller diameters and chirality of the boron nanotube [42, 120]. The spectrum recorded for the boron nanotube sample, showed peaks attributed to the tangential vibration mode of boron which is visible in the $1045 - 1094\text{ cm}^{-1}$ region. These peaks in the Raman breathing mode region are attributed to tubular structures [120, 134, 259]. The three peaks at 788 , 878 and 965 cm^{-1} respectively, occurred from α -boron nanotubes (α - BNTs) with α – boron sheets structures [15]. In agreement with the literature, α – BNTs formed from α – boron sheets are the most stable structures [15].



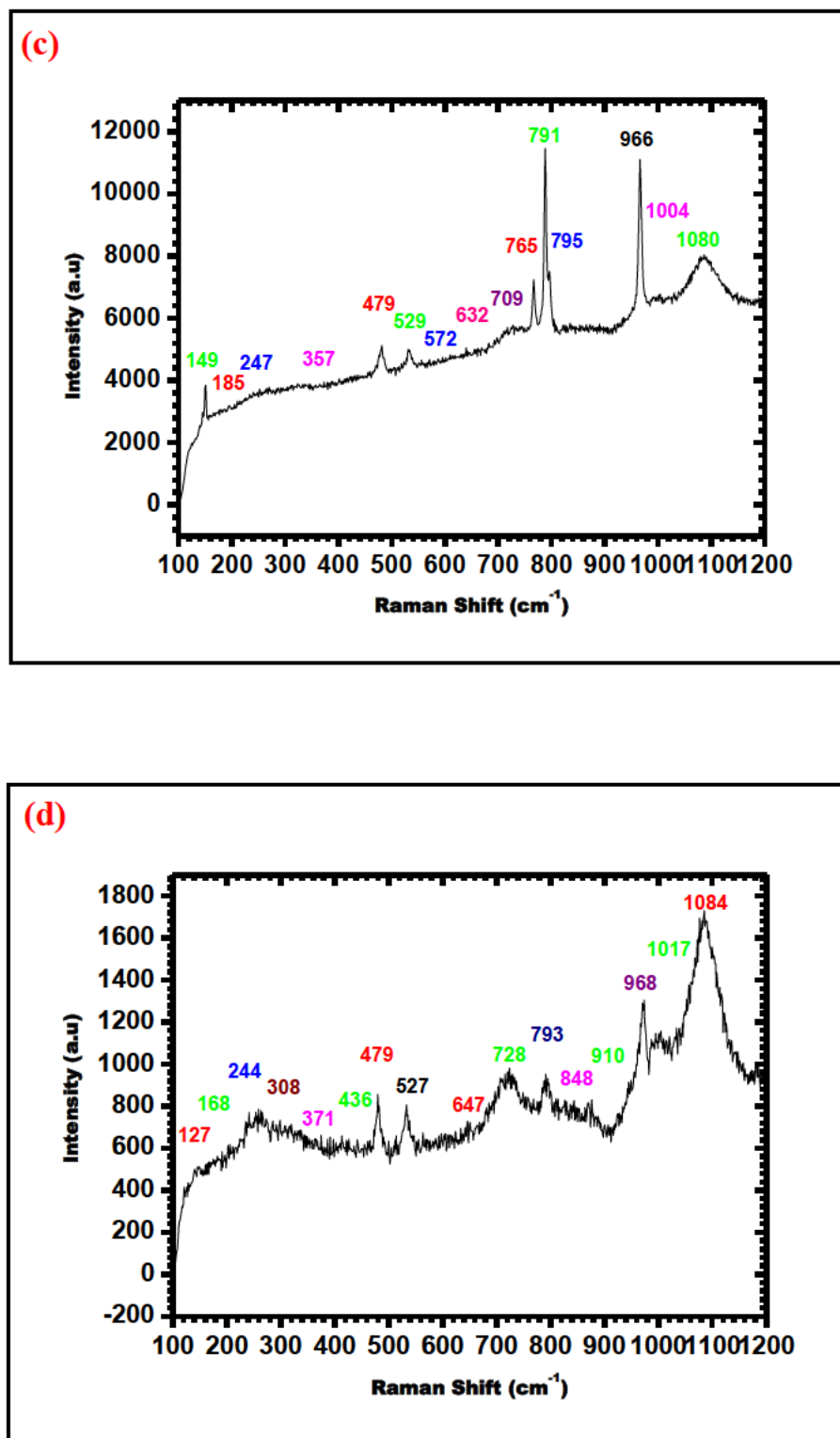


Figure 4.5: Raman spectra of boron nanomaterials synthesized from *h*-BN target at different pressures, nitrogen flow rates and temperatures (a) BN 400P 200F 1100T, showed BNTs, (b) BN 1000P 500F 1100T, showed bamboo nanotubes, (c) BN 400P 400F 1000T, revealed BNWs and (d) BN 400P 200F 1000T, showed BNRs.

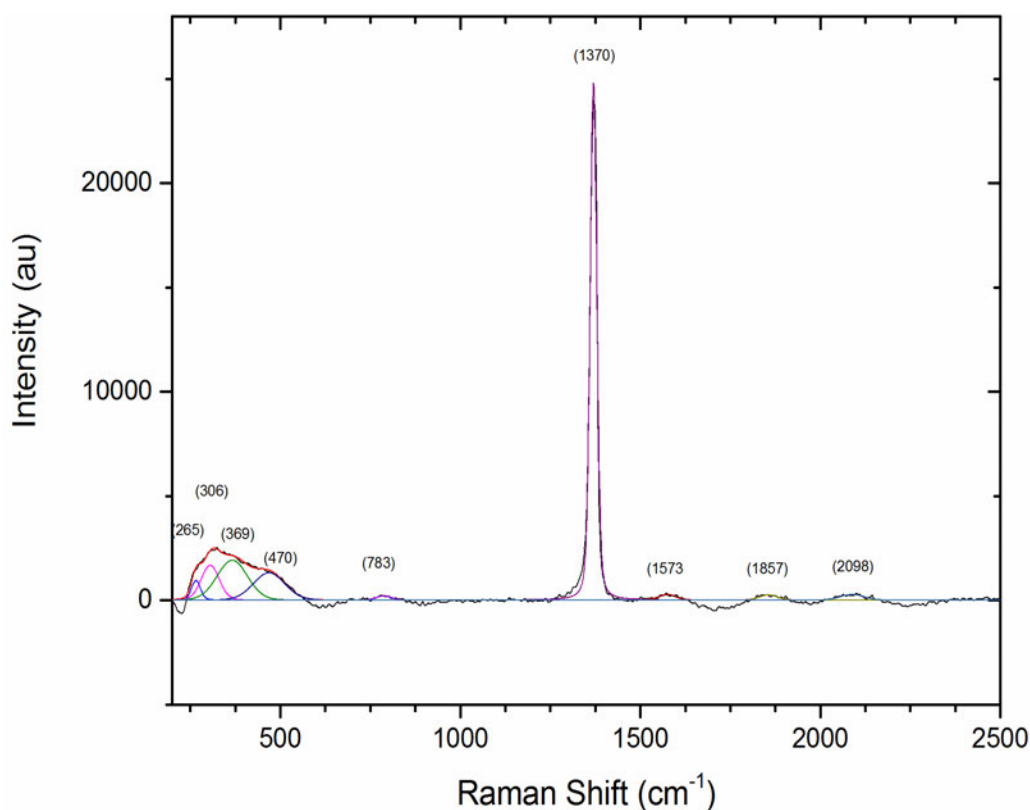


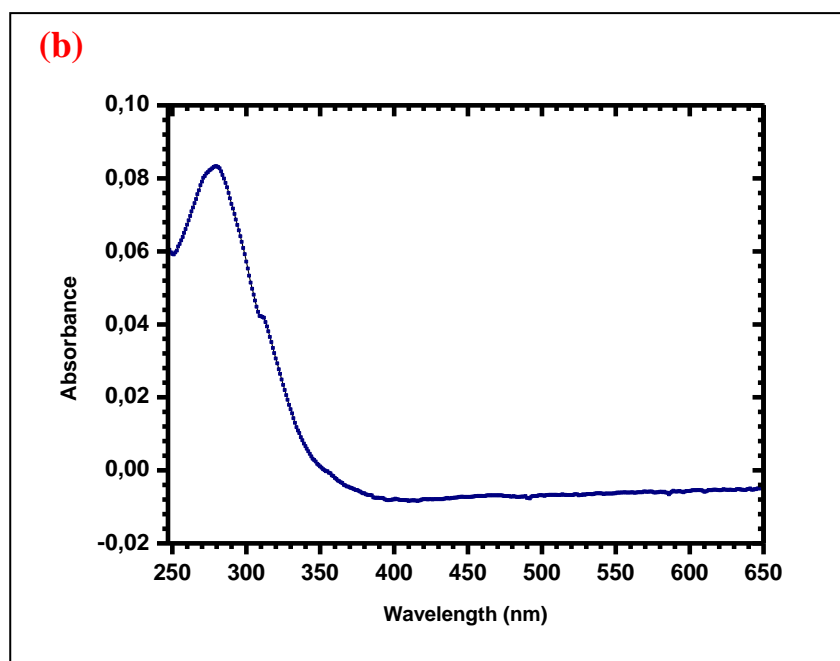
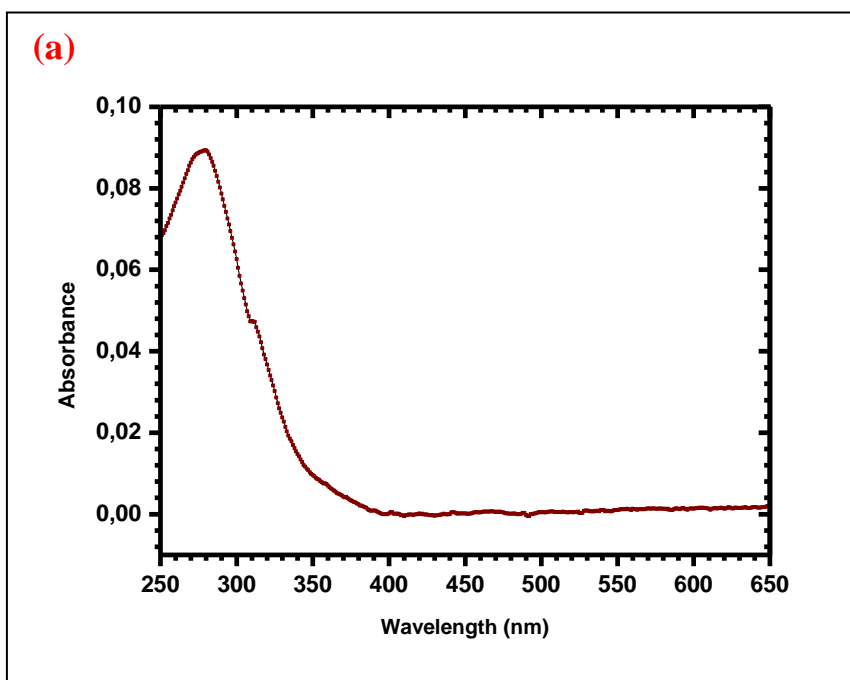
Figure 4.5: (e) Raman spectra of the bulk hexagonal boron nitride powder (h-BN, Sigma Aldrich)

The α -BNTs formed from α -boron sheets were confirmed through the XRD and Raman spectra results. The structural stabilities of the α -BNTs rolled from α -boron sheets were strongly dependent on the diameters [15], according to Victor *et al.* It was observed that the atomic structures of α -BNTs formed are corresponding or related to α -boron sheets [15]. The other peaks which may occur from mixed BNWs with α -tetragonal boron structure and peak with higher frequencies resulting from α -boron clusters still required further investigation. In addition, by looking at the Raman spectrum of the boron nanotubes (BNTs) sample in Figure 4.5 (a), and making a comparison with Raman spectrum obtained from bulk hexagonal-boron nitride powder (h-BN, Sigma Aldrich) in Figure 4.5 (e), it was clearly observed that no peaks from any of the h-BN were noticed from the Raman spectrum of as-prepared BNTs obtained in Figure 4.5 (a).

With this evidence, it was strongly confirmed that as – prepared BNTs sample synthesized in the laboratory contained boron nanomaterials rather than boron nitride nanomaterials. On this basis, we can suggest that our BNTs have a structure with an α - rhombohedral boron configuration, which is consistent with the results obtained from XRD analyses.

4.6 Ultraviolet-Visible (UV-VIS) Analyses

Figure 4.6 (a-d) shows the ultraviolet-visible spectra of the samples (nanotubes, bamboo-like nanotubes, nanowires, and nanorods). The optical absorption spectra of materials synthesized were measured at room temperature. The UV-VIS spectra displayed indicate (a) BN 400P 200F 1100T, (b) BN 1000P 500F 1100T, (c) BN 400P 400F 1000T and (d) BN 400P 200F 1000T with a strong exciton absorption peak at (a) 279 nm, (b) 277 nm, (c) 274 nm and (d) 270 nm wavelength respectively. The peak at 279 nm observed in BNTs synthesized from sample BN 400P 200F 1100T, closely matched with the value reported by Yang et al, [260], for the strong exciton peak of the boron nanotubes and other boron nanostructures [261]. The peak located around 320 nm corresponding to absorption shoulder due to some defect level found in the boron nanotubes and related boron nanostructures [262]. The peak threshold was observed in boron nanotubes at 300 nm in which the boron nanotubes achieved its maximum absorption peak at 279 nm. Most especially sample BN 400P 200F 1100T, that produced boron nanotubes, in which absorption peak is due to van Hove singularities [263]. Other nanomaterials (bamboo-like nanotubes, wires, and rods) synthesized found their peak threshold between 300 to 302 nm and achieved their maximum absorption peak around 270 to 277 nm due to van Hove singularities.



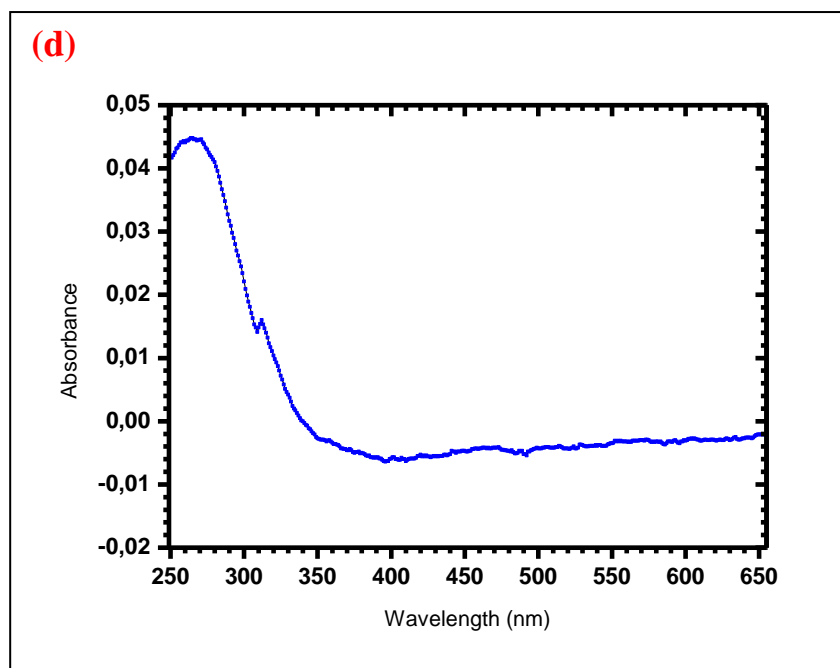
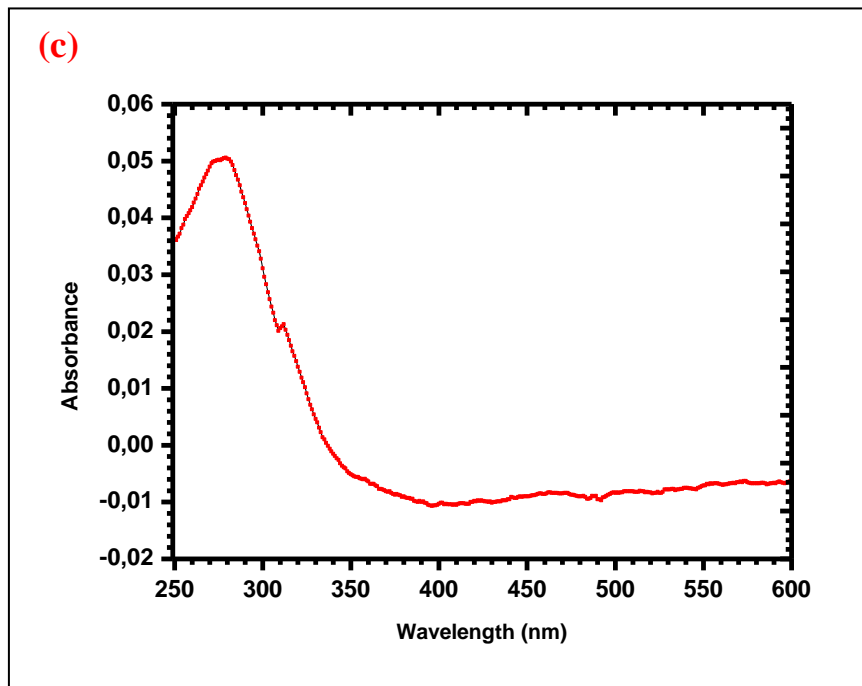
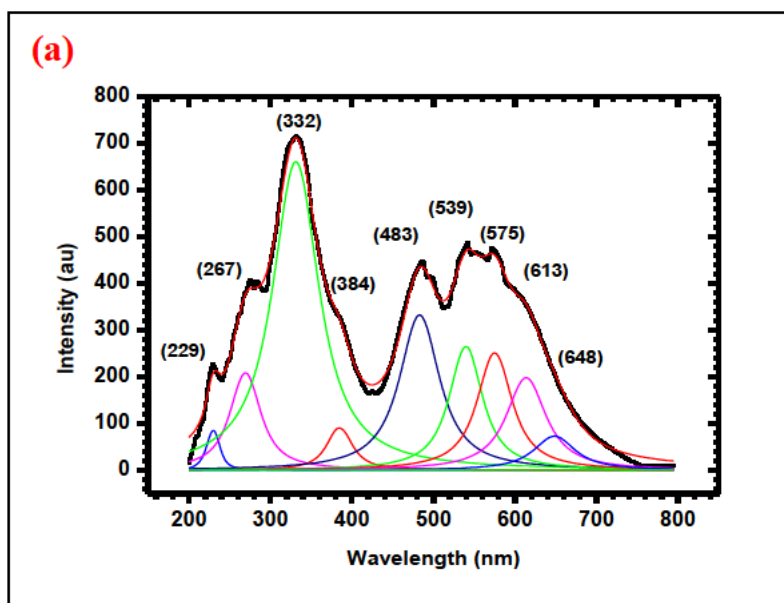


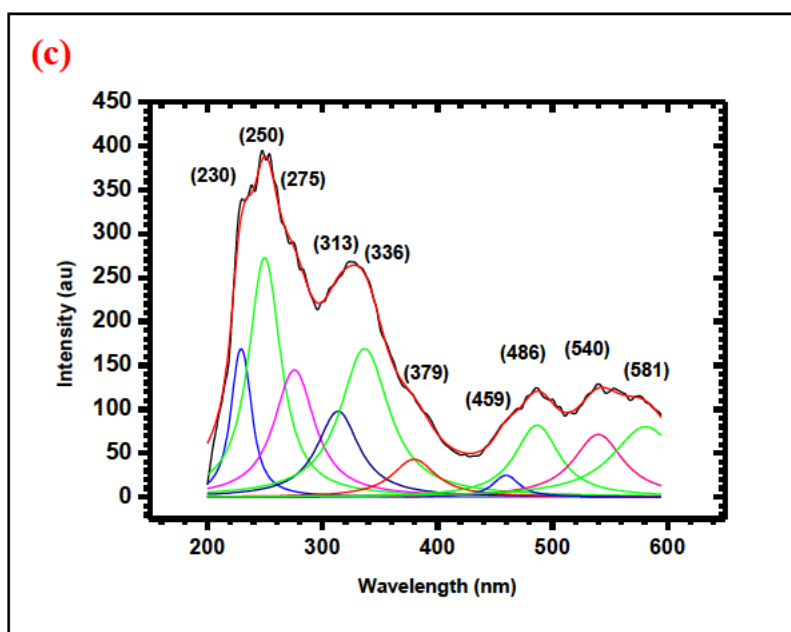
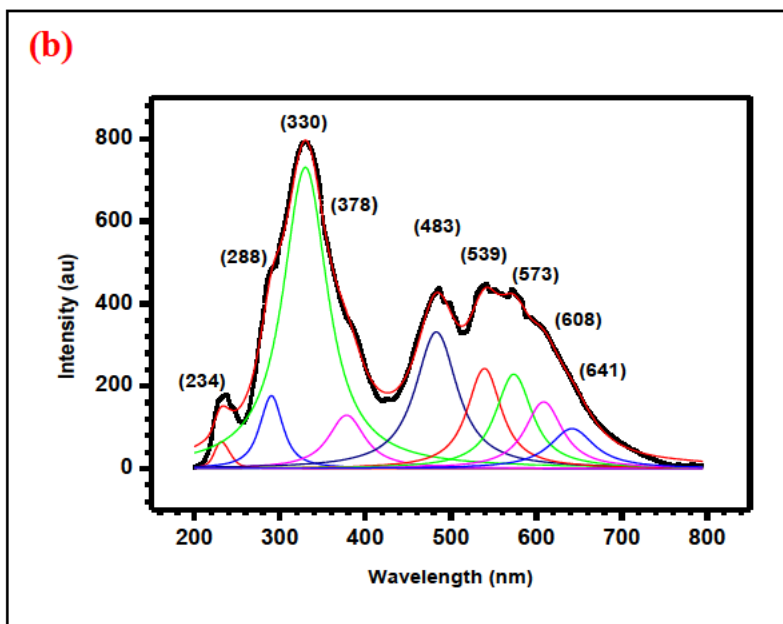
Figure 4.6: UV-VIS spectra of boron nanomaterials synthesized from h-BN target at different pressures, nitrogen flow rates and temperatures (a) BN 400P 200F 1100T, showed BNTs, (b) BN 1000P 500F 1100T, showed bamboo nanotubes, (c) BN 400P 400F 1000T, revealed BNWs and (d) BN 400P 200F 1000T, showed BNRs.

Boron nanotubes and other three nanomaterials are transparent up to 400 nm within the limitation of the measuring instrument whose working range is 200 to 800 nm. The absorption spectrum of boron nanotubes together with spectra of other boron nanostructures are relatively featureless and the broad and overall constant low absorbance from 450 to 600 nm is consistent with the reported values for bulk boron single crystals and network-like nanomaterials, thus demonstrating that it is transparent from ultraviolet to the visible regions [264].

4.7 Photoluminescence (PL) Analyses

The PL spectra measured at room temperature of the synthesized boron nanotubes and other boron nanomaterials are shown in Figure 4.7 (a-d) with the excitation wavelength at 200 nm. The spectra of boron nanotubes and other boron nanostructures (bamboo shoots, wires, and rods) consist of a strong ultraviolet (UV) emission peak and relatively weak defect emission peaks.





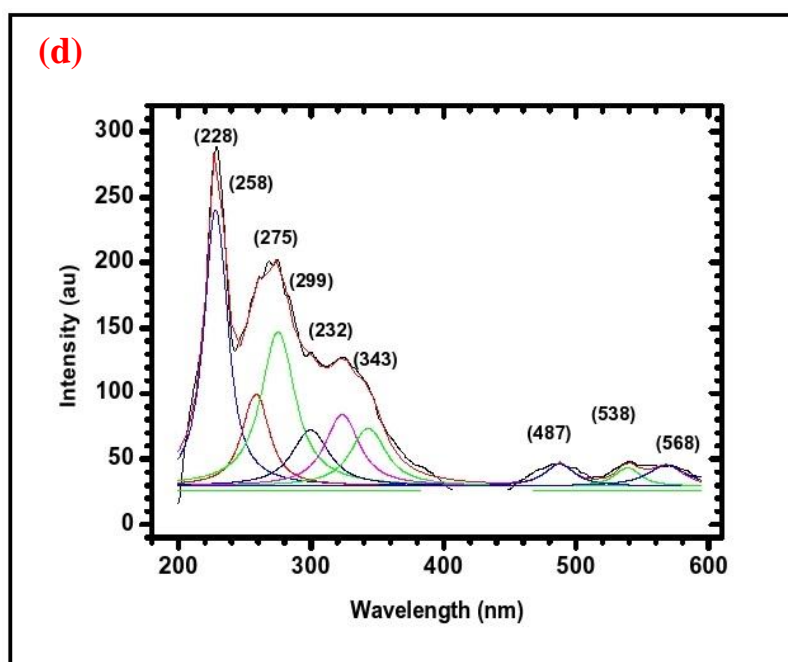


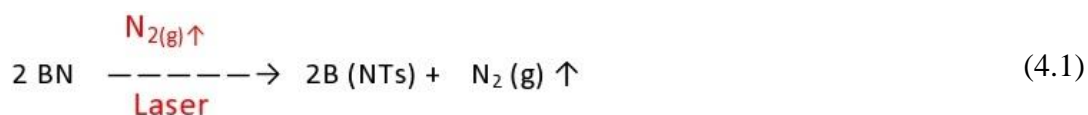
Figure 4.7: Photoluminescence spectra of boron nanomaterials synthesized from *h*-BN target at different pressures, nitrogen flow rates and temperatures (a) BN 400P 200F 1100T, showed BNTs, (b) BN 1000P 500F 1100T, showed bamboo nanotubes, (c) BN 400P 400F 1000T, revealed BNWs and (d) BN 400P 200F 1000T, showed BNRs.

The strong UV luminescence peaks observed in nanotubes, bamboo-like nanotubes, nanowires, and nanorods are, at (a) 229 nm, (b) 234 nm, (c) 230 nm and (d) 228 nm respectively that corresponds to luminescence of free excitons [265, 266]. The peak observed in the samples at (a) 334 nm, (b) 330 nm, (c) 250 nm and (d) 258 nm which are attributed to the PL emission band were found in nanotubes, bamboo shoot, wires and rods [267, 268]. Typical emission peaks in the UV region are related to near band edge emission (NBE) of boron itself which originated from the direct exciton recombination [260]. There are some defects related emission peaks observed in boron nanotubes. These emission peaks were found at 483, 486, and 487 nm, that are associated with O₂ and C impurities. The PL band area at peaks around 575, 573, 581, and 568 nm are ascribed to heavy metal impurities which might probably emanate from the sample holder.

4.8 Vapour Liquid Solid (VLS) mechanism process

In this research, metal nitrates were used as catalysts in the ablation target for the synthesis of the boron nanomaterials, and thus Ni and Co play an important role in information. The vapor-liquid-solid (VLS) mechanism process is the most probable growth mechanism in the laser synthesis method [269]. The schematic diagram of this mechanism process was shown in Figure 4.8 (a, b). The exact mechanism of nucleation in this type of nanomaterials is yet not fully understood. We observed variations in the diameters of boron nanotubes and three other boron nanomaterials grown by the suggested VLS mechanism [258], which are usually heavily influenced by the synthesis temperature. The higher energy laser fluence at the target surface and plasma plume generated by the impinging laser causes the local temperature to be momentarily for a few microseconds higher than the furnace temperature of 1100 °C to the point that the Ni and Co become catalytic active faster than other synthesis methods. The magnetic properties of these materials tend to support the synthesis of tubular nanostructures. As in the case of boron nitride and carbon nanotubes since the vast majority of synthesized tubular and caged nanostructures required the use of transition metal catalysts. The growth of nanomaterials is initiated within the plasma plume via VLS process. The nanomaterials grow in the hot zone of the furnace and are only limited by the available feedstock. The existence of purely boron nanomaterial in the synthesis process could be explained as follows.

The ablated BN material is decomposed into B and N with the high-temperature plasma plume. The nitrogen in the hexagonal boron nitride (h-BN Sigma Aldrich 99.99%) has combined with carrier gas nitrogen (N_2) which decomposes in the furnace to produce N radicals i.e.



The result is boron vapour which was found near metal catalysts, that formed purely boron nanostructures. The pure boron nanostructure growth is limited to available boron feedstock and in these experiments, it is limited since the h-BN is itself very stable at high temperatures.

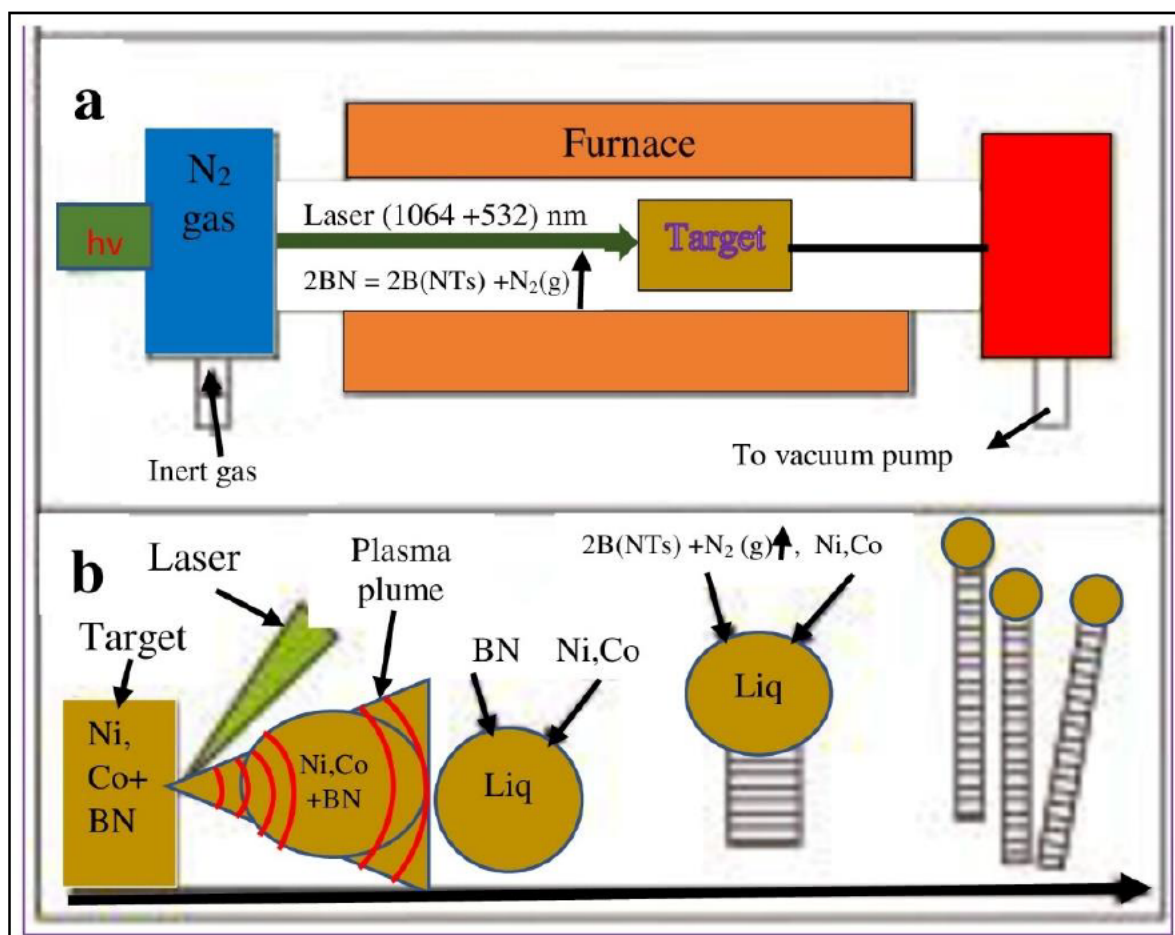


Figure 4.8: Schematic diagram of the (a) Boron nanomaterials growth apparatus. The output from a pulsed laser is focused onto a BN/NiCo target located at centre within a quartz tube, the reaction temperature is controlled by a tube furnace, (b) VLS mechanism process for the growth of boron nanomaterials grown on the surface of the catalyst

A laser of high repetition rate, with the increase in the availability of boron vapour, would be more favourable to enhance the growth of pure boron nanotubes and other related boron nanomaterials.

Finally, we have shown that boron nanomaterials in the form of nanotubes, nanowires, nanorods, and bamboo-like nanotubes can be synthesized by a dual-pulsed laser ablation technique as it was observed in HRTEM images. As-produced boron nanotubes appear to have diameters as small as 0.4 nm and few hundreds of nm in length. Also, sorts of boron nanomaterials were observed. The characterization on the nanomaterials through HRTEM - EDS spectrum using the supernatant liquid sample confirmed that boron is the major element in boron nanotubes and other nanomaterials, while XRD and SEM-EDS revealed the structural nature of as-prepared boron nanomaterials powder to be that of boron nitride. Raman spectroscopy confirmed that the material is indeed tubular in nature, with some peaks below 500 cm^{-1} and which is attributed to tubular nanotubes structures. The peaks 527, 529, 788, 791, 793, 878, 879, 965, 966 and 968 cm^{-1} showed that boron nanotubes and three other nanomaterials formed from α - boron sheets structures. Most especially sample BN 400P 200F 1100T, the most stable boron nanotubes in terms of stability, which was also identified by XRD spectra results. The spectra obtained in the Raman measurement warrants further theoretical and experimental work.

5. Single-walled boron nanotubes (SWBNTs) synthesized using a boron target

5.1 Characterization of SWBNTs by SEM

The scanning electron microscopy image of a sample prepared from laser ablation of a boron target mixed with 1% Co, 1% Ni and 0.5% B₂O₃ is shown in Figure 5.1(a). The flow of argon (Ar) gas was monitored at constant flow rates and pressures while the furnace temperature was set at 1100 °C. The synthesized single-walled boron nanotubes materials were scraped off as thin films coated on the inside walls at the end of the outer quartz tube. The SEM studies on these samples reveal a very high yield of SWBNTs synthesized under argon gas at a pressure of 400 Torr and at the flow rates of 200 sccm. The high yield is probably due to the fact that the argon pressure at 400 Torr and the flow rate of 200 sccm restrict the expansion of the vapor plume thereby reducing the rapid decrease in a temperature of the plasma plume due to adiabatic expansion. This result was in good agreement with that reported by Smalley *et al*, [270]. At 400 Torr irrespective of the flow rates, the SEM image in Figure 5.1(a) shows an excess of single-walled boron nanotubes and no amorphous boron. This is probably due to the fact that a decrease in pressure results in low collision probabilities of the evaporated species with the ambient gas molecules and therefore leads to the decrease in the cooling rates. It was also observed that, at a pressure of 400 Torr, the ablated material traveled backward up along the larger quartz tube. This means that a pressure and flow of the argon gas was sufficient to confine the constituents of the plasma plume that is, the momentum of the plume was lower than that of argon gas. In this instance, the catalysis action and the condensing of the boron plasma plume into single-walled nanotubes are increased. At 400 Torr the Raman spectra in Figure 5.5 revealed a very high yield of SWBNTs. The single-walled boron nanotubes appeared with diameters in nanometers and lengths in microns. In the SEM image, it was noticed that some catalysts are mixed in the sample which was revealed through the energy dispersive X-ray spectroscopy (EDS) in Figure 5.1(b). The EDS, in table 5.1(a) shows the percentage of each elemental component present in the as-prepared SWBNTs. In Figure 5.1(b) the strong peak of boron appeared at 200 eV. It was observed that only the smallest amount of content of

oxygen (O_2) which is 1.90% at 600 eV, can be found in the highly magnified EDS spectrum, which might have resulted from the boron oxide used as a binder.

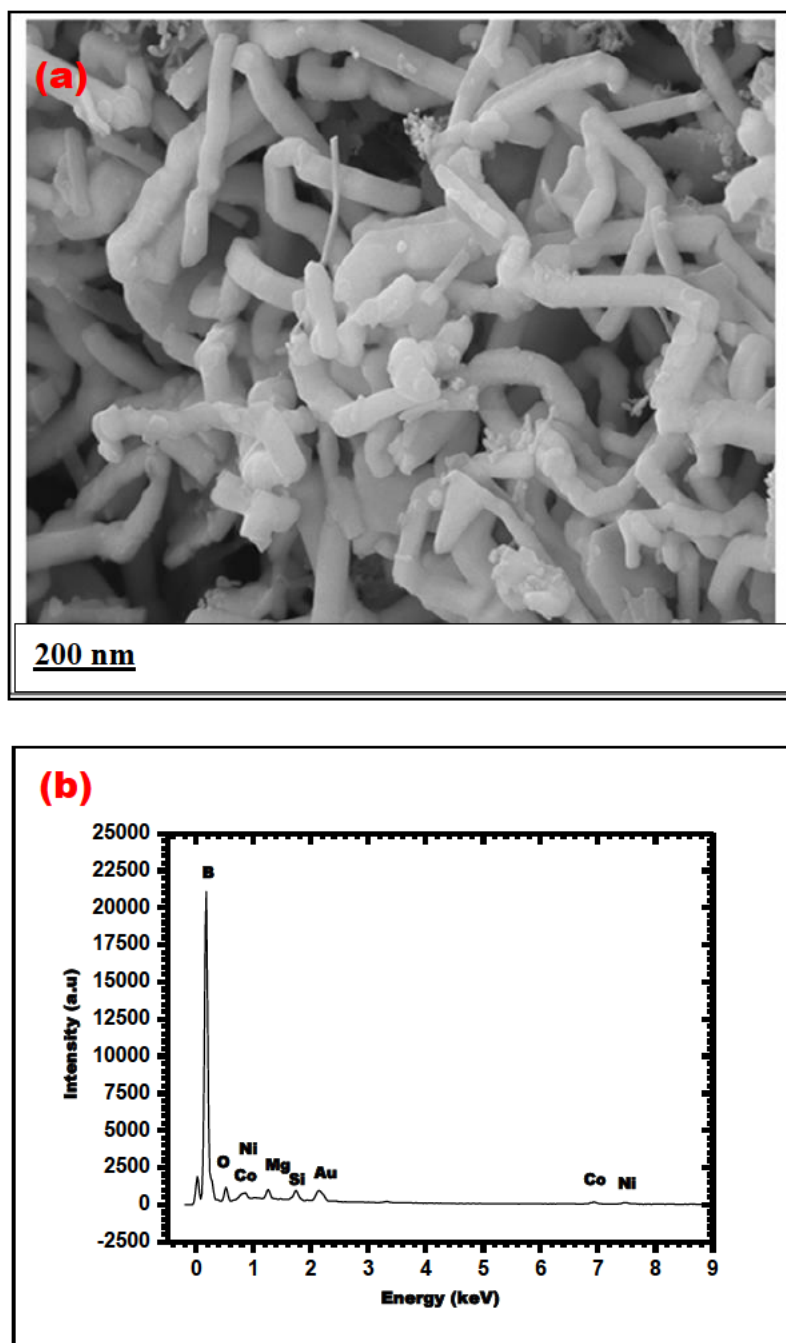


Figure 5.1: (a) SEM image shows the densely – packed of SWBNTs with lengths in micrometers and diameters in the range of nanometers. (b) EDX spectrum analyses results that revealed the highest peak of boron

The smallest peak that is not clearly visible at 1200 eV in the EDS, may be associated with the silicon peak which might come from the attachment of the quartz tube while scraping as – prepared SWBNTs from the quartz tube.

Table 5.1: Indicated EDX from the SEM spectrum with the percentage of each elemental composition that presents in the as-prepared sample.

SWBNTs	Wt.%	Wt.% Sigma
B	96.68	0.14
O	1.90	0.13
Mg	0.21	0.02
Si	0.06	0.01
Co	0.64	0.04
Ni	0.52	0.04
Total	100.00	

Very small amounts of Ni and Co were observed which is about 0.50%, at 800 eV, as catalysts used in the boron target. The peak at 2200 eV can be associated with the peak of gold, resulting from the gold used to coat the as – prepared SWBNTs sample on the carbon tape while preparing for SEM characterization. In addition, the EDS analysis revealed that the total boron content in the single-walled boron nanotubes is over 96%, which confirmed the purities of as – prepared SWBNTs.

5.2 Characterization of SWBNTs by HRTEM

To investigate the detailed crystalline structures of the single-walled boron nanotubes, a high-resolution transmission electron microscopy was employed. On an HRTEM grid 0.003 mg/ml of the supernatant suspension was put on a copper mesh coated with an amorphous holey carbon film. The ethanol was evaporated prior to the time of transmission electron microscopy characterization. In Figure 5.2 (a), which showed the HRTEM image that revealed the single-walled boron nanotube.

It was clearly noticed in Figure 5.2 (a) that the boron nanotubes synthesized are a mixture of single-walled boron nanotubes and the metallic catalyst nitrates, which are found around the region of single-walled boron nanotubes as shown in Figure 5.2 (a), with yellow arrows. The single-walled boron nanotubes have the diameters of about 1.5 nm and the length of several micrometers. It was observed that all the other boron nanostructures found in the HRTEM images are all boron nanotubes of different diameters and lengths as shown in Figure 5.2 (b).

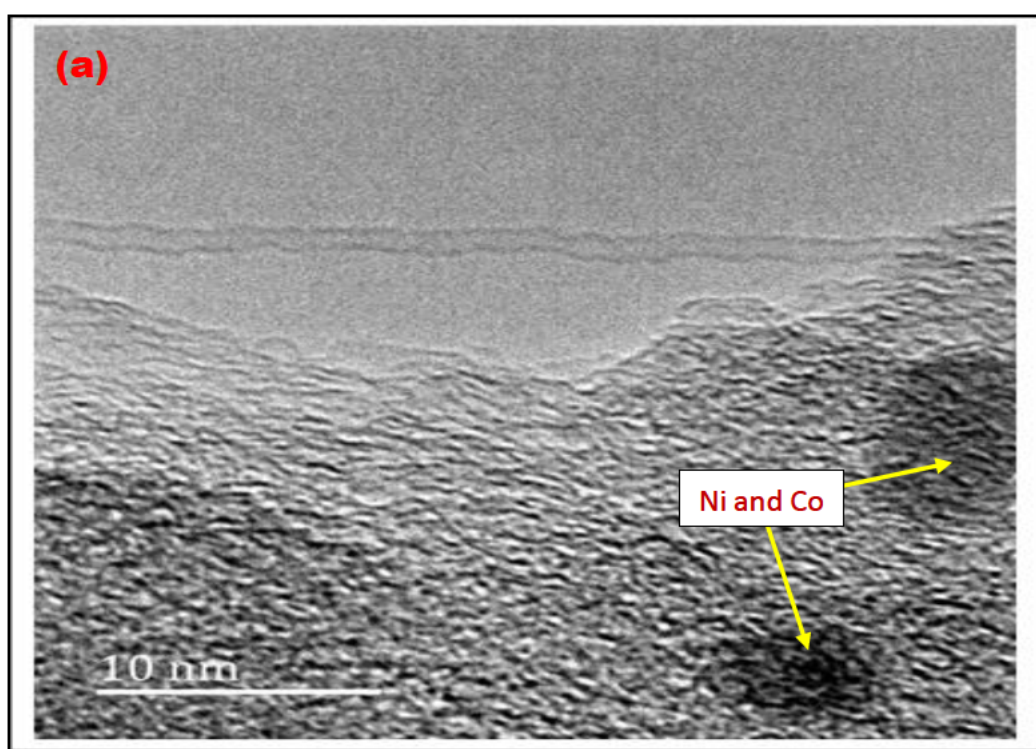


Figure 5.2: (a) The HRTEM image shown the SWBNTs of 1.5 nm in diameter and length in micrometers. Also, nickel and cobalt as catalysts found in the SWBNTs synthesized with DPLA technique were indicated by yellow arrows.

Most of the single-walled boron nanotubes have open ends and their hollow structures are clearly noticed from the HRTEM images. The morphology of the single-walled boron nanotubes observed varies which might be due to the different geometrical configurations of the boron tubular nanostructures according to the theoretical predictions [131, 166, 175, 188]. Other layered boron nanotubes structures found has an outer diameter of about 2.0 nm.

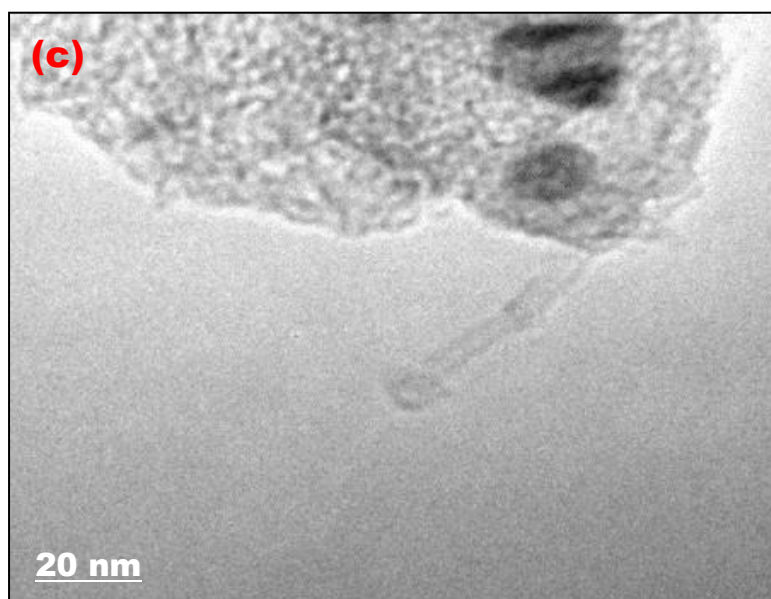
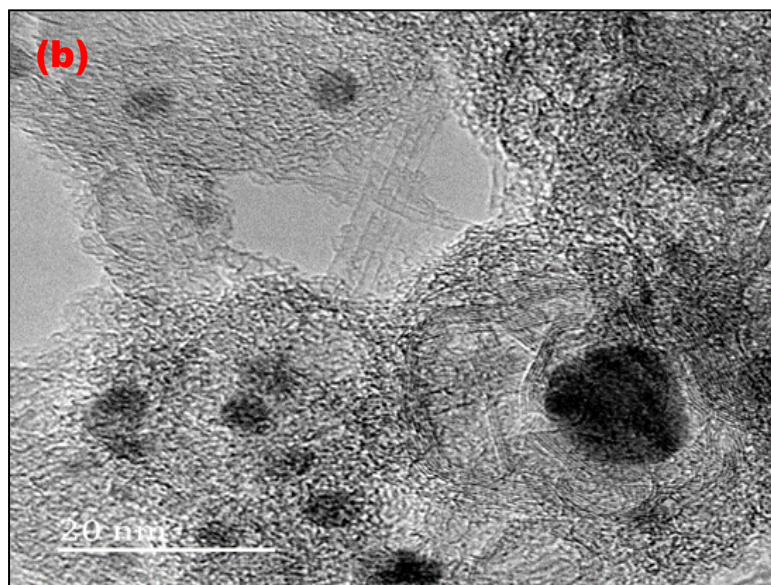


Figure 5.2: (b) The HRTEM image of the single-walled boron nanotubes of different diameters and lengths, which mixed with catalysts. (c) The HRTEM image of an SWBNT that revealed the open ends of the tube.

The open end of boron nanotubes also exhibits a polygonal morphology, as revealed in Figure 5.2 (c). Measurement of lattice fringes shown in Figure 5.2 (d) with the interlayers spacing of 0.38 nm that revealed a sharp spot pattern, which suggests that these nanotubes have good single crystalline structures, based on the lattice fringes and selected area electron diffraction (SAED) in Figure 5.2 (e).

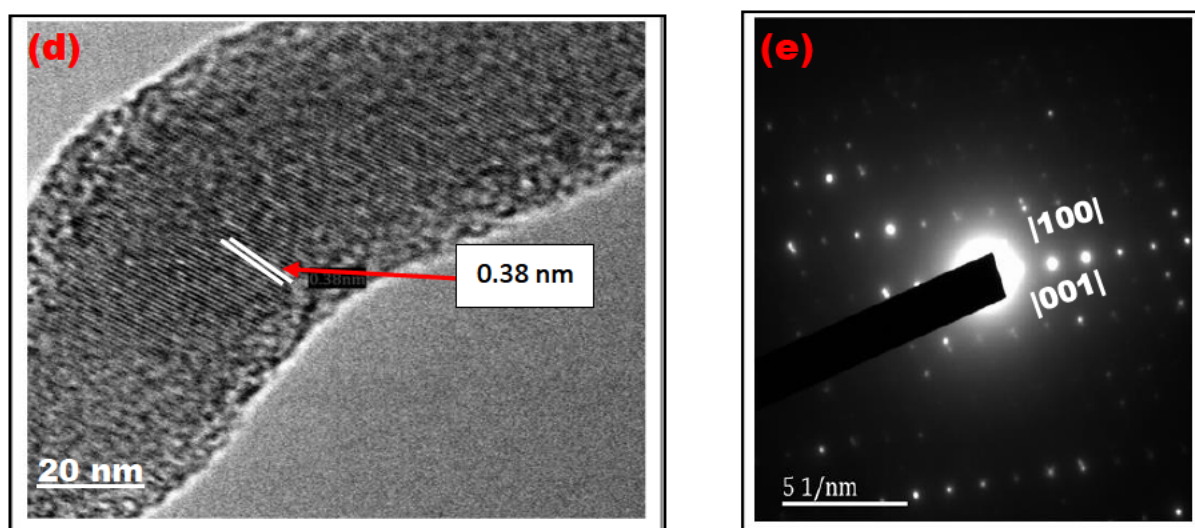


Figure 5.2: (d) Shows the lattice fringes observed with the interlayers spacing of 0.38 nm (e) Shows SAED measurement, that reveals a sharp spot pattern, which suggests that the boron nanotubes have good single crystalline structures.

We may conclude that the single-walled boron nanotubes are perfectly single – crystalline with α -boron rhombohedral structures as revealed in XRD and Raman spectrum. These single-walled boron nanotubes are grown along the [100] direction which agrees with the data of the Joint Committee for the Powder Diffraction Standards (JCPDS) card No. 01-078-1571. The verification of the elemental compositions of the single-walled boron nanotubes was carried out by utilizing energy dispersive x-ray spectroscopy (EDS) results. Figure 5.2 (f), shows the spectrum of the energy dispersive x-ray spectroscopy obtained in HRTEM. It was observed that the strongest boron peak appeared at 200 eV. It was noticed that only a few amounts of oxygen at about 0.02% at the peak of 500eV present, which is likely to come from the boron oxide used as a binder.

The smallest peak at 1200 eV was attributed to the peak of zinc, occurred from the target holder. In addition, very small contents of carbon and copper might be found in the high - resolution spectrum caused by the copper of high-resolution transmission electron microscopy grid covered with carbon film.

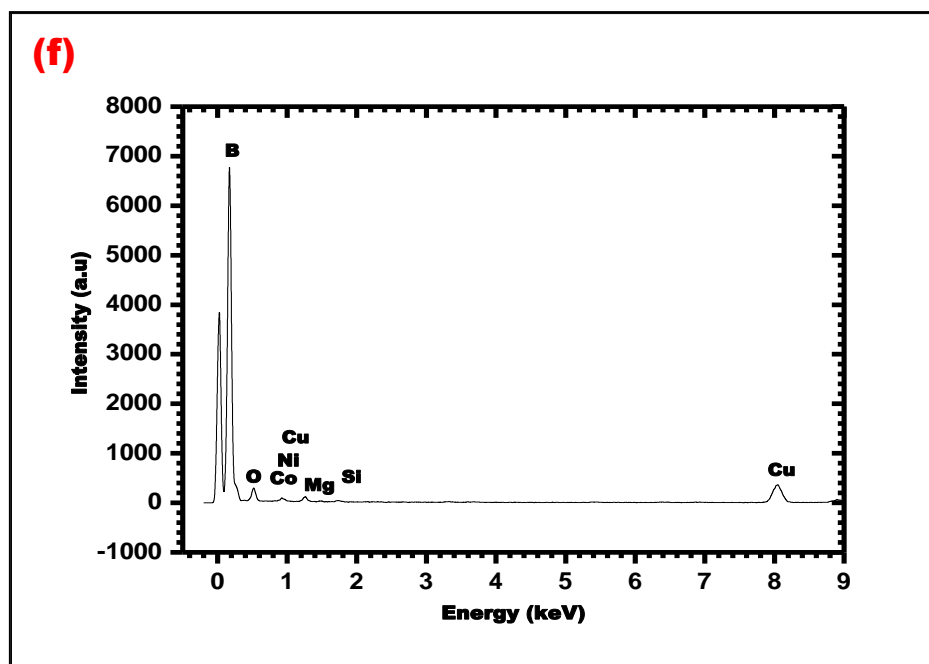


Figure 5.2: (f) The EDX spectrum of HRTEM analyses results that revealed the highest peak of boron.

Table 5.2: EDS of the HRTEM spectrum indicating the percentage of each elemental composition that presents in the SWBNTs.

Element	Peak Area	Area Sigma	k factor	Abs Corr.	Weight%	Weight% Sigma	Atomic%
B	40790	409	4.212	1.000	95.55	0.10	98.54
O	1859	98	1.069	1.000	1.11	0.06	0.77
Mg	775	66	0.608	1.000	0.26	0.02	0.12
Si	246	51	0.571	1.000	0.08	0.02	0.03
K	150	44	0.554	1.000	0.05	0.01	0.01
Cr	143	39	0.640	1.000	0.05	0.01	0.01
Ni	235	125	0.725	1.000	0.01	0.01	0.01
Co	103	38	0.721	1.000	0.04	0.02	0.01
Cu	6469	136	0.796	1.000	2.86	0.06	0.50
Totals					100.00		

Nickel and cobalt occurred from catalysts were used in the synthesis. Energy dispersive x-ray spectroscopy measurements analyses on single-walled boron nanotubes show that the content of boron in the single-walled boron nanotubes is above 98 % which verified that as-synthesized single-walled boron nanotubes are pure with no impurities.

5.3 Image analysis on the HRTEM micrograph of SWBNTs

In this chapter, the image analysis was performed on the HRTEM and images of single-walled boron nanotubes (SWBNTs) obtained. The HRTEM micrograph of the SWBNTs were obtained after the characterization was shown in Figure 5.3 (a). The HRTEM image used for the analysis was taken randomly. This was analyzed to detect the diameters and density of the SWBNTs. The HRTEM image was analyzed to determine the distribution of diameters along the SWBNT and also, to detect the mean, median, minimum, maximum, variance, and standard deviation of SWBNT. This was carried out by finding the diameters of SWBNT present in the HRTEM micrograph at a different point to obtain the real diameter. The SWBNT was found to have different diameters at a different point. The reason is that the SWBNT was very sensitive to the electron beam and this actually affected the uniformity of the diameter. The results obtained were analyzed to deduce the distribution of diameters of the SWBNTs obtained from HRTEM micrograph. The results of the graph distribution obtained HRTEM was shown in Figure 5.3(b).

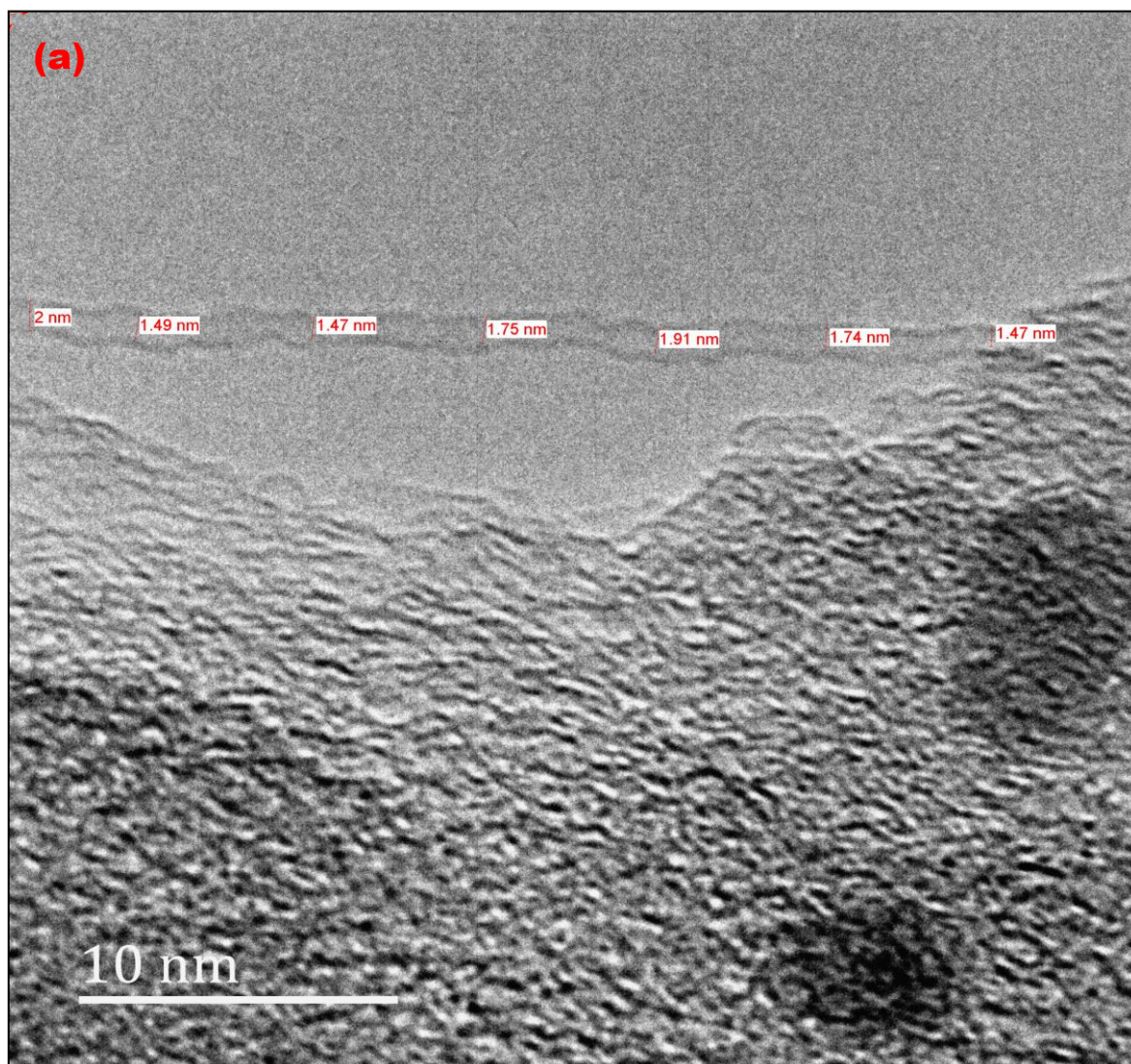


Figure 5.3 (a): HRTEM of SWBNTs diameters measured.

The histogram graphs obtained in Figure 5.3 (b) revealed the ranges in their diameters. Also, the range in the boron nanotubes diameters obtained from micrograph is shown in Table 5.3(a). The distribution of boron nanotubes diameters shown in Figure 5.3 (b) was fitted to the lognormal distribution. The results obtained were stated in Table 5.3a, for HRTEM. The density of SWBNTs at a specific area was determined. The images were analyzed to obtain the number of nanotubes per nm^2 . This was carried out by counting the number of nanotubes observed in a known area on the micrographs.

The density of nanotubes obtained from the HRTEM image is shown in Table 5.3(b). The percentage error was calculated by using the expression in equation 5.1.

$$\% \text{ Error} = \frac{\text{Exact value} - \text{Approximate value}}{\text{Exact value}} \times 100 \quad (5.1)$$

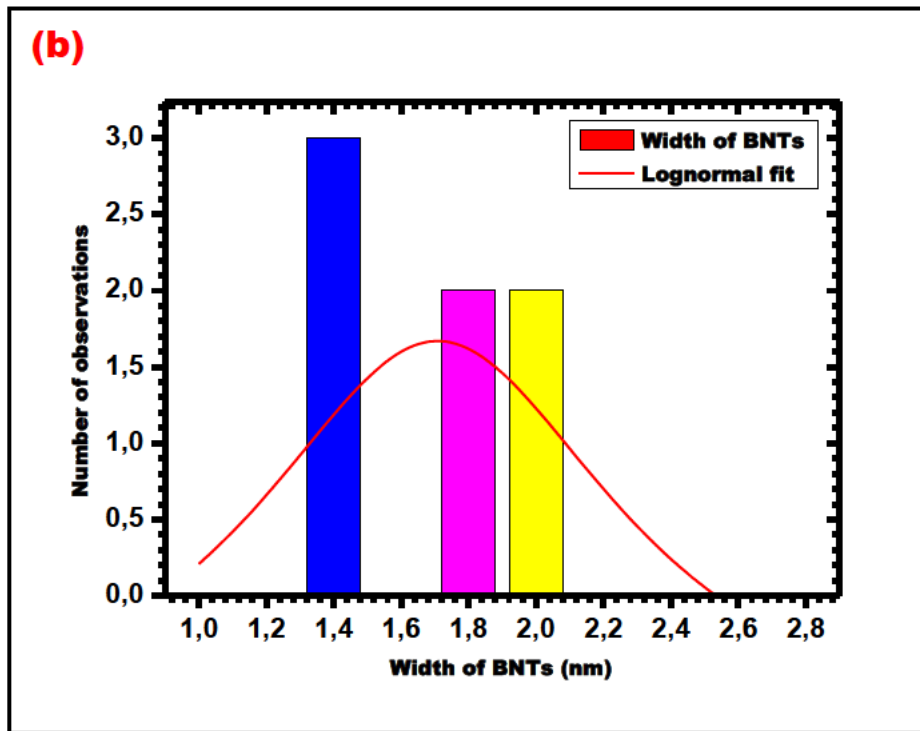


Figure 5.3b: Distribution of SWBNTs diameters measured in the HRTEM image and fitted to the log-normal distribution

Table 5.3a: SWBNTs diameters measured in HRTEM image and statistical parameters for lognormal distribution fitting

Sample	Mean (nm)	Median (nm)	Minimum (nm)	Maximum (nm)	Variance (nm ²)	SD (nm)
BNT	1.691	1.743	1.475	2.100	0.050	0.224

Table 5.3b: *The Density of SWBNTs synthesized at P400 F200 T1100 in the HRTEM image*

Sample	No of BNTs per nm ²	% Error
BNTs	0.330	0.030

The distributions in Figure 5.3 (a) shows that the average diameters of SWBNTs obtained from the HRTEM through the image analyses and revealed the minimum and maximum diameters. The difference in the diameters of SWBNTs at a different position is due to the sensitivity of the SWBNTs to the electron beams. In addition, we are able to determine the diameters of SWBNTs through the image analysis. We can utilize the results of image analysis obtained from HRTEM micrograph to determine the minimum and maximum range in diameters and lengths of any SWBNTs.

5.5 Raman spectroscopy

Figure 5.5 shows a typical Raman spectrum of the SWBNTs. SWBNTs sample was characterized using Raman spectroscopy instrument, a Jobin Yvon labram HR800, at an excitation wavelength of 514 nm laser. To carry out the analyses on SWBNTs, as – prepared SWBNTs sample was placed on a quartz substrate. We took the advantages of the laser size of microns while focusing the laser beam on the SWBNTs materials. The analysis of the Raman data collected is subjected to corrections, by subtracting the quartz substrate background signal data from the additional data of as – prepared SWBNTs sample and a quartz substrate. The result later yields the data for as – prepared SWBNTs sample only. This data was used to plot the Raman spectrum in Figure 5.5 above. The SWBNTs spectrum is characterized by peaks centered at A_{1g} and E_g modes, the two modes are present in all boron. The G peak is corresponds to planar vibrations of boron atoms in boron like materials. The G peak is associated with the E_g mode (stretching vibrations) in the basal plane of boron, therefore the peaks at 493 and 621 cm⁻¹ are corresponding to the G peak in SWBNTs.

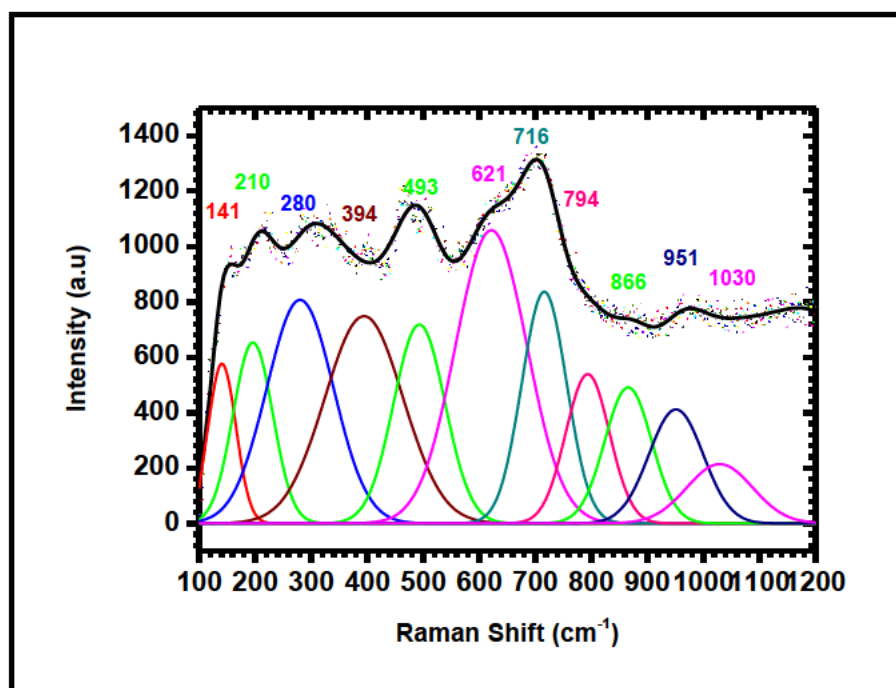


Figure 5.5: Revealed Raman spectrum of SWBNTs excited at the 514 nm laser on as – prepared sample synthesized at the temperature of 1100 °C

At wavenumbers below 500 cm^{-1} , the presence of tubular structures has been verified through the presence of spectral features in the Raman breathing mode below this frequency region [120]. Raman spectroscopy results also confirmed the tubular structures evidence from HRTEM characterization. Another peak was detected at 210 cm^{-1} this peak might be assigned as a radial breathing mode (RBM) typically for tubular structures [120]. The RBM corresponds to the radial expansion contract of the boron nanotube, its frequency V_{RBM} depends on the nanotube diameter. Typical RBM range is $100 - 350\text{ cm}^{-1}$. In between 300 and 500 cm^{-1} frequencies, the spectrum features may be associated with tubular structures as well. The occurring peaks from 300 to 600 cm^{-1} , especially peaks at 394 and 493 cm^{-1} may be attributed to boron nanotubes of different chirality or diameters [120, 271]. Also, peaks between 400 to 600 cm^{-1} , most especially peak at 493 cm^{-1} , might be related to boron nanotubes of smaller diameters or another boron nanostructures [120], such as sheets, rods, ribbons, and wires, in CNTs, the same Raman spectra peaks were confirmed [272]. It was observed that the peak of 493 cm^{-1} that is properly shown is associated with one of the peaks resulting from α – boron clusters at 493 cm^{-1} [45, 273].

The peaks at 621 and 716 cm^{-1} results from the mixture of boron nanostructures such as boron nanowires (BNWs) with α -boron structures [42]. SWBNTs of approximately 1.5 nm in diameter were synthesized and analyzed in the thesis. From ab-initio calculations, the electronic properties of boron nanotubes have been predicted, but it has never been reportedly synthesized. The types of SWBNTs synthesized are very sensitive to the beams because of that, the possibility to determine their helicity, accurate diameters and actual length was found to be extremely difficult. SWBNTs observed were attributed to the catalysts supports which confirmed that the growth of SWBNTs is supported by catalysts, most especially cobalt and nickel. According to the theoretical calculations, the estimation of an electronic band gap of SWBNTs was found to be in between 1.0 eV to 0.8 eV [179]. Through the prediction of theoretical calculations, some intensity peaks, in the Raman spectra of α - boron were predicted [45, 179].

Table 5.5: Raman active modes in BNTs synthesized by the DPLA method at the temperature of 1100 °C compared with α - boron (in cm^{-1}) predicted and synthesized through theoretical calculations and experimental values respectively.

α - boron		α - boron			Boron nanotubes	
Theory		Experiment			Experiment Results	Raman active
Vast <i>et al</i> [43]	Shirai <i>et al</i> [49, 274]	Vast <i>et al</i> [43]	Ekimov <i>et al</i> [273]	Richter <i>et al</i> [42]		
Frequency	Frequency	Frequency	Frequency	Frequency	Frequency	Mode
-	-	-	-		210	-
-	-	-	272		280	-
-	-	-	-		394	-
529	497	525	493	524	493	E_g
608	572	586	645	587	621	E_g
708	710	692	749	710	716	A_{1g}
815	759	793	749	796	794	A_{1g}
947	965	925	917	931	951	A_{1g}

These peaks were associated with the transverse optical A_{1g} mode and Raman active optical E_g mode of α – boron [36]. This α – boron is the only one that has the simplest crystal structures among the icosahedral boron-rich solid. According to group theory, ten Raman active modes were predicted [43], that is $4A_{1g}$ singlets and $6E_g$ doublets for α – boron. These A_{1g} and E_g vibrations corresponded to Raman active modes in α - boron in the region from 500 to 1200 cm^{-1} mode frequencies. Theoretical calculations predicted twelve Raman active peaks from Raman spectra of α – boron. Richter and Ploog were the first persons to report on the experimental Raman spectrum of α – boron which showed twelve Raman peaks [42] which was later confirmed [44, 179]. The Raman spectrum measured for Raman shifts below 1000 cm^{-1} , confirmed the Raman active peaks in the spectral range for α – boron nanotubes. In Figure 5.5, Raman line at 493 cm^{-1} corresponding to the peaks at 497, 493, 529, 525 and 524 cm^{-1} mode [45, 179, 273] as stated in Table 5.5, for both theoretical and experimental results which corresponds to the rotation of the rigid B_{12} icosahedra of α – boron. According to theoretical calculations of Vast *et al*, and Shirai *et al*, groups, in addition to experimental results of Vast *et al*, Ekimov *et al*, and Richter *et al*, the Raman active peaks at 708, 815, 947, and 710, 759, 965, and 692, 793, 925 cm^{-1} and 749, 917 and 710, 796, 931 respectively were described to A_{1g} mode (see the Table 5.5). These peaks were found close to the experimental peaks at 716, 794 and 951 cm^{-1} which were attributed to the A_{1g} mode in α – boron [42, 43, 273, 274], this refers to as symmetric with respect to rotation about the principal C_n axis of icosahedra boron-rich. The theoretically calculated values of A_{1g} modes by Vast *et al* and Sharai *et al*, as well as experimental results obtained by Vast *et al*, Ekimov *et al* and Richter *et al* [43, 274], are related to the results obtained as A_{1g} modes in α –boron. There are no discrepancies on the A_{1g} modes observed in our experimental results and theoretical calculations [43]. The calculated values by Vast *et al* and Sharai *et al* in Raman active peaks of E_g modes were given at 529, 608, and 497, 572 cm^{-1} modes respectively. Vast *et al*, Ekimov *et al* and Richter *et al*, experimental results of E_g at 525, 586, and 493, 645, and 524, 587 cm^{-1} was found near our experimental values obtained at 493 and 621 cm^{-1} , as shown in Table 5.5 [43, 274]. There is less discrepancies in the E_g values observed from both theoretical calculations and our experimental results, especially

when comparing our experimental results to the experimental values obtained by Vast *et al* [42, 43, 273]. Raman peak at 1030 cm^{-1} corresponds to luminescence due to electronics transitions between the gap states of α – boron [44, 45]. In addition, through all the comprising from both theoretical and experimental results. It was showed that the SWBNTs synthesized is α - BNTs which were also confirmed by the XRD results.

5.6 X-Ray Diffraction (XRD)

The crystallinity of SWBNTs synthesized was examined through XRD. Figure 5.6 shows the XRD spectrum of SWBNTs, in which diffraction peaks of α – boron was found, indicating that the SWBNTs synthesized are α -BNTs, that has been confirmed through the results obtained from Raman spectrum in Figure 5.5. In Figure 5.6, the impurities phases like silicon and carbon were discovered. A simple explanation for this is that the silicon peak (111) at 28.4° might have resulted from a quartz tube used [275], while the carbon peak (002) at 26.9° formed from the graphite utilized to support the target holder [276].

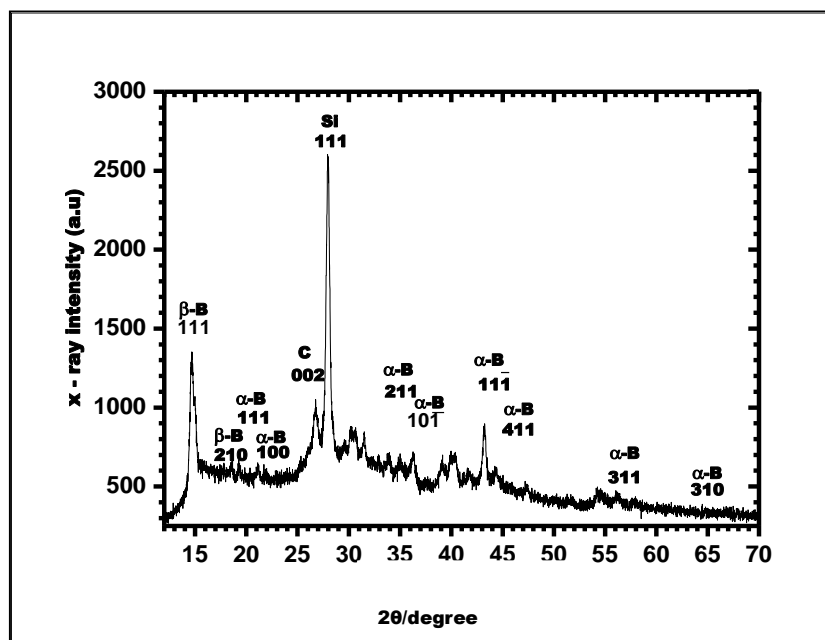


Figure 5.6: XRD spectra of BNTs synthesized by DPLA technique, revealed the peak around 22.0° at 100 (h k l) which indicate that the growth of BNTs is along 100 directions

Very small significant β – boron peaks (111) and (210) at 11.1° and 19.7° respectively [59] appeared due to some β – boron that was not totally transformed to α – boron nanotubes during the synthesis process because β – boron transforms to α – boron at a higher temperature. The XRD pattern has a peak at approximately 22.0° which correspond to the (100) plane of α – boron as shown in Table 5.6. The XRD pattern indicated that the single-walled boron nanotubes synthesized are preferentially grown in the c – axis direction of α - boron.

Table 5.6: X-ray diffraction peaks of BNTs synthesized by the dual pulsed laser ablation technique at the temperature of 1100°C

Element	h	k	l	d (Å)	2 θ (degree)
β -B	1	1	1	7.938	11.137
β -B	2	1	0	4.501	19.706
C	0	0	2	4.268	26.917
Si	1	1	1	3.453	28.441
α -B	1	1	1	4.186	21.192
α -B	1	0	0	4.040	21.981
α -B	2	1	1	2.529	35.459
α -B	1	0	$\bar{1}$	2.464	36.442
α -B	1	1	$\bar{1}$	2.103	42.965
α -B	4	1	1	1.957	46.357
α -B	3	1	1	1.626	56.541
α -B	3	1	0	1.435	64.947

It can be indexed to the phase of α – boron Intensified Charge Coupled Devices (ICCD) PDF detector, database file no : 01- 078 – 1571, with lattice constant $a = 5.057 \pm 0.003 \text{ \AA}$, $\alpha = 58.06^\circ \pm 0.05$, $Z = 12$ and with the space group of $R\bar{3}m$ [38, 277].

5.7 Ultra Violet-Visible (UV – VIS) Spectroscopy

The optical properties and crystal structure of single-walled boron nanotubes have been theoretically reported by many authors [278, 279]. The UV characterization of single-walled boron nanotubes was done on a Perkin Emer Precisely, Lambda 35 UV-VIS Spectrometer.

Two drops of 0.02ml of a supernatant sample obtained after density gradient ultracentrifugation (DGU), was mixed in 5ml ethanol and sonicated for thirty seconds, using probe sonicator. The acquired data results through the characterization were used to plot the graph in Figure 5.7. The UV-VIS spectrum indicating the optical absorption spectrum of single-walled boron nanotubes at room temperature with a strong exciton absorption peak at 272 nm.

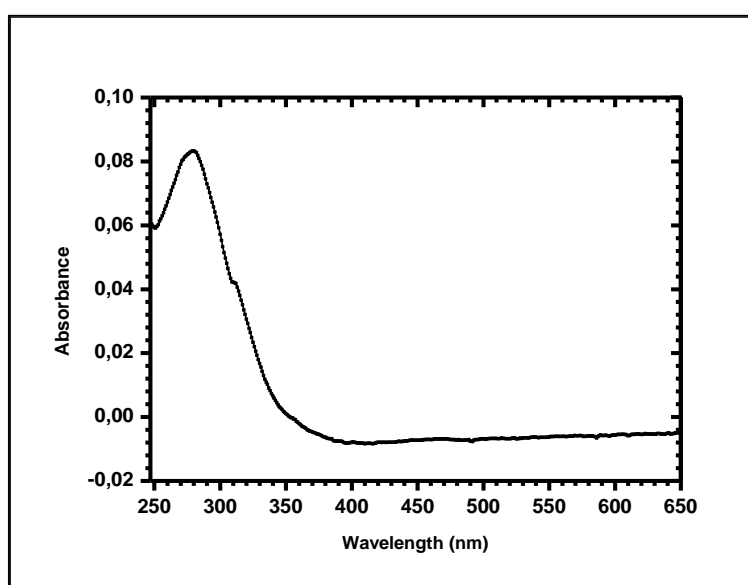
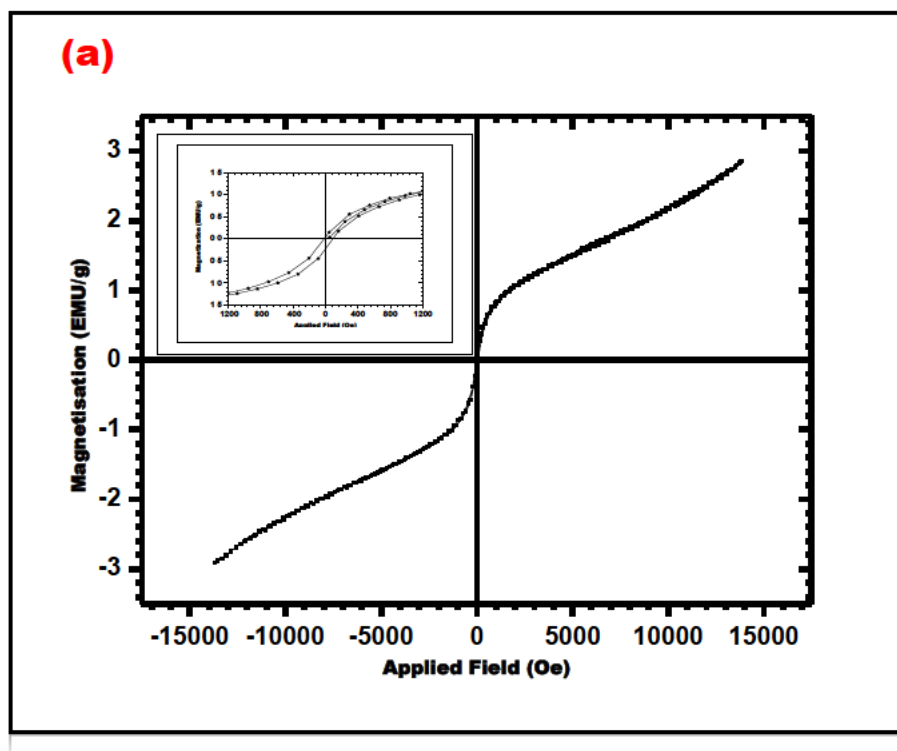


Figure 5.7: UV – VIS spectrum of SWBNTs synthesized by the DPLA method at a temperature of 1100 °C with a strong absorption peak at 272 nm.

The values reported by Yang *et al* recently is closely matched with the peak observed at 272 nm [278]. The peak observed at 310 nm, corresponds to the peak threshold which later found its maximum peak at 272 nm. SWBNTs are transparent from 250 to 650 nm within the limitation of the instrument, whose working range is 250 to 650 nm. The absorption spectrum is relatively featureless and the broad and overall constant low absorbance from 250 to 650 nm, including the nearly no absorbance from 400 to 650 nm, is consistent with the reported values for bulk boron [225], thus demonstrating that it is transparent from ultraviolet to the visible region.

5.8 Vibrating Sample Magnetometer (VSM)

VSM instrument was used for the characterization of magnetic properties of single-walled boron nanotubes, pure bulk boron, and DGU sediment. SWBNTs were also centrifuged at 20 °C for three hours (below the room temperature) with the intention of separating the supernatant from sediment. Each sample material was loaded in a sample holder. The holder was carefully inserted into the instrument and characterization was performed at room temperature for each sample. Magnetic data was collated for the as-prepared SWBNTs, pure bulk boron and DGU sediment samples. Data acquired from each material was used to plot the graphs shown in Figure 5.8 (a to c). SWBNTs that yielded a saturation magnetization (M_s) of 3.499 emu/g and coercivity (H_c) of 272 Oe was sought. SWBNTs, with these magnetic properties, would be ideal for application in high-density storage [280]. DGU sediment stood out in terms of magnetic data after the ultracentrifugation process with saturation magnetization and coercivity values in the correct region of $M_s = 5.945$ emu/g and $H_c = 149$ Oe as shown in Table 5. It can be observed that the SWBNTs reveal typical ferromagnetic behaviour. The ferromagnetic is clearly shown (inset graph) by the coercivity (H_c), saturation magnetization (M_s), remanent magnetization (M_r), and saturation field (H_s) values listed in Table 5.



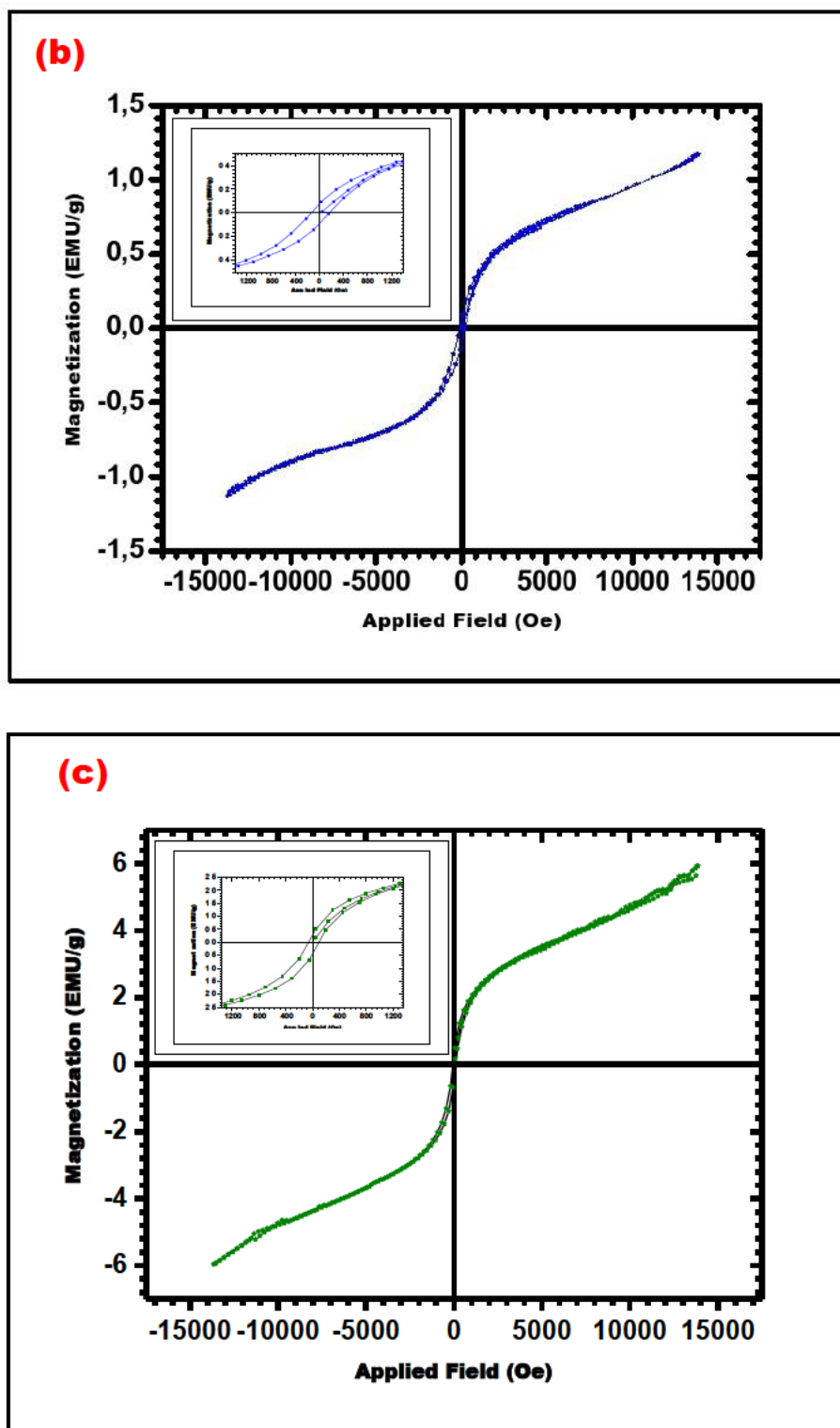


Figure 5.8: Magnetic measurements (a) Single walled boron nanotubes synthesized by the DPLA method at a temperature of 1100°C, (b) Bulk boron material, (c) Sediment from Density gradient ultracentrifugation material. The inset in each graph shown ferromagnetic properties of each material. Recorded at room temperature with the VSM instrument.

A higher saturation magnetization (M_s) is a key factor for information storage although real devices also require intense studies on magnetization interactions, local magnetization reversal characterization and other important issues [280, 281].

Table 5: Magnetization data of SWBNTs, pure bulk boron and along with DGU sediment at room temperature.

Parameter	Room Temperature		
	SWBNTs	Bulk boron	DGU sediment
Coercivity, H_c (Oe)	272	242	149
Saturation Magnetization, M_s (emu/g)	3.499	1.148	5.945
Remanent Magnetization, M_r (emu/g)	0.073	0.036	0.357
Saturated Field, H_s (emu/g)	8000	8000	8000
Squareness	0.021	0.031	0.060

The first row in Table 5 shows the room-temperature coercivity (H_c) of DGU sediment is 149 Oe which is about half of the value of the corresponding pure bulk boron material (242 Oe) and lower than the value of SWBNTs (272 Oe). Nanostructures usually have coercivity (H_c) higher than that of the bulk materials [281, 282]. A logical explanation for this may be as follows: in the case of SWBNTs the small specific area and the perfection of the crystalline structure of SWBNTs at the surface may also lead to a significant increase in the SWBNTs coercivity [281, 283]. However, in the case of the DGU sediment, the catalysts atoms could be responsible for the formation of the coercivity dead layer, the high surface area enhances oxidation of the surface of the catalysts which may create a coercivity dead layer [280, 281]. The second row in Table 5 shows the average saturation magnetization (M_s) of the SWBNTs, pure bulk boron and the DGU sediment. As shown, the synthesized SWBNTs exhibit good saturation magnetization at room temperature, which is about 3 times the magnitude of the pure bulk boron material. The average ferromagnetic at room temperature is 3.499 emu/g while it is 1.148 emu/g for the pure bulk boron material.

The magnetic properties of the SWBNTs sample are only due to its pure metallic [280, 283]. Coercivity and hysteresis loops with remanence were observed in the room temperature magnetization curve (at origin) of the single-walled boron nanotubes which confirmed the ferromagnetic nature of single-walled boron nanotubes. The saturation magnetization (M_s) value was found to be 3 emu /g with squareness (0.021) M_r/M_s indicating an appreciable fraction of ferromagnetic of nanotubes [282]. The coercivity (H_c) of 272 Oe of SWBNTs at room temperature is higher than that of bulk boron materials of 1 emu / g with squareness 0.031 and coercivity 242 Oe. Higher M_s value of single-walled boron nanotubes ascribed to size, surface and magnetic on the surface of the nanotubes [280, 282]. For the saturation field (H_s) of the SWBNTs, pure bulk boron and DGU sediment, there is an unnoticeable effect of temperature as shown in Table 5. Saturation field value remained constant at room temperature. The three samples maintain a constant value without any change (8000 Oe). One can say that for the synthesized SWBNTs, pure bulk boron material and DGU sediment, the thermal energy has no effect on the saturation field [281].

5.9 Vapour Liquid Solid (VLS) mechanism

The VLS growth mechanism is used to interpret the growth of SWBNTs with help of catalyst metal nitrates as shown in Figure 5.9 (a, b). An extended VLS model was proposed that explained the SWBNTs growth on the surfaces of the catalyst, which was suitable for experimental results. The VLS has been proposed for nucleation of nanostructures and nanomaterials [284] in which the catalytic metal nitrate serves as a base of growth and acts as the energetically favorable condition for the synthesis of SWBNTs. Catalyst metal nitrates and other parameters play an important role in the formation of SWBNTs. The VLS model process is the most probable growth mechanism. There are variations in the diameters of SWBNTs grown, which is affected by the synthesis temperature [285]. The spot area where the laser beam hits the target at a very high temperature, led to an increase in the surface temperature of the target [286].

The SWBNTs formed far and near the target surface suggesting that the growth of SWBNTs involves a process called VLS because part of SWBNTs formed very near to the target, while the rest was transported to the back of a quartz tube with the help of argon gas, since the growth of SWBNTs is governed by the VLS model. The laser energy is strong enough to ablate the boron target and decompose it. The vapour (plasma plume) formed from the boron target at a high temperature turns to a liquid and finally formed SWBNTs and deposited it in a lower temperature site by carrier gas where it was collected. Boron has a higher melting point of 2300 °C and was engraved by the higher temperature plume of laser ablation [148, 287-289]. The boron target will evaporate after it has been combined with the argon gas, then formed boron vapour in the form of plasma plume. When ablation proceeded further, more boron vapor is generated and grown as single-walled boron nanotubes. The synthesis of SWBNTs is briefly described as shown from diagram in Figure 5.9 (a, b). When the target is irradiated by the laser beam, some of the clusters of boron and metals will be ablated from the target and in the meantime, the temperature of the target will be increased due to acceptance of the energy from laser beam. The temperature must distribute according to the distance from the target the laser beam hit. Boron nanotubes synthesis is achieved by laser ablation of a B/NiCo target at temperatures of 1100 °C (Figure 5.9 a,b). Laser ablation of the B/NiCo target produces a vapour of plasma plume of B and NiCo that rapidly condenses into B-rich liquid NiCo nanoclusters, and when the nanoclusters become supersaturated in B, the coexisting pure B phase precipitates, grows and crystallizes as nanotubes. Ultimately, the growth terminates when the gas flow carries the nanotubes out of the hot zone of the furnace. From the schematic diagram and discussion above, it was clear that the growth of single-walled boron nanotubes proceeds from plasma plume via the VLS mechanism. The possibility of this VLS model cannot be ruled out since laser ablation will produce a pulse of extremely high temperature, which led to boron melting. In addition, we report here the first dual pulsed laser ablation technique of the synthesis of a single-walled boron nanotube structure at 1100 °C temperature using a boron target. Single-walled boron nanotubes diameter was observed to be in nanometers, with the usage of catalysts and the carrier argon gas. The elemental composition of SWBNTs was confirmed by EDS spectroscopy.

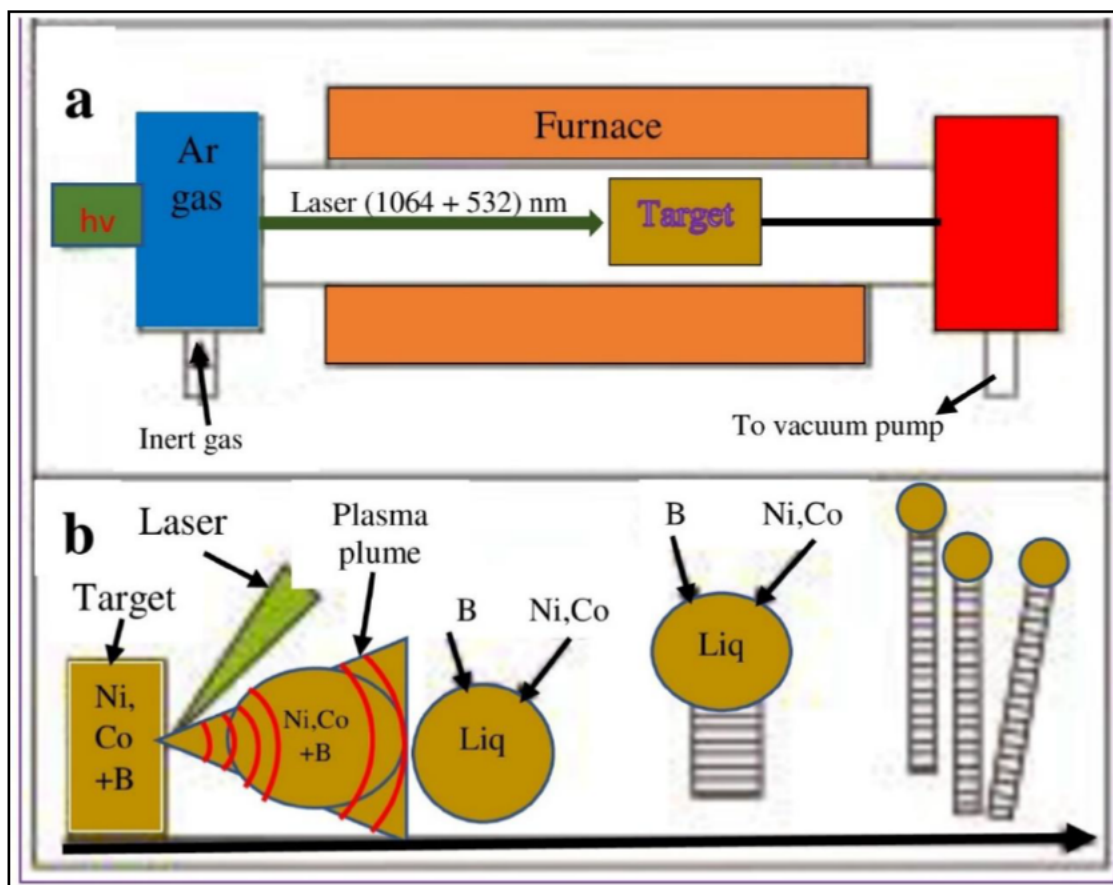


FIGURE 5.9. (a) Schematic diagram of the boron nanotubes growth apparatus. The output from a pulsed laser is focused onto a B/NiCo target located at centre within a quartz tube; the reaction temperature is controlled by a tube furnace. (b) Boron nanotubes growth process. Laser ablation of the B/NiCo target creates a dense plasma plume, hot vapor that condenses into nanoclusters as the B and NiCo species cool through collisions with the buffer gas. The furnace temperature is controlled to maintain the NiCo nanocluster in a liquid state. Boron nanotube growth begins after the liquid becomes supersaturated in B and continues as long as the NiCo nanoclusters remain in a liquid state and B reactant is available. Growth terminates when the boron nanotube passes out of the hot zone of the reactor.

While the structural conformation of SWBNTs was obtained through high-resolution transmission electron microscopy, SWBNTs of diameter range from 1.4 to 2.0 nm were observed. Bundles of SWBNTs of a diameter range, with some spherical structure nanotubes, were observed under the scanning electron microscopy. The XRD spectra revealed some characteristic peaks that are corresponds to α – boron and few impurity peaks. The Raman active mode of SWBNTs observed below 500 cm^{-1} indicates the tubular structures and characteristics of nanotubes. This was also confirmed by Ciuparu *et al*, in Raman active peaks of carbon nanotubes as well. The growth mechanism of the single-walled boron nanotubes may be attributed to plasma plume via VLS model. The reason is that boron nanotubes growth was found near in front of the target and transported by carrier gas to the rear end of the quartz tube where the growth is finally terminated. The type of single-walled boron nanotubes synthesized may give more possible ways of providing new applications for all these one-dimensional nanomaterials.

6. Density gradient ultracentrifugation (DGU) of SWBNTs

6.1 Introduction

SWBNTs, as one-dimensional structures, have a variety of physical, biological and chemical properties. SWBNTs have a wide range of applications due to these numerous desirable applications, such as biosensors, optics, and electronics. The electrical nature of some of these SWBNTs is widely spread and used in most of the applications. Various separation techniques have been used for the past few years to achieve the separation of some different kinds of nanomaterials into their various specific chirality and electronics type [290]. Of all these techniques, the density gradient ultracentrifugation techniques employed by Arnold *et al* for the separation of single-walled carbon nanotubes (SWCNTs) into diameter, length, chirality, and electronics type, is considered as one of the most promising and effective tools [291].

6.1.1 Theory of density gradient ultracentrifugation

One of the most widely used separation mechanism in nanomaterials, colloid science, nanoparticles, cellular and molecular biology is the ultracentrifugation technique (UCT) [292] due to gravity, objects denser than a liquid settled spontaneously. This took a very long period for very small particles, nanomaterials, and nanostructures, such as nanoparticles, nanotubes, nanorods, nanofiber, nanoribbon, nanosheets, and nanowires.

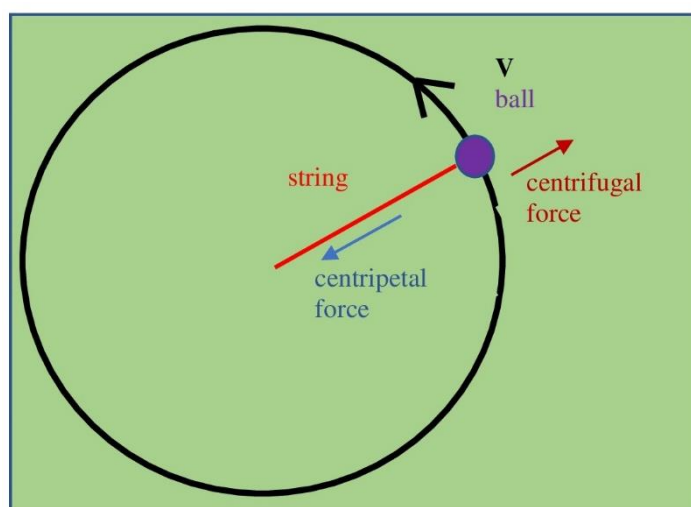


Figure 6.1: Centrifugation of SWBNTs in a centrifuge.

Where the gravitational energy is commensurate with thermal energy, the nanotubes will not be separated from the solvent. The nanoparticles were centrifuged in a horizontal rotor, the force diagrams are shown in Figure 6.1 and 6.2. We consider that the forces acting on a nanoparticle consist of centrifugal force, F_c , buoyant force F_b , and frictional force F_f , as follows.

$$F_c = \rho_{NT} V \omega^2 r \quad (6.1)$$

the second one is a buoyant force (F_b),

$$F_b = -\rho_{solvent} V \omega^2 r \quad (6.2)$$

and the third one is a frictional force (F_f).

$$F_f = -f v \quad (6.3)$$

All these forces play an important role in centrifugation and sedimentation. In equations (6.1) - (6.3) ρ_{NT} and $\rho_{solvent}$ are the density of the nanotubes and the solvent respectively. V is the nanoparticles volume, ω is angular velocity, r is the distance of the nanotube from the axis of rotation, f is the frictional coefficient which generally depended on nanotube diameters and lengths, and finally, v is the nanoparticles velocity. When these forces reach a balance, this relationship can be expressed as,

$$F_c + F_b = F_f \quad (6.4)$$

By substituting F_c , F_b , and F_f into Equation (6.4), it can be written as

$$\rho_{NT} V \omega^2 r = f v + \rho_{solvent} V \omega^2 r \quad (6.5)$$

and we can obtain the sedimentation velocity v , by the following equation:

$$v = \frac{V \omega^2 r (\rho_{NT} - \rho_{solvent})}{f} \quad (6.6)$$

The nanoparticles with different diameters and lengths move with different velocities in the medium, this provides a basis for nanoparticles (NPs) separation into distinct bands or layers, but if the nanoparticles diameters and lengths are the same, the qualities of separation into distinct layers will be very difficult.

Where v is the sedimentation velocity, V is the volume of NTs , ω is the angular velocity, R is the centrifugal radius (distance from the center of the centrifuge to the location of the nanotube), ρ_{NT} is the density of the nanotube, $\rho_{solvent}$ is the density of the surrounding medium, and f is the friction coefficient between the nanotube and the surrounding medium. Compared with sedimentation velocity, the sedimentation shift is easily described in terms of the response to the effect of separation. With the sedimentation of nanotubes, the centrifuge diameter is increased correspondingly in the process of centrifugation. Thus, the centrifugal acceleration is a variable that is related to the centrifugal angular velocity and nanotube shifts. This relationship can be written as:

$$x\omega^2 R = RCFx \frac{A-S(t)}{R} \quad (6.7)$$

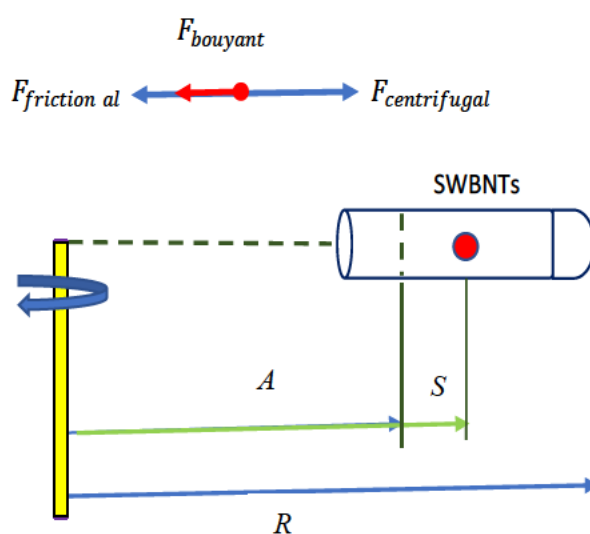


Figure 6.2. Centrifugation schematic of the separation of SWBNTs in a centrifuge with a horizontal rotor.

Where RCF is the relative centrifugal force, A is the distance from the axis to the original position of nanotubes, and $S(t)$ is the nanotube shift. The force on NTs can be calculated by the Stokes formula:

$$f = 3\pi\eta d \quad (6.8)$$

where η is the viscosity and d is the diameter of the nanotube. We can obtain the sedimentation shift by the following integral:

$$S = \int_0^t v dt \quad (6.9)$$

We integrate Equation (6.9) to obtain the relation between shift and time:

$$S(t) = A \left(e^{dt^2 \times RCF \frac{(\rho_{NT} - \rho_{solvent})}{18\eta R^{-1}}} \right) \quad (6.10)$$

Equation (6.10) relates the sedimentation shift to the centrifugation time when the *NTs* are centrifuged. For a given nanotube, the radius R and density ρ_{NT} are fixed. In a given centrifugal medium, the viscosity of the medium solution η in the same medium layer and the density $\rho_{solvent}$ are fixed. We assume that: (a) the thickness of each medium layer d is the same, and that (b) the change in instantaneous velocity when the nanotubes pass through the upper to the lower interface occurs during a very short period of time. That is, the process of acceleration and deceleration can be ignored. If we obtain the total time of the nanotubes' movement in this medium layer, the nanotube shift in the individual medium layer can be calculated by Equation (6.10).

6.2 Experimental method

The ultracentrifugation technique was used in the separation of SWBNTs. The SWBNTs synthesized from boron target (B, Sigma Aldrich 99.99%), by the dual pulsed laser ablation (DPLA) technique. SWBNTs sample is dispersed in a diluted solution of 0.4% w/v sodium cholate (SC, Sigma Aldrich) prepared via distilled water, which later formed a micelle around the SWBNTs. Through this, different wrapping morphologies form micelle of different sizes and density of SWBNTs. Based on the small densities differences that occurred, the ultracentrifugation technique is used to separate the SWBNTs into various distinct layers. After the separation, we observed that the use and choice of surfactant, with respect to the density gradient medium (DGM), seem to be more important. The surfactant played the most critical roles in the separation, compared to when SWBNTs sample was dispersed in distilled

water without the surfactant, no layers were found after the centrifugation. In addition, surfactant recipes have been the most effective in isolating and separating of SWBNTs. The most commonly used surfactants in separating the nanomaterials and nanoparticles in ultracentrifugation are anionic salts, such as sodium dodecyl sulfate (SDS) and bile salts such as sodium deoxycholate (DOC) or sodium cholate (SC). SC is the best surfactant used in this work, all these surfactants have different affinities to different nanomaterials and nanoparticles due to their specific molecular structures [293]. The results in surfactants wrapping depend on the structures and electronics types of the nanomaterials. Various theoretical calculations, numerical simulations, TEM measurements have been proposed on these nanomaterials and nanoparticles [294-296]. The clarification of the separation mechanism of these nanomaterials and nanoparticles are yet to be clarified. In this work, we designed a method that involved two different steps which resulted in the separation of SWBNTs into various layers. The designed DGU mechanism separated SWBNTs into four distinct layers that led to different diameters and lengths. The results from each layer are analyzed. This technique is also used in the separation of SWCNTs into different layers. The results obtained using the new methods are supported by the results achieved by other authors [297]. The details regarding the experimental procedures of synthesis of SWBNTs used in this chapter six will be found in chapter three. A brief explanation of the separation mechanism will be explained before addressing the experimental results.

6.2.1 Surfactant DGU separation and preparation of density gradient medium (DGM)

The critical aspect of this method is to find out the morphology of the surfactant that is suitable for the SWBNTs during the ultracentrifugation. This suitability is due to the affinities between the nanomaterials and a surfactant present in the gradient medium. The dynamic equilibrium state of the surfactant absorbed onto the nanomaterials and free surfactant molecules present in the medium is very important. The significance of a surfactant occurs in the dispersion steps and continues during the ultracentrifugation.

The significance of surfactants can be proved, if the surfactant is removed from the materials and the results compared when the material is dispersed in distilled water.

Step I: SWBNTs separation by DGU

Density gradient centrifugation

Linear density gradient profile (DGP) Optiprep (Sigma–Aldrich Co., Ltd) solutions were prepared by mixing pure Optiprep in deionized water by stirring. The Optiprep solutions with different mass fractions were carefully added to the tubes layer by layer. The gradient solution from top to bottom consisted of Optiprep solutions with mass fractions of 40% and 80% v/v, with added volumes of 4 mL each. As-prepared SWBNTs is dispersed with an equal volume of 0.4% w/v sodium cholate and ultrasonicated for 20 minutes at 400 W/cm² using a horn–type ultrasonicator (UP–400s, Hielscher Ultrasonic). After the ultrasonication, the SWBNTs suspension to be separated was floated on these two layers and centrifuged at 32,000 rpm (with rotor 32 Ti) for 3 hours in a Beckman Coulter MLA–80 fixed angles (90°) at 20 °C temperature. After ultracentrifugation, gradient linearization separation of SWBNTs into four different layers of diameters was obtained as shown in Figure 6.2 (b). This occurred at the end of the first step and each layer was extracted using a micropipette. Figure 6.3 (c) shows the results obtained after ultracentrifugation when the sodium cholate is absent in the ultracentrifugation.

Step II: Purification of SWBNTs from sodium cholate

SWBNTs extracted in each layer is purified from sodium cholate. The second step of the ultracentrifugation was performed to get rid of surfactant and optiprep. Figure 6.3(b) corresponds to each layer obtained in Figure 6.3(a). Each layer is mixed in 5 ml ethanol absolute (100 %, Sigma Aldrich) in Seton, ultra–clear centrifuge tube Polyallomer 25 x 89 mm, 39 ml capacity (Bell top Quick-Seal, Beckmann–Coulter centrifuge tubes) and ultrasonicated for 30 minutes at 400 W/cm² using a horn–type ultrasonicator (UP–400s, Hielscher Ultrasonic) prior to the centrifugation.

After ultrasonication, each layer is centrifuged for 2 hours with a speed of 50,000 rpm (with rotor 70 Ti) at a temperature of 4 °C in a Beckman Coulter MLA–80 fixed angle rotors at 45°.

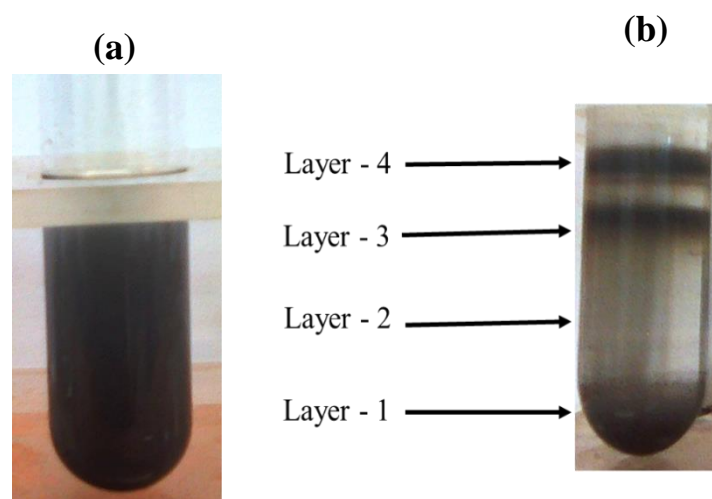


Figure 6.2: (a) Before DGU, SWBNTs mixed with a sodium cholate in Optiprep density gradient solution (b) After DGU, sorted isolated small SWBNTs bundles on top and sediments of large SWBNTs bundles at the bottom.

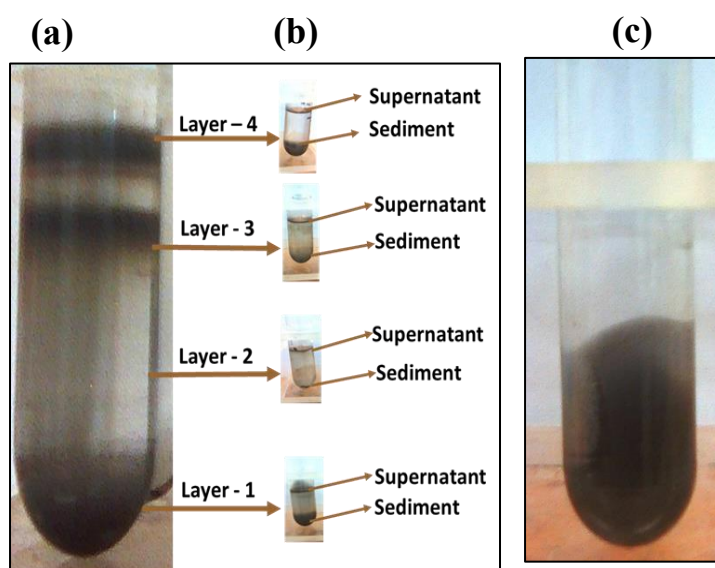


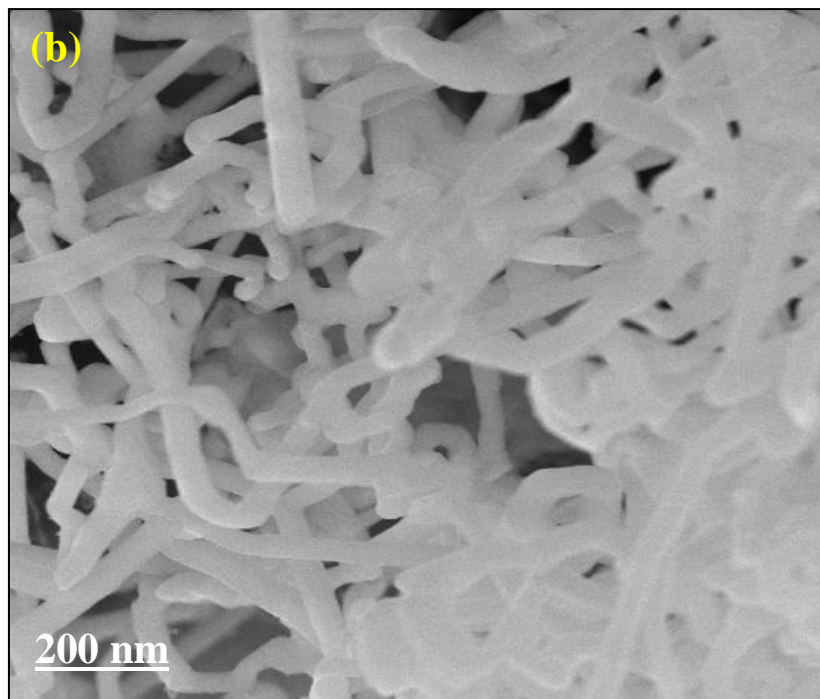
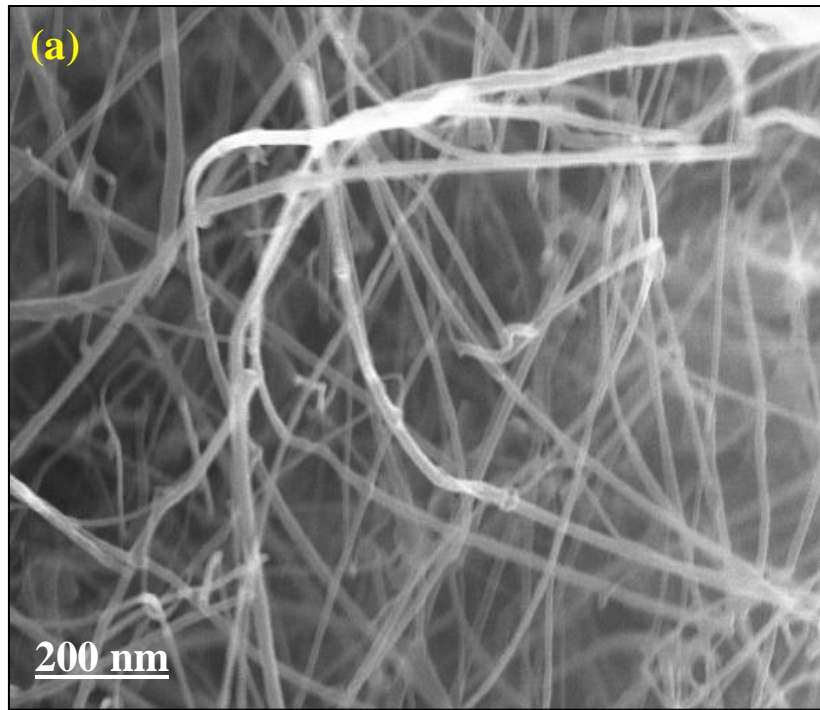
Figure 6.3: (a) The final position of SWBNTs separated into four layers, at 32,000 rpm for 3hrs, (b) Corresponding to each layer obtained in Figure 6.3(a) from different layers, at 50,000 rpm for 2 hrs and (c) The final position of SWBNTs when distilled water is used.

The top 70 % of the supernatant layer in each test tube is decanted, which are already purified from the sodium cholate and Optiprep. Each layer was characterized using, the following characterization, scanning electron microscopy (SEM), high-resolution transmission electron microscopy (HRTEM), energy dispersive X-ray spectroscopy (EDS) and Raman spectroscopy (RS).

6.3 Results and Discussions

6.3.1 Characterization of SWBNTs by SEM and EDS

The SEM and EDS analyses were performed on an LEO Gemini1525 FEGSEM at an accelerating voltage of 10 keV for SEM and 20 keV for EDS. The supernatant samples from each layer were prepared on the glass substrate and adhered to the aluminum or copper SEM holder with the help of carbon tape, which was later coated with gold (Au) before characterization. The SEM images in Figure 6.4 (a-d) shows the results obtained from four layers, with the EDS spectrum in Figure 6.4 (e) and EDS results in Table 6.1. The SEM images revealed the microscopic bundles of SWBNTs of nanometers in diameter with metal catalysts particles, predominantly nickel (Ni) and cobalt (Co) which were observed on the EDS spectrum. SEM analyses also revealed tubular and spherical structures of SWBNTs in all layers. EDS spectrum is used to analyze the elemental compositions that were found in SWBNTs. In Figure 6.4(e) the strong peak of boron appeared at about 200 eV. It was detected that only a small amount of oxygen (O₂) found (0.2% at 600 eV), this might have resulted from the boron oxide (B₂O₃) used as a binder. A small percentage of Ni and Co was noticed, which is about 0.05%, at 800 eV, as the catalysts used in boron target. The peak at 2200 eV is attributed to the gold (Au) peak resulting from the gold used to coat the supernatant SWBNTs sample on the glass substrate. Finally, SEM images in Figure 6.4(a-d) revealed the presence of metallic catalysts found in the EDS. Table 6.1. shows elemental components of each element present in SWBNTs. The SEM identifying the presence of low level of the amorphous boron formed from SWBNTs synthesized.



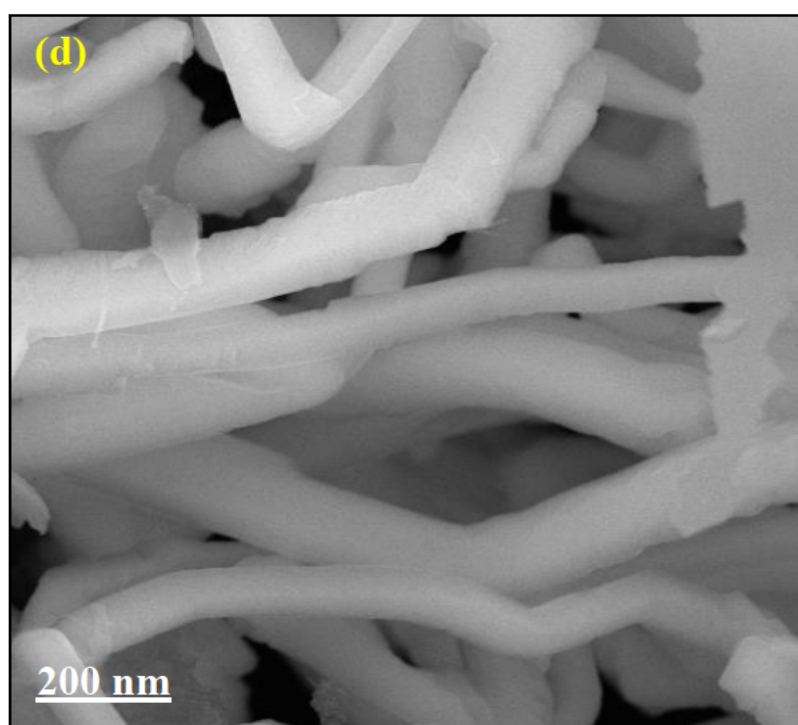
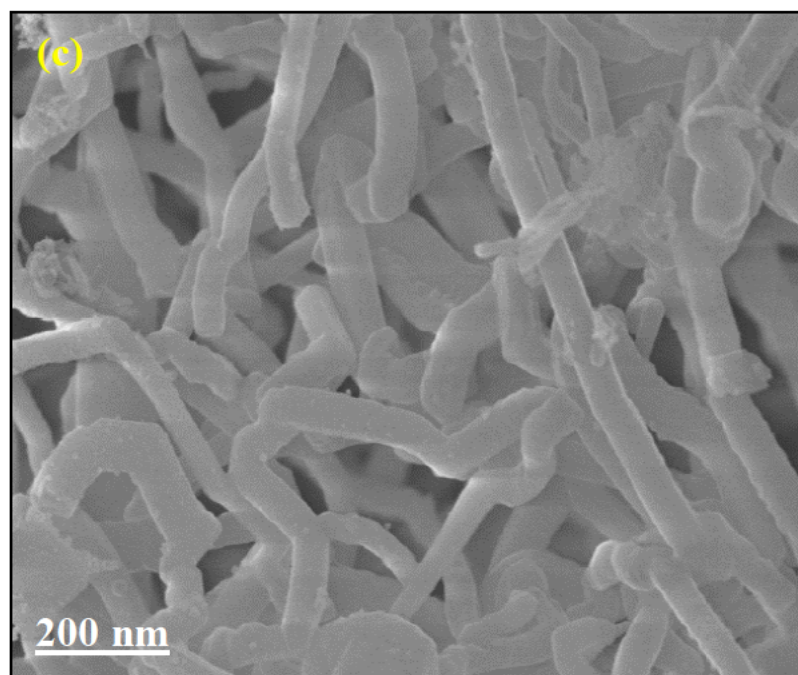


Figure 6.4: The SEM images of SWBNTs obtained from different layers after the DGU operated at 50,000 rpm for 2 hours (a) Layer four, (b) Layer three, (c) Layer two and (d) Layer one. Each of this layer depicted the bundles of SWBNTs.

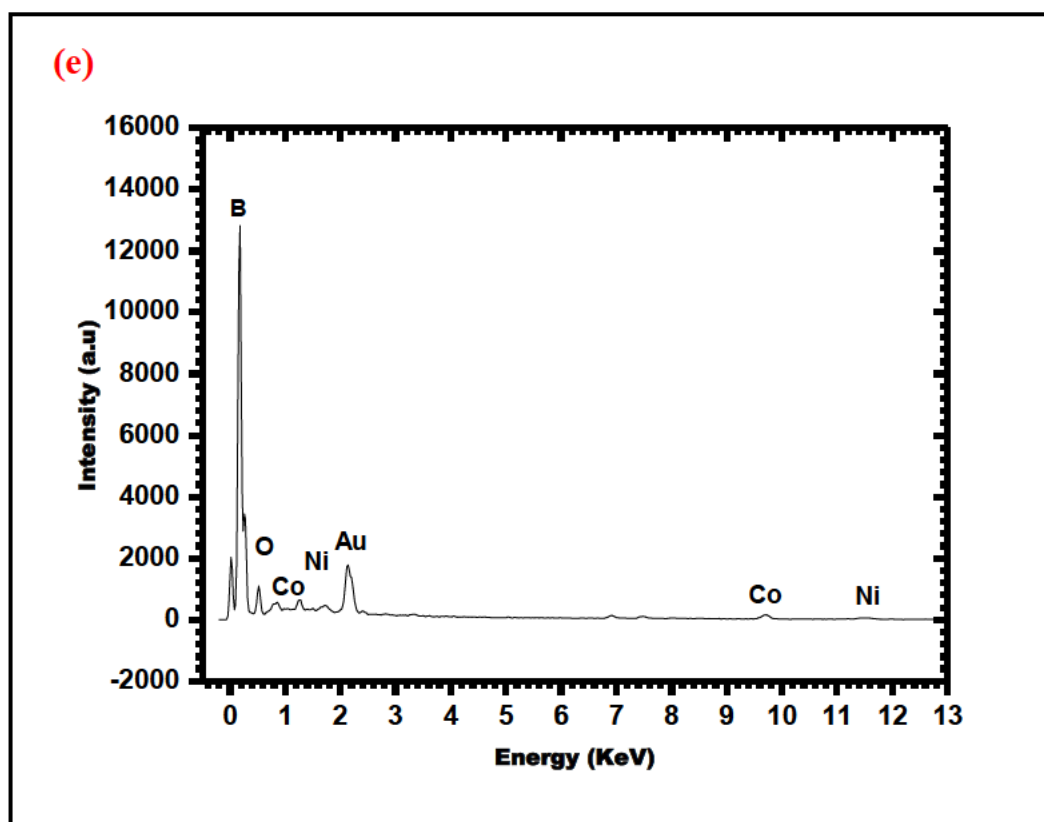


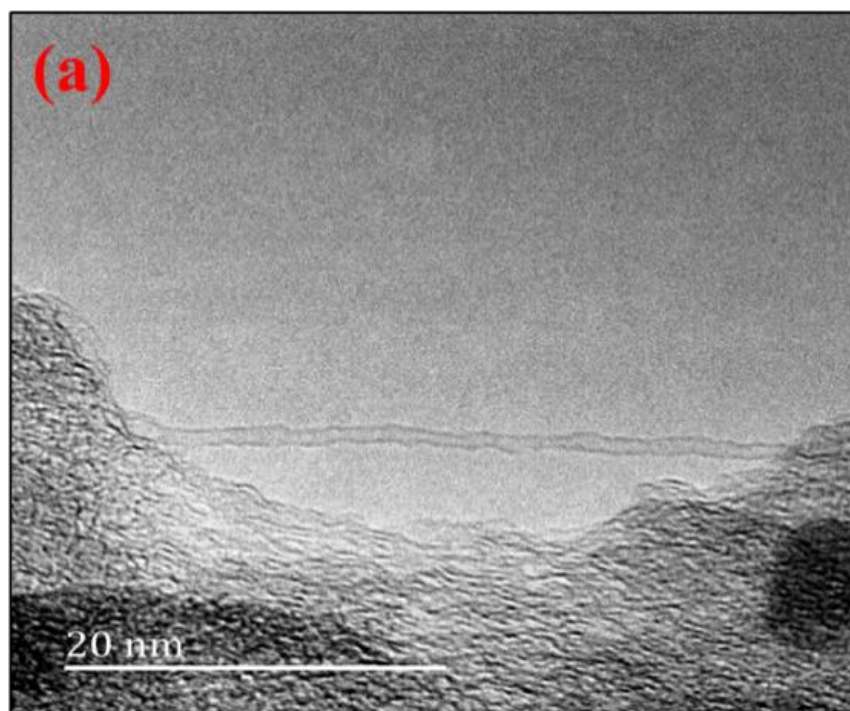
Figure 6.4(e): The EDS spectrum obtained from SEM image after the DGU at 50,000 rpm for 2 hours confirming the purity of the SWBNTs.

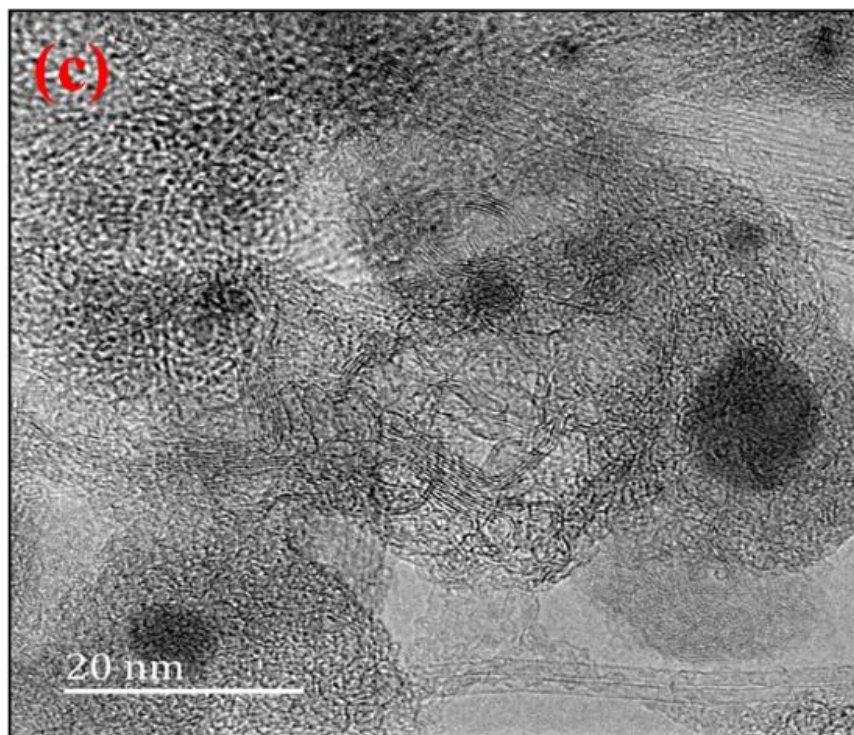
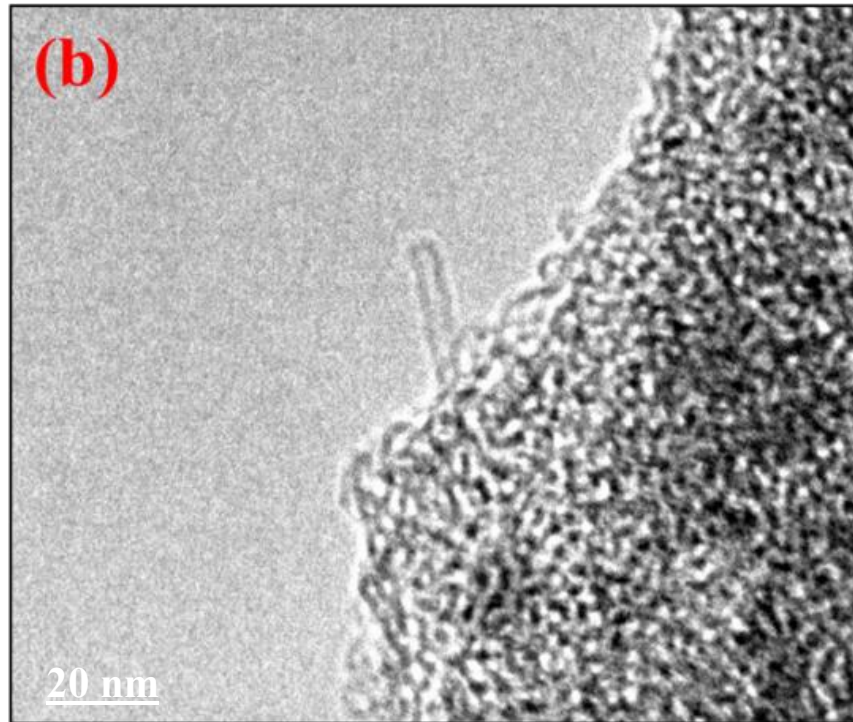
Table 6.1: The elemental composition of each element presents in the SWBNTs.

BNTs	Wt.%	Wt.% Sigma
B	93.32	0.21
O	5.76	0.20
Co	0.46	0.05
Ni	0.46	0.05
Total	100.00	

6.3.2 Characterization of SWBNTs by HRTEM and EDS

The supernatant SWBNTs samples for HRTEM were bath sonicated and dropped onto a carbon grid and dried for thirty minutes before characterization. The HRTEM was performed on a JEOL 2100 at 200 keV. The SWBNTs can be seen to be relatively long from the micrographs, with the outer diameters between 1.43 to 2.05 nm. The EDS spectrum found with HRTEM images was used to analyze the elemental compositions that were found in SWBNTs. Figure 6.5 (e) shows the strongest peak of boron at 200 eV. It was detected that only a small amount of oxygen (O_2) was found, this must have resulted from the boron oxide (B_2O_3) used as a binder material. The small amount of Ni and Co was perceived which is about 0.56%, as catalysts used in the boron target. A small percentage of copper (Cu) was found, resulting from HRTEM grid, during characterization. The EDS analyses revealed that the total content of boron in the SWBNTs is over 95 %, which confirmed the purity of as – prepared SWBNTs.





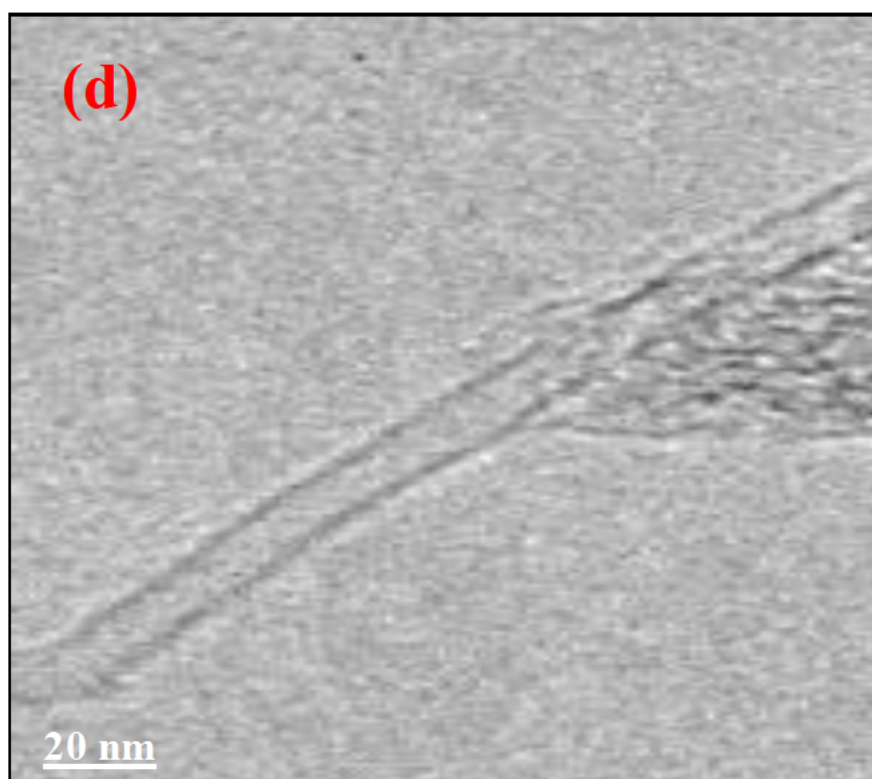


Figure 6.5: The HRTEM images of SWBNTs obtained from the DGU at 50.000 rpm in 2 hours at different levels **(a)** Layer 4, SWBNTs of 1.43 nm in diameter, **(b)** Layer 3, SWBNTs diameter of 1.71 nm **(c)** Layer 2, SWBNTs of 1.93 nm in diameter and **(d)** Layer 1, SWBNTs of 2.05 nm in diameter with a catalyst at the top.

The analyses of HRTEM obtained in this research revealed the differences in diameters of the SWBNTs separated after the ultracentrifugation. The SWBNTs with small diameters of 1.43 nm were observed from lower densities (i.e. Layer 4) at the topmost part of the centrifuge tube as shown in Figure 6.3 (a). Large diameters of 2.05 nm of SWBNTs were observed at the higher density (i.e. Layer 1) at the bottom part of the centrifuge tube as shown in Figure 6.3(a). Similar observations about the separation of diameters and lengths of different nanoparticles and nanomaterials have been reported, for instance in single-walled carbon nanotubes (SWCNTs) [298-300].

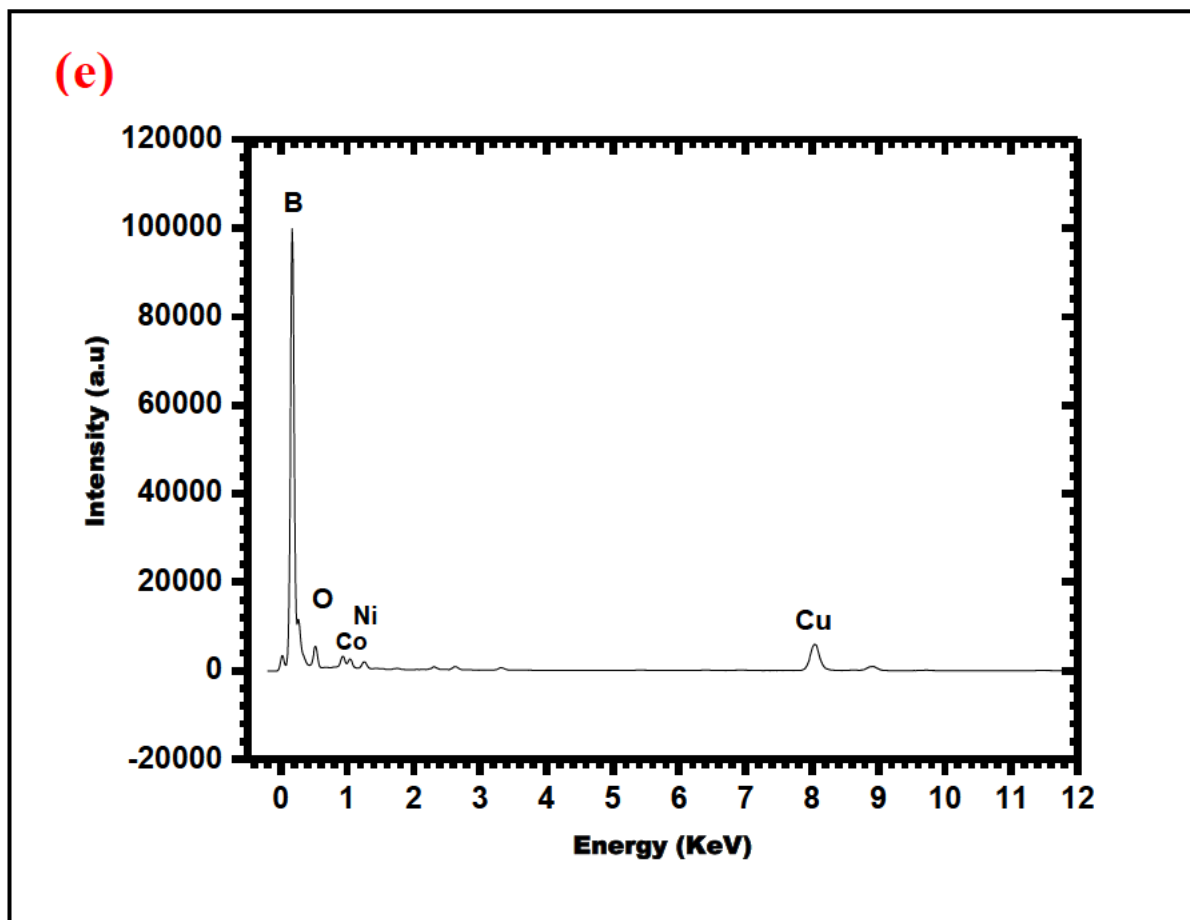


Figure 6.5 (e): The EDS spectrum obtained from HRTEM images after the DGU at 50,000 rpm for 2 hours confirming the purity of the SWBNTs.

Table 6.2: EDS table from HRTEM analysis shown the elemental composition of each element present in the SWBNTs

Element	Weight%	Weight% Sigma	Atomic%
B	92.40	0.04	95.39
C	4.34	0.04	4.04
Co	0.05	0.00	0.01
Ni	0.01	0.00	0.56
Cu	3.16	0.02	0.56
Zn	0.04	0.01	0.01
Totals	100.00		

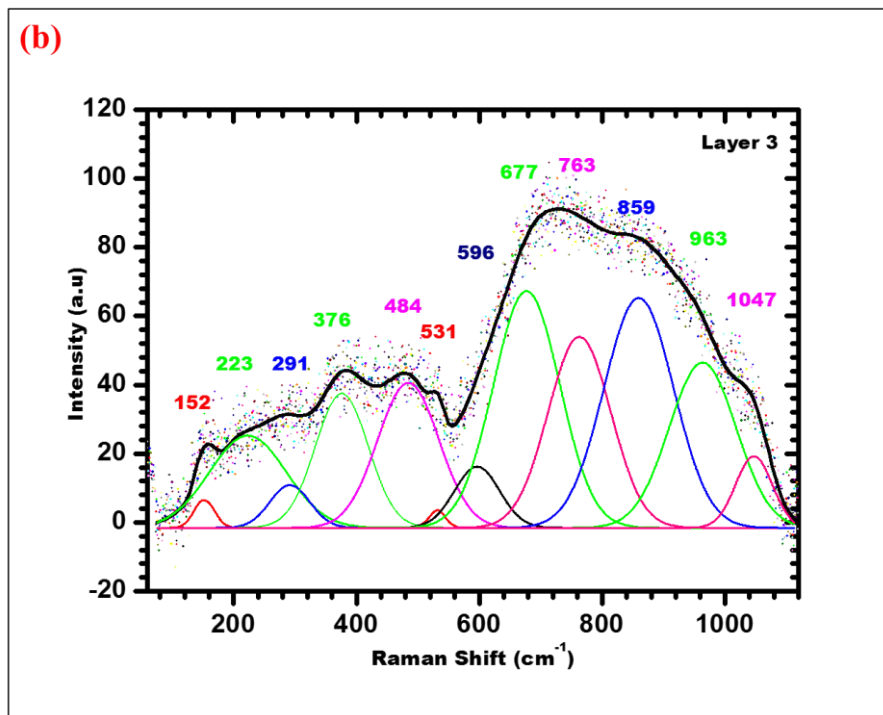
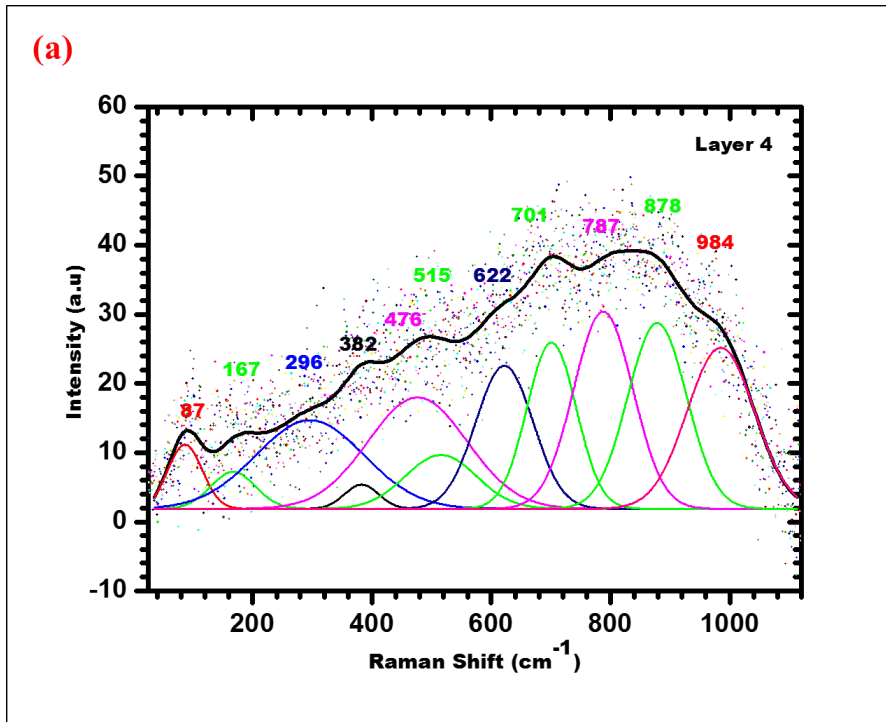
Similarly, in layer 3 and 2, the SWBNTs of outer diameters 1.71 and 1.93 nm were obtained. There was high deviation in the diameters of SWBNTs separated at different layers by centrifugation. This might have resulted from the presence of smaller diameters SWBNTs separated along with larger diameters SWBNTs through the help of surfactant that wrapped as-prepared SWBNTs sample in the DGM. Different outer diameters and lengths were observed in nanometres (10^{-9}) and microns (10^{-6}) respectively, although the uniform separation of the SWBNTs was not observed. In Figure 6.5(a-d), different densities contained a significant portion of specific SWBNTs. For instance, in Figure 6.3 (a), the lower density gradient (at layer 4) of the Optiprep could separate most smaller SWBNTs, accompanied by SWBNTs of smaller diameters in nanometres and lengths in microns as shown in HRTEM in Figure 6.5 (a). In Figure 6.3 (a), the higher densities from layer 1 to 3 of Optiprep could separate SWBNTs of different diameters and lengths. The concentration gradient of Optiprep (i.e. layer 1) at the bottom of the centrifuge tube could separate the SWBNTs of larger diameters. In addition, wires, rods, sheets and different shapes of other nanomaterials could be featured in the sediment in layer 1, if carefully examined. There is some evidence of separation between tube diameters. The exclusive separation of the specific shape of other nanomaterials types is not observable, that is a separation between sheets, wires, and rods at a different density gradient did not occur. These observations are similar to those of other researchers in CNTs separation using ultracentrifugation technique, who have reported that diameter separation between sheets, wires, and rods with similar diameters was difficult [298].

6.3.3 Characterization of SWBNTs by Raman

Raman spectroscopy (RS) was used to analyze SWBNTs samples obtained from different layers. RS measurements were performed on a Jobin Yvon Labram HR 800 micro-Raman spectrometer, using an excitation wavelength of 514 nm laser. Due to the inhomogeneity in diameters of SWBNTs synthesized it enabled us to obtain four layers after the ultracentrifugation. These four layers required measurements to be ascertained that indeed each layer contained SWBNTs and this was done through HRTEM. Each of this layer was transferred on an HRTEM grid to be sure that each layer obtained contained SWBNTs prior to the RS analyses.

We examined the sample layers morphologies, and their chemical compositions on the carbon grid through EDS. Figure 6.5 (a-d), revealed the HRTEM micrographs of four layers obtained on the HRTEM grid. The experimental details on the synthesis of the as-prepared SWBNTs used in this chapter six are described in chapter three of this dissertation. The Raman peaks observed in α -boron was predicted through theoretical studies [45, 301]. The phonon modes of boron are observed under resonance conditions [302]. This is intensively used for probing the electronic structures of boron nanotubes [302]. The electronic band gap of boron nanotubes (BNTs) is estimated to be between 1.0 eV to 0.8 eV from the theoretical calculations [179]. We worked in the visible wavelength range to get a close possible range to resonance. The Raman measurement was performed at an excitation visible wavelength up to 514 nm. The only visible wavelength used in the Raman measurements throughout was a 514 nm laser. On each layer, micro-Raman was measured and characterized. All the Raman data collected are corrected, by subtracting the quartz substrate background signal data from the data obtained in both SWBNTs and quartz substrate. The subtraction was done before plotting each data to obtain all the Raman spectra in Figure 6.6 (a-d). The Raman spectra obtained has SWBNTs fingerprint that was clearly shown in the HRTEM micrographs in Figure 6.5 (a-d). These areas observed on Raman spectra has more SWBNTs. Some intensity peaks were predicted theoretically in the α - boron Raman spectra [36, 45]. These peaks are related to A_{1g} and E_g modes [44, 45]. In table (6.3-6.6), we compared the peaks in the experiment with the α -boron peaks obtained in the theoretical calculations [36, 44, 45, 301] and experimental values [44, 303]. The electron density distribution in the icosahedra of α -rhombohedral boron and boron carbide are similar as reported by Hosoi *et al* [304]. Bonds and vibration spectra are expected to be closely related. For α -rhombohedral boron, the simplest icosahedral boron-rich solid, the phonon frequencies were determined by Beck *et al* [45] and in agreement with the experimental Raman spectra reported by Vast *et al* [43]. According to the group theory, ten Raman active modes of 4 A_{1g} singlets and 6 E_g doublets are predicted for α -rhombohedral boron with D_{3d} point symmetry [45, 305]. According to their expectation, the A_{1g} and E_g vibrations are the Raman-active peaks [45] in the region from 500 to 1200 cm^{-1} modes.

The calculated Raman spectra predicted were twelve Raman active peaks. The first experimental Raman spectrum of α -rhombohedral boron was published by Richter and Ploog, [42] showing twelve Raman peaks and was subsequently confirmed by other groups of researchers [36, 303, 306, 307]. It was observed that the initial theoretical simulations of the Raman spectrum of α -rhombohedral boron were not satisfactory [53]. Vast *et al*, with their ab initio lattice dynamics calculations, later yielded a very good agreement between mode frequencies and the measured Raman spectrum [43]. Shirai and Katayama–Yoshida studied the phonon spectrum of α -rhombohedral boron from the viewpoint of anharmonic effects [274]. The phonon spectrum was calculated by evaluating the anharmonic force constants of individual bonds obtained from the pressure dependence of phonon frequencies [45]. The detection of some weak spectral features and several weak Raman bands were found in addition to the well-known modes. For large atomic clusters, the mass difference of vibrating groups of atoms is reduced by the statistical distribution of isotopes. This effect is observed for the 527 cm^{-1} modes and was close to the experimental peak at 529 cm^{-1} modes in Figure 6.6(c), which corresponds to the rotation of the rigid B_{12} icosahedra [36, 45]. The Raman active phonons are predicted theoretically, four strong peaks and probably two very weak ones at 1094 and 1238 cm^{-1} , not featured in the experimental results [36, 45]. Polarization-resolved measurement by Tallant *et al*, assigned one of the main peaks to an E_g mode (doublet) and three others peaks to A_{1g} (singlet) symmetry [308]. Beckel *et al*, described the movement of the atoms in these modes. The E_g mode is a mixture of vibrations modes of the B_{12} cluster having frequencies ω_1 and ω_2 . For ω_1 , all six external two center bonds of the icosahedra are compressed simultaneously. While for ω_2 , at a given moment, two of the six are compressed, two are stretched and two are strained [45]. A_{1g} modes predominantly originate from the radial movement of the polar atom belonging to the triangles of the icosahedra which induced double stress and the double compression of the two - center bonds between the icosahedra. In table (6.3-6.6), the calculated and experimental values A_{1g} modes (708, 947, and 710, 965, and 692, 925 cm^{-1}) are close to the experimental results (701 cm^{-1} layer four, 677, 963 cm^{-1} layer three, 782, 975 cm^{-1} layer two, and 685, 859, 949 cm^{-1} layer one). They were all related to the A_{1g} mode according to the theoretical and experimental values [43, 274].



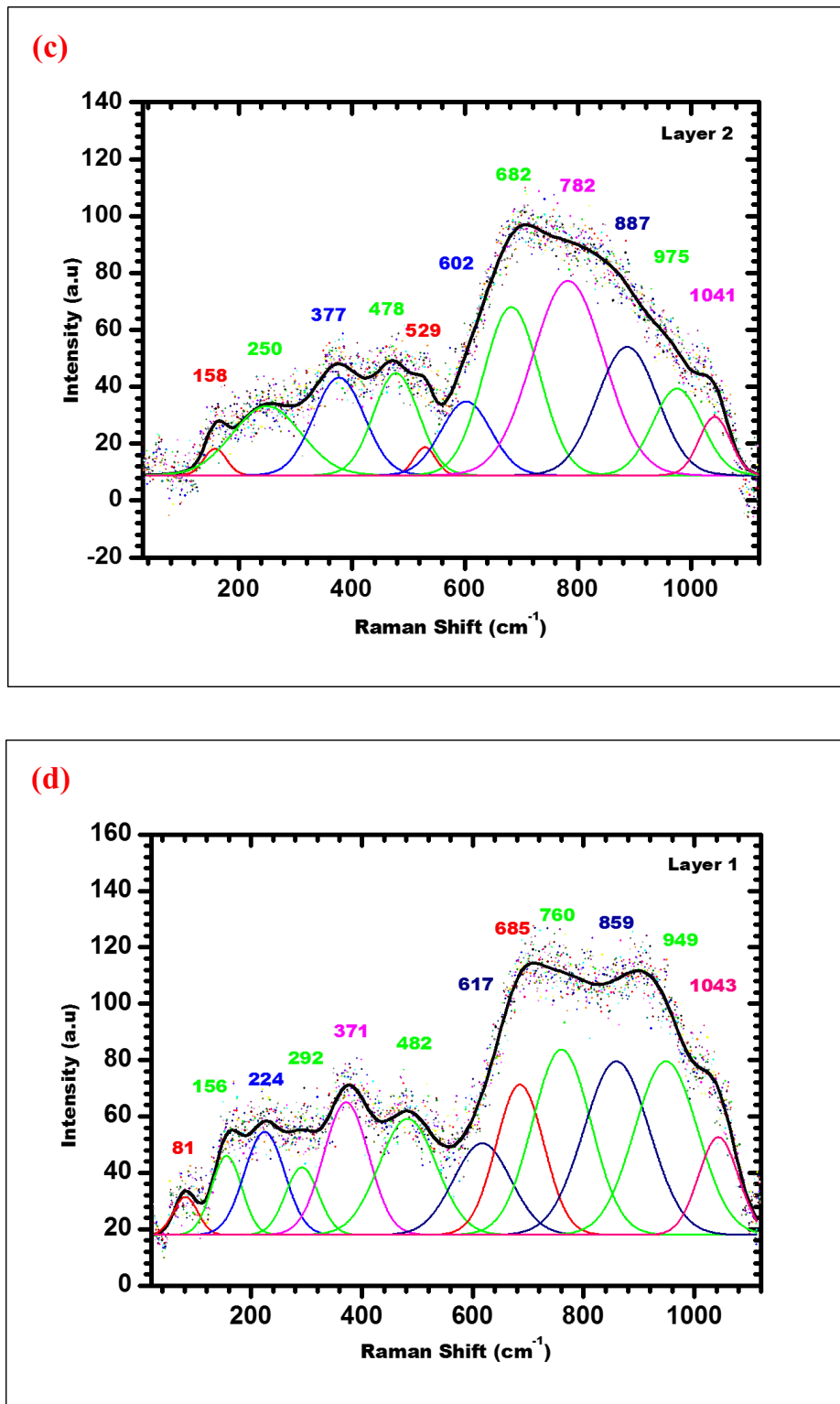


Figure 6.6: Raman spectra excited at 514 nm laser on (a) Layer 4 (b) Layer 3, (c) Layer 2 and (d) Layer 1, which correspond to the results obtained from the four layers, in the centrifuge tube after the DGU.

The calculated values A_{1g} modes (708, 947 and 710, 965 cm^{-1}) [43, 274] are nearly the same as the experimental results (701, 963, 975 and 949 cm^{-1}) in Table (6.3-6.6), there were no discrepancies including the experimental values of Vast *et al* in Table (6.3-6.6) [43]. In Table (6.3-6.6), the calculated E_g modes (529, 790, 890 and 497, 818, 884 cm^{-1}) are close to the experimental results (515, 787, 878 layer four, and 531, 596 layer three, and 529, 602, 887 layer two, and 617 cm^{-1} layer one) [43, 274].

Table 6.3: Raman active modes in α – boron (in cm^{-1}) and the experimental results obtained from layer 4 of BNTs is compared with theoretical calculations and experimental results of Vast *et al* and theoretical calculations by Shirai *et al*.

Layer 4		α - boron		
Vast <i>et al</i> [43] Theory	Shirai <i>et al</i> [49] Theory	Vast <i>et al</i> [43] Experiment	Experimental Results (BNTs)	Raman active
Frequency	Frequency	Frequency	Frequency	Mode
529	497	525	515	E_g
708	710	692	701	A_{1g}
790	818	774	787	E_g
890	884	870	878	E_g

Table 6.4: Raman active modes in α – boron (in cm^{-1}) and experimental results obtained from layer 3 of the BNTs is compared with theoretical calculations and experimental results of Vast *et al* and theoretical calculations by Shirai *et al*.

Layer 3		α - boron		
Vast <i>et al</i> [43] Theory	Shirai <i>et al</i> [49] Theory	Vast <i>et al</i> [43] Experiment	Experimental Results (BNTs)	Raman active
Frequency	Frequency	Frequency	Frequency	Mode
529	497	525	531	E_g
608	572	586	596	E_g
708	710	692	677	A_{1g}
947	965	925	963	A_{1g}

There is a lesser discrepancy for the E_g mode observed from both theoretical and the experimental values most especially when we compared our results to the experimental values of Vast *et al* [43]. This suggests splitting of the E_g doublets, an assumption which is not supported by the polarization resolved measurement [44]. In Figure 6.6 (a-d) the Raman spectra peaks at 984, 1047, 1041 and 1043 cm^{-1} coincide with absorption maxima and thus can be related to luminescence due to electronics transitions between gap states [44, 45].

Table 6.5: The Raman active modes in α – boron (in cm^{-1}) and experimental results obtained from layer 2 of the as-prepared BNTs is compared with theoretical calculations and experimental results of Vast *et al* and theoretical calculations by Shirai *et al*.

Layer 2		α - boron		
Vast <i>et al</i> [43] Theory	Shirai <i>et al</i> [49] Theory	Vast <i>et al</i> [43] Experiment	Experimental Results (BNTs)	Raman active
Frequency	Frequency	Frequency	Frequency	Mode
529	497	525	529	E_g
608	572	586	602	E_g
708	710	692	782	A_{1g}
890	884	870	887	E_g
947	965	925	975	A_{1g}

Table 6.6: Raman active modes in α – boron (in cm^{-1}) and experimental results obtained from layer 1 of the BNTs is compared with theoretical calculations and experimental results of Vast *et al* and theoretical calculations by Shirai *et al*.

Layer 1		α - boron		
Vast <i>et al</i> [43] Theory	Shirai <i>et al</i> [49] Theory	Vast <i>et al</i> [43] Experiment	Experimental Results (BNTs)	Raman active
Frequency	Frequency	Frequency	Frequency	Mode
608	572	586	617	E_g
708	710	692	685	A_{1g}
815	759	793	859	A_{1g}
947	965	925	949	A_{1g}

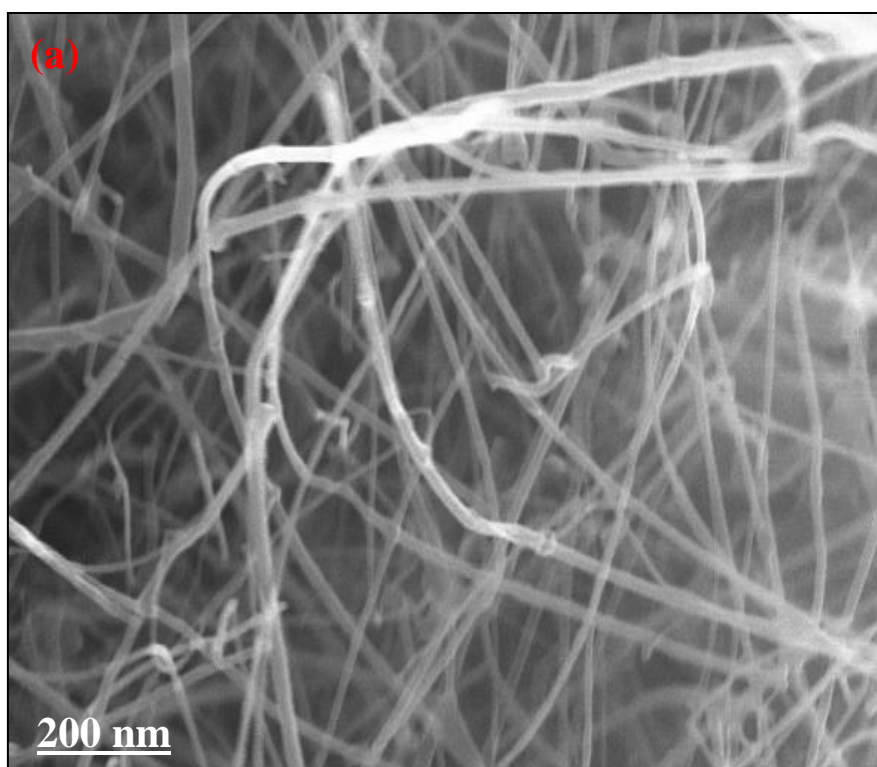
According, to Beckel *et al*, the line 934 cm^{-1} mode corresponds to the experimental results ($984, 963, 975$ and 949 cm^{-1}), involves distortions of the polar triangles as well as the equatorial hexagon, where two of the six bonds are stretched [45]. The 873 cm^{-1} mode is close to the experimental results ($878, 859, 887$ and 859 cm^{-1}), and is essentially an isolated icosahedral mode which mainly stresses the chemical bonds of the icosahedral [303]. The strongest peak at 795 cm^{-1} , corresponds to the experimental results (787 and 782 cm^{-1}) and is attributed to the external three-centered bonds which are compressed at an instant when two centered bonds are stressed [301, 303]. The 694 cm^{-1} modes found close to the experimental results ($701, 677, 682$ and 685 cm^{-1}) shown in Table (6.3-6.6) coincide with those of the α -tetragonal boron phase [44, 303]. The peaks in the Raman spectra of the experiment results ($622, 596, 602$ and 617 cm^{-1}) coincide with the calculated Raman line at 589 cm^{-1} [44, 309], has been reported for crystalline β -rhombohedral and features are attributed to Raman active covalent inter icosahedral B-B bonds. Vast *et al*, assigns the Raman peak at 527 cm^{-1} to the vibrational modes of the entire icosahedron α -boron, and is close to the peaks in the Raman spectra of boron nanotubes ($515, 531, 529$ and 482 cm^{-1}) shown in Figure 6.6 (a-d) [43]. Raman spectra do not show any sharp features. We observed the weak statistics with data noise on the Raman spectra obtained, this due to weak signal and small amount of material. The broad features in the spectra are similar to the spectrum of β -rhombohedral boron reported [310]. The absence of sharp bands is due to partial amorphous nature of the sample which is also confirmed by XRD pattern which observed a similar phenomenon and reported that the Raman effect in amorphous was very weak [311]. In the Raman spectra, the G peak, corresponds to planar vibrations of boron atoms in boron like materials. The G peaks are associated with the E_g mode, stretching vibrations, in the basal plane of boron. Other peaks were detected at $152, 156, 158, 167, 223, 224, 250, 291, 292,$ and 296 cm^{-1} , these peaks might be assigned as a radial breathing mode (RBM) as this has been detected in a single-walled carbon nanotube. The RBM corresponds to the radial expansion-contraction of the boron nanotube (BNTs), its frequency ω_{RBM} depends on the nanotube diameter. Typical RBM range is $100\text{-}350\text{ cm}^{-1}$ [312]. Peaks located at $1041, 1043$ and 1047 cm^{-1} has been attributed to the vibration mode of inter icosahedra B-B bonds.

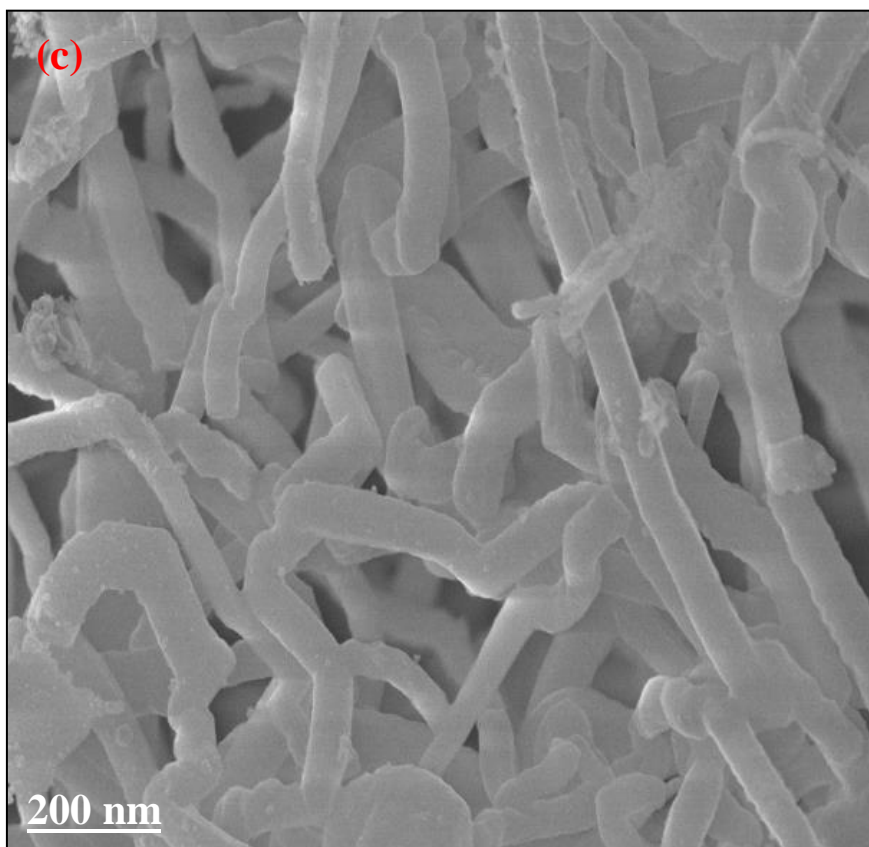
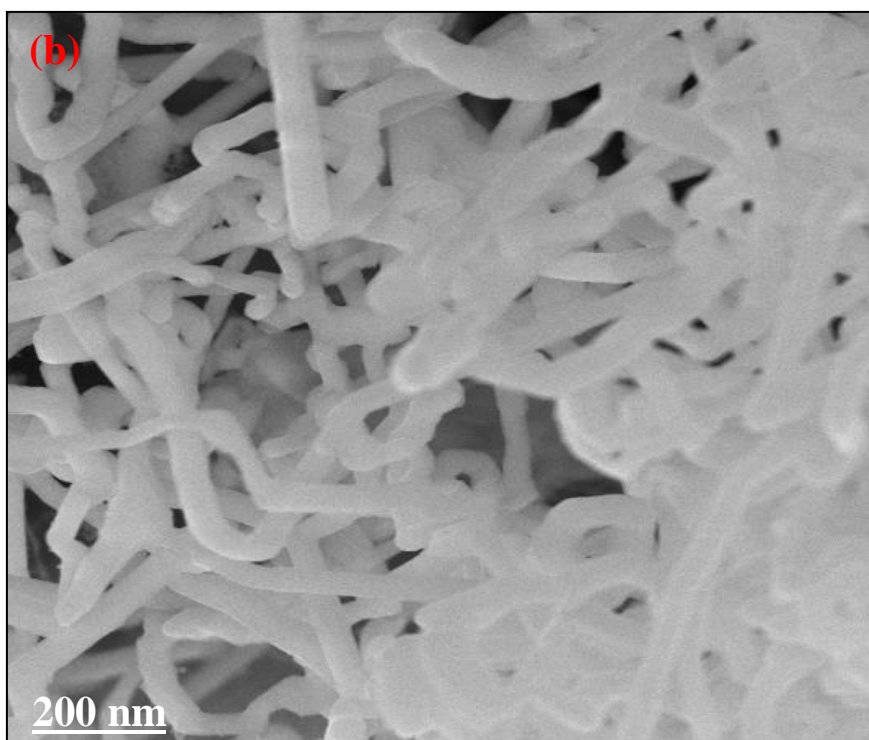
A few frequencies in the range 500-900 cm^{-1} represent intra icosahedra vibration modes. The spectra also showed peaks features at 476, 478, 482 and 484 cm^{-1} , can be assigned to a B-B stretching mode corresponding to the tangential mode in carbon nanotubes and bonds between B and foreign atoms [313].

The spectral features between 300 and 500 cm^{-1} may also be attributed to tubular structures. Ciuparu *et al* and Liu *et al* attributed the Raman peaks below 500 cm^{-1} to BNTs signature and the characteristics of tubular structures [120, 126]. Similar peaks were reported for single-walled carbon nanotubes [272]. The peaks between 300 and 600 cm^{-1} can be attributed to nanotubes of different diameters and chirality [126]. The spectral features between 400 and 600 cm^{-1} belong to nanotubes of smaller diameters and other boron nanostructures [126]. Overall, it was found that SEM images revealed that indeed as-prepared materials consist of microscopic bundles of SWBNTs with metal catalyst particles present, which revealed in the EDX spectrum. Structural characterization of SWBNTs separated through ultracentrifugation into different layers was carried out by HRTEM. All SWBNTs found varies with respect to their layers. The SWBNTs of outer diameters and lengths, found through the HRTEM measurement are in the range between nanometres in (10^{-9}) and microns (10^{-6}) respectively. It is demonstrated that Raman spectroscopy is a very sensitive tool for detecting different types of modification of crystalline structures. The SWBNTs have been studied by Raman spectroscopy using visible excitation energy and Raman scattering in the visible range at a 514 nm laser. It provides pre- resonant conditions which allowed us to identify the tangential modes at A_{1g} and E_g frequencies. The Raman spectra of SWBNTs did not show any sharp peaks, but the spectra were compared with the theoretical calculations and experimental results that revealed similar features. The Raman active modes of SWBNTs that was experimentally measured from the acquired data, showed the frequencies of the A_{1g} and E_g modes of α -boron. The peaks resulting from α -boron cluster was observed at frequencies above 500 cm^{-1} , while the Raman peaks below 500 cm^{-1} were also attributed to SWBNTs signatures according to Ciuparu *et al* and Liu *et al* experimental results because the same peaks were observed in SWCNTs.

6.4 Image analyses on the SEM and HRTEM micrographs of SWBNTs

In this chapter, the image analyses were performed on the scanning electron microscopy (SEM) and high-resolution transmission electron microscopy (HRTEM) micrographs of single-walled boron nanotubes (SWBNTs) obtained from different layers after the ultracentrifugation. The HRTEM images used for the analyses were taken randomly and these were analyzed to detect the trend in diameters. The density of tubular structures of boron and SWBNTs was found in each layer for both SEM and HRTEM micrographs shown in Figure 6.7 (a-d) and 6.8 (a-d) respectively. This series of SEM images from the four different layers produced show the changing density of each layer. The images were analyzed to obtain the number of tubular structures of boron per nm^2 .





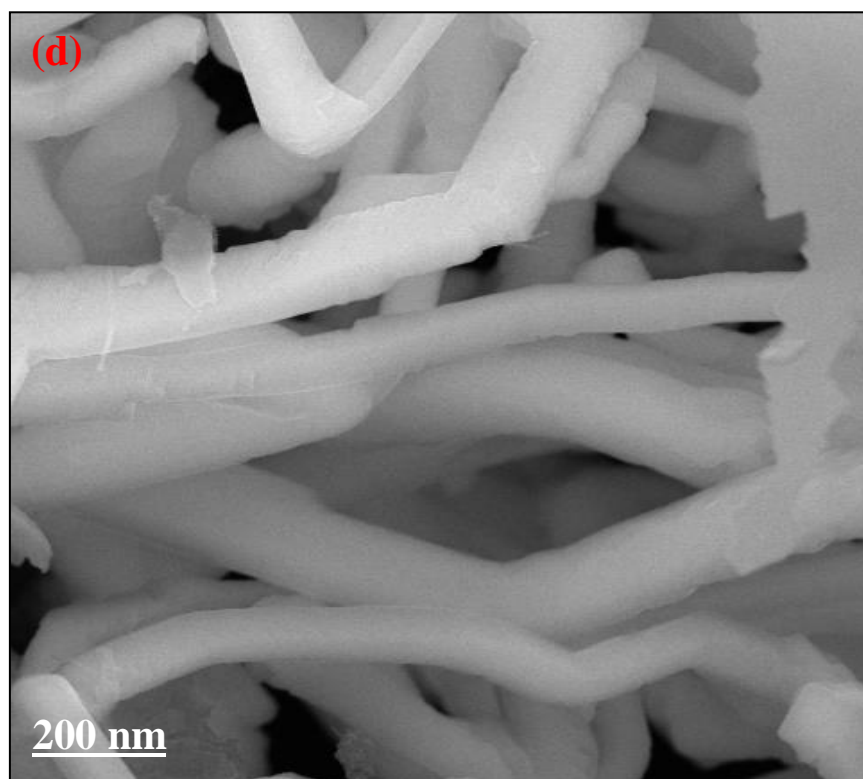


Figure 6.7: SEM images of tubular structures of boron taken randomly in each layer after ultracentrifugation (a) Layer 4 (Top), (b) Layer 3 (c) Layer 2, (d) Layer 1 (Bottom)

This was done by counting the number of tubular structures of boron present in a known area of each layer. The density of tubular structures of boron obtained from each layer is shown in Table 6.7.

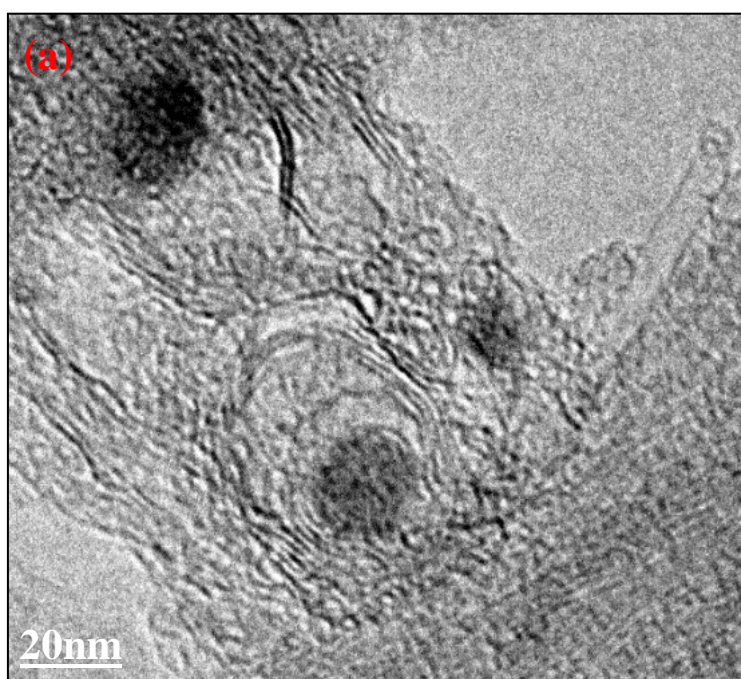
Table 6.7: Density of tubular structures of boron observed in the SEM images of each layer

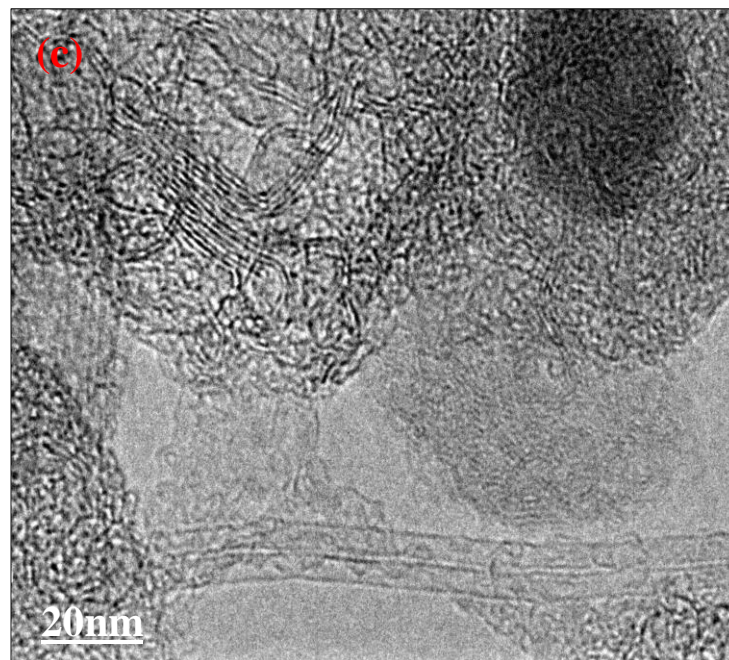
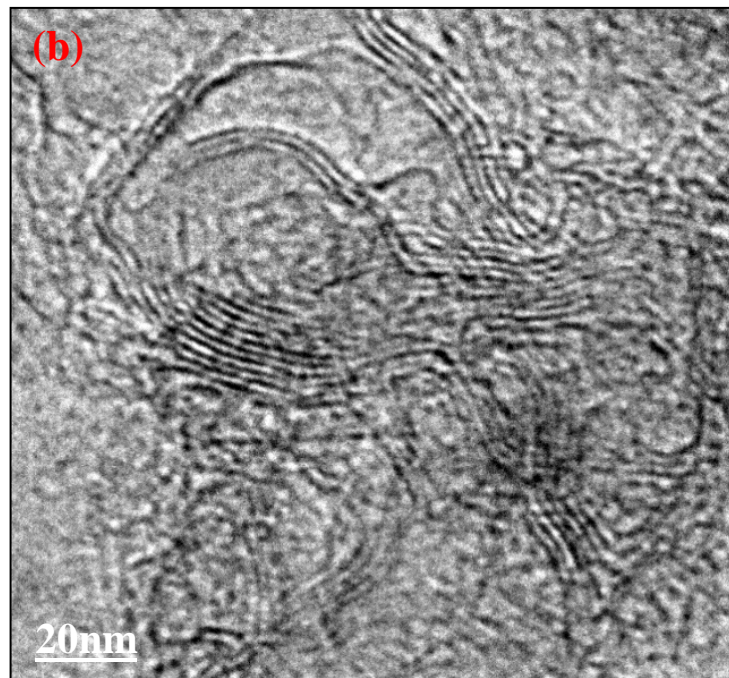
Sample layers	Number of tubular structures of boron per nm ²	% Error
Layer 4	2.5	0.20
Layer 3	2.0	0.11
Layer 2	1.0	0.09
Layer 1	0.8	0.07

Table 6.7. shows an increment in the trend of the density of tubular structures of boron obtained from layer 1 to 4. The percentage error was calculated by using the expression in the equation (6.6), as shown in Table 6.7.

$$\% \text{ Error} = \frac{\text{Exact value} - \text{Approximate value}}{\text{Exact value}} \times 100 \quad (6.6)$$

The same HRTEM micrographs were also analyzed to determine the distribution of diameters of the SWBNTs in each layer. This was carried out by measuring the diameters of nanotubes present in each layer of samples. The results obtained were analyzed to deduce the distribution of diameters of the SWBNTs found at different layers. The graphs distribution plotted for each layer were shown in Figure 6.9 for HRTEM. The histogram graphs plotted for each layer revealed the trend in their diameters. Table 6.8 showed a trend in the mean diameters of SWBNTs obtained from each layer. The distribution of the diameters of SWBNTs measured in HRTEM micrographs were fitted to the lognormal distribution. The results obtained are displayed in Table 6.8, for HRTEM.





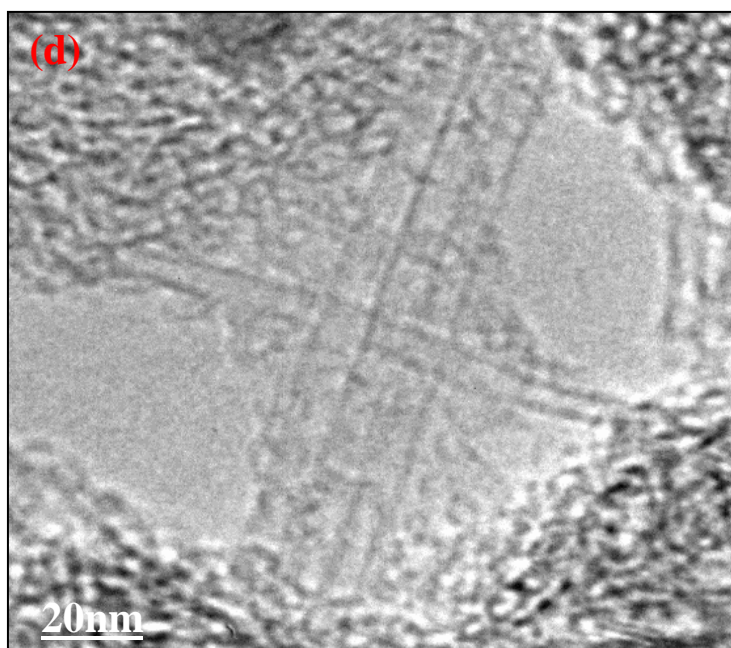
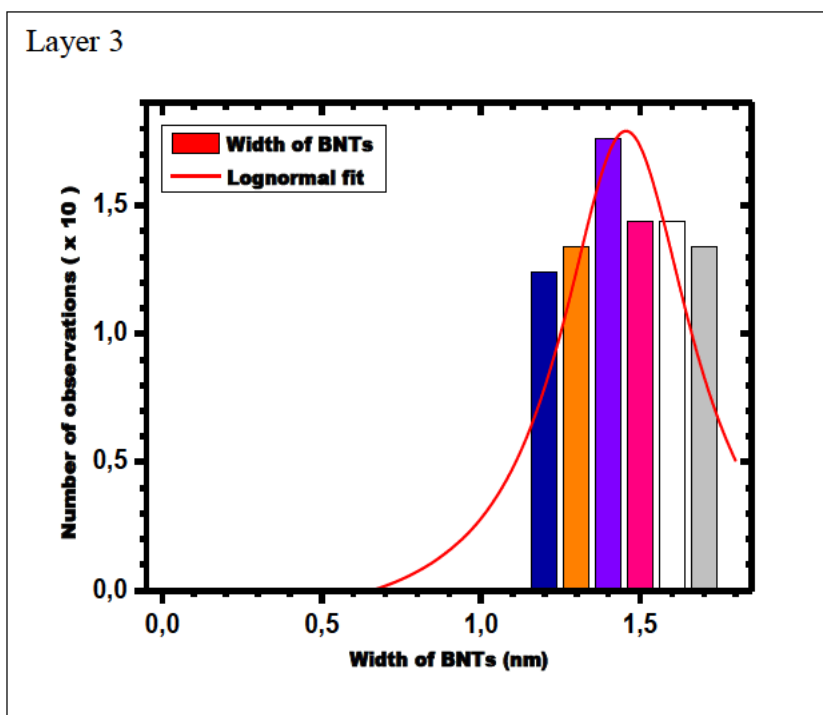
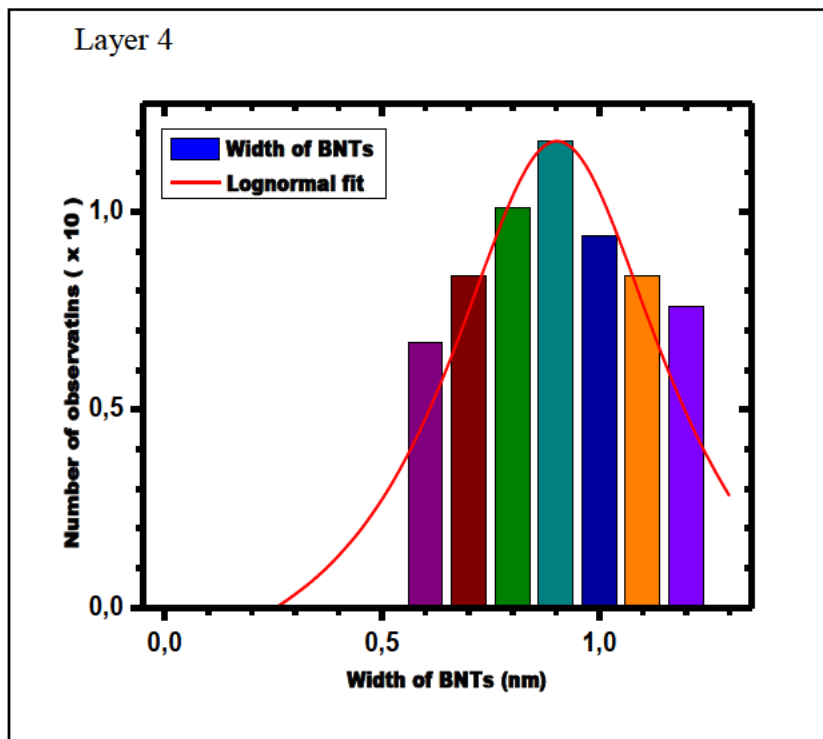


Figure 6.8: HRTEM images of SWBNTs taken at random positions after ultracentrifugation (a) Layer 4(Top), (b) Layer 3 (c) Layer 2, (d) Layer 1(Bottom)

Table 6.8: SWBNTs diameters measured in HRTEM images from layer 4 to 1 and statistical parameters for lognormal distribution fitting.

Sample layers	Mean	Median	Minimum	Maximum	Variance	Standard deviation
Layer 4	0.90	0.90	0.67	1.20	0.03	0.18
Layer 3	1.14	1.30	1.20	1.72	0.08	0.28
Layer 2	1.43	1.39	1.50	2.10	0.03	0.18
Layer 1	1.69	1.74	1.60	2.30	0.05	0.22



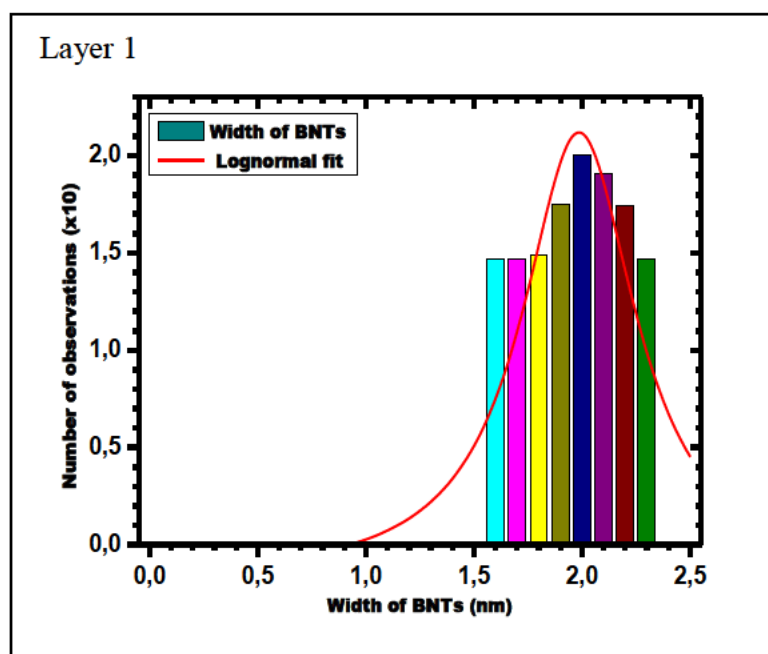
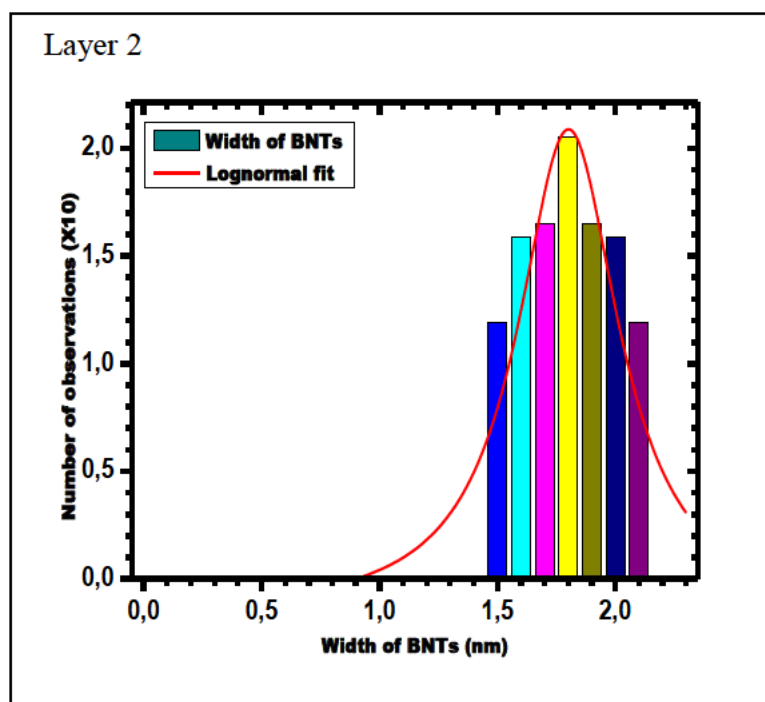


Figure 6.9: Distribution of the diameters of SWBNTs measured in HRTEM images from layer 4 to 1 and fitted to log-normal distribution

The distributions in Figure 6.9 showed the average diameters of SWBNTs obtained from different layers. The ultracentrifugation revealed the differences in the diameters obtained in HRTEM, according to the position of each layer. The difference in the diameter of SWBNTs is due to the position layer at which each sample was collected. Variation in the diameters also depend on the density gradient medium (DGM) of each layer. In summary, we can separate SWBNTs with variation in the diameters according to their layers via the ultracentrifugation method. We can use these results obtained from image analyses to confirm that the separation of any SWBNTs can be performed through the ultracentrifugation technique.

7. Conclusions and Future Work

7.1 Conclusions

In this dissertation, a dual pulse laser ablation technique was set up and optimized for the synthesis of single-walled boron nanotubes (SWBNTs) and other related boron nanomaterials (BNMs) in a scalable manner. This technique is advantageous over other methods such as chemical vapour deposition, ball milling, and arc discharge etc, because this technique is repeatable. The technique involved the use of argon/nitrogen as carrier gas, pressure, furnace temperature and catalysts to synthesize SWBNTs. This was achieved by ablating the targets simultaneously with laser wavelengths of 1064 and 532 nm for thirty minutes, to synthesize nanomaterials having SWBNTs. It was found that nickel (Ni) and cobalt (Co) when utilized as catalysts assisted in the synthesis of SWBNTs. Also, the optimum conditions for SWBNTs growth using dual pulse laser ablation set up were determined. It was discovered that SWBNTs growth initiates at a high temperature of 1100 °C.

Purification of SWBNTs was done to remove Optiprep which was used as a density gradient medium and sodium cholate as a surfactant. This was achieved by mixing the supernatant of SWBNTs obtained after centrifugation, with 10 ml of ethanol and subsequently sonicated. Thereafter, the mixture was centrifuged using an ultracentrifuge.

Extensive characterization of the SWBNTs was carried out with different techniques such as field emission scanning electron microscopy (FESEM), high-resolution transmission electron microscopy (HRTEM), energy dispersive x-ray spectroscopy (EDS), x-ray diffraction (XRD), Raman spectroscopy (RS), ultraviolet-visible (UV-VIS), photoluminescence (PL), and vibration sample magnetometer (VSM). The results to this characterization can be summarized as follows.

Firstly, a variation of the nitrogen gas pressure, gas flow rate, and furnace temperature influenced the quantity and type of as-prepared BNMs synthesized using hexagonal boron nitride (h-BN), since these parameters affected the plasma dynamics. SEM analysis revealed the spherical and tubular structures of SWBNTs synthesized using h-BN, with a diameters in nanometers and length in microns.

The HRTEM image of the SWBNTs showed a significant hollow structure with a diameter of 0.4 nm and 2 microns in length. HRTEM analysis revealed lattice spacing of 0.34 nm from their lattice fringes in accordance with a theoretical calculation. EDS data from electron microscopy revealed the composition of the SWBNTs to be 99% pure boron with small percentage of 0.05% Ni and Co which were used as catalysts in the synthesis. Raman spectroscopy revealed Raman active lines below 500 cm^{-1} (144, 210, 267, 343 and 502 cm^{-1}) which was consistent with tubular boron structure and corresponding to the radial breathing mode (RBM) of similar peaks that were also reported for the single-walled carbon nanotubes (SWCNTs). Raman spectrum showed three peaks at 788, 878 and 965 cm^{-1} that occurred in α -boron which confirmed SWBNTs to be α -BNTs. Overall it was found that nitrogen pressure of 400 Torr, flow rate of 200 sccm and temperature of $1100\text{ }^{\circ}\text{C}$ produced SWBNTs at a rate of 100 mg/h, with the small diameter of 0.4 nm and RBM below 500 cm^{-1} .

Secondly, SWBNTs synthesized using boron target with parameters such as an argon gas pressure, gas flow rate, furnace temperature and catalysts influenced the quality and quantity of as-prepared SWBNTs. SEM analysis showed the tubular structure of SWBNTs with a diameter in nanometers and microns in length. HRTEM analysis revealed open ends and hollow structures of the SWBNTs, with diameter, ranging from 1.47 to 2 nm and 2 microns in length. The lattice spacing of 0.38 nm from lattice fringes was observed in HRTEM analysis in accordance with a theoretical calculation. EDS analysis from both SEM and HRTEM revealed the composition of the SWBNTs to be 97% pure boron with 0.04% Ni and Co which were used as catalysts in the synthesis. Raman spectrum of SWBNTs is characterized by peaks centered at A_{1g} and E_g modes. The G peak is associated with E_g mode (stretching vibration) in the basal plane of boron, therefore the peak at 493 cm^{-1} and 621 cm^{-1} are corresponding to the G peak in SWBNTs. At wavenumber below 500 cm^{-1} (210 cm^{-1}) assigned as a radial breathing mode typically for tubular structures, the peak at 493 cm^{-1} is associated with one of the peaks from alpha-boron clusters at 493 cm^{-1} and confirmed the material to be alpha-SWBNTs. It was found that an argon gas pressure (400 Torr), gas flow rate (200 sccm), and furnace temperature ($1100\text{ }^{\circ}\text{C}$) produced alpha-SWBNTs of 97% pure boron, at a rate of 98 mg/h, with diameter ranging from 1.47 to 2 nm and RBM below 500 cm^{-1} (210 cm^{-1}).

Thirdly, the dissertation also focused on the separation of SWBNTs into different diameters by using the density gradient ultracentrifugation (DGU) method. SEM analysis revealed that SWBNTs were tubular and spherical in all the layers with a diameter in nanometers and length in microns. HRTEM analysis showed different kinds of SWBNTs obtained with variations in their diameters between 1.43 to 2.05 nm and a length of 1.20 to 2.10 microns with respect to the layers. It was noticed that SWBNTs showed a significant hollow structure with small diameters of 1.43 nm were found at a lower density in contrast to SWBNTs with large diameters of 2.05 nm which were observed at a higher density of optiprep. EDS analysis from both electron microscopy revealed the composition of the SWBNTs to be 96% pure boron with a small percentage of 0.06% Ni and Co which were utilized as catalysts in the synthesis. Micro Raman spectroscopy analysis was also performed on each layer with the excitation 514 nm wavelength laser. The Raman active mode below 500 cm^{-1} (157 , 223 , 224 and 250 cm^{-1}) was observed from all the layers which were attributed to tubular structures, corresponding to the radial breathing mode and similar peaks were observed in single-walled carbon nanotubes. Raman active peaks from alpha- boron clusters were observed at 782 , 787 , 878 , 887 , 949 , and 963 cm^{-1} which confirmed boron nanotubes as alpha-SWBNTs. Overall, it was found that SWBNTs with small diameters of 1.43 nm were observed from lower density (layer 4). In layers 2 and 3 the SWBNTs of outer diameters 1.71 and 1.93 nm were obtained, whereas large diameters of 2.05 nm SWBNTs were observed at higher density (layer 1).

In conclusion, the dual pulsed laser ablation technique for synthesizing SWBNTs was investigated and optimized. The type and quality of SWBNTs which were synthesized could be achieved by using parameters and catalysts while investigating the type of SWBNTs that could be synthesized. The application of DGU to separate SWBNTs into different diameters at different layers was carried out. This method could be used to determine which particular SWBNTs species would be suitable for a particular application.

7.2 Future Work

While, in this dissertation, the DGU was used to separate SWBNTs into different diameters, the technique employed could be applied to other materials. Further work is also required in scaling up of the dual pulse laser ablation method on developed SWBNTs for commercialization. Raman spectra analysis, electrical and mechanical measurements of SWBNTs need more investigations. Optical emission spectroscopy (OES) should be used to study nucleation and growth of SWBNTs and it could also be applied to other materials systems where significant self-assembly of the atom from the vapour phase into an ordered superstructure occurs. The Boltzmann plot method should be employed to determine electron temperature, also the use the of Saha- Boltzmann equation to evaluate emissions from successful ionization to determine the electron temperature of SWBNTs. Overall, future research should focus on the optimization and separation of SWBNTs with the density gradient ultracentrifugation technique. In addition, the purification of SWBNTs after the separation with chemical methods for better application should be investigated. This anticipated much-improved SWBNTs can be marketed as new products to companies in the world for various technological applications.

References

1. Golikova, O., *et al.*, *Thermal conductivity of boron and of its crystal structure analoges*. *physica status solidi (a)*, 1974. **21**(2): p. 405-412.
2. Davidson, G.R. and R.L. Bassett, *Application of boron isotopes for identifying contaminants such as fly ash leachate in groundwater*. *Environmental science & technology*, 1993. **27**(1): p. 172-176.
3. Samsonov, G., *et al.*, *Boron and refractory borides*. 2012: Springer Science & Business Media.
4. Takeshima, E., *et al.*, *Radiation shield and shielding material with excellent heat-transferring property*. 1991, Google Patents.
5. Coderre, J.A. and G.M. Morris, *The radiation biology of boron neutron capture therapy*. *Radiation research*, 1999. **151**(1): p. 1-18.
6. Barth, R.F., *A critical assessment of boron neutron capture therapy: an overview*. *Journal of Neuro-oncology*, 2003. **62**(1-2): p. 1-5.
7. Barth, R., *et al.*, *Boron neutron capture therapy for cancer*. *Scientific American*, 1990. **263**(4): p. 100-107.
8. Tilekar, K., *et al.*, *Preparation of high purity amorphous boron powder*. *Defence Science Journal*, 2005. **55**(4): p. 471.
9. Lin, J.-F., *et al.*, *Amorphous boron gasket in diamond anvil cell research*. *Review of scientific instruments*, 2003. **74**(11): p. 4732-4736.
10. Mondal, S., *et al.*, *Disorder and defects are not intrinsic to boron carbide*. *Scientific Reports*, 2016. **6**: p. 19330.
11. Mondal, S., *et al.*, *Experimental evidence of orbital order in α -B 12 and γ -B 28 polymorphs of elemental boron*. *Physical Review B*, 2013. **88**(2): p. 024118.
12. Mondal, S., *et al.*, *Electron-Deficient and Polycenter Bonds in the High-Pressure γ - B 28 Phase of Boron*. *Physical review letters*, 2011. **106**(21): p. 215502.
13. Eremets, M.I., *et al.*, *Superconductivity in boron*. *Science*, 2001. **293**(5528): p. 272-274.
14. Albert, B. and H. Hillebrecht, *Boron: elementary challenge for experimenters and theoreticians*. *Angewandte Chemie International Edition*, 2009. **48**(46): p. 8640-8668.
15. Parakhonskiy, G., *et al.*, *Experimental pressure-temperature phase diagram of boron: resolving the long-standing enigma*. *Scientific reports*, 2011. **1**: p. 96.

16. Masago, A., *et al.*, *Crystal stability of α - and β -boron*. Physical Review B, 2006. **73**(10): p. 104102.
17. Garrett, D.E., *Borates: Handbook of deposits, processing, properties, and use*. 1998: Elsevier.
18. Hayun, S., *et al.*, *The effect of aluminum on the microstructure and phase composition of boron carbide infiltrated with silicon*. Materials Chemistry and Physics, 2009. **118**(2-3): p. 490-495.
19. Telle, R., *Borides-a new generation of highly resistant materials?* Chemie in Unserer Zeit, 1988. **22**(3): p. 93-99.
20. Riedel, R., *Novel ultrahard materials*. Advanced materials, 1994. **6**(7-8): p. 549-560.
21. Amendola, S., *High energy density boride batteries*. 1999, Google Patents.
22. Schell, G., *et al.*, *Electronic structure and superconductivity in metal hexaborides*. Physical Review B, 1982. **25**(3): p. 1589.
23. Werheit, H., *Boron-rich solids: a chance for high-efficiency high-temperature thermoelectric energy conversion*. Materials Science and Engineering: B, 1995. **29**(1-3): p. 228-232.
24. Imai, Y., *et al.*, *Screening of the possible boron-based n-type thermoelectric conversion materials on the basis of the calculated densities of states of metal borides and doped β -boron*. Intermetallics, 2001. **9**(8): p. 721-734.
25. Kitamura, J., *et al.*, *Formation of boron carbide coating by electromagnetically accelerated plasma spraying*. Surface and Coatings Technology, 2003. **169**: p. 324-327.
26. Kitamura, J., *et al.*, *Boron carbide coating by electromagnetically accelerated plasma spraying*. Journal of thermal spray technology, 2003. **12**(1): p. 70-76.
27. Fanchini, G., *et al.*, *Behavior of disordered boron carbide under stress*. Physical review letters, 2006. **97**(3): p. 035502.
28. Parakhonskiy, G., *et al.*, *High pressure synthesis and investigation of single crystals of metastable boron phases*. High Pressure Research, 2013. **33**(3): p. 673-683.
29. Weintraub, E., *Preparation and properties of pure boron*. Trans. Amer. Electrochem. Soc., 1909. **16**: p. 165-184.
30. McCarty, L., *et al.*, *A new crystalline modification of boron*. Journal of the American Chemical Society, 1958. **80**(10): p. 2592-2592.

31. Horn, F.H., *On the crystallization of simple rhombohedral boron from platinum*. Journal of the electrochemical society, 1959. **106**(10): p. 905-906.
32. Amberger, E. and W. Dietze, *Zur Bildung von α -rhomboedrischem, rotem Bor*. Zeitschrift für anorganische und allgemeine Chemie, 1964. **332**(3-4): p. 131-139.
33. Wald, F., *STABILITY OF THE RED ALPHA-RHOMBOHEDRAL B MODIFICATION*. Electron Technol, 1970. **3**(1): p. 103-108.
34. Parakhonskiy, G., *et al.*, *High pressure synthesis of single crystals of α -boron*. Journal of Crystal Growth, 2011. **321**(1): p. 162-166.
35. Will, G. and B. Kiefer, *Electron Deformation Density in Rhombohedral α -Boron*. Zeitschrift für anorganische und allgemeine Chemie, 2001. **627**(9): p. 2100-2104.
36. Parakhonskiy, G., *et al.*, *Raman spectroscopy investigation of alpha boron at elevated pressures and temperatures*. Solid State Communications, 2013. **154**: p. 34-39.
37. Decker, B. and J. Kasper, *The crystal structure of a simple rhombohedral form of boron*. Acta Crystallographica, 1959. **12**(7): p. 503-506.
38. Morosin, B., *et al.* *Rhombohedral crystal structure of compounds containing boron-rich icosahedra*. in *AIP Conference Proceedings*. 1986. AIP.
39. Switendick, A. and B. Morosin. *Electronic charge density and bonding in α -boron: An experimental-theoretical comparison*. in *AIP Conference Proceedings*. 1991. AIP.
40. Parakhonskiy, G., *Synthesis and investigation of boron phases at high pressures and temperatures*. 2012.
41. Terauchi, M., *et al.*, *Electron Energy-Loss Spectroscopy Study of the Electronic Structure of α -Rhombohedral Boron*. Journal of Solid State Chemistry, 1997. **133**(1): p. 156-159.
42. Richter, W. and K. Ploog, *Raman-active phonons in α -boron*. physica status solidi (b), 1975. **68**(1): p. 201-205.
43. Vast, N., *et al.*, *Lattice dynamics of icosahedral α -boron under pressure*. Physical review letters, 1997. **78**(4): p. 693.
44. Werheit, H., *et al.*, *Raman effect in icosahedral boron-rich solids*. Science and technology of advanced materials, 2010. **11**(2): p. 023001.
45. Beckel, C.L., *et al.*, *Lattice vibrations of the icosahedral solid α -boron*. Physical Review B, 1991. **44**(6): p. 2535.

46. Shirai, K. and H. Katayama–Yoshida, *The Narrow Raman Linewidth of a Librational Mode of α -Rhombohedral Boron and Its Anharmonic Effects*. Journal of the Physical Society of Japan, 1998. **67**(11): p. 3801-3808.
47. Chuvashova, I., *et al.*, *High-pressure behavior of α -boron studied on single crystals by X-ray diffraction, Raman and IR spectroscopy*. Journal of Solid State Chemistry, 2017. **245**: p. 50-60.
48. Kaneshige, M., *et al.*, *Measurement of electrical resistance and raman spectrum of α -boron under high pressure*. Journal of the Physical Society of Japan, 2007. **76**(Suppl. A): p. 19-20.
49. Shirai, K., *et al.*, *Structural Study of α -Rhombohedral Boron at High Pressures*. Journal of the Physical Society of Japan, 2011. **80**(8): p. 084601.
50. Werheit, H. and H. Haupt, *Lattice Vibrations, MIR and FIR Optical Properties of Boron and Icosahedral Boron-Rich Borides I. Alpha-Rhombohedral Structure Group*. Zeitschrift für Naturforschung A, 1987. **42**(9): p. 925-934.
51. Shirai, K. and S. Gonda, *Polar Vibrations and the effective charges of the icosahedral boron solid*. Journal of Physics and Chemistry of Solids, 1996. **57**(1): p. 109-123.
52. Werheit, H. and U. Kuhlmann, *Is the established structure of α -rhombohedral boron correct? Comparative study of IR-active phonons with B₆O, B₄, 3C and β -rhombohedral boron*. Journal of Physics: Condensed Matter, 2012. **24**(30): p. 305401.
53. Weber, W.t. and M. Thorpe, *Vibrations in icosahedral boron molecules and in elemental boron solids*. Journal of Physics and Chemistry of Solids, 1975. **36**(9): p. 967-974.
54. Cueilleron, J. and J. Viala, *The chemical and pyrometallurgical purification of β rhombohedral boron*. Journal of the Less Common Metals, 1979. **67**(2): p. 333-337.
55. Sands, D.E. and J. Hoard, *Rhombohedral elemental boron*. Journal of the American Chemical Society, 1957. **79**(20): p. 5582-5583.
56. Hughes, R., *et al.*, *The structure of β -rhombohedral boron*. Journal of the American Chemical Society, 1963. **85**(3): p. 361-362.
57. Hoard, J., *et al.*, *The structure analysis of β -rhombohedral boron*. Journal of Solid State Chemistry, 1970. **1**(2): p. 268-277.
58. Callmer, B., *An accurate refinement of the β -rhombohedral boron structure*. Acta Crystallographica Section B, 1977. **33**(6): p. 1951-1954.

59. Slack, G., *et al.*, *The crystal structure and density of β -rhombohedral boron*. Journal of Solid State Chemistry, 1988. **76**(1): p. 52-63.
60. Spitzer, W. and W. Kaiser, *Optical properties of crystalline boron*. Physical Review Letters, 1958. **1**(7): p. 230.
61. Greiner, E. and J. Gutowski, *Electrical resistivity of boron*. Journal of Applied Physics, 1957. **28**(11): p. 1364-1365.
62. Tsagareishvili, G., *et al.*, *Estimation of some thermoelastic properties of β rhombohedral boron in wide ranges of temperature and pressure*. Journal of the Less Common Metals, 1980. **75**(1): p. 141-145.
63. Mailhot, C., J. Grant, and A. McMahan, *High-pressure metallic phases of boron*. Physical Review B, 1990. **42**(14): p. 9033.
64. Albert, B. and H. Hillebrecht, *Boron: elementary challenge for experimenters and theoreticians*. Angew Chem Int Ed Engl, 2009. **48**(46): p. 8640-68.
65. Nelmes, R., *et al.*, *Neutron-and x-ray-diffraction measurements of the bulk modulus of boron*. Physical Review B, 1993. **47**(13): p. 7668.
66. Ma, Y., *et al.*, *High-pressure high-temperature x-ray diffraction of β -boron to 30 GPa*. Physical Review B, 2003. **67**(17): p. 174116.
67. Sanz, D., *et al.*, *Equation of state and pressure induced amorphization of β -boron from X-ray measurements up to 100 GPa*. Physical review letters, 2002. **89**(24): p. 245501.
68. Zarechnaya, E.Y., *et al.*, *Synthesis of an orthorhombic high pressure boron phase*. Science and technology of advanced materials, 2009. **9**(4): p. 044209.
69. Zarechnaya, E.Y., *et al.*, *Superhard semiconducting optically transparent high pressure phase of boron*. Physical review letters, 2009. **102**(18): p. 185501.
70. Oganov, A.R., *et al.*, *Ionic high-pressure form of elemental boron*. Nature, 2009. **457**(7231): p. 863.
71. Yu, T., *et al.*, *Ionic high-pressure form of elemental boron*. 2009.
72. Zarechnaya, E., *et al.*, *Polarized Raman spectroscopy of high-pressure orthorhombic boron phase*. High Pressure Research, 2009. **29**(4): p. 530-535.
73. Fan, C., J. Li, and L. Wang, *Phase transitions, mechanical properties and electronic structures of novel boron phases under high-pressure: A first-principles study*. Scientific reports, 2014. **4**: p. 6786.

74. Aydin, S. and M. Simsek, *First-principles calculations of elemental crystalline boron phases under high pressure: Orthorhombic B28 and tetragonal B48*. Journal of Alloys and Compounds, 2011. **509**(17): p. 5219-5229.
75. Solozhenko, V., *et al.*, *On the hardness of a new boron phase, orthorhombic γ -B 28*. Journal of superhard materials, 2008. **30**(6): p. 428-429.
76. Zarechnaya, E., *et al.*, *Pressure-induced isostructural phase transformation in γ -B 28*. Physical Review B, 2010. **82**(18): p. 184111.
77. Dubrovinskaia, N., *et al.* *Pressure-induced isostructural phase transformation in gamma-B28 (poster)*. in *26th European Crystallographic Meeting (ECM26)*. 2010.
78. Laubengayer, A., *et al.*, *Boron. I. Preparation and properties of pure crystalline boron*. Journal of the American Chemical Society, 1943. **65**(10): p. 1924-1931.
79. Will, G. and K. Ploog, *Crystal structure of I-tetragonal boron*. Nature, 1974. **251**(5474): p. 406.
80. Longuet-Higgins, H.C. and M.d.V. Roberts, *The electronic structure of the borides MB6*. Proc. R. Soc. Lond. A, 1954. **224**(1158): p. 336-347.
81. Parakhonskiy, G., *Synthesis and investigation of boron phases at high pressures and temperatures*. 2012.
82. Oxford, O.E., *The Oxford English Dictionary*. 2018, Oxford: Oxford University Press.
83. Martínez, I.G.G., *Synthesis and characterization of boron-and aluminium-based nanostructures*. 2011, IFW Dresden.
84. Lea, S., *Growth and Characterisation of Boron Rich Nanomaterials*. 2010, University of York.
85. Xia, Y., *et al.*, *One-dimensional nanostructures: synthesis, characterization, and applications*. Advanced materials, 2003. **15**(5): p. 353-389.
86. Tian, J., *et al.*, *Patterned boron nanowires and field emission properties*. Applied Physics Letters, 2009. **94**(8): p. 083101.
87. Calabri, L., *et al.*, *Resonance of curved nanowires*. Journal of Physics: Condensed Matter, 2006. **18**(33): p. S2175.
88. Huang, Y., *et al.*, *Logic gates and computation from assembled nanowire building blocks*. Science, 2001. **294**(5545): p. 1313-1317.
89. Wu, B., *et al.*, *Microstructure-hardened silver nanowires*. Nano letters, 2006. **6**(3): p. 468-472.

90. Wang, X., *et al.*, *Single crystalline boron nanocones: Electric transport and field emission properties*. *Advanced Materials*, 2007. **19**(24): p. 4480-4485.
91. Pan, Z., *et al.*, *Nanobelts of semiconducting oxides*. *Science*, 2001. **291**(5510): p. 1947-1949.
92. Shan, G.-B. and G.P. Demopoulos, *The synthesis of aqueous-dispersible anatase TiO₂ nanoplatelets*. *Nanotechnology*, 2009. **21**(2): p. 025604.
93. Yan, H., *et al.*, *Correction: ZnO Nanoribbon Microcavity Lasers; Advanced Materials, 2003, 15, 1907*. *Advanced Materials*, 2003. **15**(24): p. 2052-2052.
94. Xu, J., *et al.*, *Ultrathin Single-Crystalline Boron Nanosheets for Enhanced Electro-Optical Performances*. *Advanced Science*, 2015. **2**(6): p. 1500023.
95. Xu, T.T., *et al.*, *Crystalline boron nanoribbons: synthesis and characterization*. *Nano Letters*, 2004. **4**(5): p. 963-968.
96. Wang, Z., *et al.*, *Catalyst-free fabrication of single crystalline boron nanobelts by laser ablation*. *Chemical Physics Letters*, 2003. **368**(5-6): p. 663-667.
97. Yu, J., *et al.*, *Interfacial modification of boron nitride nanoplatelets for epoxy composites with improved thermal properties*. *Polymer*, 2012. **53**(2): p. 471-480.
98. Lin, C.H., *et al.*, *In situ Nanomechanical Characterization of Single-Crystalline Boron Nanowires by Buckling*. *Small*, 2010. **6**(8): p. 927-931.
99. Ding, W., *et al.*, *Mechanics of crystalline boron nanowires*. *Composites Science and Technology*, 2006. **66**(9): p. 1112-1124.
100. Otten, C.J., *et al.*, *Electrical Properties of Boron Nanowires*. 2005. **917**: p. 362-375.
101. Wang, D., *et al.*, *Electrical transport in boron nanowires*. *Applied physics letters*, 2003. **83**(25): p. 5280-5282.
102. Favia, P., *et al.*, *Order and disorder in boron phases*. *Microscopy Microanalysis Microstructures*, 1996. **7**(4): p. 225-234.
103. Yunpeng, G., *et al.*, *Crystalline boron nanowires grown by magnetron sputtering*. *Materials Science and Engineering: A*, 2006. **434**(1-2): p. 53-57.
104. Liu, F., *et al.*, *Effect of Contact Mode on the Electrical Transport and Field-Emission Performance of Individual Boron Nanowires*. *Advanced Functional Materials*, 2010. **20**(12): p. 1994-2003.
105. Sun, L., *et al.*, *Pressure-induced superconducting state in crystalline boron nanowires*. *Physical Review B*, 2009. **79**(14).

106. Tian, Y., *et al.*, *Synthesis of monodisperse CoPt₃ nanocrystals and their catalytic behavior for growth of boron nanowires*. Nano Research, 2011. **4**(8): p. 780-787.
107. Sun, L., *et al.*, *Pressure-induced superconducting state in crystalline boron nanowires*. Physical Review B, 2009. **79**(14): p. 140505.
108. Tian, Y., *et al.*, *Synthesis of monodisperse CoPt₃ nanocrystals and their catalytic behavior for growth of boron nanowires*. Nano Research, 2011. **4**(8): p. 780.
109. Rupesinghe, N.L., *et al.*, *Field emission vacuum power switch using vertically aligned carbon nanotubes*. Journal of Vacuum Science & Technology B: Microelectronics and Nanometer Structures, 2003. **21**(1): p. 338.
110. Palnitkar, U.A., *et al.*, *Remarkably low turn-on field emission in undoped, nitrogen-doped, and boron-doped graphene*. Applied Physics Letters, 2010. **97**(6): p. 063102.
111. Tian, J., *et al.*, *Boron nanowires for flexible electronics*. Applied Physics Letters, 2008. **93**(12): p. 122105.
112. Otten, C.J., *et al.*, *Electrical properties of boron nanowires*. 2006, ACS Publications.
113. Sezer, A.O. and J. Brand, *Chemical vapor deposition of boron carbide*. Materials Science and Engineering: B, 2001. **79**(3): p. 191-202.
114. Guo, L., *et al.*, *Nucleation and Growth of Boron Nanowires on ZrB₂ Particles*. Chemical Vapor Deposition, 2006. **12**(7): p. 448-452.
115. Wang, Y., *et al.*, *Amorphous feather-like boron nanowires*. Chemical physics letters, 2003. **367**(3): p. 495-499.
116. Yang, Q., *et al.*, *Aligned single crystal boron nanowires*. Chemical Physics Letters, 2003. **379**(1-2): p. 87-90.
117. Yoon, J.-W. and K.B. Shim, *Growth of crystalline boron nanowires by pulsed laser ablation*. Journal of Ceramic Processing Research, 2011. **12**(2): p. 199-201.
118. Zhang, Y.J., *et al.*, *Study of the growth of boron nanowires synthesized by laser ablation*. Chemical Physics Letters, 2004. **385**(3-4): p. 177-183.
119. Hao, Z., *et al.*, *Influences of Si and Ni Catalysts on the Growth of Boron Nanowires*. Rare Metal Materials and Engineering, 2012. **41**(10): p. 1717-1720.
120. Ciuparu, D., *et al.*, *Synthesis of pure boron single-wall nanotubes*. The Journal of Physical Chemistry B, 2004. **108**(13): p. 3967-3969.
121. Liu, F., *et al.*, *Metal-like single crystalline boron nanotubes: synthesis and in situ study on electric transport and field emission properties*. Journal of Materials Chemistry, 2010. **20**(11): p. 2197.

122. Liu, J. and Z. Iqbal, *Facile synthesis of pure boron nanotubes and nanofibers*. MRS Online Proceedings Library Archive, 2011. **1307**.
123. Iijima, S., *Helical microtubules of graphitic carbon*. nature, 1991. **354**(6348): p. 56.
124. Zhu, W., *et al.* *Very large current density from carbon nanotube field emitters*. in *Electron Devices Meeting, 1999. IEDM'99. Technical Digest. International.* 1999. IEEE.
125. Coville, M.K.M.a.P.N.J., *Synthesis and Characterization of Single-Walled Carbon Nanotubes by Dual Laser Vaporization*. 2010.
126. Liu, F., *et al.*, *Metal-like single crystalline boron nanotubes: synthesis and in situ study on electric transport and field emission properties*. Journal of Materials Chemistry, 2010. **20**(11): p. 2197-2205.
127. Wang, X.J., *et al.*, *Single Crystalline Boron Nanocones: Electric Transport and Field Emission Properties*. Advanced Materials, 2007. **19**(24): p. 4480-4485.
128. Tian, J., *et al.*, *One-dimensional boron nanostructures: Prediction, synthesis, characterizations, and applications*. Nanoscale, 2010. **2**(8): p. 1375-1389.
129. Bullett, D., *Structure and bonding in crystalline boron and B12C3*. Journal of Physics C: Solid State Physics, 1982. **15**(3): p. 415.
130. Boustani, I. and A. Quandt, *Nanotubules of bare boron clusters: Ab initio and density functional study*. EPL (Europhysics Letters), 1997. **39**(5): p. 527.
131. Boustani, I., *et al.*, *New boron based nanostructured materials*. The Journal of Chemical Physics, 1999. **110**(6): p. 3176-3185.
132. Lau, K.C., *et al.*, *First-principles study of the stability and electronic properties of sheets and nanotubes of elemental boron*. Chemical Physics Letters, 2006. **418**(4-6): p. 549-554.
133. Kunstmann, J. and A. Quandt, *Broad boron sheets and boron nanotubes: An ab initio study of structural, electronic, and mechanical properties*. Physical Review B, 2006. **74**(3).
134. Bezugly, V., *et al.*, *Highly conductive boron nanotubes: transport properties, work functions, and structural stabilities*. ACS nano, 2011. **5**(6): p. 4997-5005.
135. Gay-Lussac, J.L. and L.J. Thénard, *Sur la décomposition et la recomposition de l'acide boracique*. Ann. Chim. Phys, 1808. **68**: p. 169-174.
136. Davy, H., *The Bakerian Lecture: An Account of Some New Analytical Researches on the Nature of Certain Bodies, Particularly the Alkalies, Phosphorus, Sulphur,*

- Carbonaceous Matter, and the Acids Hitherto Undecomposed; With Some General Observations on Chemical Theory.* Philosophical Transactions of the Royal Society of London, 1809. **99**: p. 39-104.
137. Blint, R.J. and W.A. Goddard, *The orbital description of the potential energy curves and properties of the lower excited states of the BH molecule.* Chemical Physics, 1974. **3**(3): p. 297-316.
138. Pople, J.A. and P. von Ragué Schleyer, *Singlet-triplet separation in borylene. comparison with the methylidyne cation, methylene and the amino cation.* Chemical physics letters, 1986. **129**(3): p. 279-281.
139. Dickerson, R.E. and W.N. Lipscomb, *Semitopological Approach to Boron-Hydride Structures.* The Journal of Chemical Physics, 1957. **27**(1): p. 212-217.
140. Eberhardt, W., *et al.*, Lipscomb, *The valence structure of the boron hydrides.* The Journal of Chemical Physics, 1954. **22**(6): p. 989-1001.
141. Meng, X., *et al.*, *Boron nanowires synthesized by laser ablation at high temperature.* Chemical physics letters, 2003. **370**(5-6): p. 825-828.
142. Yang, J., *et al.*, *Enhanced and switchable nanoscale thermal conduction due to van der Waals interfaces.* Nature nanotechnology, 2012. **7**(2): p. 91-95.
143. Saxena, S. and T.A. Tyson, *Insights on the atomic and electronic structure of boron nanoribbons.* Physical review letters, 2010. **104**(24): p. 245502.
144. Wang, Y. and X. Duan, *Crystalline boron nanowires.* Applied physics letters, 2003. **82**(2): p. 272-274.
145. Otten, C.J., *et al.*, *Crystalline boron nanowires.* Journal of the American Chemical Society, 2002. **124**(17): p. 4564-4565.
146. Evans, M., *et al.*, *Electronic and mechanical properties of planar and tubular boron structures.* Physical Review B, 2005. **72**(4): p. 045434.
147. Yang, J., *et al.*, *Enhanced and switchable nanoscale thermal conduction due to van der Waals interfaces.* Nature Nanotechnology, 2012. **7**(2): p. 91.
148. Zhang, Y., *et al.*, *Synthesis of crystalline boron nanowires by laser ablation.* Chemical Communications, 2002(23): p. 2806-2807.
149. Singh, A., *et al.*, *Probing properties of boron α -tubes by ab initio calculations.* Nano letters, 2008. **8**(5): p. 1314-1317.

150. Liu, F., *et al.*, *Fabrication of Vertically Aligned Single-Crystalline Boron Nanowire Arrays and Investigation of Their Field-Emission Behavior*. *Advanced Materials*, 2008. **20**(13): p. 2609-2615.
151. Weir, B., *et al.*, *Growth and structural analysis of an ordered boron monolayer in Si (100)*. *Physical Review B*, 1992. **46**(19): p. 12861.
152. Headrick, R., *et al.*, *Si (100)-(2× 1) boron reconstruction: Self-limiting monolayer doping*. *Applied physics letters*, 1990. **57**(26): p. 2779-2781.
153. Wang, Y., *et al.*, *Atomic structure and bonding of boron-induced reconstructions on Si (001)*. *Physical review letters*, 1995. **74**(3): p. 403.
154. Headrick, R., *et al.*, *Ordered monolayer structures of boron in Si (111) and Si (100)*. *Journal of Vacuum Science & Technology A: Vacuum, Surfaces, and Films*, 1991. **9**(4): p. 2269-2272.
155. Cabria, I., *et al.*, *Buckling in boron sheets and nanotubes*. *physica status solidi (a)*, 2006. **203**(6): p. 1105-1110.
156. Lau, K.C., *et al.*, *First-principles study of the stability and electronic properties of sheets and nanotubes of elemental boron*. *Chemical physics letters*, 2006. **418**(4): p. 549-554.
157. Lau, K.C. and R. Pandey, *Stability and electronic properties of atomistically-engineered 2D boron sheets*. *The Journal of Physical Chemistry C*, 2007. **111**(7): p. 2906-2912.
158. Zope, R.R., *et al.*, *Boron fullerenes: from B 80 to hole doped boron sheets*. *Physical Review B*, 2009. **79**(16): p. 161403.
159. Tang, H. and S. Ismail-Beigi, *Novel precursors for boron nanotubes: the competition of two-center and three-center bonding in boron sheets*. *Physical review letters*, 2007. **99**(11): p. 115501.
160. Galeev, T.R., *et al.*, *Deciphering the mystery of hexagon holes in an all-boron graphene α -sheet*. *Physical Chemistry Chemical Physics*, 2011. **13**(24): p. 11575-11578.
161. Wei, D., *et al.*, *Controllable unzipping for intramolecular junctions of graphene nanoribbons and single-walled carbon nanotubes*. *Nature Communications*, 2013. **4**: p. 1374.
162. Han, M.Y., *et al.*, *Energy band-gap engineering of graphene nanoribbons*. *Physical review letters*, 2007. **98**(20): p. 206805.

163. Hanley, L. and S.L. Anderson, *Production and collision-induced dissociation of small boron cluster ions*. Journal of Physical Chemistry, 1987. **91**(20): p. 5161-5163.
164. Kawai, R. and J.H. Weare, *Anomalous stability of B⁺ 13 clusters*. Chemical physics letters, 1992. **191**(3-4): p. 311-314.
165. Sowa-Resat, M.B., *et al.*, *Interaction of small boron cluster ions with HF*. The Journal of chemical physics, 1997. **106**(23): p. 9511-9522.
166. Boustani, I., *Systematic ab initio investigation of bare boron clusters: mDetermination of the geometry and electronic structures of B_n (n= 2–14)*. Physical Review B, 1997. **55**(24): p. 16426.
167. Boustani, I., *Structure and stability of small boron clusters. A density functional theoretical study*. Chemical Physics Letters, 1995. **240**(1-3): p. 135-140.
168. Lau, K.C. and R. Pandey, *The 2D-3D structural transition and chemical bonding in elemental boron nanoclusters*. Computing Letters, 2005. **1**(4): p. 259-270.
169. Li, Q.S., *et al.*, *Structure and stability of B₆, B₇, and B₈ clusters*. International Journal of Quantum Chemistry, 2003. **94**(5): p. 269-278.
170. Arvanitidis, A.G., *et al.*, *Quantum rules for planar boron nanoclusters*. Physical Chemistry Chemical Physics, 2014. **16**(34): p. 18311-18318.
171. Grimm, D., *et al.*, *Rolled-up nanomembranes as compact 3D architectures for field effect transistors and fluidic sensing applications*. Nano letters, 2012. **13**(1): p. 213-218.
172. Saxena, S., *Introduction to Boron Nanostructures*. Handbook of Boron Nanostructures, 2016. **1**.
173. Mukhopadhyay, S., *et al.* *Novel spherical boron clusters and structural transition from 2D quasi-planar structures to 3D double-rings*. in *Journal of Physics: Conference Series*. 2009. IOP Publishing.
174. Boustani, I., *New convex and spherical structures of bare boron clusters*. Journal of Solid State Chemistry, 1997. **133**(1): p. 182-189.
175. Gindulytė, A., *et al.*, *Proposed boron nanotubes*. Inorganic chemistry, 1998. **37**(25): p. 6544-6545.
176. Dresselhaus, S., *et al.*, *Science of fullerenes and carbon nanotubes: their properties and applications*. 1996: Academic press.
177. Odom, T.W., *et al.*, *Atomic structure and electronic properties of single-walled carbon nanotubes*. Nature, 1998. **391**(6662): p. 62-64.

178. Quandt, A. and I. Boustani, *Boron nanotubes*. ChemPhysChem, 2005. **6**(10): p. 2001-2008.
179. Yang, X., *et al.*, *Ab initio prediction of stable boron sheets and boron nanotubes: structure, stability, and electronic properties*. Physical Review B, 2008. **77**(4): p. 041402.
180. Liu, J., *Synthesis and Development of Boron Nanotubes and Metal/ceramic-carbon Nanotube Composites*. 2011, New Jersey Institute of Technology, Committee for the Interdisciplinary Program in Materials Science and Engineering.
181. Gonzalez Szwacki, N., *et al.*, *Erratum: B80 Fullerene: An Ab Initio Prediction of Geometry, Stability, and Electronic Structure [Phys. Rev. Lett. 98, 166804 (2007)]*. Physical Review Letters, 2008. **100**(15).
182. Yang, J. and R. Schaller, *Mechanical spectroscopy of Mg reinforced with Al₂O₃ short fibers and C nanotubes*. Materials Science and Engineering: A, 2004. **370**(1-2): p. 512-515.
183. Lau, K., *et al.*, *First-principles study of crystalline bundles of single-walled boron nanotubes with small diameter*. Journal of Physics: Condensed Matter, 2008. **20**(12): p. 125202.
184. Lau, K.C. and R. Pandey, *Thermodynamic stability of novel boron sheet configurations*. The Journal of Physical Chemistry B, 2008. **112**(33): p. 10217-10220.
185. Dinh, L., *et al.*, *Synthesis and characterization of Si/Cs/O nanocluster thin films with negative electron affinity*. Physical Review B, 1999. **59**(23): p. 15513.
186. Van der Weide, J. and R. Nemanich, *Influence of interfacial hydrogen and oxygen on the Schottky barrier height of nickel on (111) and (100) diamond surfaces*. Physical Review B, 1994. **49**(19): p. 13629.
187. Matkovich, V. and J. Economy, *Structural determinants in the higher borides*, in *Boron and Refractory Borides*. 1977, Springer. p. 78-95.
188. Niu, J., B. Rao, and P. Jena, *Atomic and electronic structures of neutral and charged boron and boron-rich clusters*. The Journal of chemical physics, 1997. **107**(1): p. 132-140.
189. She, J., *et al.*, *Laser welding of a single tungsten oxide nanotip on a handleable tungsten wire: A demonstration of laser-weld nanoassembly*. Applied physics letters, 2007. **90**(7): p. 073103.

190. She, J., *et al.*, *Vacuum breakdown of carbon-nanotube field emitters on a silicon tip*. Applied physics letters, 2003. **83**(13): p. 2671-2673.
191. Milne, W., *et al.*, *Electrical and field emission investigation of individual carbon nanotubes from plasma enhanced chemical vapour deposition*. Diamond and Related Materials, 2003. **12**(3-7): p. 422-428.
192. Xu, Z., *et al.*, *Field emission of individual carbon nanotube with in situ tip image and real work function*. Applied Physics Letters, 2005. **87**(16): p. 163106.
193. Dai, H., *et al.*, *Probing electrical transport in nanomaterials: conductivity of individual carbon nanotubes*. Science, 1996. **272**(5261): p. 523-526.
194. Chen, G., *et al.*, *Enhanced field emission properties of vertically aligned double-walled carbon nanotube arrays*. Nanotechnology, 2008. **19**(41): p. 415703.
195. Frank, S., *et al.*, *Carbon nanotube quantum resistors*. science, 1998. **280**(5370): p. 1744-1746.
196. Lv, R., *et al.*, *Enhanced field emission of open-ended, thin-walled carbon nanotubes filled with ferromagnetic nanowires*. Carbon, 2009. **47**(11): p. 2709-2715.
197. Zhang, Y., *et al.*, *Study of high-brightness flat-panel lighting source using carbon-nanotube cathode*. Journal of Vacuum Science & Technology B: Microelectronics and Nanometer Structures Processing, Measurement, and Phenomena, 2008. **26**(1): p. 106-109.
198. Yang, X., *et al.*, *Ab initio prediction of stable boron sheets and boron nanotubes: Structure, stability, and electronic properties*. Physical Review B, 2008. **77**(4).
199. Hu, H., *et al.*, *Influence of the zeta potential on the dispersability and purification of single-walled carbon nanotubes*. The Journal of Physical Chemistry B, 2005. **109**(23): p. 11520-11524.
200. Hillert, M. and N. Lange, *The structure of graphite filaments*. Zeitschrift für Kristallographie-Crystalline Materials, 1959. **111**(1-6): p. 24-34.
201. Arnold, M.S., *et al.*, *Sorting carbon nanotubes by electronic structure using density differentiation*. Nat Nanotechnol, 2006. **1**(1): p. 60-5.
202. Yu, A., *et al.*, *Application of centrifugation to the large-scale purification of electric arc-produced single-walled carbon nanotubes*. Journal of the American Chemical Society, 2006. **128**(30): p. 9902-9908.
203. Chen, Y., *et al.*, *Boron nitride nanotubes: Pronounced resistance to oxidation*. Applied Physics Letters, 2004. **84**(13): p. 2430-2432.

204. Gore, J.P. and A. Sane, *Flame synthesis of carbon nanotubes*, in *Carbon Nanotubes-Synthesis, Characterization, Applications*. 2011, InTech.
205. Thess, A., *et al.*, *Crystalline ropes of metallic carbon nanotubes*. *Science*, 1996: p. 483-487.
206. Lee, R.S., *et al.*, *Catalyst-free synthesis of boron nitride single-wall nanotubes with a preferred zig-zag configuration*. *Physical Review B*, 2001. **64**(12).
207. Arenal, R., *et al.*, *Root-growth mechanism for single-walled boron nitride nanotubes in laser vaporization technique*. *Journal of the American Chemical Society*, 2007. **129**(51): p. 16183-16189.
208. Endo, M., *et al.*, *The production and structure of pyrolytic carbon nanotubes (PCNTs)*. *Journal of Physics and Chemistry of Solids*, 1993. **54**(12): p. 1841-1848.
209. Kamarudin, M.A., *et al.*, *A review on the fabrication of polymer-based thermoelectric materials and fabrication methods*. *The Scientific World Journal*, 2013. **2013**.
210. Kong, J., *et al.*, *Chemical vapor deposition of methane for single-walled carbon nanotubes*. *Chemical Physics Letters*, 1998. **292**(4): p. 567-574.
211. Zhang, Y., *et al.*, *Electric-field-directed growth of aligned single-walled carbon nanotubes*. *Applied physics letters*, 2001. **79**(19): p. 3155-3157.
212. Li, Y., *et al.*, *Growth of single-walled carbon nanotubes from discrete catalytic nanoparticles of various sizes*. *The Journal of Physical Chemistry B*, 2001. **105**(46): p. 11424-11431.
213. Dai, H., *et al.*, *Controlled chemical routes to nanotube architectures, physics, and devices*. 1999, ACS Publications.
214. Nikolaev, P., *et al.*, *Gas-phase catalytic growth of single-walled carbon nanotubes from carbon monoxide*. *Chemical physics letters*, 1999. **313**(1): p. 91-97.
215. Dai, H., *et al.*, *Single-wall nanotubes produced by metal-catalyzed disproportionation of carbon monoxide*. *Chemical Physics Letters*, 1996. **260**(3-4): p. 471-475.
216. Maruyama, S., *et al.*, *Low-temperature synthesis of high-purity single-walled carbon nanotubes from alcohol*. *Chemical physics letters*, 2002. **360**(3): p. 229-234.
217. Li, Y., *et al.*, *Preferential growth of semiconducting single-walled carbon nanotubes by a plasma enhanced CVD method*. *Nano Letters*, 2004. **4**(2): p. 317-321.
218. Chen, J., *et al.*, *Large on-off ratios and negative differential resistance in a molecular electronic device*. *Science*, 1999. **286**(5444): p. 1550-1552.
219. Patil, S.T., *Design and Optimization of Ball Mill for Clinker Grinding in Cement Plant*.

220. Ahn, C.C., *Transmission electron energy loss spectrometry in materials science and the EELS atlas*. 2006: John Wiley & Sons.
221. Krätschmer, W., *et al.*, *Solid C60: a new form of carbon*. *Nature*, 1990. **347**: p. 27.
222. Ebbesen, T. and A. P M, *Large-scale synthesis of carbon*. *Nature*, 1992. **358**: p. 16.
223. Bethune, D., *et al.*, *Cobalt-catalysed growth of carbon nanotubes with single-atomic-layer walls*. *Nature*, 1993. **363**(6430): p. 605-607.
224. Iijima, S. and T. Ichihashi, *Single-shell carbon nanotubes of 1-nm diameter*. *nature*, 1993. **363**: p. 603-605.
225. Chopra, N.G., *et al.*, *Boron nitride nanotubes*. *Science*, 1995. **269**(5226): p. 966.
226. Shifrina, P., *Synthesis of carbon nanotubes*. 2011.
227. Biswas, A., *et al.*, *Single metal nanoparticle spectroscopy: optical characterization of individual nanosystems for biomedical applications*. *Nanoscale*, 2010. **2**(9): p. 1560-1572.
228. Harris, D.C. and M.D. Bertolucci, *Symmetry and spectroscopy: an introduction to vibrational and electronic spectroscopy*. 1978: Courier Corporation.
229. Le Ru, E., *et al.*, *Surface enhanced Raman scattering enhancement factors: a comprehensive study*. *The Journal of Physical Chemistry C*, 2007. **111**(37): p. 13794-13803.
230. Nie, S. and S.R. Emory, *Probing single molecules and single nanoparticles by surface-enhanced Raman scattering*. *science*, 1997. **275**(5303): p. 1102-1106.
231. Zamborini, F.P., *et al.*, *Distance-dependent electron hopping conductivity and nanoscale lithography of chemically-linked gold monolayer protected cluster films*. *Analytica Chimica Acta*, 2003. **496**(1-2): p. 3-16.
232. Alberti, G. and G. Nuzzaci, *1.6. 5 SEM and TEM techniques*. *World Crop Pests*, 1996. **6**: p. 399-410.
233. Williams, D.B. and C.B. Carter, *The transmission electron microscope*, in *Transmission electron microscopy*. 1996, Springer. p. 3-17.
234. Bhattacharya, S., *et al.*, *Polymeric nanocomposites theory and practice*. 2008: Carl Hanser Publishers.
235. Todokoro, H. and M. Ezumi, *Scanning electron microscope*. 1999, Google Patents.
236. Egerton, R.F., *Electron energy-loss spectroscopy in the electron microscope*. 2011: Springer Science & Business Media.

237. Callister, W.D., *Materials Science and Engineering: An Introduction*, 94-95. 1997, John Wiley and Sons, 4th Edition, New York.
238. Cao, G., *Nanostructures and nanomaterials: synthesis, properties and applications*. 2004: World Scientific.
239. Adiguzel, Y., *Utilization of Dialysis Membrane for Biosensor Applications by UV Spectrophotometric Detection*.
240. O'connell, M.J., *et al.*, *Band gap fluorescence from individual single-walled carbon nanotubes*. *Science*, 2002. **297**(5581): p. 593-596.
241. Xiao, Y., *et al.*, *Single-nanowire single-mode laser*. *Nano Lett*, 2011. **11**(3): p. 1122-6.
242. Bachilo, S.M., *et al.*, *Structure-assigned optical spectra of single-walled carbon nanotubes*. *Science*, 2002. **298**(5602): p. 2361-2366.
243. Wang, J., *et al.*, *Photocatalytic degradation of acetone over a V2O5/LaF3 catalyst under visible light*. *The Journal of Physical Chemistry C*, 2008. **112**(26): p. 9723-9729.
244. Arepalli, S., *et al.*, *A parametric study of single-wall carbon nanotube growth by laser ablation*. *Journal of nanoscience and nanotechnology*, 2004. **4**(7): p. 762-773.
245. Gorbunoff, A. and O. Jost, *Laser Ablation Synthesis of Single-Wall Carbon Nanotubes: The SLS Model*. *Pulsed Laser Deposition of Thin Films: Applications-Led Growth of Functional Materials*: p. 611-632.
246. Yudasaka, M., *et al.*, *Causes of different catalytic activities of metals in formation of single-wall carbon nanotubes*. *Applied Physics A: Materials Science & Processing*, 2002. **74**(3): p. 377-385.
247. Rummeli, M.H., *et al.*, *Catalyst volume to surface area constraints for nucleating carbon nanotubes*. *The Journal of Physical Chemistry B*, 2007. **111**(28): p. 8234-8241.
248. Avouris, P., *Carbon nanotube electronics and photonics*. *Physics Today*, 2009. **62**(1): p. 34-40.
249. Patel, R.B., *et al.*, *Boron-Filled Hybrid Carbon Nanotubes*. *Sci Rep*, 2016. **6**: p. 30495.
250. Patel, R., *et al.*, *Synthesis of boron nanowires, nanotubes, and nanosheets*. *Journal of Nanomaterials*, 2015. **16**(1): p. 14.
251. Yang, H.T., *et al.*, *Self-assembly and magnetic properties of cobalt nanoparticles*. *Applied Physics Letters*, 2003. **82**(26): p. 4729-4731.
252. Sun, C., *et al.*, *Synthesis of light-field raw data from RGB-D images*. in *Image Processing (ICIP), 2015 IEEE International Conference on*. 2015. IEEE.

253. Motaung, D.E., *et al.*, *In situ optical emission study on the role of C2 in the synthesis of single-walled carbon nanotubes*. Journal of Applied Physics, 2010. **107**(4): p. 044308.
254. Harris, P.J.F., *Solid state growth mechanisms for carbon nanotubes*. Carbon, 2007. **45**(2): p. 229-239.
255. Wang, Z., *et al.*, *Effect of substrate position on the morphology of boron products by laser ablation*. Applied Physics A, 2004. **79**(4-6): p. 891-893.
256. Huang, H., *et al.*, *Preparation and characterization of superhard boron-suboxide films*. Journal of Vacuum Science & Technology A: Vacuum, Surfaces, and Films, 2003. **21**(5): p. 1595-1602.
257. Kumar, C.S., *Metallic Nanomaterials: Nanomaterials for Life Sciences (Vch)*. 2009: Wiley.
258. Kurakevych, O.O., *et al.*, *Comparison of solid-state crystallization of boron polymorphs at ambient and high pressures*. High Pressure Research, 2012. **32**(1): p. 30-38.
259. Shirai, K. and S. Emura, *Lattice vibrations and the bonding nature of boron carbide*. Journal of Physics: Condensed Matter, 1996. **8**(50): p. 10919.
260. Lee, S., *et al.*, *Bands and bonds of B 12*. Physical Review B, 1990. **42**(2): p. 1316.
261. Chakrabarti, A., *et al.*, *Synthesis of boron nanorods by smelting non-toxic boron oxide in liquid lithium*. Journal of Nanomaterials, 2010. **2010**: p. 9.
262. Jin, M.-S. and N.-O. Kim, *Photoluminescence of hexagonal boron nitride (h-BN) film*. Journal of Electrical Engineering and Technology, 2010. **5**(4): p. 637-639.
263. Ishigami, M., *et al.*, *Observation of the giant Stark effect in boron-nitride nanotubes*. Physical review letters, 2005. **94**(5): p. 056804.
264. Casey, J.D. and J.S. Haggerty, *Laser-induced vapour-phase syntheses of boron and titanium diboride powders*. Journal of materials science, 1987. **22**(2): p. 737-744.
265. Taniguchi, T. and K. Watanabe, *Synthesis of high-purity boron nitride single crystals under high pressure by using Ba–BN solvent*. Journal of crystal growth, 2007. **303**(2): p. 525-529.
266. Museur, L., *et al.*, *Defect-related photoluminescence of hexagonal boron nitride*. Physical Review B, 2008. **78**(15): p. 155204.
267. Jaffrennou, P., *et al.*, *Optical properties of multiwall boron nitride nanotubes*. physica status solidi (b), 2007. **244**(11): p. 4147-4151.

268. Wu, J., *et al.*, *Raman spectroscopy and time-resolved photoluminescence of BN and B_xC_yN_z nanotubes*. Nano letters, 2004. **4**(4): p. 647-650.
269. Moodley, M.K. and N.J. Coville, *Experimental evidence for the early nucleation of single-walled carbon nanotubes*. Chemical Physics Letters, 2010. **498**(1-3): p. 140-144.
270. Guo, T., *et al.*, *Catalytic growth of single-walled nanotubes by laser vaporization*. Chemical physics letters, 1995. **243**(1-2): p. 49-54.
271. Spear, K., *Rare earth-boron phase equilibria*, in *Boron and Refractory Borides*. 1977, Springer. p. 439-456.
272. Ciuparu, D., *et al.*, *Uniform-diameter single-walled carbon nanotubes catalytically grown in cobalt-incorporated MCM-41*. The Journal of Physical Chemistry B, 2004. **108**(2): p. 503-507.
273. Ekimov, E.A. and I.P. Zibrov, *High-pressure high-temperature synthesis and structure of α -tetragonal boron*. Science and technology of advanced materials, 2011. **12**(5): p. 055009.
274. Shirai, K. and H. Katayama-Yoshida, *The narrow Raman linewidth of a librational mode of α -rhombohedral boron and its anharmonic effects*. Journal of the Physical Society of Japan, 1998. **67**(11): p. 3801-3808.
275. Dube, C.L., *et al.*, *Synthesis of Silicon Nanowires Using Microwave Energy for Optical Devices*. International Journal of Green Nanotechnology: Materials Science & Engineering, 2009. **1**(1): p. M11-M15.
276. Sharma, P. and R.K. Sharma, *Platinum functionalized multiwall carbon nanotube composites as recyclable catalyst for highly efficient asymmetric hydrogenation of methyl pyruvate*. RSC Advances, 2015. **5**(124): p. 102481-102487.
277. Widom, M. and M. Mihalkovič, *Symmetry-broken crystal structure of elemental boron at low temperature*. Physical Review B, 2008. **77**(6): p. 064113.
278. Yang, Q., *et al.*, *Aligned single crystal Al-catalyzed boron nanorods on Si substrates*. The European Physical Journal B, 2007. **56**(1): p. 35-39.
279. Li, D., *et al.*, *Electronic structures, total energies, and optical properties of α -rhombohedral B 12 and α -tetragonal B 50 crystals*. Physical Review B, 1992. **45**(11): p. 5895.
280. Patel, J., *et al.*, *Synthesis and properties of nickel–cobalt–boron nanoparticles*. IOP Publishing.

281. Barakat, N.A.M., *et al.*, *Cobalt nanofibers encapsulated in a graphite shell by an electrospinning process*. Journal of Materials Chemistry, 2009. **19**(39): p. 7371-7378.
282. Çalik, A., *et al.*, *The Effect of Boronizing on the Magnetization Behaviour of Low Carbon Microalloyed Steels*. Journal of Magnetism, 2012. **17**(2): p. 96-99.
283. Nayak, B.B., *et al.*, *Ni and Ni–nickel oxide nanoparticles with different shapes and a core–shell structure*. Thin Solid Films, 2006. **505**(1-2): p. 109-112.
284. Wagner, R. and W. Ellis, *Vapor-liquid-solid mechanism of single crystal growth*. Applied Physics Letters, 1964. **4**(5): p. 89-90.
285. Givargizov, E., *Fundamental aspects of VLS growth*, in *Vapour Growth and Epitaxy*. 1975, Elsevier. p. 20-30.
286. Westwater, J., *et al.*, *Growth of silicon nanowires via gold/silane vapor–liquid–solid reaction*. Journal of Vacuum Science & Technology B: Microelectronics and Nanometer Structures Processing, Measurement, and Phenomena, 1997. **15**(3): p. 554-557.
287. Adams, R.M., *Boron, metallo-boron compounds, and boranes*. 1964: Interscience Publishers.
288. Newkirk, A., *Boron, metallo-boron compounds, and Boranes*. John Wiley and Sons, New York, 1964) p, 1964. **233**.
289. Pastor, H. and V. Matkovich, *Boron and refractory borides*. Springer-Verlag, New York, 1977) p, 1977. **457**.
290. Usrey, M., *et al.*, *Evidence for a two-step mechanism in electronically selective single-walled carbon nanotube reactions*. Journal of the American Chemical Society, 2005. **127**(46): p. 16129-16135.
291. Arnold, M., *et al.*, *Enrichment of single-walled carbon nanotubes by diameter in density gradients*. Nano Letters, 2005. **5**(4): p. 713-718.
292. Brakke, M.K., *Density gradient centrifugation and its application to plant viruses*. Advances in Virus Research, 1961. **7**: p. 193-224.
293. Wang, H., *et al.*, *Dispersing single-walled carbon nanotubes with surfactants: a small angle neutron scattering study*. Nano Letters, 2004. **4**(9): p. 1789-1793.
294. Hennrich, F., *et al.*, *Diameter sorting of carbon nanotubes by gradient centrifugation: Role of endohedral water*. physica status solidi (b), 2007. **244**(11): p. 3896-3900.
295. Nair, N., *et al.*, *Dynamics of surfactant-suspended single-walled carbon nanotubes in a centrifugal field*. Langmuir, 2008. **24**(5): p. 1790-1795.

296. Richard, C., *et al.*, *Supramolecular self-assembly of lipid derivatives on carbon nanotubes*. *Science*, 2003. **300**(5620): p. 775-778.
297. Zhao, P., *et al.*, *Controllable expansion of single-walled carbon nanotube dispersions using density gradient ultracentrifugation*. *The Journal of Physical Chemistry C*, 2010. **114**(11): p. 4831-4834.
298. Bonaccorso, F., *et al.*, *Density gradient ultracentrifugation of nanotubes: Interplay of bundling and surfactants encapsulation*. *The Journal of Physical Chemistry C*, 2010. **114**(41): p. 17267-17285.
299. Suresh, A.K., *et al.*, *Size-separation of silver nanoparticles using sucrose gradient centrifugation*. *Journal of Chromatography & Separation Techniques*, 2015. **6**(5).
300. Antaris, A.L., *et al.*, *Sorting single-walled carbon nanotubes by electronic type using nonionic, biocompatible block copolymers*. *ACS nano*, 2010. **4**(8): p. 4725-4732.
301. Massote, D.V., *et al.*, *Electronic, vibrational, Raman, and scanning tunneling microscopy signatures of two-dimensional boron nanomaterials*. *Physical Review B*, 2016. **94**(19): p. 195416.
302. Arenal, R., *et al.*, *Raman spectroscopy of single-wall boron nitride nanotubes*. *Nano letters*, 2006. **6**(8): p. 1812-1816.
303. Jain, A., *et al.*, *Structural characterization of electrodeposited boron*. *Bulletin of Materials Science*, 2013. **36**(7): p. 1323-1329.
304. Hosoi, S., *et al.*, *Electron density distributions in derivative crystals of α -rhombohedral boron*. *Journal of the Physical Society of Japan*, 2007. **76**(4): p. 044602-044602.
305. Binnenbruck, H. and H. Werheit, *IR-active phonons of boron and boron carbide*. *Zeitschrift für Naturforschung A*, 1979. **34**(7): p. 787-798.
306. Shelnutt, J., *et al.* *Raman spectroscopy of boron carbides and related boron-containing materials*. in *AIP Conference Proceedings*. 1986. AIP.
307. Tallant, D., *et al.*, *Boron carbide structure by Raman spectroscopy*. *Physical review B*, 1989. **40**(8): p. 5649.
308. Tallant, D., *et al.*, *Structure of icosahedral borides by Raman spectroscopy*. in *AIP Conference Proceedings*. 1991. AIP.
309. Beckel, C.L. and M. Yousaf. *Lattice vibrations of icosahedral boron-rich solids*. in *AIP Conference Proceedings*. 1991. AIP.

310. Kurakevych, O.O. and V.L. Solozhenko, *300-K equation of state of rhombohedral boron subnitride, B13N2*. Solid State Communications, 2009. **149**(47-48): p. 2169-2171.
311. Kuhlmann, U. and H. Werheit, *Raman effect of boron carbide (B4. 3C to B10. 37C)*. Journal of alloys and compounds, 1994. **205**(1-2): p. 87-91.
312. Fantini, C., *et al.*, *Optical transition energies for carbon nanotubes from resonant Raman spectroscopy: Environment and temperature effects*. Physical review letters, 2004. **93**(14): p. 147406.
313. Jain, A., *et al.*, *Structural characterization of electrodeposited boron*. Bulletin of Materials Science, 2013. **36**(7): p. 1323-1329.